

Northumbria Research Link

Citation: Aresh, Balaji (2012) Fundamental Study into the Mechanics of Material Removal in Rock Cutting. Doctoral thesis, Northumbria University.

This version was downloaded from Northumbria Research Link:
<https://nrl.northumbria.ac.uk/id/eprint/22076/>

Northumbria University has developed Northumbria Research Link (NRL) to enable users to access the University's research output. Copyright © and moral rights for items on NRL are retained by the individual author(s) and/or other copyright owners. Single copies of full items can be reproduced, displayed or performed, and given to third parties in any format or medium for personal research or study, educational, or not-for-profit purposes without prior permission or charge, provided the authors, title and full bibliographic details are given, as well as a hyperlink and/or URL to the original metadata page. The content must not be changed in any way. Full items must not be sold commercially in any format or medium without formal permission of the copyright holder. The full policy is available online: <http://nrl.northumbria.ac.uk/policies.html>

Fundamental Study into the Mechanics of Material Removal in Rock Cutting

Balaji Aresh

A thesis submitted in partial fulfilment
of the requirements of the
University of Northumbria at Newcastle upon Tyne
for the degree of
Doctor of Philosophy

Research undertaken in the
School of Computing, Engineering and Information Sciences

November 2012

Abstract

The objective of this work was to understand the mechanics of material removal during rock cutting. The exact nature of the failure of the rock material at the tool tip was investigated using a single cutting tooth test rig coupled with high speed photography, for various rock-like specimens. Linear cutting tests were performed using a tungsten carbide tipped orthogonal cutting tool with three different rake angles on low and high strength simulated rocks. Statistical analysis together with high speed video analysis were supported by numerical simulation, performed using a commercially available code called ELFEN; a hybrid finite-discrete element software package.

The material removal process was modelled by studying the cutting and thrust forces in relation to the high speed videos, specific cutting energy and the chip removal process. Although considerable amounts of published work are available, which describe the mechanism of material removal while machining rocks, no systematic, dedicated research investigating the material behaviour at the extreme cutting edge has been carried out, in particular, at the microscale level. The material behaviour at the extreme cutting edge contributes to the mechanism of the material removal. Compared with its counterpart such as metal cutting, which is a highly established and well understood domain, the heterogeneous nature of rocks renders it difficult to apply a particular study simply based on one variety of rock.

In order to ensure repeatability and consistency in experimental data, the use of rock-like specimens was considered critical. Hence, using various concrete mixes, samples were manufactured and categorised by testing their mechanical properties, i.e. Compressive strength, Flexural strength, Young's Modulus and Density. Linear cutting tests were performed on the samples and force readings using a tri-axial dynamometer were recorded and analysed. High speed video system incorporated in the test rig also recorded the cutting process. Specific cutting energy was calculated and correlated with other cutting parameters such as depth of cut and rake angle of the cutting tool.

Exhaustive statistical analysis was carried out to understand the influence of specific cutting parameters and mechanical properties on the cutting process. Finally, numerical simulation of the cutting process was modelled using ELFEN, a Finite-Discrete Element coupled code. This yielded the important results as to the stress encountered in the specimen in the immediate vicinity of the cutting tool and also insights into the fracture initiation and propagation.

The influence of cutting parameters on the measured cutting force and thrust force showed the effect of material strength, cutting tool geometry and depth of cut were important. General observations showed the increase of cutting force as the depth of cut increases. Specific energy was found to decrease as the depth of cut increased. The formation of the crushed zone was studied using the high speed video camera and found to play an important role in the cutting force component; as the crushed zone built up the cutting force was found to increase until failure. Numerical simulations also showed the formation of crushed zone and the state of stress at the tool tip.

Acknowledgements

I would like to express my sincere gratitude to Dr Ali Daadbin without whose help this research would not have seen completion. With extreme patience he has guided me at every stage of this work. Under his tutelage, he has not only provided me with sound academic and professional advise but also provided pastoral care and has always steered me in the right direction. His caring nature has pulled me through some tough times and I shall always be in debt to him for his efforts. Through our numerous discussions I have imbibed a great amount of knowledge and skills from him and he has always stood out as a role model for undertaking work in a professional and ethical manner.

I would like to thank Prof Mohammed Sarwar and Dr James Burnell-Gray for introducing me to this topic of research and for their guidance in carrying out this research. This research was carried out within the School of Computing, Engineering and Information Science at Northumbria University in collaboration with BIOS Technologies LLP, Gateshead. I would like to them for providing me the studentship and funding to carry out this research.

I would like to thank Dr Roger Penlington for his help and advise on numerical simulation work. I would like to thank Rockfield Software Limited (Swansea) for providing me with the ELFEN software and technical advise. I would like to thank Dr Alan Richardson for his advise on specimen mix and preparation. I would also like to thank EPSRC for providing on loan the high speed video camera Phantom V7.3.

I would like to thank the technical team at CEIS especially Phil Donnelly, Sam Hutchinson, Simon Neville and Bob Best for their technical support. I would also like to thank the team from Built Environment lab especially Steve Colvin, Stewart Wilkin, Leon Ames and Christopher Walton for their help in sample preparation and testing.

I would like to thank the administrative staff especially Gillian Brooks for her timely advise and also ensuring that paper work doesn't get in the way of my research!

I would also like to thank Dr Alireza Maheri, Dr Krishna Busawon, Dr Noel Perera, Dr John Tan and Prof Fary Ghassemlooy for their advise and support during my research.

A great heap of thanks to my friends and colleagues Fahd Khan, Sajjad Khan and Andrew Naylor who helped me to huge doses of fun and lively conversations which helped me keep my rationality intact! I would like to thank the ‘merry’ bunch of E409 and E411ers. Thank you Larry, Xiao, Pietro, Remi, Karen, Marta, Mary, St. Andrew, Paul, Gobind, Joaquin, Jiri, Lei, Dehao, Azadeh, Arash, Al Arash, Thava, Rupak Jr, Rupak Sr, Sujan, Matthew, Sul, It Lee, Xuan, Yuan, Kade, Panu, Wichian, Tom, Okan, Terrence, Draco, Sofia, Juliette, Maria, Caroline, Abheesha, Kugen, Sham, Freeborn, Salem, Ijaz, Jean-Pierre, Lalith, Moji, Mutsam, Philip, Rajesh and Samir..to name a few!

I would like to thank my friends Wilfred Martin, Kevin David, Hiran Kumar, Ashok ‘Vicky’, Harish Hanumanthappa, Shaji Luke a.k.a iDa, Subha Kadackel and Jagadeep Thota for their support.

My parents, I cannot thank you enough for the love and care that you have given me. My Dad, Aresh Balasundaram and Ma, Kalpana Aresh, you have always encouraged and supported me in whatever I have ventured out to do. To you I dedicate this work.

I would like to thank my brother Dr Lokesh Aresh for supporting me in every aspect of my life, my sister-in-law Kadambari Lokesh for all the lively conversations and my dearest nephew Anurag a.k.a Jiggy who has taught me that life’s greatest problems can be solved by trampolining, chocolates and chicken nuggets.

Last but not the least, the love of my life, Preeti Singh, you are my pillar of support. Thank you for your patience and your constant encouragement against all odds.

Declaration

I declare that the work presented in this thesis has not been submitted for any other award and that is it all my own work.

Name

Table of Contents

Abstract	i
Acknowledgements	iii
Declaration	v
List of Figures	x
List of Tables	xiv
List of Abbreviations	xv
CHAPTER 1: INTRODUCTION	
1.1. Introduction	1
1.2. Aim and objectives	4
1.3. Novel aspects of this research	4
1.4. Thesis structure	5
CHAPTER 2: LITERATURE REVIEW	
2.1. Introduction	6
2.2. Overview of Fracture Mechanics	6
2.3. Rock Fracture Mechanics	11
2.3.1 Failure criteria for rocks	12
2.3.1.1 Tresca Yield Criterion	12
2.3.1.2 Mohr-Coulomb Criterion	13
2.3.1.3 Hoek-Brown Criterion	15
	vi

2.3.1.4.	Griffith Energy Criterion	16
2.3.1.5.	Drucker-Prager Criterion	17
2.3.2.	Failure mechanisms	18
2.3.2.1.	Merchant's Model	18
2.3.2.2.	Evan's Model	19
2.3.2.3.	Nishimatsu's Model	20
2.4.	Rock Drilling Systems	22
2.4.1.	A note on drilling of rocks	22
2.4.2.	Machining of rocks	23
2.4.2.1.	Rotary Percussive	23
2.4.2.2.	Rotary Crushing	24
2.4.2.3.	Cutting	24
2.5.	Specific Energy	26
2.6.	A review on the use of simulated rock materials	27
2.7.	Overview of Numerical Methods	29

CHAPTER 3: EXPERIMENTAL PROCEDURE

3.1.	Introduction	32
3.2.	Sample preparation	32
3.3.	Sample Characterization- Testing for mechanical properties	34
3.3.1.	Uni-axial Compressive Strength Test	34
3.3.2.	Flexural strength test	36
3.4.	Experimental Rig	39
3.4.1.	Single Cutting Tooth Test Rig	39
3.4.2.	Calibration of Dynamometer	42
3.4.3.	Orthogonal cutting tools	43
3.5.	Linear Cutting Tests	43

CHAPTER 4: RESULTS AND DISCUSSION

4.1.	Introduction	45
4.2.	Preliminary Cutting Test	45
4.3.	Summary of experimental results	48
4.4.	Force signal analysis	51
4.5.	Effect of Rake Angle and Depth of Cut on the cutting performance of the tool	53
4.5.1.	Variation of cutting force and thrust force	53
4.5.1.1.	Low strength sample	54
4.5.1.1.1.	Cutting test using 0° rake angle cutting tool	54
4.5.1.1.2.	Cutting test using 10° rake angle cutting tool	57
4.5.1.1.3.	Cutting test using 20° rake angle cutting tool	60
4.5.1.1.4.	Statistical analysis of cutting test on low strength sample	63
4.5.1.1.5.	Summary of cutting test on low strength sample	67
4.5.1.2.	High strength sample	68
4.5.1.2.1.	Cutting test using 0° rake angle cutting tool	68
4.5.1.2.2.	Cutting test using 10° rake angle cutting tool	71
4.5.1.2.3.	Cutting test using 20° rake angle cutting tool	74
4.5.1.2.4.	Statistical analysis of cutting test on high strength sample	77
4.5.1.2.5.	Summary of cutting test on high strength sample	81
4.5.2.	Variation of specific energy	82
4.6.	Effect of the Crushed Zone on the Cutting Performance of the Tool	88
4.6.1.	Characteristics of the crushed zone	88
4.6.1.1.	Failure Mechanism in Mode A	91
4.6.1.2.	Failure Mechanism in Mode B	94
4.6.1.3.	Force analysis	97
4.7.	Numerical modeling of the cutting process	99

4.7.1.	ELFEN	99
4.7.2.	Modelling	101
4.7.3.	Numerical analysis of the cutting process on low strength sample	106
4.7.4.	Numerical analysis of the cutting process on high strength sample	113
4.7.5.	Summary	117
CHAPTER 5: CONCLUSION AND FUTURE WORK		
5.1.	Conclusions	118
5.2.	Critical Appraisal	119
5.3	Future Work	121
	REFERENCES	122
	APPENDIX A: CALIBRATION RESULTS OF THE TRI-AXIAL DYNAMOMETER	133
	APPENDIX B: STATISTICAL ANALYSIS OF THE INFLUENCE OF RAKE ANGLE ON THE CUTTING FORCE FOR LOW STRENGTH SAMPLE	136
	APPENDIX C: STATISTICAL ANALYSIS OF THE INFLUENCE OF RAKE ANGLE ON THE THRUST FORCE FOR LOW STRENGTH SAMPLE	139
	APPENDIX D: STATISTICAL ANALYSIS OF THE INFLUENCE OF RAKE ANGLE ON THE CUTTING FORCE FOR HIGH STRENGTH SAMPLE	142
	APPENDIX E: STATISTICAL ANALYSIS OF THE INFLUENCE OF RAKE ANGLE ON THE THRUST FORCE FOR HIGH STRENGTH SAMPLE	145

APPENDIX F:	CHARACTERISTICS OF CHIPS	148
APPENDIX G:	NUMERICAL SIMULATION OF CUTTING A LOW STRENGTH SAMPLE USING A 20° RAKE ANGLE CUTTING TOOL	164
APPENDIX H:	NUMERICAL SIMULATION OF CUTTING A HIGH STRENGTH SAMPLE USING A 20° RAKE ANGLE CUTTING TOOL	166

List of Figures

Figure 1.1	Chip formation in metal cutting.....	2
Figure 1.2	Chip formation in rock cutting.....	2
Figure 2.1	Inglis work on thin plates with elliptical hole.....	7
Figure 2.2	A stressed cracked plate explaining the derivation of the Griffith criterion.....	8
Figure 2.3	Splitting of mica using a glass slab having a single point of contact..	9
Figure 2.4	Three modes of deformation.....	10
Figure 2.5	a) Representation of the Mohr-Coulomb failure plane b) Mohr Envelope.....	14
Figure 2.6	Curved envelope defined by the Hoek-Brown criterion.....	16
Figure 2.7	Schematic of Merchant cutting model.....	18
Figure 2.8	Schematic representation of Evans's model.....	19
Figure 2.9	Schematic representation of Nishimatsu's theory of rock cutting and the rock cutting process.....	21
Figure 2.10	Rock removal process: a) Rotary percussive drill bit b) Rotary Crushing c)Cutting.....	23
Figure 2.11	Effect of confining pressure on the chip production in rock cutting...	25
Figure 2.12	a) Roadheader b) Tunnel Boring Machine.....	26
Figure 2.13	Stimpson's simple classification of modelling materials.....	28

Figure 2.14	Capabilities of ELFEN.....	31
Figure 3.1	Uni-axial compressive strength testing machine.....	35
Figure 3.2	Failure observed in compression testing of rock-like samples.....	35
Figure 3.3	Centre-point loading arrangement to test flexural strength.....	37
Figure 3.4	Schematic of the single cutting tooth test rig.....	39
Figure 3.5	Single cutting tooth test rig and associated components.....	40
Figure 3.6	Tri-axial force components.....	41
Figure 3.7	Calibration of the tri-axial dynamometer using the Instron testing machine.....	42
Figure 3.8	Orthogonal cutting tools.....	43
Figure 3.9	The matrix of experiments.....	44
Figure 4.1	Failure to complete the cut at lower speed setting.....	48
Figure 4.2	Force signals obtained from tri-axial dynamometer measuring a single cut showing- Side force (F_s), Thrust force (F_p) and Cutting force (F_v).....	49
Figure 4.3	Typical tri-axial forces measured for the duration of a single cut.....	49
Figure 4.4	Variation of cutting and thrust force with increase in depth of cut.....	52
Figure 4.5	Variation of the cutting force and thrust force.....	53
Figure 4.6	Variation of the cutting force (F_v) and thrust force (F_p) with respect to depth of cut using a 0° rake angle cutting tool.....	54
Figure 4.7	Comparison of a typical cutting force trace at depths of cut of 0.5 mm and 2.5 mm on a low strength sample using a 0° rake angle cutting tool.....	55
Figure 4.8	Comparison of a typical thrust force trace at depths of cut 0.5 mm and 2.5 mm on a low strength sample using a 0° rake angle cutting tool.....	55
Figure 4.9	Characteristics of chips obtained at (a) 0.5 mm and (b) 2.5 mm.....	56
Figure 4.10	Variation of cutting force (F_v) and thrust force (F_p) with respect to depth of cut using a 10° rake angle cutting tool.....	57
Figure 4.11	Comparison of a typical cutting force trace at depths of cut at 0.5 mm and 2.5 mm on a low strength sample using a 10° rake angle cutting tool.....	58
Figure 4.12	Comparison of a typical thrust force trace at depths of cut of 0.5 mm and 2.5 mm on a low strength sample using a 10° rake angle cutting tool.....	58

	tool.....	
Figure 4.13	Characteristics of chips obtained at (a) 0.5 mm and (b) 2.5 mm.....	59
Figure 4.14	Variation of the cutting force (F_v) and thrust force (F_p) with respect to depth of cut using a 20° rake angle cutting tool.....	60
Figure 4.15	Comparison of a typical cutting force trace at depths of cut of 0.5 mm and 2.5 mm on a low strength sample using a 20° rake angle cutting tool.....	61
Figure 4.16	Comparison of a typical thrust force trace at depths of cut of 0.5 mm and 2.5 mm on a low strength sample using a 20° rake angle cutting tool.....	61
Figure 4.17	Characteristics of chips obtained at (a) 0.5 mm and (b) 2.5 mm.....	62
Figure 4.18	Empirical relation between cutting force and rake angle.....	63
Figure 4.19	Empirical relation between cutting force and depth of cut.....	64
Figure 4.20	Residual plots obtained for cutting force via rake angle and depth of cut.....	65
Figure 4.21	Empirical relation between thrust force and rake angle.....	65
Figure 4.22	Empirical relation between thrust force and depth of cut.....	66
Figure 4.23	Variation of the cutting force (F_v) and thrust force (F_p) with respect to depth of cut using a 0° rake angle cutting tool.....	69
Figure 4.24	Comparison of typical cutting force trace at depth of cut of 0.5 mm and 2.5 mm on a high strength sample using a 0° rake angle cutting tool.....	69
Figure 4.25	Comparison of typical thrust force trace at depth of cut of 0.5mm and 2.5 mm on a high strength sample using a 0° rake angle cutting tool.....	69
Figure 4.26	Characteristics of chips obtained at (a) 0.5 mm and (b) 2.5 mm.....	70
Figure 4.27	Variation of the cutting force (F_v) and thrust force (F_p) with respect to depth of cut using a 10° rake angle cutting tool.....	71
Figure 4.28	Comparison of typical cutting force trace at depth of cut 0.5 mm and 2.5 mm on a high strength sample using a 10° rake angle cutting tool.....	72
Figure 4.29	Comparison of typical thrust force trace at depth of cut 0.5 mm and 2.5 mm on a high strength sample using a 10° rake angle cutting tool	72
Figure 4.30	Characteristics of chips obtained at (a) 0.5 mm and (b) 2.5 mm.....	73
Figure 4.31	Variation of the cutting force (F_v) and thrust force (F_p) with respect to	74

	depth of cut using a 20° rake angle cutting tool.....	
Figure 4.32	Comparison of typical cutting force trace at depth of cut 0.5 mm and 2.5 mm on a high strength sample using a 20° rake angle cutting tool	75
Figure 4.33	Comparison of typical thrust force trace at depth of cut 0.5mm and 2.5 mm on a high strength sample using a 20° rake angle cutting tool.....	75
Figure 4.34	Characteristics of chips obtained at (a) 0.5 mm and (b) 2.5 mm.....	76
Figure 4.35	Empirical relation between cutting force and rake angle.....	77
Figure 4.36	Empirical relation between cutting force and depth of cut.....	78
Figure 4.37	Residual plots obtained for cutting force via rake angle and depth of cut.....	79
Figure 4.38	Empirical relation between thrust force and rake angle.....	80
Figure 4.39	Empirical relation between thrust force and depth of cut.....	80
Figure 4.40	Variation of Specific Energies with depth of cut and rake angle for low strength sample.....	83
Figure 4.41	Variation of Specific Energies with depth of cut and rake angle for high strength sample.....	84
Figure 4.42	Comparison of specific energies.....	85
Figure 4.43	Variation of chip size with depth of cut while cutting with 0 rake angle tool for a high strength sample.....	86
Figure 4.44	Profile of the crushed zone for different rake angles.....	90
Figure 4.45	Mode A failure mechanisms.....	91
Figure 4.46	Sequence of images showing the shear failure of a high strength specimen cut with a 10 rake angle at 2 mm depth of cut.....	93
Figure 4.47	Types of Mode A chips.....	94
Figure 4.48	Mode B failure mechanisms.....	95
Figure 4.49	Sequence of images showing crushed zone influenced fracture.....	96
Figure 4.50	Influence of the crushed zone on the force signals.....	98
Figure 4.51	Geometric model of the workpiece and cutting tool.....	102
Figure 4.52	Direction of application of velocity load on the cutting tool.....	103
Figure 4.53	Boundary conditions applied to the model.....	103
Figure 4.54	Numerical model of the sample and cutting tool.....	105
Figure 4.55	Sequence of images showing the numerical simulation of cutting a low strength sample at 2 mm depth of cut using a 0° rake angle cutting	109

	tool.....	
Figure 4.56	Sequence of images showing the numerical simulation of cutting a low strength sample at 2 mm depth of cut using a 10° rake angle cutting tool.....	112
Figure 4.57	Sequence of images showing the numerical simulation of cutting a high strength sample at 2 mm depth of cut using a 0° rake angle cutting tool.....	116

List of Tables

Table 2.1	Typical fracture toughness values of some materials.....	11
Table 3.1	Modelling materials mix design.....	33
Table 3.2	Modelling material mix design for mould of 0.001m ³ by volume.....	33
Table 3.3	Results obtained from the uni-axial compressive strength test.....	36
Table 3.4	Flexural strength of low and high strength rock-like samples.....	38
Table 4.1	Effect of cutting speed on force measurements and specific energy on a low strength sample.....	46
Table 4.2	Effect of cutting speed on force measurements and specific energy on a high strength sample.....	47
Table 4.3	Results of linear cutting tests on low strength sample.....	50
Table 4.4	Results of linear cutting tests on high strength sample.....	50
Table 4.5	Comparison of experimental and predicted forces for low strength sample.....	67
Table 4.6	Comparison of experimental and predicted forces for high strength sample.....	81
Table 4.7	Average size of the chips for low strength material.....	87
Table 4.8	Average size of the chips for high strength material.....	87
Table 4.9	Profile of crushed zone for low strength sample.....	89
Table 4.10	Profile of crushed zone for high strength sample.....	89
Table 4.11	Material properties used in numerical simulation.....	101
Table A.1	Applied load Vs Measured load data when load is applied in z-axis...	133
Table A.2	Applied load Vs Measured load data when load is applied in y-axis..	134
Table A.3	Applied load Vs Measured load data when load is applied in x-axis.....	135

List of Abbreviations

SE	Specific Energy (MJ/m ³)
F _v	Mean Cutting Force (N)
F _p	Mean Thrust Force (N)
F _s	Mean Side Force (N)
σ_{\max}	Maximum stress at tip / Inglis equation
σ_a	Applied stress / Inglis equation
a	Half-crack length / Inglis equation
ρ	Radius of curvature / Inglis equation
G	Strain release energy / Griffith equation
S	Surface energy / Griffith equation
γ	Specific surface energy / Griffith equation
Q	Surface energy / Obreimoff equation
γ_p	Surface energy for plastic deformation / Irwin and Orowan equation
K	Stress intensity factor
E	Elastic Modulus
τ_{\max}	Maximum shear stress / Tresca yield criterion
c	Cohesion of the material / Mohr-Coulomb criterion
μ	Internal friction coefficient / Mohr-Coulomb criterion
J_2	Invariant of the stress tensor / Drucker-Prager criterion
α	Material constant / Drucker-Prager criterion
ϕ	Angle of internal friction of rock / Merchant's model
n	Stress distribution factor / Nishimatsu's model

CHAPTER 1: INTRODUCTION

1.1. Introduction

Hard rock drilling is not only associated with the search for natural energy resources such as oil, gas and geothermal energies but also in areas such as collection of geological materials (*e.g.* cores and cuttings) for scientific research, space exploration, data logging, search for water and in mining and civil engineering. Rock drilling tools have evolved over the years, undergoing changes in their design and in the materials used for their manufacture. The feasibility and economic viability of treatment of rocks (drilling, cutting, crushing, *etc.*) and the choice of rock machining tools are dependant, *inter alia*, on the rocks. This research was undertaken to understand the exact nature of the failure mechanism at the tool/rock interface.

Rocks being inhomogeneous impose a complexity in understanding the behaviour at the rock and tool interface. Their physical and mechanical properties vary according to their mineral and element makeup and geographic locations, for example, the selection of a drill bit is based on whether it is drilling through soft rock (*e.g.* limestone, sandstone) or hard rock (*e.g.* granite). It is understood that the harder the rock, the more abrasive it is and hence a faster wear of the drill bit will occur: but based on mechanical properties, there are rocks categorised as hard, for example diorite, with an Uniaxial Compressive Strength of 375.2 MPa which is three times than that of granite at 106.15 MPa, but displays lower bit wear rate (measured as weight loss of drill bit button per distance travelled by the button) than granite – diorite measured 9.5 g/m while granite measured 12.8 g/m [1]. The study highlights the importance of studying the rock properties (chemical and mechanical) and the drill operating parameters, such as, penetration rate and weight on drill bit.

Modern day rock drill bits are equipped with steel cylinders containing cemented carbide or Polycrystalline Diamond Compacts (PDC) teeth or milled steel with tungsten carbide coating or button inserts. Improvement in the drilling and cutting of rocks needs a better understanding of the breakage and disintegration of polycrystalline materials. The efficiency of a drilling system (drill bit, drill string, drilling motor) depends on various geological and mechanical parameters such as types of rocks, strength of rocks, tool wear, temperature, porosity of rocks and other operating factors such as drill operator and climate [1, 2].

In machining of metals, the material removal process leading to chip formation is well understood [3], as shown in Figure 1.1, it can be observed that as the cutting tool exerts force on the workpiece, the metal ahead of the cutting edge is compressed and slides over the rake face, the chip is sheared off the workpiece along a shear plane (A-B in Figure 1.1) by plastic deformation.

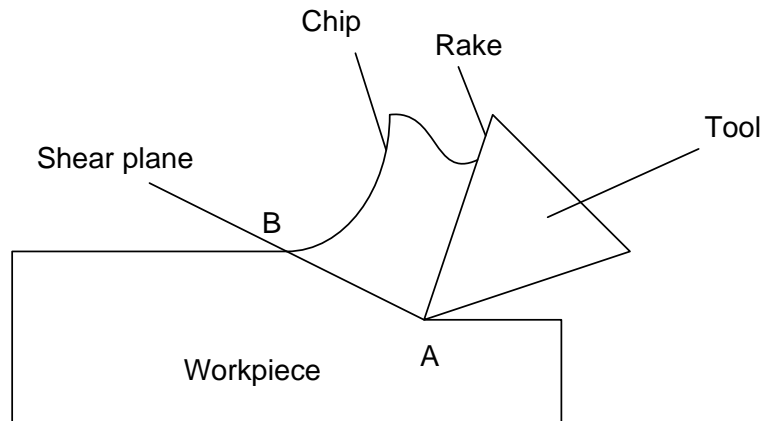


Figure 1.1 Chip formation in metal cutting [3]

The chip formation in rocks is due to elastic brittle deformation [4, 5], Figure 1.2, depicts the process of chip formation. As the tool pushes into the specimen, the material ahead of the extreme cutting edge is crushed into a fine powder, this is known as the ‘crushed zone’ analogous to the built up edge in metal cutting [3].

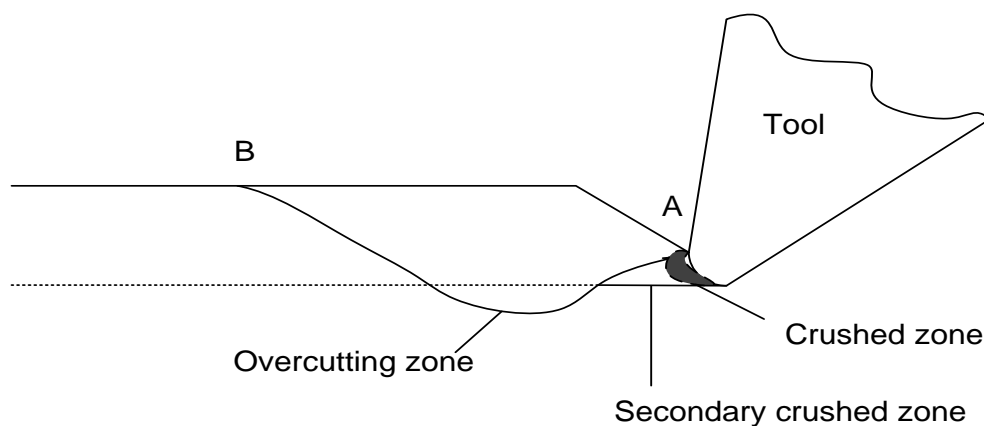


Figure 1.2 Chip formation in rock cutting [4]

The compaction of the crushed zone leads to the formation of a secondary crushed zone, this zone initiates the formation of a crack. The crack then propagates downwards, extending below the depth of cut and later rapidly rises up to the free surface resulting in a sudden fracture and the formation of a chip. The tool then moves on to meet a fresh face of the workpiece and the process repeats.

The crack patterns are complex to understand given the anisotropy present in brittle materials like rocks and they vary according to the tools used [6-9]. The study of the state of stress will provide a better understanding of the crack patterns, crack initiation and propagation. The crushed zone influences the fracturing of rocks; though the fracture mechanism itself is elastic brittle deformation, the zone remains inelastic [10] and since it propagates the energy from the tool to the rock, the importance of this zone cannot be overlooked.

Similar to metal cutting, specific energy (SE) is a parameter used in assessing the efficiency of rock cutting. Specific energy is the energy expended in removing a unit volume of rock, this value has been correlated with cutting force and thrust force and other rock properties to gain valuable knowledge of the state of material at the tool-rock interaction.

Rock fracture analyses using numerical methods have gained popularity with the advent of higher computing power [11, 12]. Several methods such as finite element methods (FEM), discrete element methods (DEM), boundary element method (BEM), hybrid FEM/DEM [13] have been successfully used in the study of fracture mechanics of rock [14-17]. The hybrid FEM/DEM was used in this research for its ability to easily model both the continuum and the discontinuum state of a material. ELFEN proprietary software by Rockfield Software Limited [18] was used in this research as previous studies using ELFEN [19, 20] have shown its capability to model anisotropy, inhomogeneity and rock faults/discontinuities.

1.2. Aim and objectives

The aim of this research is to gain fundamental knowledge of the mechanics of material removal while machining rocks, especially at the tool/rock interface. The formation of the crushed zone and its influence of the force transmission from tool to the rock will be studied through the following objectives:

1. To produce and characterise rock like samples by the use of modelling materials such as cement, sand and water. Test the samples for their mechanical properties and to use that data in numerical simulation.
2. To investigate the influence of cutting tool geometries and the depths of cut on the material removal process by studying their relationship with cutting force, thrust force and specific energy.
3. Use high speed video system to record the material removal process of a single cutting tooth over different samples and to analyse the video and observe the fracture mechanism associated with different tool geometries, samples and depths of cut.
4. Establish a failure model from empirical data such as the cutting forces, chip formation process and the specific cutting energy. Use finite element techniques to assess the model of the material removal process in rock cutting.

1.3. Novel aspects of this research

Very little literature exists which describes the interaction of the tool and rock at the extreme cutting edge especially at the microscale level. This research will produce new knowledge of the rock cutting/deformation action at the extreme cutting edge using single cutting tooth test rig, high speed photography and the use of synthetic rocks. The knowledge gained from this research will then be able to describe the tool and rock behaviour.

1.4. Thesis structure

Chapter 2 provides a comprehensive review of the literature available on rock mechanics. It shows the inferences drawn from study on metal failure and their subsequent modification to explain brittle failure of rocks. Various cutting models are introduced along with failure modes and mechanisms. Cutting tools and their geometries are discussed and their influence on the cutting process is reviewed. Specific energy is introduced and its correlation with other cutting parameters is discussed.

Experimental methodologies are presented in chapter 3 which discusses the single tooth cutting tests; modelling materials and sample preparation are presented. Experimental setup presents the calibration of dynamometer, tri-axial force measurements, and high speed video system to record the material removal process.

Chapter 4 presents the results of experimental tests and the analysis of the data obtained. Specific energy, depth of cut, rake angle, the cutting and thrust forces are plotted and their relationship explored and supported by high speed video footage. Statistical analysis provides an exhaustive research into the distribution of the cutting and thrust force and regression analysis is performed to provide governing equations based on the empirical data. It also presents the use of ELFEN, a finite-discrete element code, to simulate the cutting process. The results are compared with experimental data.

Finally, chapter 5 provides the conclusions drawn from the experimental and numerical work. The section on future work proposes research that can be carried to further the knowledge at the tool/rock interaction.

CHAPTER 2: LITERATURE SURVEY

2.1. Introduction

This chapter provides a brief review of the evolution of fracture mechanics and its application to rock fracture. A study on drilling of rocks in context of this research is presented which introduces different types of drilling and cutting tools. Specific energy is discussed here as a parameter to assess drillability and is compared against cutting parameters such as rake angle of the tool and the depth of cut. This research uses materials such as cement, sand and water to model rock like specimen. Therefore, a brief review shows the different types of modelling materials that have been used by other investigators in the past. A section on numerical methods introduces the most commonly used methods in rock fracture mechanics, their advantages and limitations.

2.2. Overview of Fracture Mechanics

Fracture mechanics deals with the study of material failure due to fracturing either by ductile or brittle mode; The early thought experiments of Plato in his work *Timaeus* and *Physica* of Aristotle influenced later works by Leonardo da Vinci and Galileo Galilei [21]. Leonard da Vinci's simple experiments on the strength test of steel wires of different lengths was conducted using a bag tied to the end of the string and sand being poured into this bag through a trap, when the string snapped, the trap would close and the sand in the bag was weighed to know how much was required before it failed. This experiment was analogous to present known tensile testing methods, but Leonard da Vinci concluded from his tests that wires of longer length would break more easily than compared to shorter length, this offers a paradox to known classical mechanics. A suitable explanation for this paradox was provided by Lund *et al* [22] where he concluded that the heterogeneity of wires dating to Leonard da Vinci's times were the cause, since the production method produced more number of defects to be present in a longer length of wire than present in a shorter one. This experiment highlights the importance of material heterogeneity.

Galileo Galilei (1638) in his work titled ‘*Dialogues Concerning Two New Sciences*’ [23] offers the very first explanation of resistance of solids to fracture. It discusses the bending of cylinders and prisms, self-weight of supporting structures, cantilevers, the influence of thickness and length of solids, the alignment of wood grains and the resistance it offers to loading across and along the grain and furthermore it discusses the strength of solid and hollow cylinders.

A rigorous mathematical analysis of great importance was produced by Inglis in 1913 [24]; this paper studied the stress distribution around the edge of a crack produced due to an elliptical and circular hole. It was based on the theory of elasticity and provided equations to calculate stress based on the dimension of the crack edge and length of crack. Figure 2.1 illustrates a plate with an elliptical hole and A refers to the point of high stress concentration.

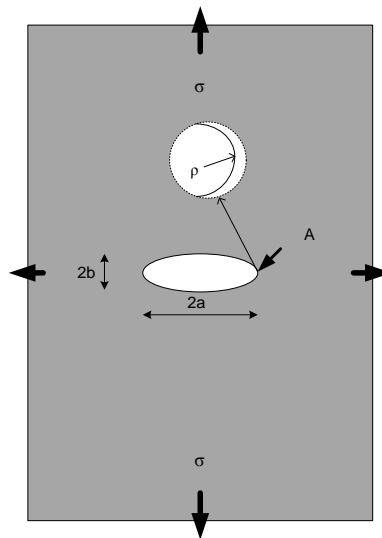


Figure 2.1 Inglis work on thin plates with elliptical hole

He found that the tensile stress varied directly to the square root of the crack length, a , and inversely proportional to the radius of curvature, ρ , at the ends of the major axis [24].

$$\sigma_{\max} = 2\sigma_a \sqrt{\frac{a}{\rho}} \quad (2.1)$$

where σ_{\max} is the maximum stress at the tip

σ_a is the applied stress

a is the half major axis; and ρ is the radius of curvature

Crack growth increases by longitudinal load rather than a load parallel to crack length [24]. Building upon Inglis's solution, Griffith [25, 26] experimented with glass rods of different lengths to understand the effects of inherent flaws in solids. Using theoretical investigation, he explained fracture through an energy balance criterion whereby the extension of a crack was possible by the decrease/release of the stored strain energy to create surface energy of the newly created cracks, that is, the energy balance is given by:

$$\text{Total energy} = \text{Elastic Strain Energy} + \text{Energy required to create new crack surface}$$

Griffith considered a plate of unit thickness carrying a certain amount of stress as shown in Figure 2.2.

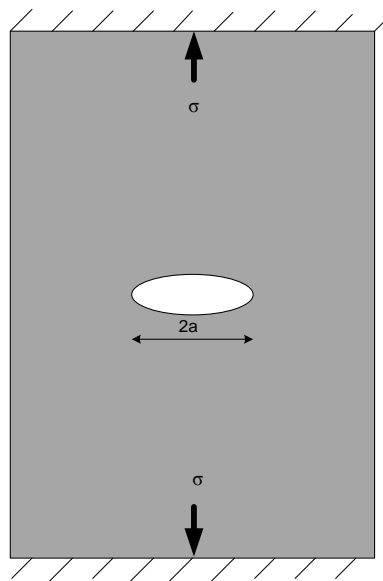


Figure 2.2 A stressed cracked plate explaining the derivation of the Griffith criterion

When the crack extends by a very small amount then it causes a relaxation of the load which means there is a decrease in the stored elastic strain energy, hence a crack can grow only when the energy released provides all the energy for a crack to propagate. Griffith arrived at the equation of strain release for crack growth given by:

$$G = \frac{\pi\sigma^2 a}{E} \quad (2.2)$$

and surface energy given by

$$S = 4\gamma a \quad (2.3)$$

where E is the Young's modulus and a is the half-crack length, σ the applied stress and γ is the specific surface energy. Since the rest of the Equation 2.2 are constant values, the crack propagation occurs when $\sigma^2 a$ reaches a critical value. This result also indicates that the criterion favours a brittle and unstable failure, and though it could explain crack propagation, it couldn't explain occurrence of a crack.

While Griffith's investigation supports unstable crack and fracture of the body, this is not the case for most materials since crack propagation does not necessarily mean that the body will fracture. Many structures undergo stable crack propagations, and this was the basis of the investigations carried out by Obreimoff in 1930 [27]. Obreimoff realised that two freshly split mica foils will adhere with considerable force just as two finely polished glass plates adhere[27]; Obreimoff experimented with mica foils to find the force required to split a fresh sheet of mica and compare it with the force required to split two sheets of mica adhered together. Figure 2.3, illustrates the work carried out under vacuum conditions. The experiment demonstrated that the cracks were stable for much of the fracturing process.

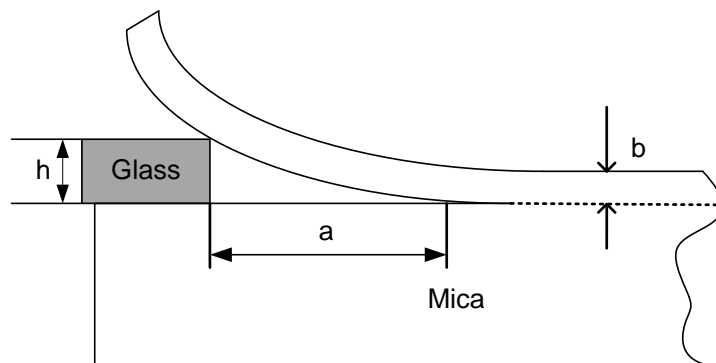


Figure 2.3 Splitting of mica using a glass slab having a single point of contact

Obreimoff also demonstrated the reversibility of fracture when the split surfaces adhered once the glass wedge was removed, an impossible feature of the Griffith crack. He arrived at the equation for surface energy using the beam theory, given by:

$$Q = \frac{Eb^3h^2}{3a^4} \quad (2.4)$$

and the surface energy given by $S = 2\gamma a$ (2.5)

where, E is the Young's modulus of mica, b is the thickness of the cleaved layer, h is the height of the wedge, a is the crack length and γ is the specific surface energy.

Irwin and Orowan independently modified Griffith's formula to explain the observed plastic deformation present in steel. Griffith's critical stress for failure was given by:

$$\sigma = \sqrt{\frac{2E\gamma}{\pi a}} \quad (2.6)$$

Irwin and Orowan [24, 25] suggested that for a ductile material the energy dissipation was not only used to create new surface energy γ but a bulk of it was used for plastic deformation γ_p . Hence the modified equation is:

$$\sigma = \sqrt{\frac{2E(\gamma + \gamma_p)}{\pi a}} \quad (2.7)$$

Irwin observed and categorised three basic modes of deformation of a body under tension. Figure 2.4 illustrates the three modes, designated as I, II and III.

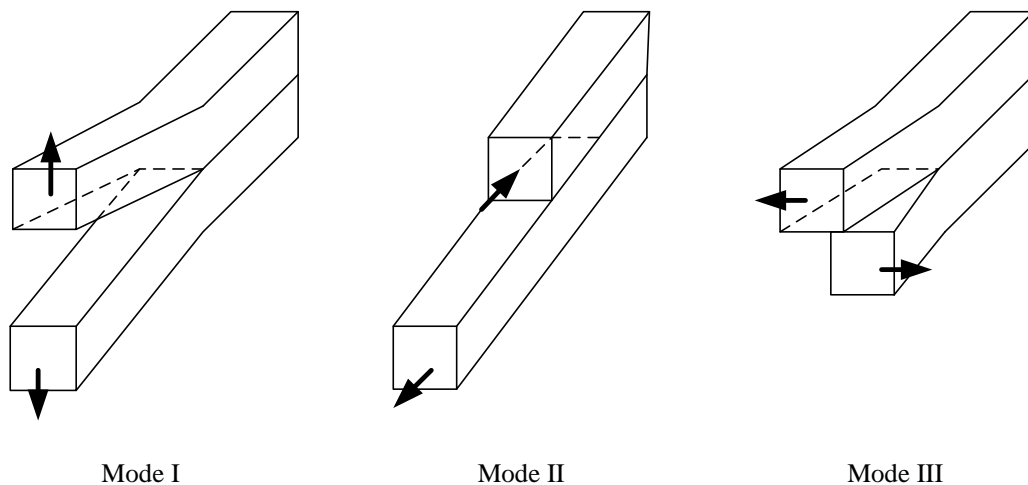


Figure 2.4 Three modes of deformation

Mode I deformation is by *opening*, where fracture plane is normal to load (tensile). Mode II is *sliding* deformation and Mode III is *tearing* deformation, both arises due to shear but in Mode II the fracture propagates in direction of shear, whereas in the later the deformation is perpendicular to shear [25].

Irwin also introduced the concept of stress intensity factor K (also known as fracture toughness) and energy release rate G and the relationship between them. Though Griffith related crack propagation to the energy release, Irwin using the theory of linear elasticity

showed that the stress field around the vicinity of the crack is critical to the energy system around the crack tip. The Stress Intensity Factor (SIF) is given by,

$$K = \sigma\sqrt{\pi a} \quad (2.8)$$

and the relationship with energy release rate is given as,

$$G = \frac{K^2(1-\nu^2)}{E} \quad \text{in Plane Strain} \quad (2.9)$$

$$G = \frac{K^2}{E} \quad \text{in Plane Stress} \quad (2.10)$$

where ν is the Poisson's ratio, K is the SIF and E is the Young's modulus. The SIF is a material property; hence Irwin's criterion for crack growth was able to describe failure using material properties.

The critical value at which the material fails due to fracture is denoted by K_c , where crack growth occurs when $K_I > K_{Ic}$ (case of Mode I failure). Fracture toughness values [28] for a few materials are listed in Table 2.1.

Table 2.1 Typical fracture toughness values of some materials

Material	K_{Ic} (MPa \sqrt{m})
High strength steel	25 – 95
Ti Alloys	40 – 95
Marble	1.2 – 2
Glass	0.6 - 1.3
Concrete	0.15 – 1.4

2.3. Rock Fracture Mechanics

Fracture mechanics study has its beginning from the analysis of metals, mostly dealing with the analysis of crack growth and their practical application to prevent failure of the engineering material. But with rock as the engineering material, the fracture mechanics study is applied to both initiation (e.g. drilling and blasting) and prevention (e.g. rockbolts) of fracture.

Fracture mechanics study of rocks is directed towards understanding the failure criteria and the failure mechanism. Failure criteria provide the equation of strength and stress states while the failure mechanism describes the initiation and propagation of cracks [29]. A brief review of the failure criteria and failure mechanisms are presented here.

2.3.1. Failure criteria for rocks

Triaxial and uniaxial testing of rocks gave rise to the failure criteria being expressed as a function of stress or strain or a combination of both [26]. A few important theoretical and empirical failure criteria are discussed below.

2.3.1.1. Tresca Yield Criterion

This theoretical criterion states that the yielding occurs when the maximum shear stress, τ_{\max} , exceeds the maximum shear stress measured under uniaxial tension, τ_o [30]

$$\tau_{\max} \geq \tau_o \quad (2.11)$$

$$\tau_{\max} = \frac{\sigma_1 - \sigma_3}{2} \quad (2.12)$$

Under uniaxial tension $\sigma_2 = \sigma_3 = 0$, and $\sigma_1 = \sigma_o$, the yield stress in tension, hence

$$\tau_{\max} = \frac{\sigma_o}{2} \quad (2.13)$$

Though simple in form, this criterion is limited to use only when the principle stresses are known.

2.3.1.2. Mohr-Coulomb Criterion

The most widely used criterion, the Mohr-Coulomb criterion postulates [26] that the shear stress of rock, sand or soil system are made up of two components, i.e. the cohesion of the material and the internal friction coefficient of the normal stress. For a rock failure under compression, this shear stress develops a failure along a plane a-b as shown in Figure 2.5 (a), given as

$$|\tau| = c + \mu\sigma_n \quad (2.14)$$

where, c is the cohesion of the material or in other terms the shear resistance, μ is the internal friction coefficient and σ_n is the normal stress acting on the fracture surface a-b. Equation 2.14 is known as the Coulomb Criterion. Failure takes place when this shear stress is exceeded.

The Mohr envelope depicted in Figure 2.5 (b) defines the stable and the unstable region, for any stress-strain combination of Mohr circles within this envelope no failure will occur, but as soon as any circle touches this envelope then failure is imminent.

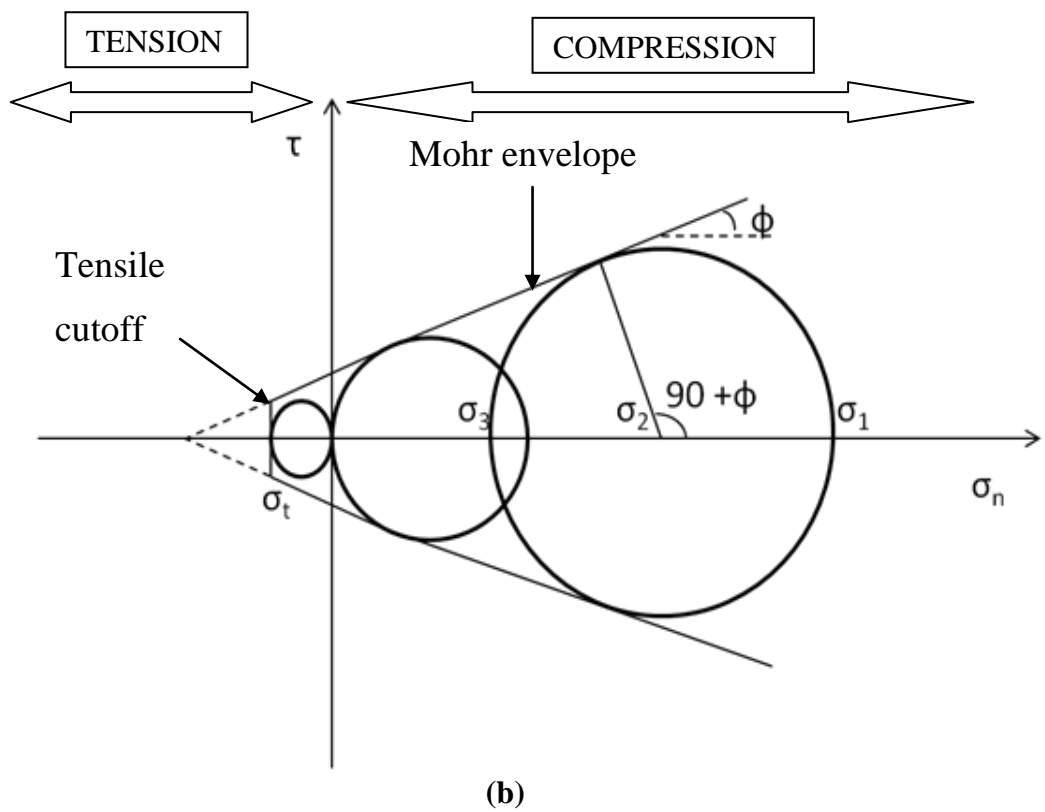
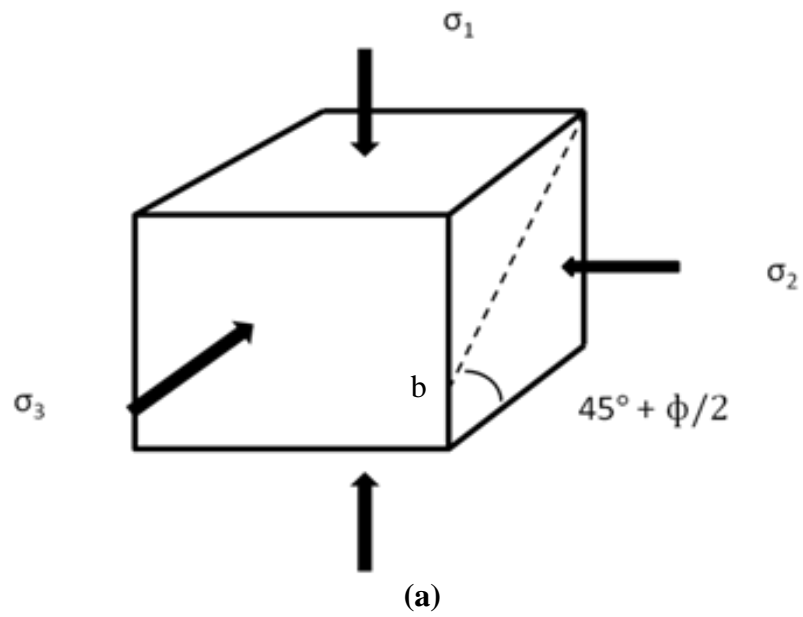


Figure 2.5 a) Representation of Mohr-Coulomb failure plane b) Mohr Envelope

The circles cannot cross into the unstable region as this will exceed the critical stress. The shear and normal stress is given by the following equations:

$$|\tau| = \frac{1}{2}(\sigma_1 - \sigma_3) \sin(90 + \phi) \quad (2.15)$$

$$\sigma_n = \frac{1}{2}(\sigma_1 + \sigma_3) + \frac{1}{2}(\sigma_1 - \sigma_3) \cos(90 + \phi) \quad (2.16)$$

Where the principle stresses are $\sigma_1 \geq \sigma_2 \geq \sigma_3$, but the Mohr-Coulomb criterion assumes that the intermediate principal stress σ_2 has no influence on the rock strength (although it satisfies Equation 2.14 since it does not influence σ_n irrespective of its magnitude (this criterion can be viewed to represent a state where $\sigma_2 = \sigma_3$)). This assumption does not hold for *in-situ* conditions as later researched by Mogi [31] which showed that as the intermediate stress increased so did the strength of the rock until a certain point beyond which the strength gradually decreased. Mohr introduced after much experimentation the tensile cut-off region which sets the limit to uniaxial tension as the Mohr envelope enters the tensile regime as shown in Figure 2.5 (b).

2.3.1.3. Hoek-Brown Criterion

The Hoek-Brown failure criterion [32] is an empirical formula and it differs from Mohr-Coulomb criterion by recognising that in practice the Mohr envelope is not a straight line but a curved envelope. Based on the interlocking between rock blocks and the surface condition between them, the failure criterion is given by

$$\sigma_1 = \sigma_3 + \sigma_c \left(m \frac{\sigma_3}{\sigma_1} + s \right)^{0.5} \quad (2.17)$$

where σ_1 and σ_3 are the principle stresses at failure, σ_c is the uniaxial compressive strength of the rock; and m and s are material constants (s is usually 1 for intact rock) [26]. The material constant m represents the particle interlocking present in rock, it is usually high for intact rock and reduces as the rock crumbles and breaks. The parameter s indicates the cohesion of the rock, it has a value of 1 for intact rock and reduces and tends towards 0 as the rock fractures [26]. Figure 2.6 depicts the curved Mohr envelope obtained using the Hoek-Brown criterion.

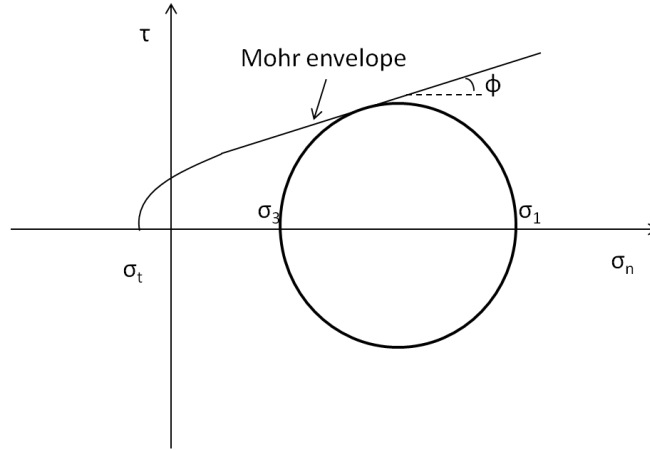


Figure 2.6 Curved envelope defined by Hoek-Brown criterion [33]

In order to use this criterion, one needs to experimentally estimate the uniaxial compressive strength σ_c of intact rock, the constant m and the value of Geological Strength Index (GSI) of the rock. GSI provides a number to estimate the reduction in rock mass for different geological conditions; a classification table of GSI is provided by Hoek *et al* [34].

2.3.1.4. Griffith Energy Criterion

Griffith's investigation on glass mentioned in Section 2.2 was adopted to describe fracture of other brittle materials such as rocks. It is known that Griffith's theory describes the onset of cracks, and in the case of compression, the rock undergoes microstructural cracks throughout the fracture process. An equation was provided to relate the principle stresses and the uniaxial compressive strength, given as

$$\sigma_1 = \sigma_3 + \sigma_c \left(2 \frac{\sigma_3}{\sigma_c} + \frac{1}{4} \right)^{\frac{1}{2}} + \frac{1}{2} \sigma_c \quad (2.18)$$

McClintock and Walsh [35] modified the above Griffith equation to take into account the crack closure by including μ , the coefficient of friction between the crack faces.

$$\sigma_1 = \sigma_3 \frac{\left(1 + \mu^2 \right)^{\frac{1}{2}} + \mu}{\left(1 + \mu^2 \right)^{\frac{1}{2}} - \mu} + \sigma_c \quad (2.19)$$

2.3.1.5. Drucker-Prager Criterion

The Drucker-Prager criterion is the extension of the von Mises yield criterion. The von Mises yield criterion is written as

$$J_2 = k^2 \quad (2.20)$$

where J_2 is the invariant of the stress tensor given as

$$J_2 = \frac{1}{6}[(\sigma_1 - \sigma_2)^2 + (\sigma_2 - \sigma_3)^2 + (\sigma_3 - \sigma_1)^2] \quad (2.21)$$

k is the material constant of the rock and depends on the cohesion and internal friction coefficient of the rock material. It is written as

$$k = \frac{6c \cos \phi}{\sqrt{3}(3 - \sin \phi)} \quad (2.22)$$

where c is the cohesion and ϕ is the angle of internal friction. The Drucker-Prager yield criterion [36] is used to determine whether a material has failed or has undergone plastic yielding, it has the form

$$\sqrt{J_2} = k + \alpha J_1 \quad (2.23)$$

$$\text{where, } J_1 = \frac{1}{3}(\sigma_1 + \sigma_2 + \sigma_3) \quad (2.24)$$

and α is a material constant which depends on the internal friction coefficient, given as

$$\alpha = \frac{2 \sin \phi}{\sqrt{3}(3 - \sin \phi)} \quad (2.25)$$

2.3.2. Failure mechanisms

The semi-empirical models of Merchant [37], Evans [38] and Nishimatsu [4] are some of the important rock cutting models discussed here.

2.3.2.1. Merchant's Model

Merchant's model was developed to describe the elastic-plastic deformation in metals while planing, the Figure 2.7 shows the schematic representation. This model assumes:

- a) failure is caused by shear stress
- b) the depth of cut is smaller compared to width of tool hence giving rise to plane strain
- c) failure occurs along a single shear line, starting from tip of tool and reaching the free surface at an angle θ
- d) the chip is in force equilibrium.

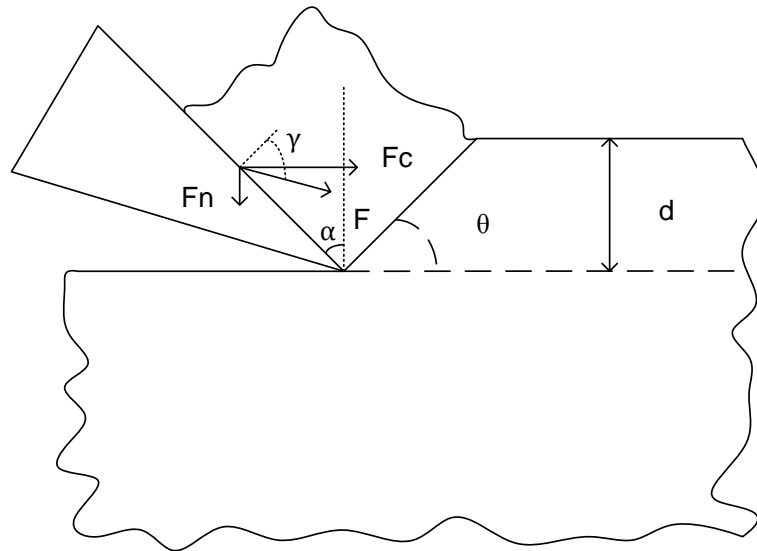


Figure 2.7 Schematic of Merchant cutting model [39]

It predicts a cutting force given in terms of material properties and geometry of the cutting tool:

$$F_c = 2d \frac{c \cos \phi \cos(\gamma - \alpha)}{1 - \sin(\phi + \gamma - \alpha)} \quad (2.26)$$

where, d is the depth of cut,

c is the cohesion,

ϕ is the angle of internal friction,

γ is the angle the resultant makes with the normal, and

α is the rake angle.

2.3.2.2. Evans's Model

Evans's [38] work on penetration of a wedge into coal led to a modified version of Merchant's model, which produces cracks due to tensile failure. His model assumes:

- i) the depth of cut is greater than wedge penetration and hence giving rise to plane strain conditions
- ii) initial friction is zero between wedge and rock
- iii) failure occurs along an arc
- iv) the resultant force T acts on the arc at right angles
- v) a force S required to maintain equilibrium at the wedge and
- vi) a force R acting at an angle Φ with the normal to wedge surface, as shown in Figure 2.8.

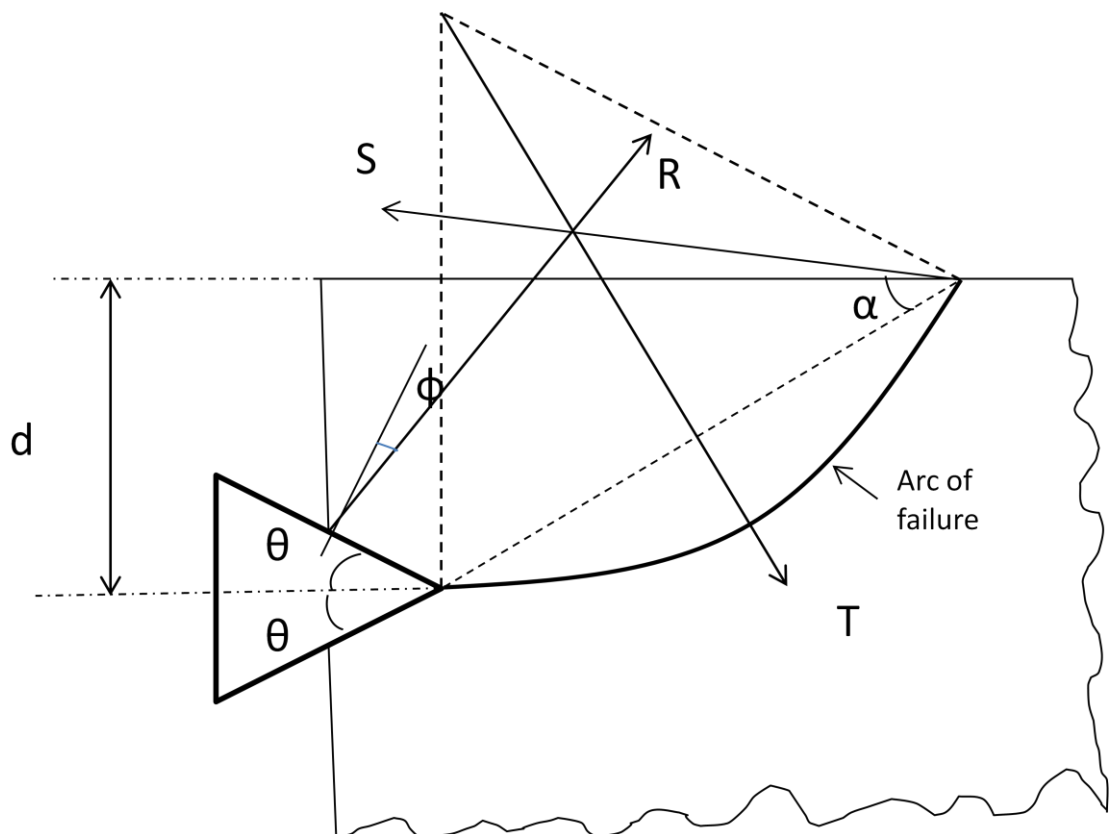


Figure 2.8 Schematic representation of Evans's model

The cutting force is given by

$$F_c = \frac{2d\sigma_t \sin \theta}{1 - \sin \theta} \quad \text{for symmetrical wedge} \quad (2.27)$$

$$F_c = \frac{2dw\sigma_t \sin \frac{1}{2}(\frac{\pi}{2} - \alpha)}{1 - \sin \frac{1}{2}(\frac{\pi}{2} - \alpha)} \quad \text{for asymmetrical wedge} \quad (2.28)$$

where d is the depth of cut,

w is the width of the cutting tool,

σ_t is the tensile stress,

θ is the wedge angle, and

α is the rake angle.

2.3.2.3. Nishimatsu's Model

Nishimatsu [4] is based on Merchant's theory and failure due to shear stress. He assumed the following:

- i) shear failure will occur along a line starting from the tip of the tool extending up to the free surface
- ii) the stress will be proportional to the distance from the tip raised to the power 'n'
- iii) the depth of cut is greater than the tip penetration hence a plain stress condition exists
- iv) failure is due to linear Mohr envelope, and
- v) the material is brittle and the crushed zone does not have plastic deformation.

He presented a cyclic removal of material; as the tool ploughs into the rock the material in the immediate vicinity of the tip gets crushed and compacted which sticks to the tool tip, this is the 'primary crushed zone' as denoted by zone a in Figure 2.9.

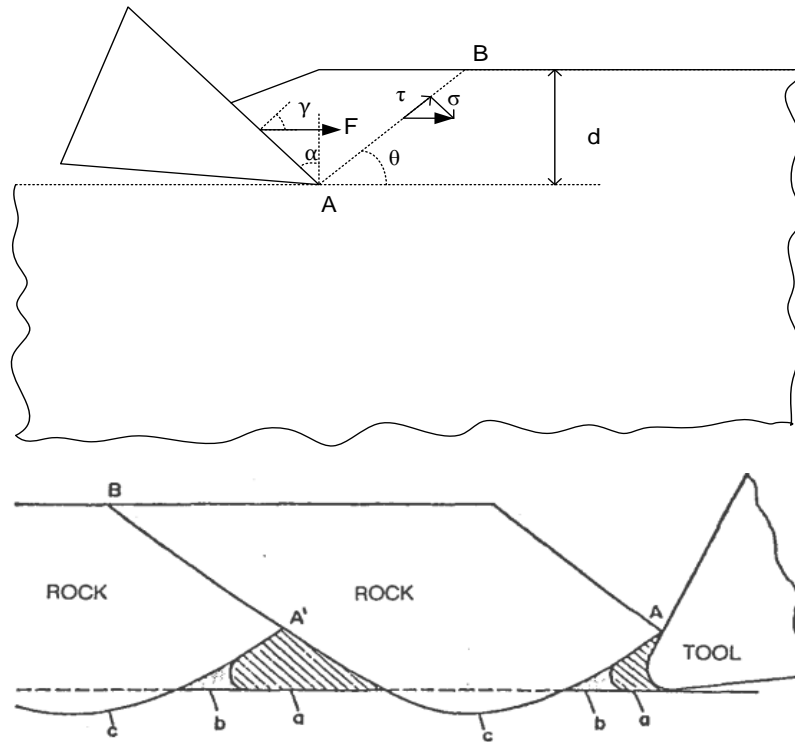


Figure 2.9 Schematic representation of Nishimatsu's theory of rock cutting and the rock cutting process [4]

As the tool moves in further, the cutting force increases and forms a 'secondary crushed zone', denoted by b , further to this, crack initiation and propagation occurs. The crack usually extend below the line of depth of cut and then curves up to meet the free surface resulting in a chip formation [4].

The cutting force is given as

$$F_c = dc \frac{2}{n+1} \cos \phi \frac{\cos(\gamma - \alpha)}{1 - \sin(\phi + \gamma - \alpha)} \quad (2.29)$$

where d is the depth of cut,

c is the cohesion,

ϕ is angle of friction,

α is the rake angle,

γ is the angle the resultant makes with the tool face, and

n is the stress distribution factor.

2.4. Rock Drilling Systems

2.4.1. A note on drilling of rocks

Essentially there are three ways in which drilling a hole is accomplished – rotary percussive, rotary crushing and cutting [40]. In all the three methods, the rock undergoes brittle fracture as defined by either one of the three modes of fracture, as depicted in Figure 2.4, or more often through a mixture of them; the three modes of fracture were discussed in Section 2.2. Fracture toughness, uniaxial compressive strength and tensile strengths are useful indicators of rock cut-ability [41], these data can be obtained by coring and collecting samples and analysing them under laboratory conditions, but data collected *in situ*, termed ‘logging’ can be even more critical to efficient drilling. Logging is done by usually sending a probe attached with various sensors down the borehole and collecting data such as water content, porosity, the presence of gases, rock material and texture, joints and fissures and also to understand the various strata of rocks and the depth to which each stratum extends. New drilling systems incorporate sensors within the drilling motor and they collect data while drilling (Logging-while-Drilling systems [LWD]) and provide a continuous feed to the operator who will use it to adjust the various drilling parameters such as Weight on Bit (WOB) (which is the downward force exerted on the drill bit by applying down pressure on the drill string) , speed, torque, RPM and also be able to choose the correct drill bit [42].

The rate at which the drill bit penetrates the rock, thrust, torque, specific energy and flushing flow are some of the operating parameters which provide an indirect measurement of the health of the drill bit and borehole. Specific energy (SE) is used as a direct measure of the cost required to fracture and remove rock [41]. The rock fragments are pumped up to the surface with the aid of either compressed air or an oil-based liquid usually termed as drilling ‘mud’ which also serves as a lubricant between the tool and the rock face. Tool wear leading to equipment breakdown is one of the most important problems faced by the drilling industry coming in next after wellbore instability, and accounts for part of the 50% of downtime of the drill rig [43]; replacing the drill bit amounts to non-productive time and

according to one industry estimate the loss is placed at nearly \$1 billion per year in downtime costs [44] and hence there is a need to gain fundamental knowledge behind the efficient fracturing of rocks. The influence of the chemical and mechanical properties of rocks on the wear of drill bits, as well as the temperature and pressure within the immediate vicinity of the drill bit tooth have been studied in previous literature [1, 40, 45-48].

2.4.2. Machining of rocks

Rock removal during drilling is accomplished by three different methods – Rotary Percussive, Rotary Crushing and Cutting as shown in Figure 2.10. A brief description of each is given below.

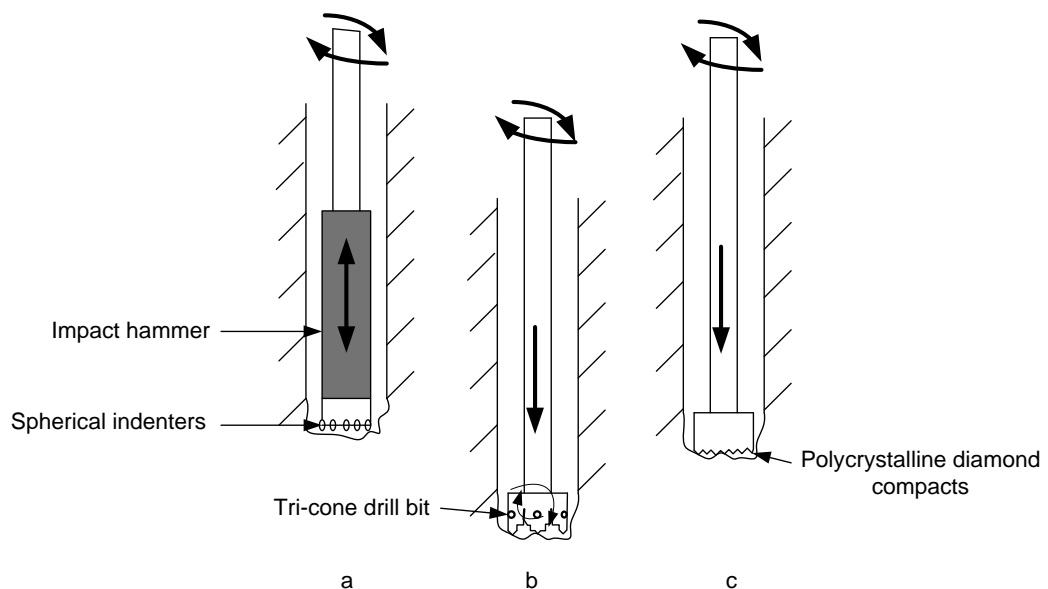


Figure 2.10 Rock removal process: a) Rotary percussive drill bit b) Rotary Crushing c)Cutting

2.4.2.1. Rotary Percussive

This drilling process involves the repeated impacts of a hammer, employing either a pneumatic or hydraulic system, to crush the rock, while the rotary movement shears the rock and also ensures fresh faces of the rock are exposed to the drill bit buttons. The hammer can be situated either at the top of the hole or at the bottom, Figure 2.10 (a)

illustrates a down-the-hole hammer. This method has the advantage of producing holes in an economic and rapid manner [49]. Kahraman *et al* [50] have provided a review of earlier works in percussive drilling and the effects of various rock properties affecting its efficiency.

2.4.2.2. Rotary crushing

This process involves breaking of the rocks, accomplished by pushing down on the rocks using a toothed drill bit under high force. The drill bit is usually of a tri-cone roller bit with tungsten carbide inserts. The rock is usually broken by brittle fracture from loading and abrasion, Figure 2.10 (b) represents this process.

2.4.2.3. Cutting

Figure 2.10 (c) depicts the cutting process; here the rocks are sheared off by overcoming their tensile strength. It is limited to soft and non-abrasive rocks such as rock salt and limestone. The drill bit has cutter inserts made up of hard metal alloys or polycrystalline diamond compact inserts.

These drill bits vary in size and the choice of the bit depends on the rock strata; diameters of 100 – 600 mm are normally used but manufacturing companies [51] can customise according to the drilling company's needs. Material removal in rotary percussive drilling is through tensile fracture while rotary crushing and cutting is through a combination of shearing and tensile fracture. The chipped rocks are flushed away to the surface by a circulating drilling fluid, usually referred to as 'mud' which is either water- or oil-based. The drilling mud not only flushes away the chipped rocks and cools the drill bits but also serves to stabilise the borehole against any collapse due to the high pressure at which it is circulated. Studies show that sometimes the rate of cooling provided by the fluid, is less than the heat generated by friction for PDC drill cutters [52] as is the case in hard rock formation where higher RPM and increased WOB causes higher rate of friction and the heat generated is not conducted away from the cutter tip fast enough irrespective of the fluid flow. The drilling fluid also influences the chip formation in rocks where the immense hydrostatic pressure can induce plastic deformation rather than brittle fracture as show by experiments conducted by Kaitkay and Lei [53] where rock samples were cut with and without confining pressure of a drilling fluid; Figure 2.11 (a) shows the schematic

representation of the chips removal and the actual chips obtained while cutting in standard atmospheric pressure and Figure 2.11 (b) shows the same with the use of confining pressure of 3.44 MPa.

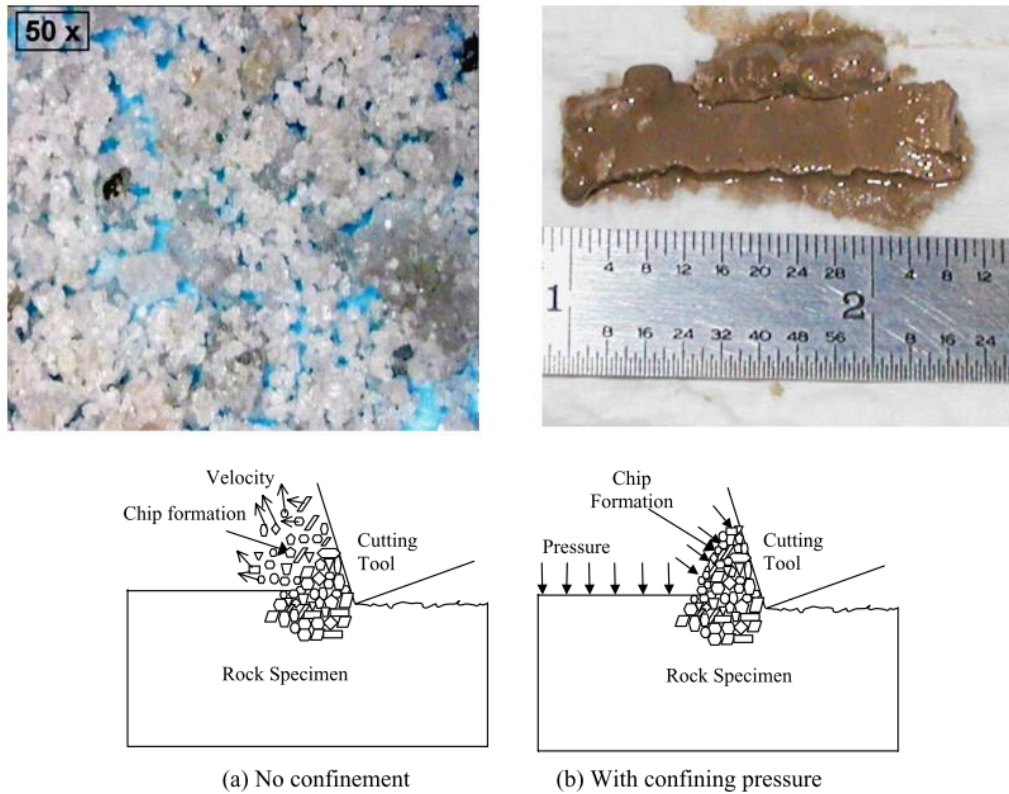


Figure 2.11 Effect of confining pressure on the chip production in rock cutting [53]

The chemical properties of the drilling fluid also add to the corrosive wear of a drill bit [54]; Thakare *et al.* conducted cutting test using an alkaline drilling fluid on tungsten carbide (WC) cutters having Cr as the binder. They observed the loss of the binder phase which exposed the Carbide leading to corrosive wear.

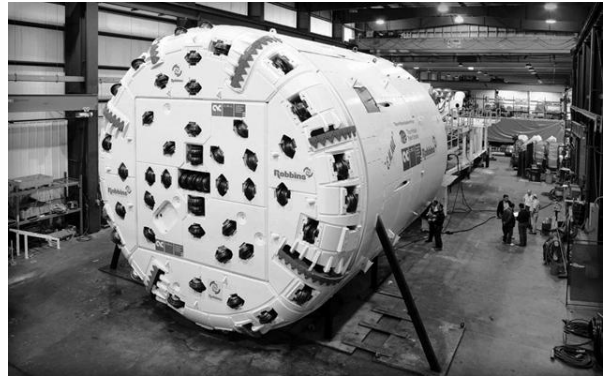
For removal of rock in mining and tunnelling, heavier and robust cutting tools are employed which are often mobile, examples are, roadheader and tunnel boring machines (TBM). Figure 2.12 (a) depicts a roadheader; they are equipped with a rotating head with chisel picks and this serves as a multipoint cutting tool which breaks rocks by shearing.

Figure 2.12 (b) shows a tunnel boring machine (TBM), they range in diameters from 1m up to 18 m [55] and fracturing of rocks is achieved by rotating disc cutters found on the face of the machine. These disc cutters are thrust upon the rock face and achieve fracturing by overcoming the tensile strength of rocks.



a

Figure 2.12 a) Roadheader [56]



b

b) Tunnel Boring Machine [55]

2.5. Specific Energy

Specific Energy (SE) is the energy expended to remove a unit volume of material, this parameter has been successfully used to characterise the efficiency of a cutting tool in metal cutting [57-59] and it has been used in the drilling industry as a measure of cost per volume of rock removed [41] and correlated with other rock properties [1, 60-63].

Atici and Ersoy [41] studied the specific energy for sawing and drilling of rocks, derived from the energy required to remove a given volume of rock. Low values of SE indicate efficient drilling. Bilgin *et al* [60] conducted detailed rock cutting tests, and showed that specific energy was not only a function of rock properties but it closely related to operational parameters such as rotational speed, cutting power of excavation machines and tool geometry. Huang and Wang [64] investigated the process of coring of rocks using diamond impregnated drill bits and found a correlation between weight-on-bit (WOB) and SE. The influence of tool geometry and depth of cut on the drilling of rocks have found good correlation in studies conducted by Copur [65]. Ersoy and Waller [1] studied the WOB and rate of penetration relationship with SE and found that as the WOB increases, so does the penetration rate, with a decrease in SE until an optimum WOB is reached.

The application of SE as performance indicators for roadheaders and TBMs have been researched by Acaroglu *et al* [66]. Cho *et al* [67] used the SE calculated from numerical simulation to derive the optimum spacing for TBM disc cutters. The influence of disc cutter spacing was studied by Chang *et al* [61] correlating the SE against the disc

penetration depth. SE was used to develop a new rippability classification system, as SE can be easily determined without detailed on-site testing [68].

SE is often correlated with other rock parameters and efficiency indicators to provide operators with optimum running conditions for all types of rocks. Roxborough [69] found an increase in SE as the compressive strength of rocks increase. Coarseness Index (CI) is the comparative size distribution of rocks, Tuncdemir *et al* [70] successfully correlated CI to SE and formed a statistical relationship defined by $SE = k/CI^n$, where k is function of rock strength and cutting tool parameters and n varies from 1.2 to 4.4 based on the cutting tool. Sengun and Altindag [71] correlated SE and mechanical properties of rocks and found high correlation with density, compressive strength and porosity. Atici and Ersoy [41] found significant statistical correlation between SE and the brittleness of rocks. Tiryaki and Dikmen [72] found positive correlation between SE and the textural and compositional properties of rocks.

The equation for calculating the specific energy is given as:

$$E_{sp} = \frac{F_c L}{V} \quad (2.30)$$

where E_{sp} is the specific energy,

F_c is the mean cutting force,

L is the length of cut, and

V is the volume of rock removed.

2.6. A review on the use of simulated rock materials

Physical models have long been employed by engineers to provide qualitative as well as quantitative data [73]. Qualitative data is provided by models which maintain geometric similarity, for example, scaled down models of buildings. This study deals with the physical models of the quantitative type where conditions of ‘similitude’ are maintained. Similitude can be achieved by simulating the physical and mechanical properties of rocks such as their brittle nature, compressive strength and elastic modulus, and as in the case with any other modelling work, perfection cannot be achieved though a fair degree of accuracy can be maintained [73]. Model materials as opposed to actual samples have the

advantage of being economically viable to produce or acquire within a short period of time, and also being able to change the mechanical properties.

Stimpson has provided an exhaustive review of modelling materials and has provided a simple classification of modelling material as illustrated in Figure 2.13.

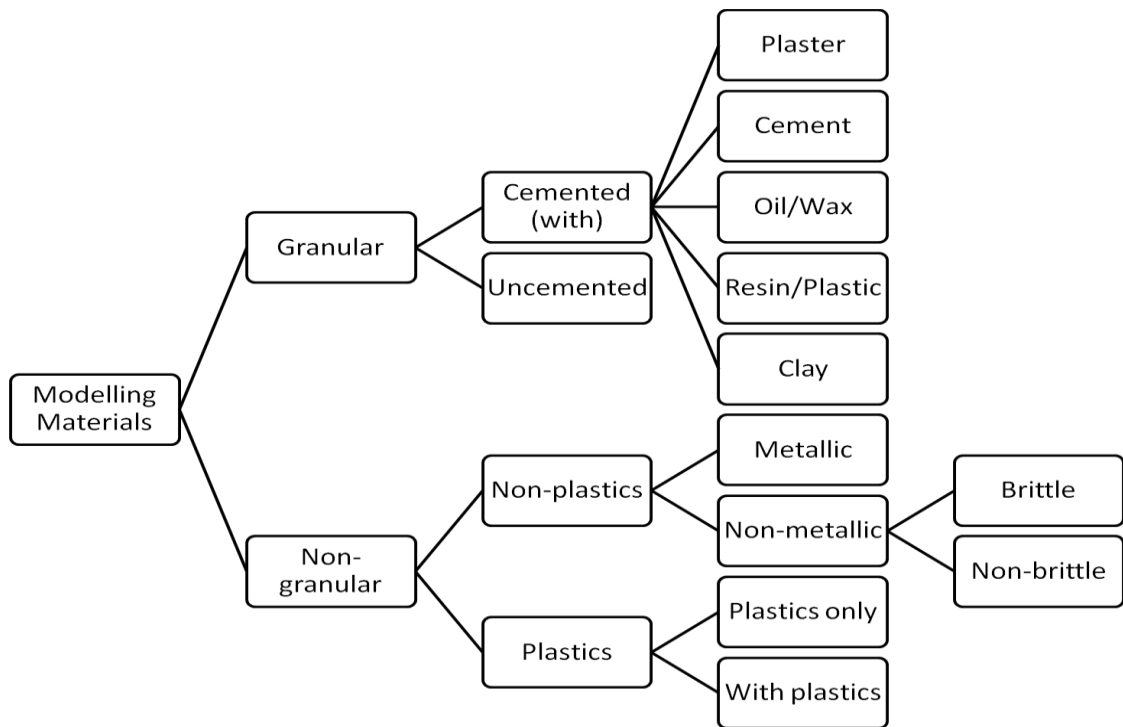


Figure 2.13 Stimpson’s simple classification of modelling materials [73]

Some examples of modelling materials are Portland cement, sand, plaster of Paris and dental plaster to name just a few. Materials are either classified as granular (e.g. sand, chalk, sawdust) and non-granular (e.g. glass, resin, ice), each having a distinctive advantages and disadvantages. The ease of sample preparation and time are some of the various factors which influence the choice of model materials. Sample preparation using model materials usually takes the form of many trials before an optimum material mixture is obtained. Tien *et al.* [74] used cement and kaolinite to simulate transversely isotropic rock, plaster of Paris was used by Ozbay *et al.* [75] to study the fracture process in highly stressed rocks, sulfaset synthetic rock was used to study the shear stress test by Cho *et al.* [76] and a mixture of barite, sand and plaster was used to study crack coalescence by Wong and Chau [77]; these example highlight the advantage of using model materials.

2.7. Overview of Numerical Methods

An in-depth review of the various methods of numerical modelling and their application to rock engineering has been carried out by Jing [12]. The author concludes that finite element method (FEM) and discrete element method (DEM) are powerful methods to analyse the large number of fractures since the continuum state of the rock mass changes to a discontinuum state when cracks initiate and propagate; this change of state is accomplished by coupled FEM/DEM method. Commercially available fracture analysis software such as ELFEN by Rockfield Software Ltd uses coupled FEM/DEM to solve a wide array of problems.

The heterogeneity present in rocks plays a vital role in the initiation of cracks and the path they travel [14, 20]; the coalescence of microfracture leads to the failure of rocks, since these microfractures are randomly distributed owing to the heterogeneity of rocks. The growth of cracks depends on the mesh shape and density [20], thus understanding the rock material properties, anisotropy and existence of cracks is vital to modelling a problem. The brittle failure of rock due to impact and shearing has been numerically modelled in the past [14, 16, 17, 20, 78, 79]. Liu *et al.* [14, 16, 78] used an interaction code R-T^{2D} developed by them using FEM to simulate various rock testing methods as suggested by the International Society of Rock Mechanics (ISRM) on an heterogeneous rock having numerical model data of compressive strength 180 MPa and elastic modulus of 60 GPa. Tests included the Uniaxial Compressive Stress (UCS), Brazilian Tensile Strength Test, Three-Point Bending and the Four-Point Shearing Test. They observed that the rock heterogeneity has a strong influence on the stress distribution, and as the load increases the stress at the tip intensified leading to stable crack propagation; after the peak stress drops, unstable failure occurs which includes microcracks, crack coalescence and chip formation. They observed that crack initiation is through tensile failure since the tensile strength of a rock is much lower than its compressive strength and the formation of a confining zone at the tip of the tool leads to the crushed zone formation due to compression.

Carpinteri *et al* [17] used FRANC2D software developed by Cornell University to simulate rock indentation and ploughing on heterogeneous material using a discrete model and homogenous material using a FEM model; they observed stress patterns which indicate tensile parting of cracks and plastic crushing.

Cai and Kaiser [20] successfully used the ELFEN software to simulate the Brazilian Tensile Strength test on homogeneous rock, layered rock and rocks with pre-existing cracks. Homogeneous model contained constant material parameters throughout (elastic modulus, poisson's ratio and tensile strength) while the heterogeneous layered rock contained two different material properties assigned to each layer of rock. Cracks were observed to initiate at the centre of the disc and move towards the platens thus splitting the disc. The ELFEN software integrates FEM/DEM to provide a seamless change from continuum state to a discontinuum state.

FEM is most common numerical method used to solve for a variety of engineering problems, but since it is based on the continuum concept, when applied to rock fracture mechanics, FEM fails to provide useful information when elements are required to open and separate [13]. FEM however has been favoured since its inception for its ability to handle heterogeneity and complex boundary conditions [80].

DEM works on the principle that the system is made up of both rigid and deformable bodies and when deformation/separation occurs then contact between the bodies are continually updated to ensure crack initiation and propagation, this however results in increase in computation cost [12]. DEM has been applied in variety of problems from large scale deformation in tunnels to rock cutting [81-83]. Rojek *et al* [81] developed a DEM code to simulate in 2D and 3D rock cutting process using a roadheader pick; the code used spherical elements of radii ranging from 0.07 to 0.3 mm for 2D and average radius of 1.02 mm for 3D simulation and they found good match with experimentally obtained tri-axial force data. The importance of porosity was studied by Schöpfer *et al* [82] using a DEM code called PFC3D which uses spherical elements. Nardin *et al* [83] studied the contact model of spherical elements.

A discrete-continuum model was reported by Pan and Reed [84] where the DEM region has rigid blocks and the FEM continuum region has non linear material behaviour [12]. Modelling the rock/tool interface based on the FEM/DEM approach has been studied in previous literature [15, 16, 85]. The simulations of the tool cutting through rock have been used to study the chip formation process, the influence of the crushed zone of fine rock particles at the tip of the tool, the modes of fracture (tensile or shear) and crack propagation to name just a few.

ELFEN employs a variety of constitutive models and failure criterion to model how materials behave to various loading conditions. It has both implicit and explicit modelling ability in 2D and in 3D [18]. ELFEN has been successfully used to understand surface subsidence in block caving mining by Vyazmensky *et al.* [86, 87], the failure of slopes by Styles *et al.* [88], simulation of the suggested rock testing methods such as the Brazilian tensile test and stresses involved in rock excavation by Cai and Kaiser [19, 20] and fracturing of rock mass by Pine *et al.*[89]. A comparative study of different modelling methods and codes has been presented by Styles *et al.* [88] and a figure representing the basis of ELFEN from their work is shown here in Figure 2.14. ELFEN simulates fracture initiation and propagation by using fracture energy and failure criterion approach either in tensile or tensile/compression domains. When a particular tensile strength is reached the crack is initiated by overcoming the contact between elements and breaking them into discrete elements, thus moving from a finite element to discrete element state. The amount of crack propagation is defined by the material softening/damaging response as defined by the fracture energy release rate. The move from FEM to DEM in ELFEN is possible due to its seamless remeshing capability [18, 86, 88].

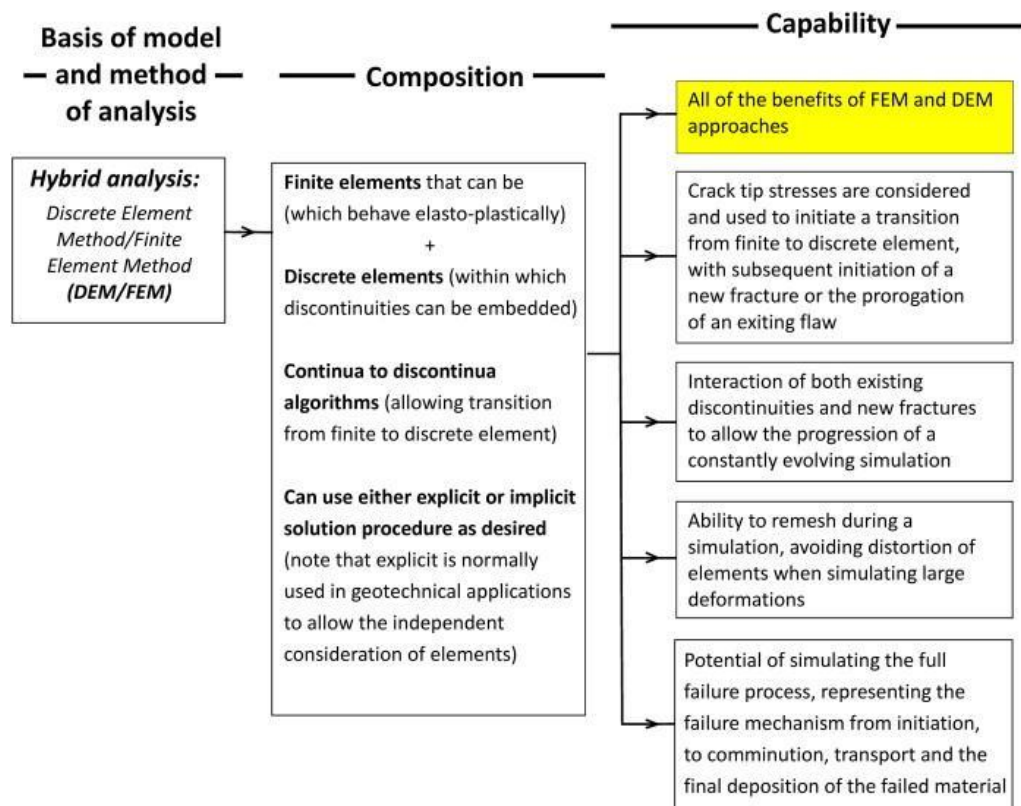


Fig 2.14 Capabilities of ELFEN (reprinted with permission [88])

CHAPTER 3: EXPERIMENTAL PROCEDURE

3.1. Introduction

This chapter discusses the sample preparation and their characterization, features of the single cutting tooth test rig, cutting tools, calibration of dynamometer and linear cutting tests.

A test rig was put together by modifying an existing shaper machine to undertake linear cutting tests on rock-like samples; it was designed and implemented to measure tri-axial cutting forces and to observe the fracture mechanism of the test specimen. The process aimed to gather data on the formation of the crushed zone at the tip of the tool and the initiation of a crack, crack propagation and ejection of the chip, by the use of a high speed video camera system. Rock-like samples were prepared to simulate low and high strength rocks and tested to record the various mechanical properties such as compressive strength and flexural strength. Orthogonal cutting tools with a tungsten carbide cutting edge were chosen having a constant clearance angle and three different rake angles. Cutting tests were performed on two sets of samples, and each sample was cut to five different depths of cut, keeping a constant cutting speed. Chips were collected and later visually analysed and categorised according to the sample strength, depth of cut and rake angle. High speed videos of the chipping process made it possible to view and analyse the failure mechanism of the chip.

3.2. Sample preparation

Section 2.6 discussed the various modelling materials used to prepare rock-like samples; Granular modelling materials were used in this investigation and Table 3.1 below provides the materials used to prepare the samples. The main constituents of the rock-like samples were a mixture of coarse and fine natural aggregates. Standard test sieves complying with BS 410 were used to determine the size of the aggregates; coarse aggregates were made up of the material passing through the sieve size of 5mm. For fine aggregates 1.18 mm was used. The binder materials were ordinary Portland cement and Silica Fume. Silica Fume in fresh concrete ensures increased cohesion and reduced bleeding (where less water seeps out due to the settling down of cement and aggregates). In hardened concrete, the silica

fume enhances the mechanical properties (such as compressive strength and modulus of elasticity) and reduces permeability.

Table 3.1 Modelling material mix design

Material	High strength sample	Low strength sample
Portland cement (BS 12)	980 kg/m ³	240 kg/m ³
Silica fume	100 kg/m ³	18 kg/m ³
Coarse aggregate	850 kg/m ³	850 kg/m ³
Fine sand	275 kg/m ³	275 kg/m ³
Water (water/cement ratio of 0.35)	343 kg/m ³	84 kg/m ³

Polystyrene cubes of 0.001 m³ by volume were used as the mould for sample preparation hence the proportion of mixtures shown in Table 3.1 were recalculated to fill 1 such cube and are shown in Table 3.2.

Table 3.2 Modelling material mix design for mould of 0.001m³ by volume

Material	High strength sample	Low strength sample
Portland cement (BS 12)	0.980 kg	0.240 kg
Silica fume	0.100 kg	0.018 kg
Coarse aggregate	0.850 kg	0.850 kg
Fine sand	0.275 kg	0.275 kg
Water	0.343 kg	0.084 kg

The cement, silica fume, coarse and fine sand were weighed out and added into a concrete mixer rotating at low speed. Water was measured according to the cement content and added steadily into the mixture; the mixer was run until a desired texture was obtained. The inside surfaces of the polystyrene cubes were coated with a thin film of mould oil to facilitate easy removal of the mould. The mixture was filled into the mould and compacted using a steel tamping rod in layers of 20 mm. Excess concrete was removed and the top surface was levelled and smoothed carefully. These moulds were left to dry in room temperature for a week, they were then de-moulded and submerged under water for a further 3 weeks, at the end of three weeks they are removed and left to dry at room

temperature for a further one week. These samples were used for compressive strength tests and also for the linear cutting tests. For the purpose of finding flexural strength and fracture toughness, rectangular moulds measuring 300 x 100 x 100 mm were used and prepared separately in a similar manner.

3.3. Sample Characterization- Testing for mechanical properties

Compressive strength and flexural strength tests were conducted on the samples in order to define accurately their mechanical properties. Compressive strength test was conducted according to BS EN 12390-3:2009 using the cube test specimens, while the flexural strength was conducted according to BS EN 12390-5:2009 using the rectangular test specimen.

3.3.1. Uni-axial Compressive Strength Test

The cube shaped specimens were visually inspected to ensure that there are no cracks or surface damage. The top and the bottom of the specimens were smoothed using a polishing stone to ensure a flat surface and to provide a contact between the platens of the testing machine. The testing machine by ELE International conforms to EN standards, and is shown in Figure 3.1, it has a lower and an upper platen which accommodates a cube shaped specimen. The platens were cleaned and dried to get rid of any grit and moisture, the specimen dimensions were measured and weighed and then placed between the platen, and a very small load was applied to ensure the specimen was held in position and that no slip occurs. A constant rate of force was applied to the platens (approximately 3 kN/s) until the specimen fails. The maximum load was recorded and the compressive stress was calculated using the formula [90],

$$f_c = \frac{F}{A_c} \quad (3.1)$$

where f_c is the compressive strength in MPa

F is the maximum load at failure, and

A_c is the cross-section area of the specimen on which the force was applied

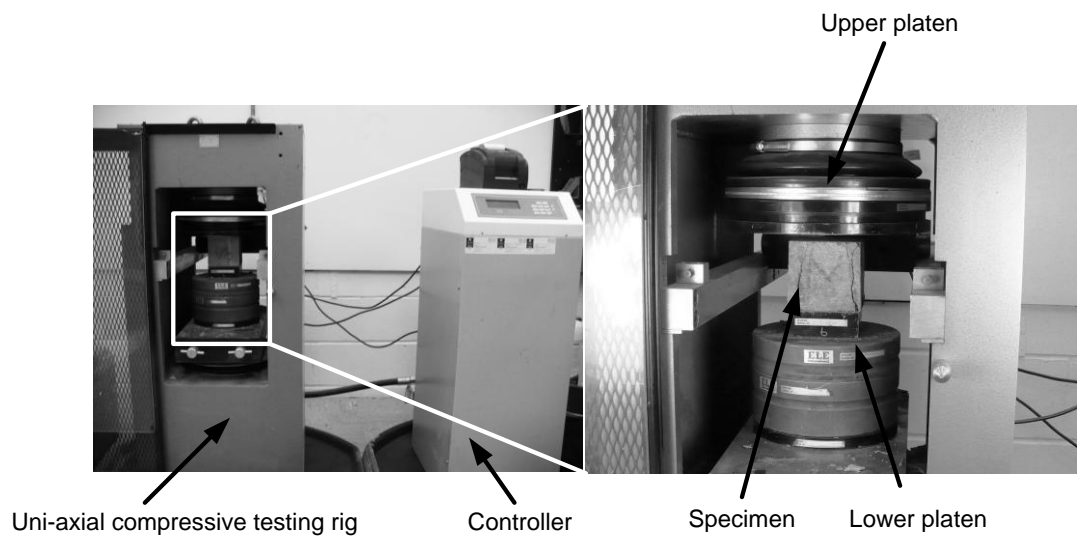


Figure 3.1 Uni-axial compressive strength testing machine

Five specimens for low and five for high strength were tested and the compressive strength calculated. The figures quoted in Table 3.3 were obtained from an average of five tests. Figure 3.2 shows the acceptable failure shapes of the samples; it can be observed that there was no damage on the top or bottom surface of the samples but the four faces on the sides have been damaged (usually in a concave manner).

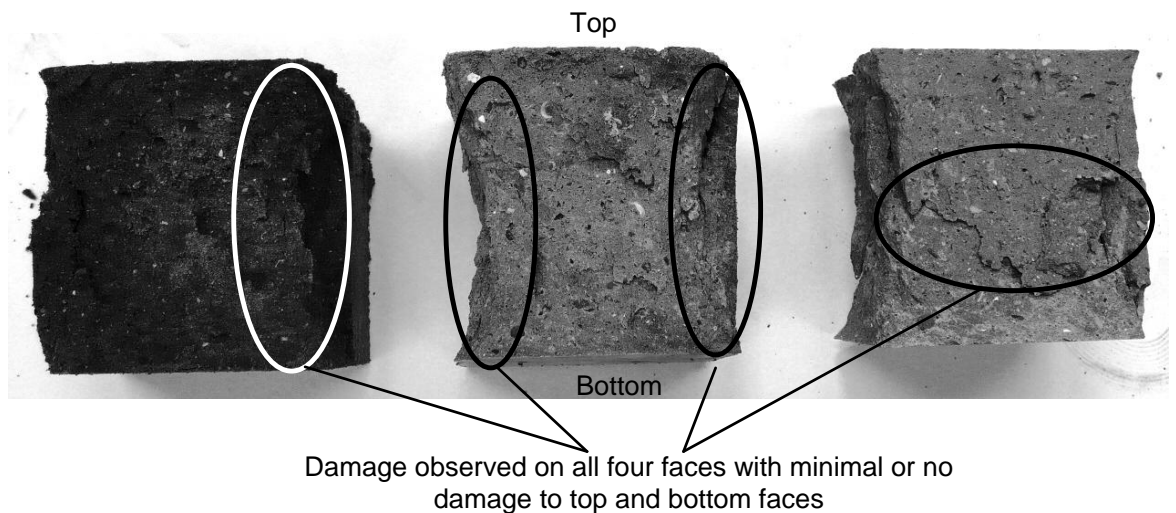


Figure 3.2 Failure observed in compression testing of rock-like samples

Table 3.3 Results obtained from the uni-axial compressive test

Sample type	Maximum load (kN)	Compressive strength f_c (MPa)	Density (kg/m ³)	Elastic Modulus E (GPa)
High strength	540.4	53.5	219	34.3
Low strength	176	17.5	217	19.4

3.3.2. Flexural strength test

The flexural strength testing of the specimen was conducted using BS EN 12390-5:2009 testing procedure. The rectangular prism specimens were subjected to a three point bending test on Denison Mayes Universal Testing Machine conforming to BS standards. The placement of the specimen in the machine is show in Figure 3.3, where the distance between the supporting rollers are 0.3 m and length of the specimen is 0.5 m.

A constant loading rate was maintained until the specimen failed, the maximum load was noted and the flexural strength was calculated using the standard formula [91],

$$f_{cf} = \frac{3FL}{2d_1d_2^2} \quad (3.2)$$

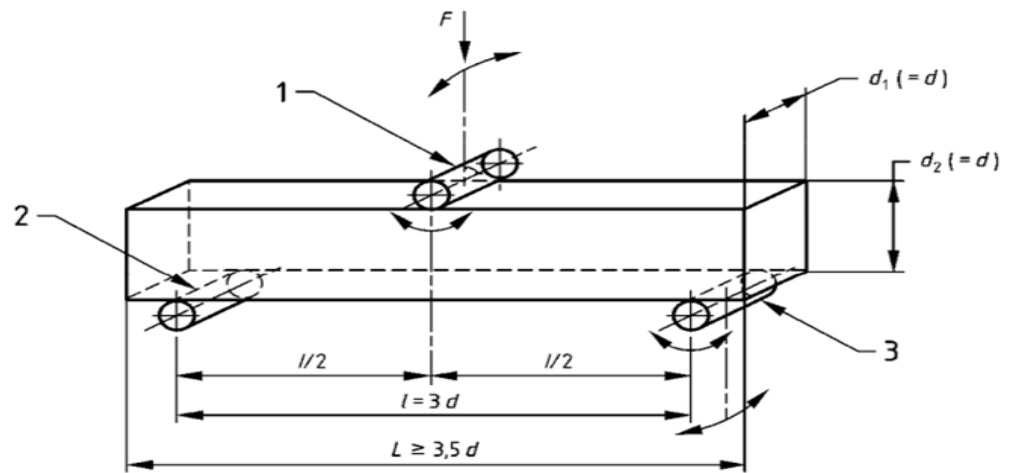
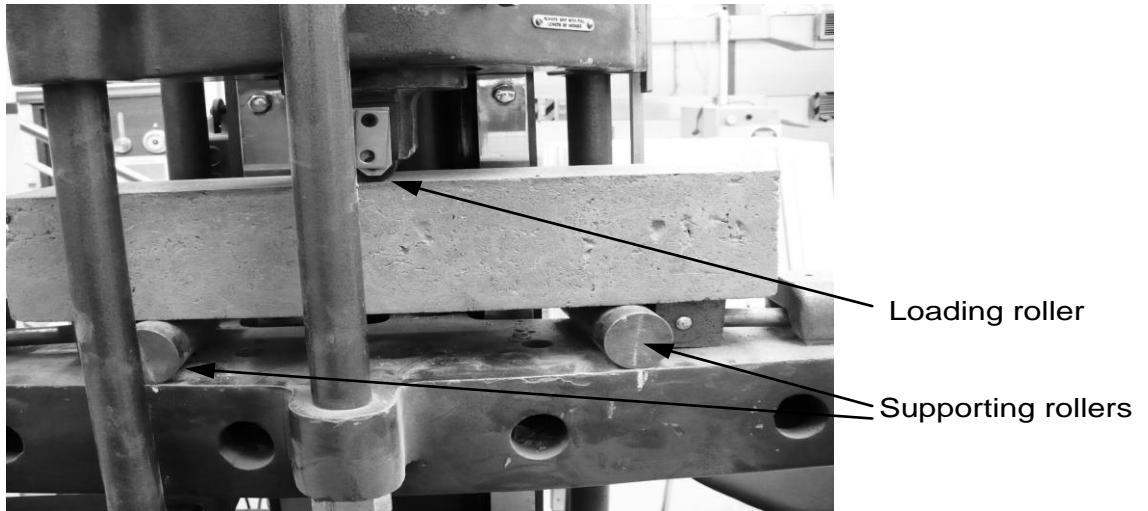
where f_{cf} is the flexural strength in MPa,

F is the maximum load in N,

L is the distance between supporting rollers in mm, and

d_1 and d_2 are the dimensions of the specimen in mm, as shown in Figure 3.4.

The results are shown in Table 3.4.



Key

- 1 Loading roller (capable of rotation and of being inclined)
- 2 Supporting roller
- 3 Supporting roller (capable of rotation and of being inclined)

Figure 3.3 Centre-point loading arrangement to test flexural strength [91]

Table 3.4 Flexural strength of low and high strength rock-like samples

Sample type	Expt no:	Flexural strength f_{cf} (MPa)	Maximum load (kN)
High strength	1	4.1	9.1
	2	5.1	11.3
	3	6.3	14.0
	4	6.3	13.9
	5	4.5	10.0
	6	7.9	17.5
	7	5.1	11.3
	8	6.0	16.2
	9	6.1	10.4
		Average	5.7
Low strength	1	3.9	8.7
	2	4.3	9.6
	3	4.5	10.1
	4	4.3	9.5
	5	4.3	9.6
	6	3.2	7.2
	7	3.5	7.7
	8	3.5	7.8
	9	4.8	10.6
		Average	4.4

3.4. Experimental Rig

3.4.1. Single Cutting Tooth Test Rig

The schematic of the single cutting tooth test rig is presented and elaborated in Figure 3.4 and Figure 3.5 shows the actual test rig and the associated components which are numbered and discussed in the following section.

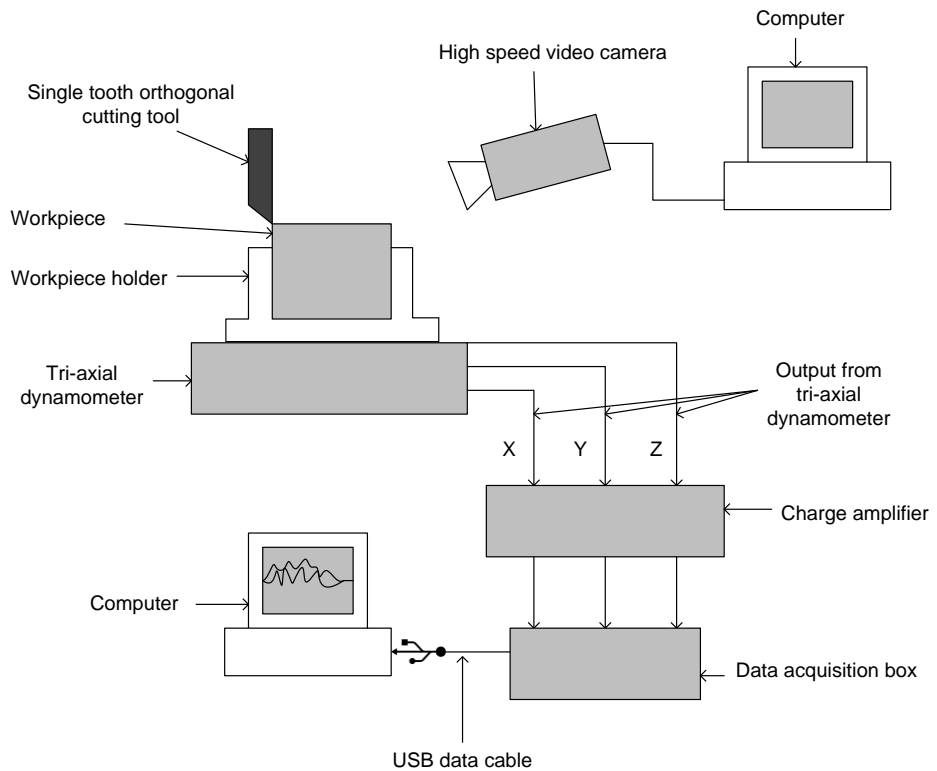


Figure 3.4 Schematic of the single cutting tooth test rig



1. High power lamp 2. Tool Holder 3. High Speed Video Camera (Phantom v7.3)
 4. Tri-axial dynamometer (Kistler 9257B) 5. Specimen holder 6. Orthogonal cutting tool
 7. Computers to collect and analyse tri-axial forces and high speed videos 8. Data Acquisition System (National Instruments USB-6221 BNC) 9. Charge amplifier (Kistler 5010A)

Figure 3.5 Single cutting tooth test rig and associated components

The single cutting tooth test rig was made up of a tool holder (labelled 2), which holds a orthogonal cutting tool (labelled 6). The cube shaped samples were held in place by the workpiece holder (labelled 5) which has an adjustable clamp to ensure a firm grip on the samples. A tri-axial dynamometer (labelled 4), by Kistler, was fixed on to the table of the shaper machine, this served as a platform for the workpiece holder. The output of the dynamometer was fed into a charge amplifier (labelled 9), the output of which was fed to the computer via a data acquisition device (labelled 8) which converts the analogue signals of the dynamometer into digital input. The schematic representation of the test rig is presented in Figure 3.4; it describes the working of the test rig. The tri-axial dynamometer (Kistler 9257B) measures forces in three axis, the force components are shown in Figure 3.6, where F_p is the thrust force, F_v is the cutting force and F_s is the side force; as the tool cuts through the sample, the three piezo-electric transducers in the dynamometer produce an electrical signal with a magnitude equivalent to the force experienced at the cutting edge. This electrical signal is weak, hence it was fed into a charge amplifier (Kistler 5010A) which amplifies the signals and in turn feeds them into a data acquisition device. This data acquisition box, by National Instruments (NI USB-6221 BNC) has 8 inputs and interfaces with a computer through a usb cable, it converts the analogue input of the charge amplifier to digital output which is read by LabVIEW software on the computer. LabVIEW reads and logs the data; the sampling rate can be defined and the force measurements are logged into data files. The post-processing of this data was undertaken using Microsoft Excel and Matlab.

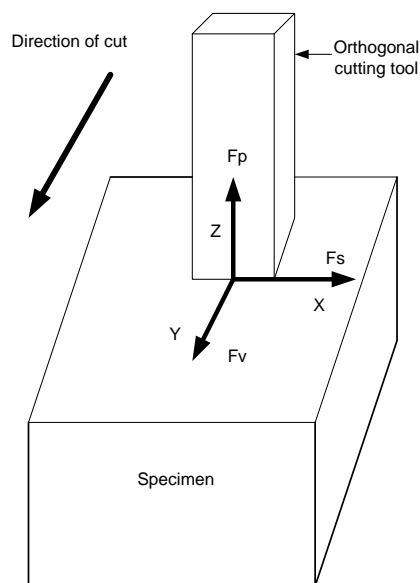


Figure 3.6 Tri-axial force components

3.4.2. Calibration of Dynamometer

Calibration of the dynamometer was undertaken before the cutting test could commence; this operation is of vital importance since the accurate measurement of forces is necessary to calculate the specific cutting energy and to describe the failure mechanism, that is, the chip formation process and how it is influenced by the depth of cut, rake angle and workpiece strength.

A precisely calibrated Instron (Model 3382) universal testing machine, complying with ASTM and EN standards was used to calibrate the dynamometer. Figure 3.7 shows the arrangement used to support the dynamometer in all three directions of force measurements. A heavy cast iron base was used on to which the dynamometer was clamped using bolts, a smooth and dirt free base plate was placed on top the dynamometer so that the contact with the moving platen was achieved without any damage to the dynamometer and to reduce any slip during the application of force. A maximum load of 5000 N was applied in all directions of the force components in steps of 500 N; the results and corresponding graphs are shown in appendix A.

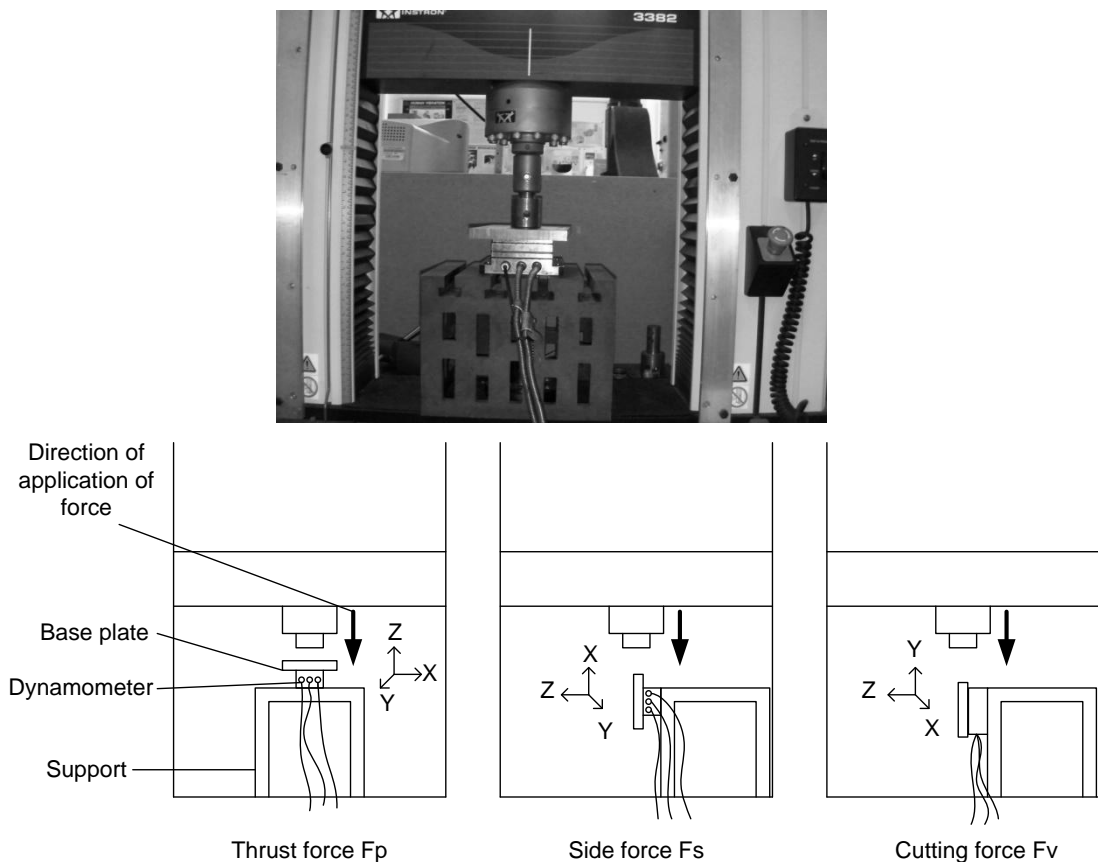


Figure 3.7 Calibration of the tri-axial dynamometer using the Instron testing machine

3.4.3. Orthogonal cutting tools

The cutting tools used in this investigation were orthogonal cutting tools with a brazed tungsten carbide tip. Rake angles range from -25° to 40° and clearance angle from -6° to 24° for use in drilling and mining. Based on previous literature [53, 72, 92], three cutting tools were designed and used for the cutting tests, each with a 5° clearance angle and rake angles featuring 0° , 10° and 20° as shown in Figure 3.8.

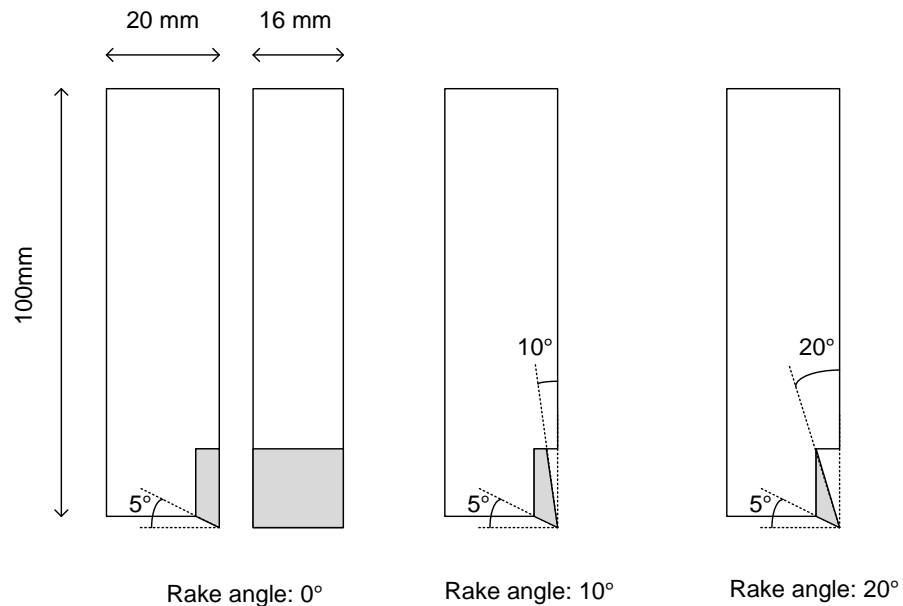


Figure 3.8 Orthogonal cutting tools

3.5. Linear cutting tests

Linear relationships between cutting force, specific energy and depth of cut has been studied in past works: Kaitkay and Lei [53] studied rock cutting using two depths of cut, 0.4 and 0.8 mm and found that cutting force increased with increase in depth of cut. Deketh *et al.* [93] researched on rock excavation machines using depths of cut ranging from 0.05 to 2.5 mm. The crushed zone of rocks were studied by Wei *et al.* [94] by cutting experiments on diabase and granite using depth of cut ranging from 0.08 mm to 7.5 mm. The depths of cut chosen for this study range from 0.5 mm to 2.5 mm in increments of 0.5 mm.

The following steps were followed to perform the linear cutting test on samples.

- i) The dynamometer and the charge amplifier were usually turned on an hour before the experiment could commence as this procedure reduced the noise in the system.
- ii) The workpiece holder was wiped clean and the specimen was firmly secured using the adjusting screws.
- iii) The cutting tool was fixed to the tool holder with the use of a spirit level to ensure a level surface was obtained on the specimen.
- iv) The shaper machine was turned on and a planning operation was undertaken to remove 2 to 3 mm by depth off the surface of the sample, this was done because this layer is usually made up of cement and needs to be removed to reach the concrete beneath. Once the concrete layer can be seen, the linear cutting test was commenced.
- v) The tool feed was done manually and initially set to 0.5 mm depth of cut. The LabVIEW software was initialised to record the signal from the dynamometer with a time step of 0.001 s, the charge amplifier was set to read 1 volt of the signal as 1000 N of force,. The shaper machine was engaged using the clutch and disengaged as soon as one forward stroke was obtained, this corresponds to a single reading at the chosen depth of cut.
- vi) The tool feed was adjusted to increase the depth by 0.5 mm; the process was repeated 4 more times to get an average of 5 readings at 0.5 mm depth of cut.
- vii) Five depth of cut were obtained starting from 0.5 mm going up to 2.5 mm in steps of 0.5 mm. The experiment was repeated for each cutting tool.

The experiment matrix is provided in Figure 3.9 below.

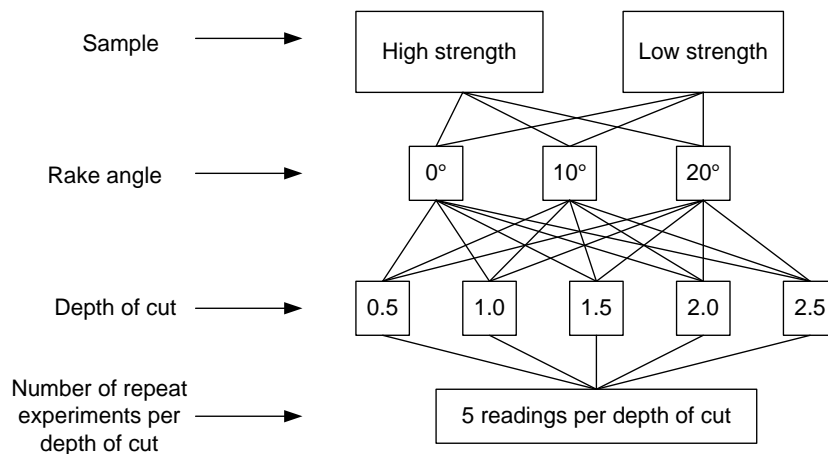


Figure 3.9 The matrix of experiments

CHAPTER 4: RESULTS AND DISCUSSION

4.1. Introduction

This chapter discusses the results obtained by linear groove cutting tests on rock-like samples as detailed in Section 3.5. A simple groove was cut using the shaping machine and the tri-axial forces were measured. Specific energy, cutting and thrust forces were carefully analysed and presented in this section. Their correlation with drilling parameters such as depth of cut, rake angle, area of cutting tooth in contact with the sample, speed of cutting tool and mechanical properties of the rock-like samples were studied. Statistical analysis was carried out using Minitab 16. Chip debris were collected and visually inspected and categorised and the chip formation was also captured using the high speed video camera and the process is presented here as a sequence of photographs and schematic diagrams. The formation of the crushed zone was studied using the high speed videos and effect of the shape and size of this zone on force transmission from the tool to the specimen was studied. Numerical modelling of the cutting process was carried out using ELFEN simulation software; stress distribution at the immediate vicinity of the tool tip for different geometries of the tool and for two different material were studied for the crack initiation and propagation.

4.2. Preliminary Cutting Test

Supplementary experiments were conducted to verify the influence of the cutting speeds; the shaper machine has a two speed settings of 263 mm/s and 333 mm/s. Table 4.1 and 4.2 gives the tabulated results of the experiment on both low and high strength sample respectively using the two speed settings. It can be observed from Table 4.2, that data was unavailable for depths greater than 1.5 mm at the slower speed setting of 263 mm/s for the high strength sample specimen; this is due to the fact that the machine stalled and failed to complete the cut.

Table 4.1 Effect of cutting speed on force measurements and specific energy on a low strength sample.

Cutting Speed (mm/s)	Rake angle	Depth of cut (mm)	Mean Cutting force (N)	Mean Thrust force (N)	Specific Energy SE (MJ/m ³)
263 mm/s	0°	0.5	436.99	570.38	54.62
		1.0	577.53	670.27	36.10
		1.5	663.69	686.75	27.65
		2.0	848.34	764.85	26.51
		2.5	1159.20	1040.10	28.98
	10°	0.5	299.02	404.07	37.38
		1.0	414.94	410.98	25.93
		1.5	446.22	378.56	18.59
		2.0	700.62	611.83	21.89
		2.5	962.71	734.04	24.07
	20°	0.5	470.33	656.99	58.79
		1.0	653.43	705.34	40.84
		1.5	765.25	669.21	31.89
		2.0	706.78	610.76	22.09
		2.5	863.21	578.88	21.58
333 mm/s	0°	0.5	449.81	633.08	56.23
		1.0	534.44	654.33	33.40
		1.5	742.68	772.82	30.94
		2.0	981.69	915.76	30.68
		2.5	1072.00	943.92	26.80
	10°	0.5	544.70	743.60	68.09
		1.0	785.76	965.17	49.11
		1.5	842.18	805.24	35.09
		2.0	972.46	714.91	30.39
		2.5	1210.40	955.61	30.26
	20°	0.5	292.87	418.95	36.61
		1.0	368.26	389.72	23.02
		1.5	570.34	526.81	23.76
		2.0	647.28	380.16	20.23
		2.5	587.27	322.24	14.68

Table 4.2 Effect of cutting speed on force measurements and specific energy on a high strength sample

Cutting Speed (mm/s)	Rake angle	Depth of cut (mm)	Mean Cutting force (N)	Mean Thrust force (N)	Specific Energy SE (MJ/m ³)
263mm/s	0°	0.5	937.58	1350.40	117.20
		1.0	1405.30	1690.50	87.83
		1.5	-	-	-
		2.0	-	-	-
		2.5	-	-	-
	10°	0.5	777.56	1000.80	97.19
		1.0	1143.80	1153.80	71.49
		1.5	1477.20	1254.80	61.55
		2.0	1631.00	1260.10	50.97
		2.5	987.85	731.38	24.70
	20°	0.5	782.69	1069.80	97.84
		1.0	1036.10	1164.40	64.76
		1.5	1261.70	1233.50	52.57
		2.0	1631.00	1318.50	50.97
		2.5	1774.60	1212.30	44.37
333mm/s	0°	0.5	920.66	1238.80	115.08
		1.0	1395.10	1711.70	87.19
		1.5	1466.90	1233.50	61.12
		2.0	1501.23	1311.02	46.91
		2.5	1688.00	1390.46	42.20
	10°	0.5	467.76	539.56	58.47
		1.0	720.11	663.90	45.01
		1.5	1066.80	823.83	44.45
		2.0	1395.10	881.75	43.60
		2.5	1610.50	807.36	40.26
	20°	0.5	741.65	982.71	92.71
		1.0	965.79	940.73	60.36
		1.5	1118.10	1000.20	46.59
		2.0	1354.10	1148.50	42.32
		2.5	1743.90	1169.70	43.60

Figure 4.1 shows a high strength sample and the failure of the shaper machine to complete the cut at depth of 1.5 mm at a cutting speed of 263 mm/s using a 0° rake angle cutting tool. It was observed that there was material build-up ahead of the tool tip and this build-up had reached a sufficient level of compaction which stopped the cutting tool from moving any further. Based on the results of cutting through high strength samples, it was concluded that the speed setting would be kept constant at 333 mm/s which was also in the best interest of health and safety. It was also observed during experimentation that the cutting tool made a large impact upon first contact with the edge of the sample; hence the leading edge of the sample was blunted or chamfered before each cut.

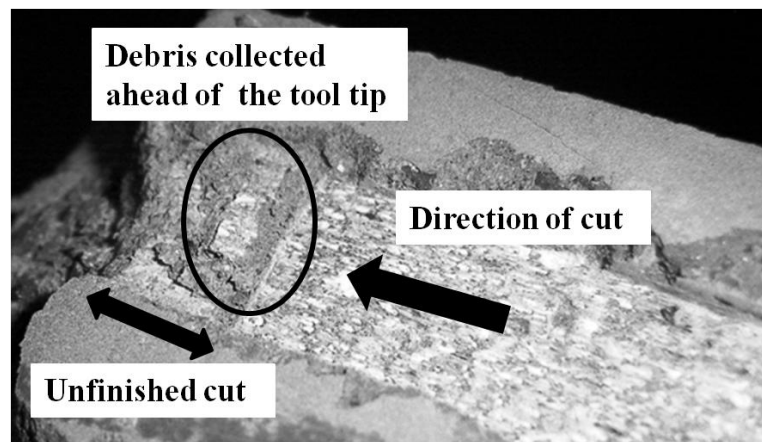


Figure 4.1 Failure to complete the cut at lower speed setting.

4.3. Summary of experimental results

A total of 150 grooves were cut on high and low strength samples in their dry state under normal temperature and pressure based on the matrix of experiments as detailed in Section 3.5. Each cut at a particular depth of cut was repeated 5 times and the cutting force (F_v), thrust force (F_p), side force (F_s) signals were recorded and analysed. A typical force signal recorded by the dynamometer is shown in Figure 4.2, and from this signal the force measurements for the duration of the cut were isolated, the end result of which is depicted in Figure 4.3. Mean values of the tri-axial forces were extracted from the signal and the averages of 5 signals was calculated and tabulated; specific energy was calculated using

Equation 2.30. In the absence of side rake angle in the cutting tool, it was observed that the sideways force was negligible in magnitude compared to the other two forces, hence only the cutting force and the thrust forces have been tabulated. All the results are tabulated in Tables 4.3 and 4.4 for low and high strength samples respectively.

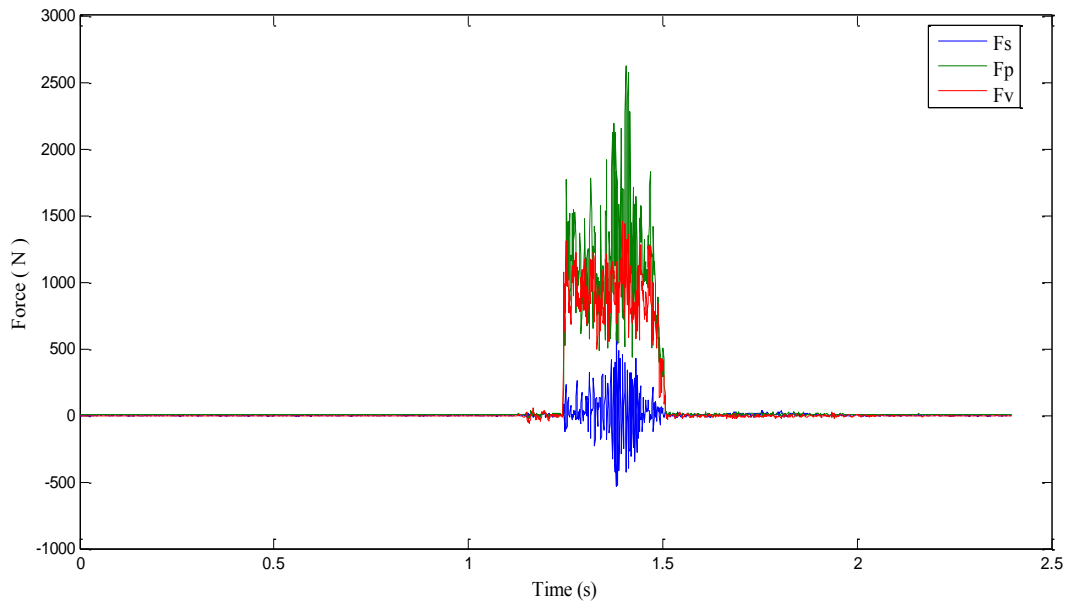


Figure 4.2 Force signals obtained from tri-axial dynamometer measuring a single cut showing- Side force (F_s), Thrust force (F_p) and Cutting force (F_v).

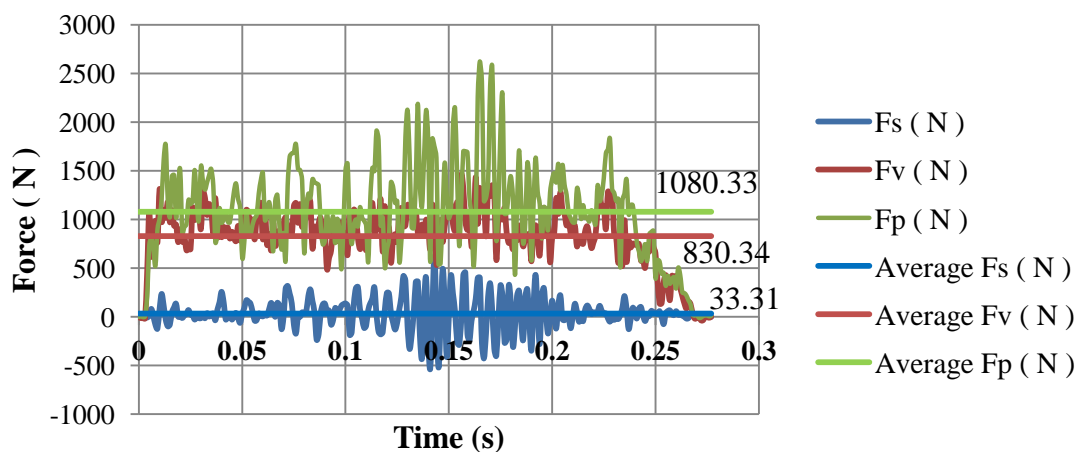


Figure 4.3 Typical tri-axial forces measured for the duration of a single cut

Table 4.3 Results of linear cutting tests on low strength sample [cutting speed 333 m/s]

Sample type	Rake angle	Depth of cut (mm)	Mean Cutting Force Fv (N)	Mean Thrust Force Fp (N)	Specific Energy SE (MJ/m ³)
Low strength	0°	0.5	431.91	588.34	53.99
		1.0	660.10	673.25	41.26
		1.5	839.41	725.32	34.98
		2.0	758.07	648.49	23.69
		2.5	840.95	649.45	21.02
	10°	0.5	424.37	552.42	53.05
		1.0	643.52	637.42	40.22
		1.5	777.25	704.07	32.39
		2.0	883.93	709.70	27.62
		2.5	783.07	509.14	19.58
	20°	0.5	422.73	563.26	52.84
		1.0	483.46	416.82	30.22
		1.5	448.58	402.15	18.69
		2.0	720.42	591.53	22.51
		2.5	727.91	494.18	18.20

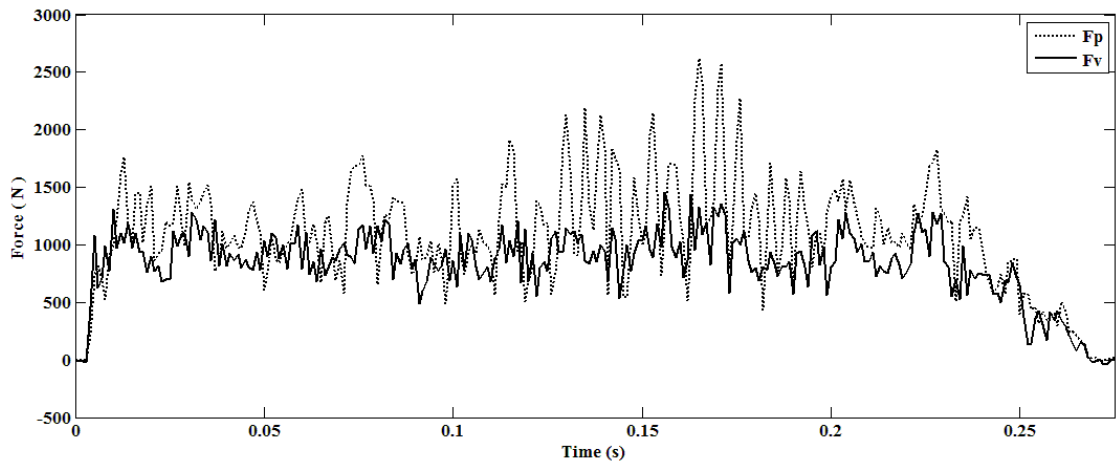
Table 4.4 Results for linear cutting on high strength sample [cutting speed 333mm/s]

Sample type	Rake angle	Depth of cut (mm)	Mean Cutting Force Fv (N)	Mean Thrust Force Fp (N)	Specific Energy SE (MJ/m ³)
High strength	0°	0.5	853.57	1091.08	106.70
		1.0	921.37	1035.22	59.80
		1.5	1284.80	1197.63	53.53
		2.0	1457.90	1177.70	45.56
		2.5	1548.96	1272.52	40.30
	10°	0.5	810.69	1029.37	101.34
		1.0	1023.75	968.36	63.98
		1.5	1195.36	1136.80	49.81
		2.0	1398.20	1196.32	43.69
		2.5	1633.10	1211.20	40.83
	20°	0.5	679.70	911.71	84.96
		1.0	956.55	931.38	59.78
		1.5	1066.41	1022.35	44.43
		2.0	1319.18	1134.66	41.22
		2.5	1313.03	1062.69	32.83

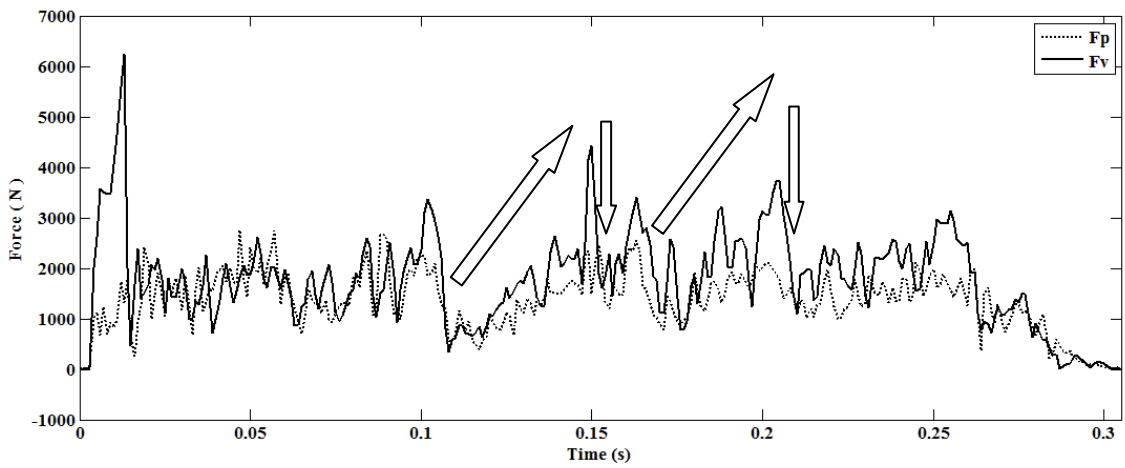
4.4. Force signal analysis

Figure 4.4a and 4.4b show typical cutting and thrust force components for the duration of a cut at 0.5 mm and 2.5 mm depth of cut respectively of a high strength sample. It was observed that at lower depths of cut the cutting force (F_v) was lower in magnitude than that of the thrust force (F_p), but as the depth of cut increases this feature reverses, that is, the cutting force becomes predominant in magnitude than the thrust force. This was observed for all cuts irrespective of sample type or the cutting tool used in this study. The nature of these signals is representative of the brittle nature of the specimens; it can be observed from both figures that as soon as the tool impacts with the rock-like sample, there was a gradual but a sudden rise in the cutting force (approximately 1000 N and 6000 N as shown in Figure 4.4a and 4.4b respectively). As the tool ploughs further into the sample, cracks initiate, usually under the tool tip and propagate down before turning up and reaching the free surface thus producing a chip and the cutting force suddenly drops, indicated in Figure 4.5 between 0.012 s and 0.014 s. Ejection of the chip from the surface is usually at high speed and velocities of upto 4 m/s have been recorded in this study; this high velocity ejection of the chip is represented by a spike in the thrust force. This cycle of local maxima and minima of the cutting and thrust force repeats for the entire duration of the cut, signifying the brittle breaking off of the chip from the surface of the sample.

At shallow depths of cut (less than 1 mm) the force signals are observed to be continuous, as seen in Figure 4.4a, while at greater depths, the force signals take a form of a 'saw-tooth' profile, as seen in Figure 4.4b indicated by the arrows; cutting events can be distinctly recognised, for example, from Figure 4.4b between 0.1s and 0.15s the cutting force is seen to gradually rise even though it is interspersed with local maxima and minima, indicating the formation of minor chips and the crushed zone ahead of the tool tip. The crushed zone is a region of highly compacted powdered material and crucial for the transmission of the cutting force from tool to the sample and the saw-tooth profile of the cutting force is characteristic of the constant build-up and breaking-off of this crushed zone. This is discussed in greater detail in Section 4.6.



a) 0.5 mm depth of cut



(b) 2.5 mm depth of cut

Figure 4.4 Variation of the cutting and thrust force with increase in depth of cut

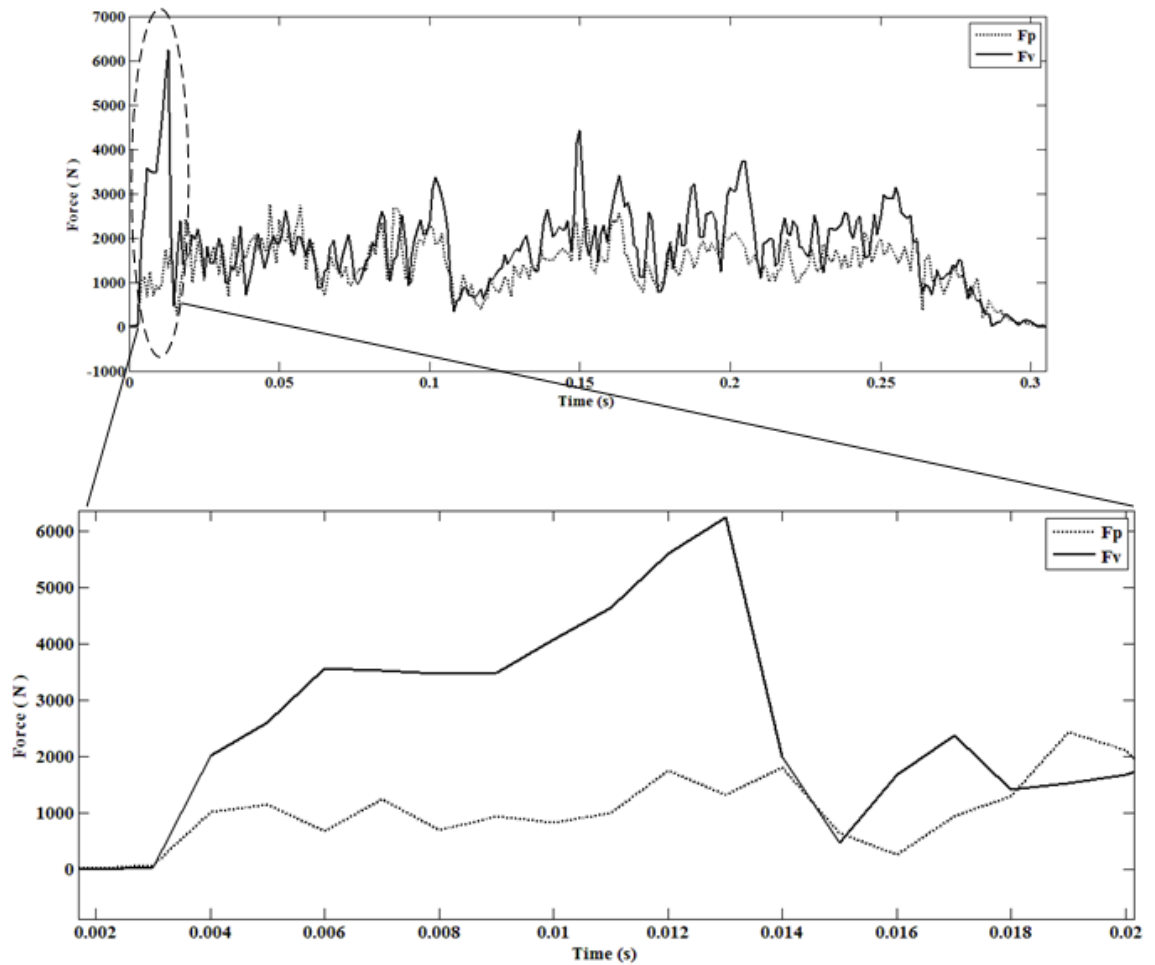


Figure 4.5 Variation of the cutting and thrust force

4.5. Effect of Rake Angle and Depth of Cut on the cutting performance of the tool

In describing the failure mechanism of rocks, presented in Section 2.3.2, it was found that the rake angle of the cutting tool and the depth of cut play a crucial role. Three rake angles were chosen to be studied in this work – 0° , 10° and 20° . Cutting force (F_v), thrust force (F_p) and specific energies (SE) was used to evaluate the cutting performance.

4.5.1. Variation of cutting force and thrust force

This section looks at the cutting and thrust force variations and characteristics of chips.

4.5.1.1. Low strength sample

4.5.1.1.1. Cutting test using 0° rake angle cutting tool

Figure 4.6 shows the F_v and F_p variation against the depth of cut. Both the forces start at a low magnitude with the thrust force being higher (approximately 590 N) than the cutting force (approximately 430 N) at depth of cut of 0.5 mm. Depth of cut was incremented in steps of 0.5 mm; it was observed that as the depth increases so does the cutting force. At the maximum depth of cut of 2.5 mm the cutting force measures an average of 840 N while the thrust force measures an average 650 N.

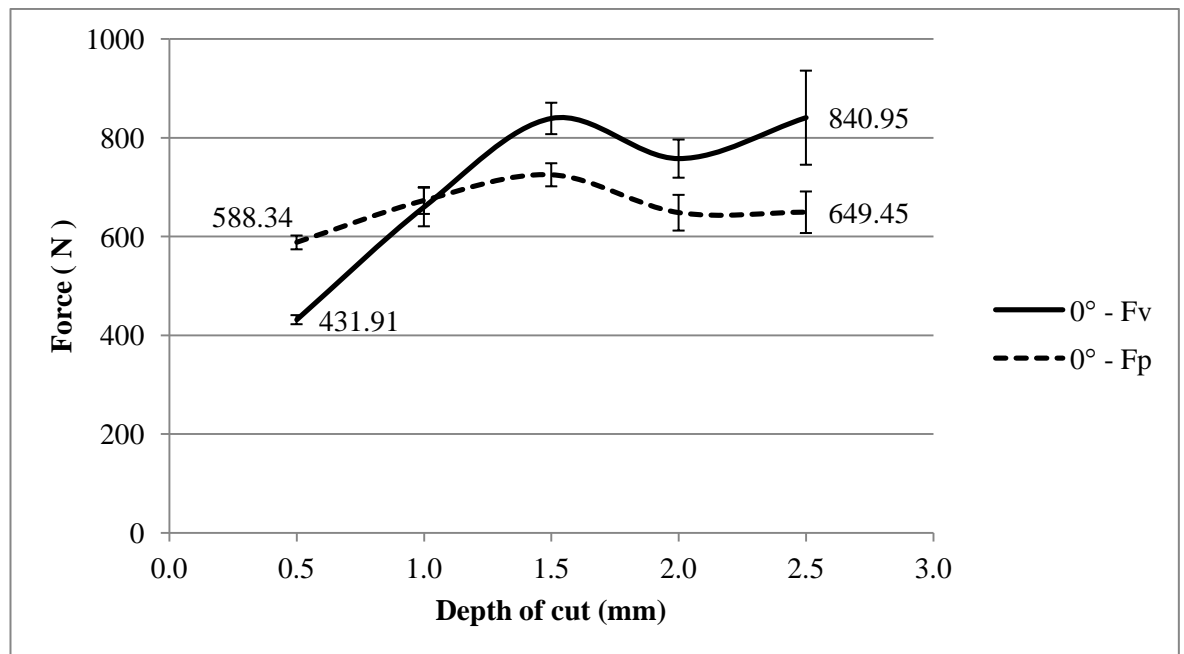


Figure 4.6 Variation of cutting force (F_v) and thrust force (F_p) with respect to depth of cut using a 0° rake angle cutting tool

Figure 4.7 shows the cutting force trace of measurements taken at 0.5 mm and 2.5 mm depth of cut. The difference clearly shows the increase in cutting force measured at different depths of cut. Figure 4.8 shows thrust force traces at the similar depths of cut, which shows the thrust force stabilising between 0.5 mm and 2.5 mm depth of cut.

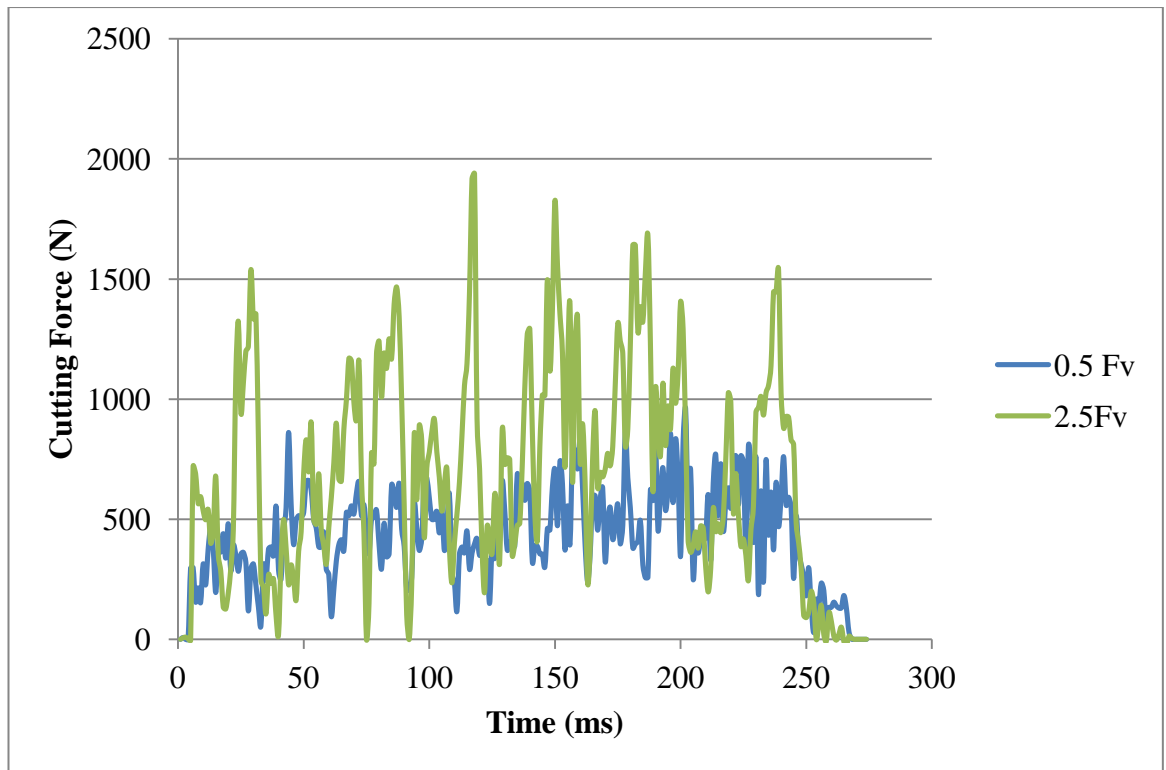


Figure 4.7 Comparison of a typical cutting force trace at depths of cut of 0.5 mm and 2.5 mm on a low strength sample using a 0° rake angle cutting tool

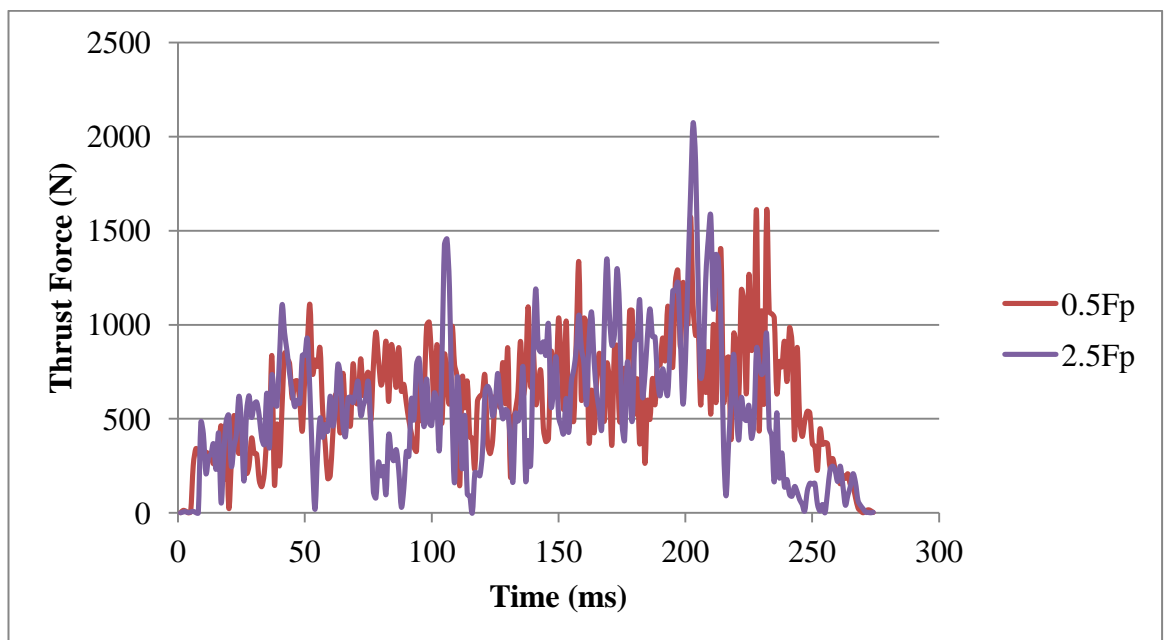
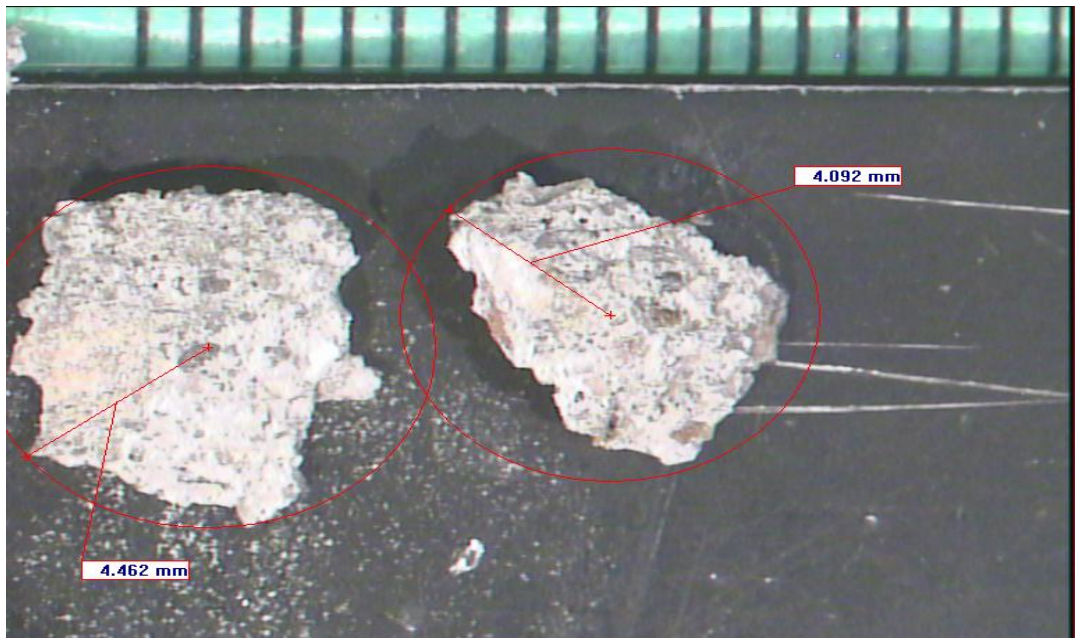


Figure 4.8 Comparison of a typical thrust force trace at depths of cut of 0.5 mm and 2.5 mm on a low strength sample using a 0° rake angle cutting tool



(a)



(b)

Figure 4.9 Characteristics of chips obtained at (a) 0.5 mm and (b) 2.5 mm

Figure 4.9 (a) and 4.9 (b) shows the chips formed at depth of cut 0.5 mm and 2.5 mm respectively; the increase of chip sizes with increasing depth of cut is clearly visible.

4.5.1.1.2. Cutting test using 10° rake angle cutting tool

Figure 4.10 shows the F_v and F_p variation against the depth of cut while cutting with a 10° rake angle cutting tool. At the initial depth of cut of 0.5 mm the thrust force (approximately 550 N) was observed to be greater than the cutting force (approximately 420 N). As the depth of cut increases the cutting force also increases; it can be observed that the thrust force was steady for depths of cut from 0.5 mm to 2.0 mm but dips at 2.5 mm depth of cut.

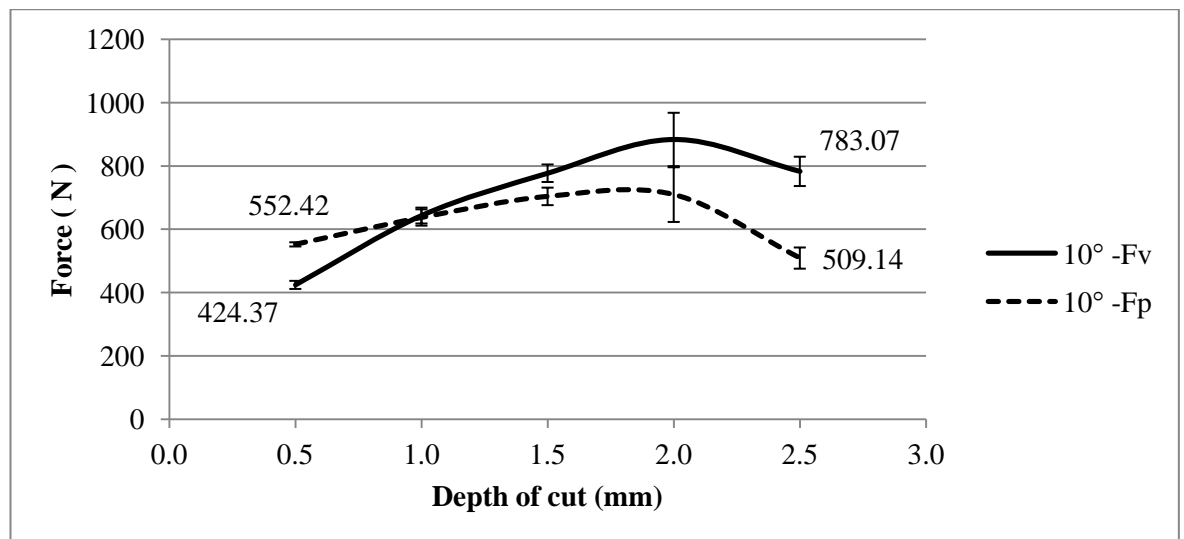


Figure 4.10 Variation of cutting force (F_v) and thrust force (F_p) with respect to depth of cut using a 10° rake angle cutting tool

Figure 4.11 shows the cutting force trace for cutting at 0.5 mm and 2.5 mm depth. From the figure it can be observed that for 2.5 mm depth of cut the cutting force trace dips below those measured for 0.5 mm depth of cut for the duration between 250 and 300 ms, this is attributed to the fact the specimen has been clamped and that as the cutting tool moves towards the end of the cut it has already taken away sizeable chunks of the material ahead of it and the tool faces minimal resistance in cutting thus reading a lower cutting force. Figure 4.12 shows the thrust force trace; minimal differences at both depths are visible.

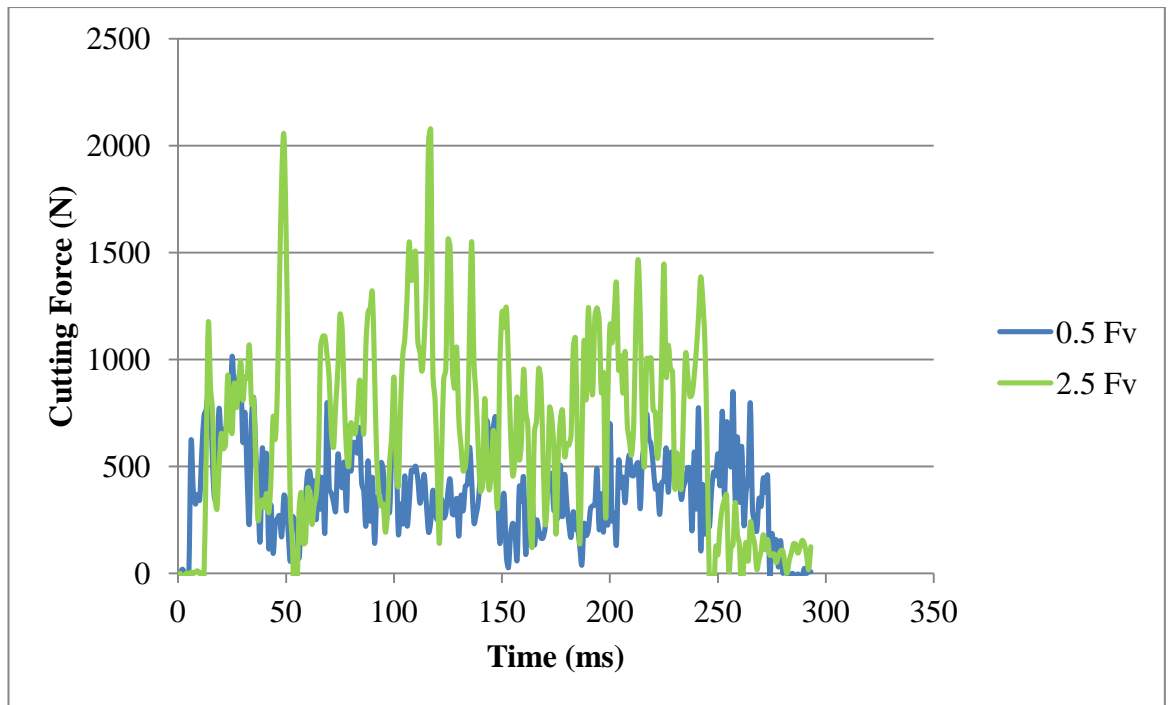


Figure 4.11 Comparison of a typical cutting force trace at depths of cut of 0.5 mm and 2.5 mm on a low strength sample using a 10° rake angle cutting tool

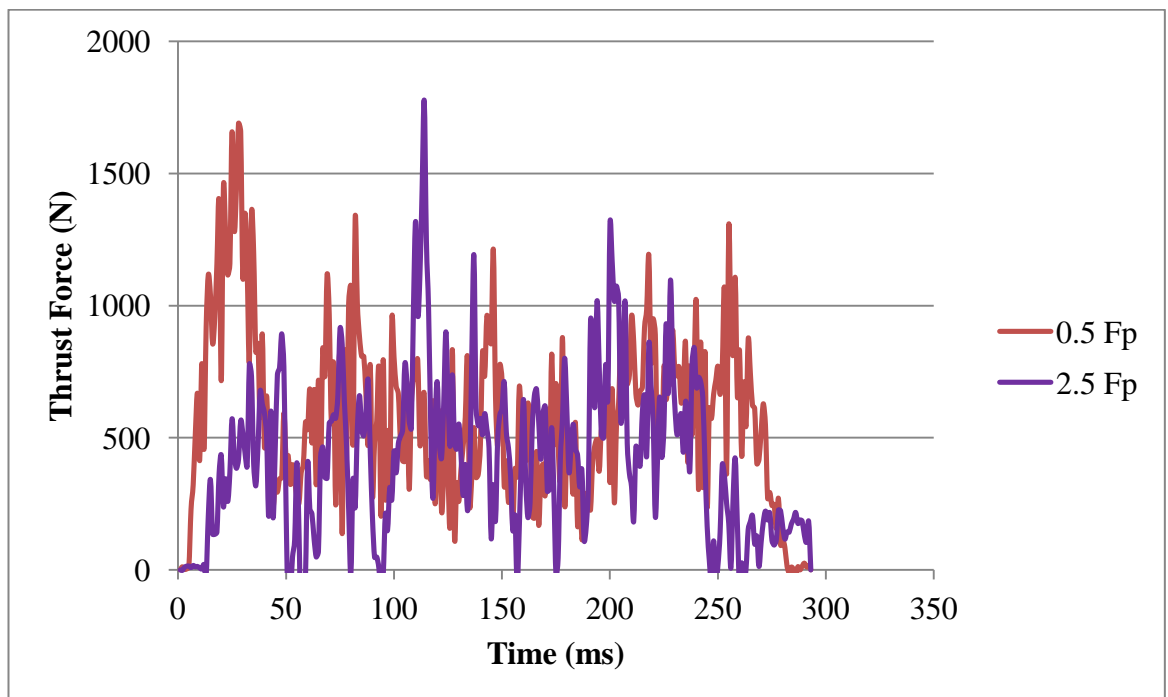
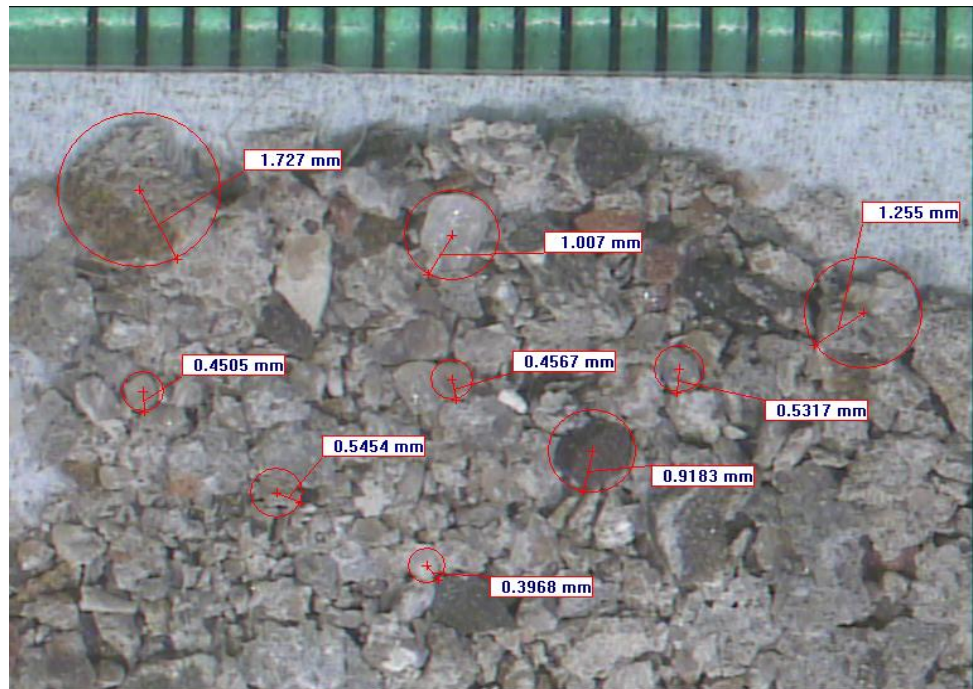


Figure 4.12 Comparison of a typical thrust force trace at depths of cut of 0.5 mm and 2.5 mm on a low strength sample using a 10° rake angle cutting tool

Figure 4.13 (a) and 4.13 (b) show the chips formed at 0.5 mm and 2.5 mm depth of cut respectively.



(a)



(b)

Figure 4.13 Characteristics of chips obtained at (a) 0.5 mm and (b) 2.5 mm

4.5.1.1.3. Cutting test using 20° rake angle cutting tool

Figure 4.14 shows the Fv and Fp variation against the depth of cut while cutting with a 20° rake angle cutting tool.

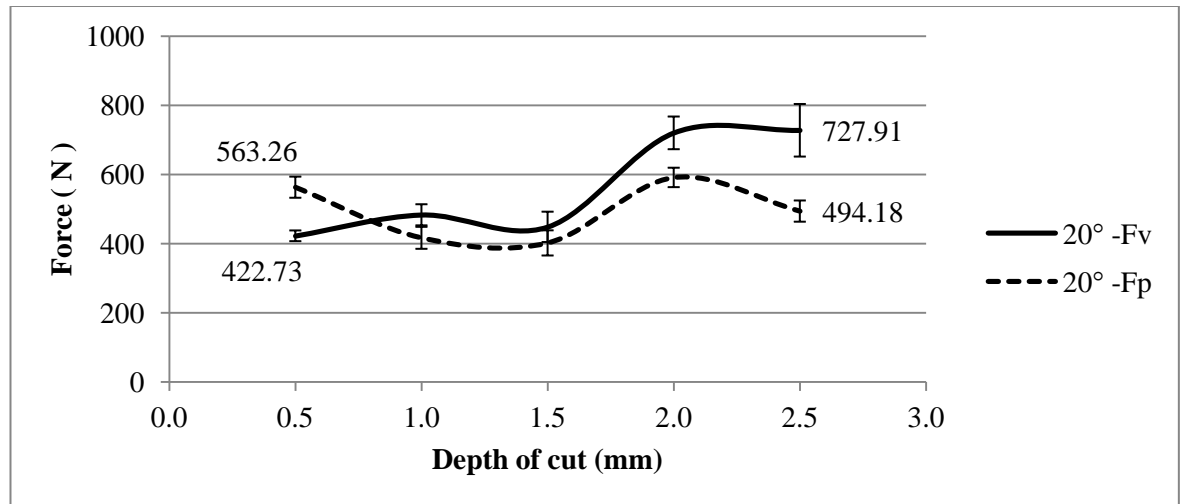


Figure 4.14 Variation of the cutting force (Fv) and thrust force (Fp) with respect to depth of cut using a 20° rake angle cutting tool

It can be observed from Figure 4.14 that the cutting force shows the rise in cutting force as the depth of cut increased. Initial cutting force recorded for this cutting tool is 420 N and it rises to 730 N at the final depth of cut, while the thrust force was stable around 500 N.

Figures 4.15 and 4.16 show the cutting force and thrust force trace respectively for depths of 0.5 mm and 2.5 mm. Figure 4.17 show the characteristics of chips collected at 0.5 and 2.5 mm depth of cut.

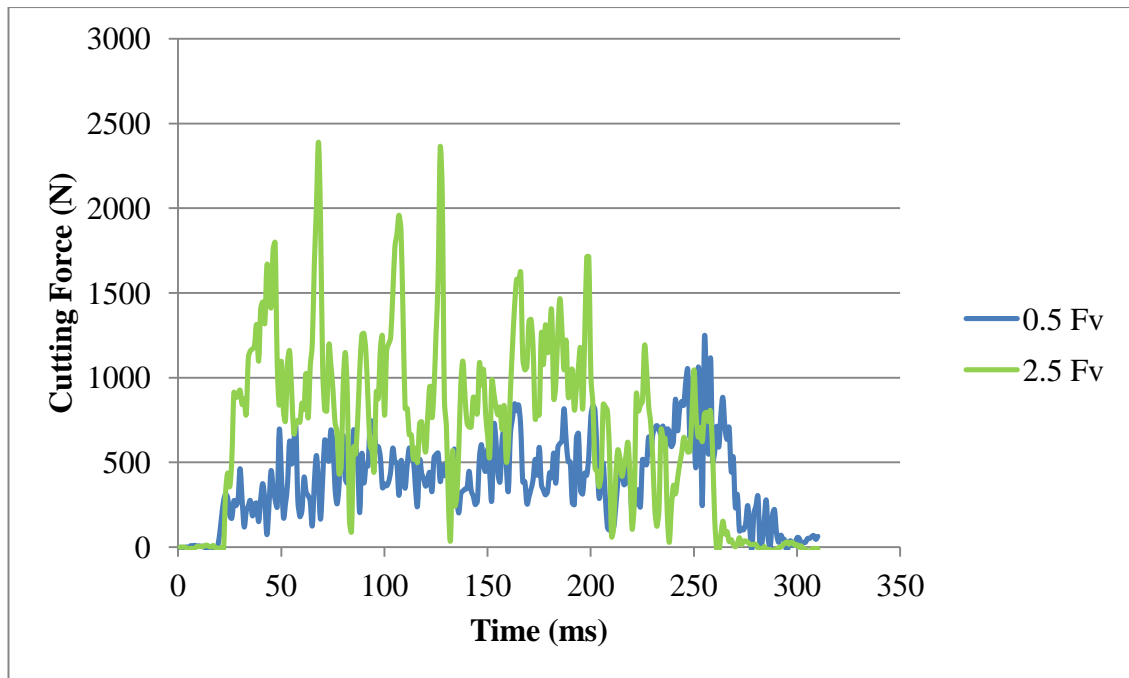


Figure 4.15 Comparison of a typical cutting force trace at depths of cut of 0.5 mm and 2.5 mm on a low strength sample using a 20° rake angle cutting tool

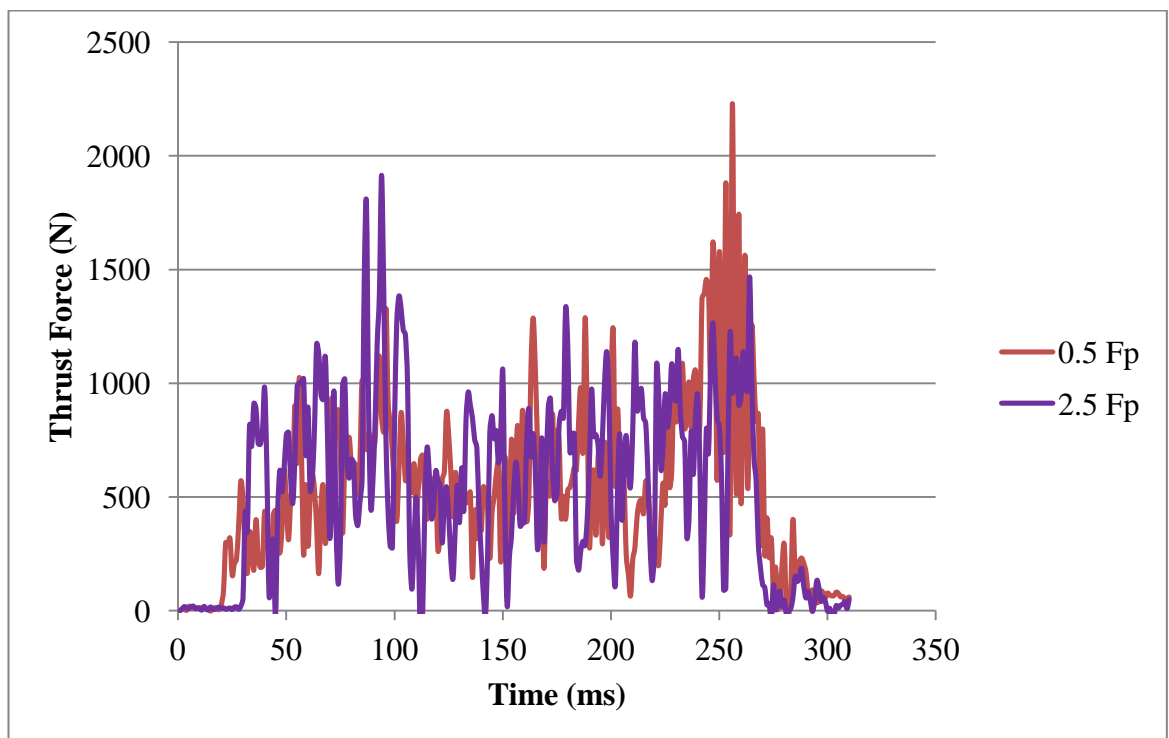


Figure 4.16 Comparison of a typical thrust force trace at depths of cut of 0.5 mm and 2.5 mm on a low strength sample using a 20° rake angle cutting tool



(a)



(b)

Figure 4.17 Characteristics of chips obtained at (a) 0.5 mm and (b) 2.5 mm

4.5.1.1.4 Statistical analysis of cutting test on low strength sample

Statistical analysis using MINITAB 16 was undertaken to find the correlation of rake angles at each depth of cut; the test results are summarised and presented in Appendix B and C for cutting and thrust force respectively. Regression analysis was undertaken to find the influence of the depth of cut and rake angle on the cutting force and thrust force and are presented in this section. Linear regression has been used in the past to provide an empirical model relating the different parameters and the force components [49, 95-98]

Figure 4.18 shows the empirical relationship obtained between the cutting force and rake angle. A linear relationship was obtained with an R^2 value of 0.09, that is, only 9% of the output variable (cutting force) was determined by the input variable (rake angle) and expressed as:

$$F_v = -7.2734 \times \text{Rake angle} + 727.4 \quad (4.1)$$

The low R^2 value is due to the scattered data as observed from the graph.

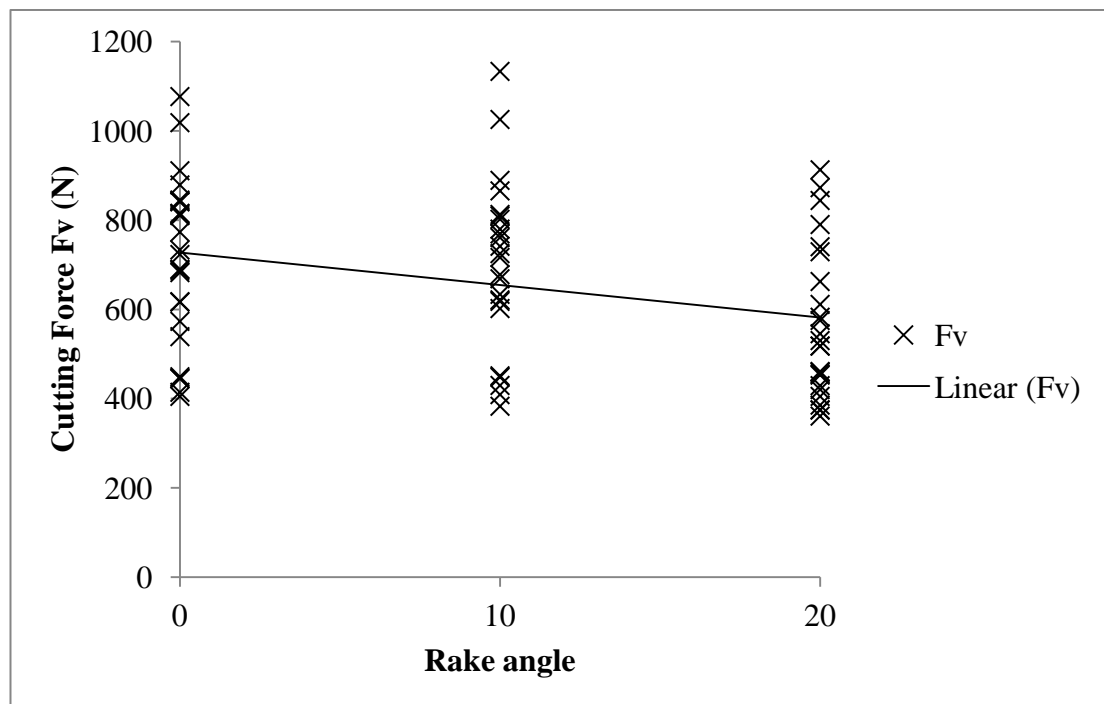


Figure 4.18 Empirical relation between cutting force and rake angle

Figure 4.19 shows the empirical relationship between the cutting force and the depth of cut, the linear equation was obtained at an R^2 value of 0.82 and given as:

$$F_v = 182.93 \times \text{Depth of cut} + 382.74 \quad (4.2)$$

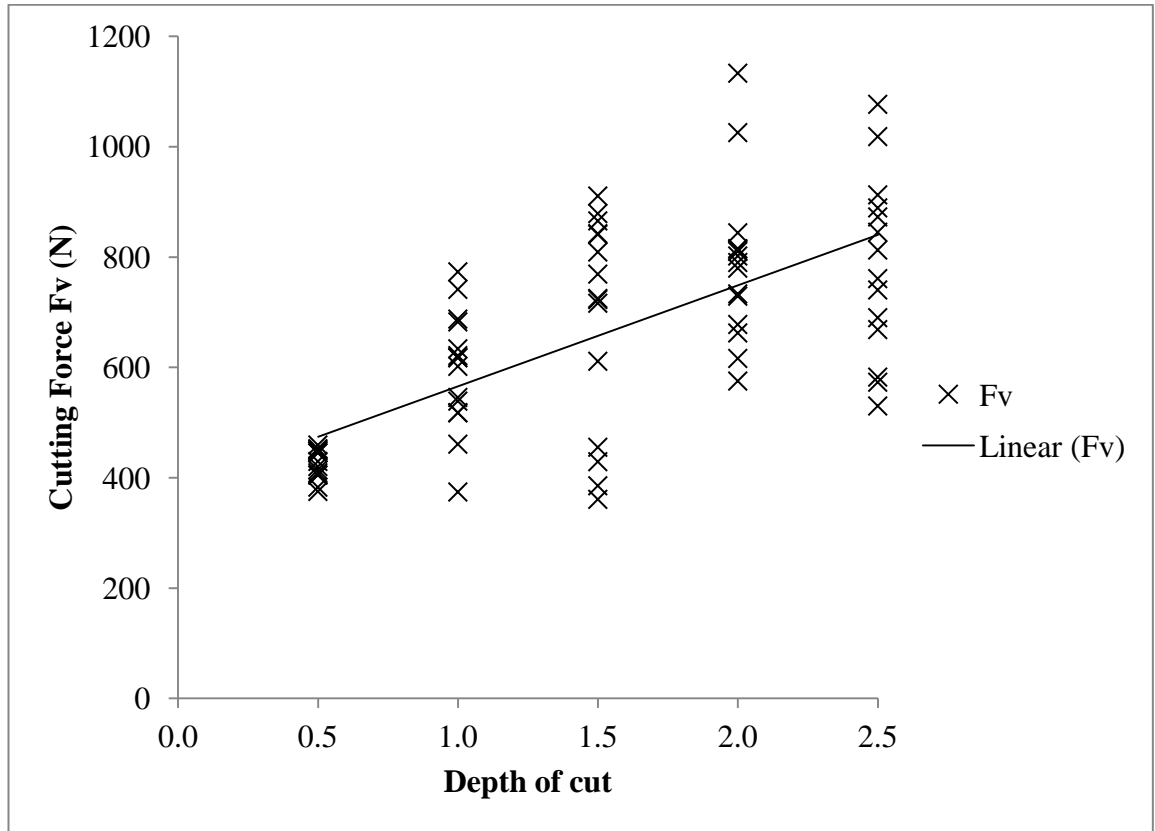


Figure 4.19 Empirical relation between cutting force and depth of cut

A regression analysis was performed using MS Excel with depth of cut and rake angle as the independent variables and F_v as the dependant variable. A linear regression model was obtained at an R^2 value of 0.55 which gave the predictor equation:

$$F_v = 455.47 - 7.27 \times \text{Rake angle} + 182.93 \times \text{Depth of cut}. \quad (4.3)$$

Residual plots are shown in Figure 4.20, it can be observed that there is no pattern in the residual plot thus showing the linear model provides a good fit for the data.

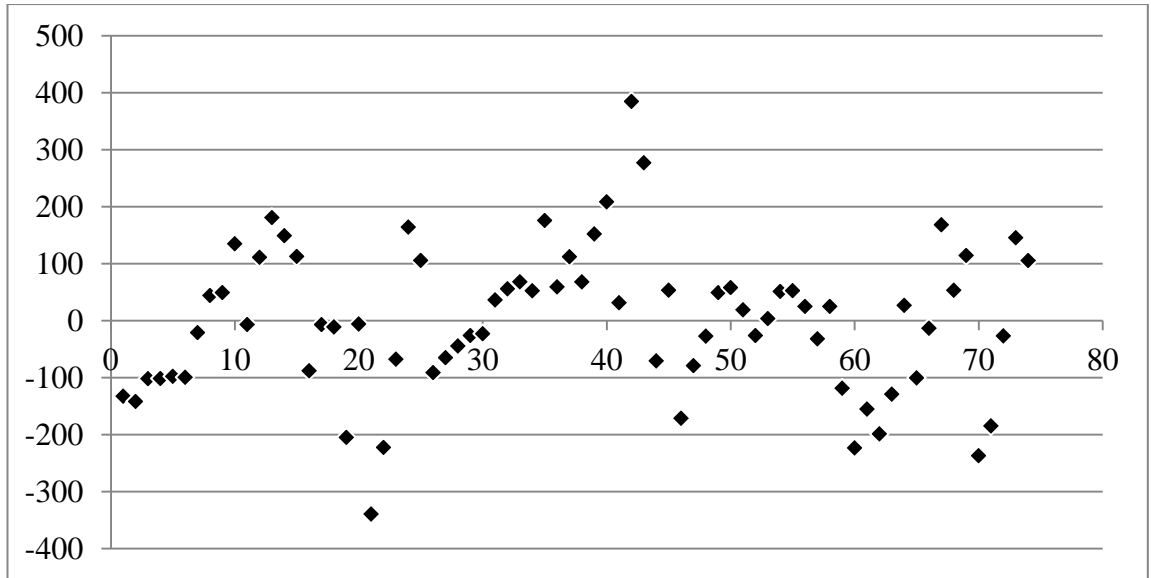


Figure 4.20 Residual plots obtained for cutting force via rake angle and depth of cut

Figure 4.21 shows the empirical relationship between the thrust force and the rake angle. A linear equation with an $R^2 = 0.98$ was obtained, given as:

$$F_p = -8.169 \times \text{Rake angle} + 673.83 \quad (4.4)$$

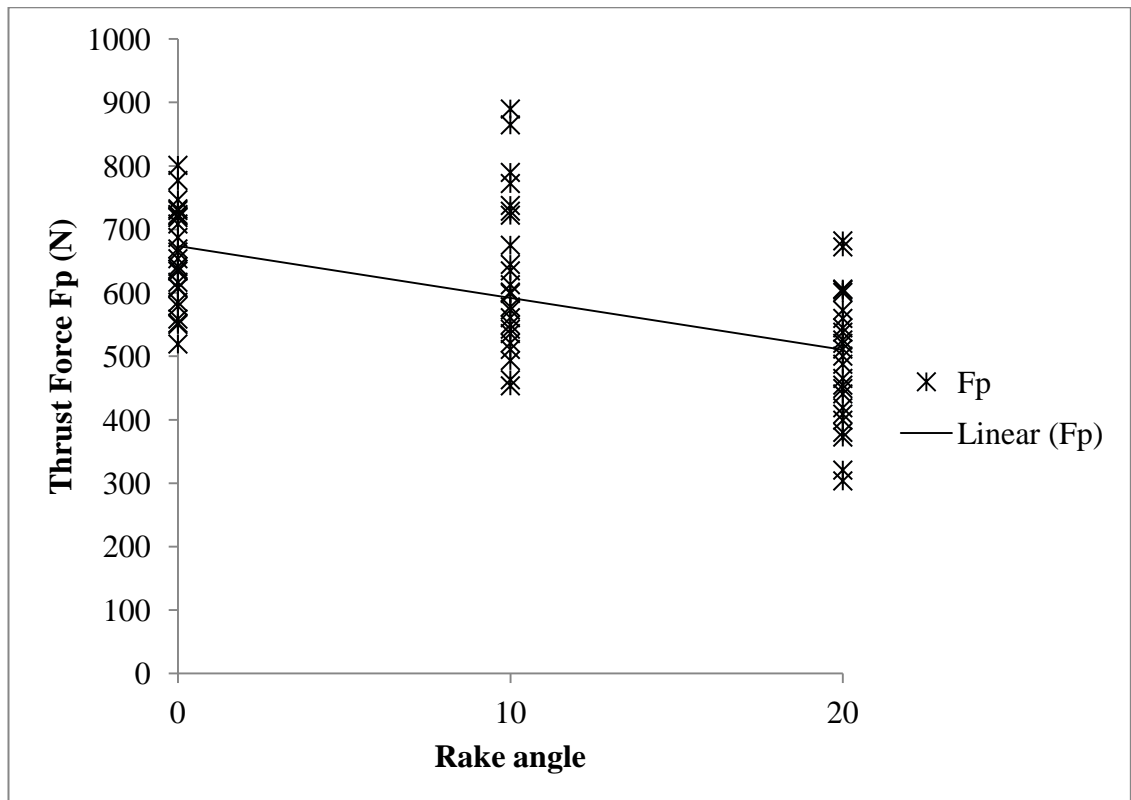


Figure 4.21 Empirical relation between thrust force and rake angle

Figure 4.22 shows the empirical relationship obtained for thrust force and depth of cut. The linear equation was obtained with a R^2 value of 0.01 and is given as :

$$F_p = 10.47 \times \text{Depth of cut} + 576.57 \quad (4.5)$$

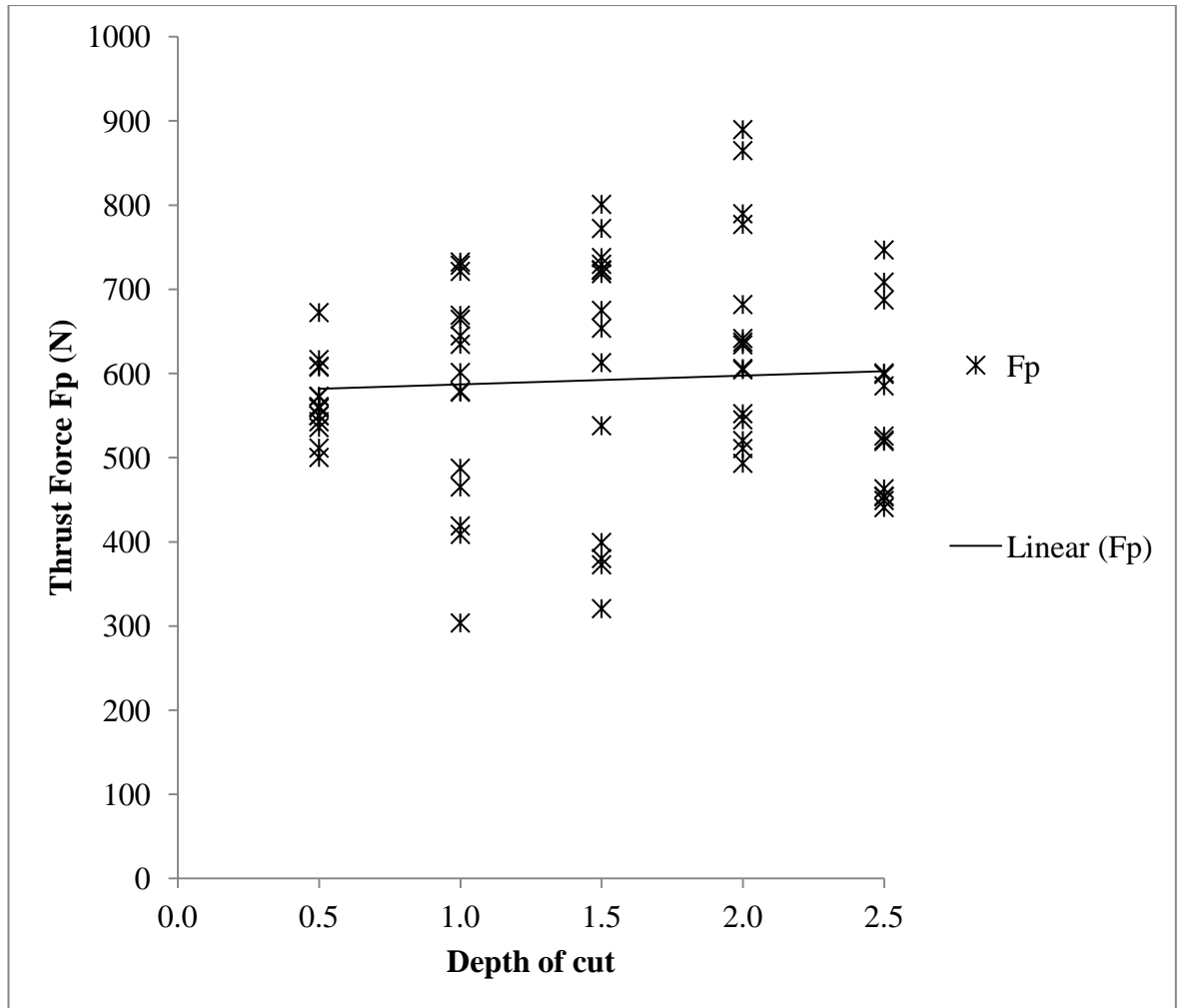


Figure 4.22 Empirical relation between thrust force and depth of cut

A linear regression model was obtained for the describing the relation between depths of cut, rake angle and thrust force. The predictor equation is given as:

$$F_p = 658.25 - 8.16 \times \text{Rake angle} + 10.47 \times \text{Depth of cut} \quad (4.6)$$

The $R^2 = 0.31$ shows that the overall accuracy of the regression equation is 30%. Table 4.5 shows the experimentally obtained and predicted cutting and thrust forces using Equations 4.3 and 4.6.

Table 4.5 Comparison of experimental and predicted forces for low strength sample

Rake angle	Depth of cut (mm)	Fv (N)	Predicted Fv (N)	Fp (N)	Predicted Fp (N)
0°	0.5	431.91	546.93	588.34	663.48
	1.0	660.10	638.40	673.25	668.72
	1.5	839.41	729.86	725.32	673.95
	2.0	758.07	821.33	648.49	679.19
	2.5	840.95	912.79	649.45	684.42
10°	0.5	424.37	474.23	552.42	581.88
	1.0	643.52	565.70	637.42	587.12
	1.5	777.25	657.16	704.07	592.35
	2.0	883.93	748.63	709.70	597.59
	2.5	783.07	840.09	509.14	602.82
20°	0.5	422.73	401.53	563.26	500.28
	1.0	483.46	493.00	416.82	505.52
	1.5	448.58	584.46	402.15	510.75
	2.0	720.42	675.93	591.53	515.99
	2.5	727.91	767.39	494.18	521.22

4.5.1.1.5 Summary of cutting test on low strength sample

The results from the test on low strength sample shows that the cutting force increases with increase in the depth of cut. The cutting force is lower than the thrust force at depth of cut 0.5 mm and is observed to increase with increase in depth of cut, while the thrust force remains stable. While it can be seen that the cutting force increases with depth of cut (from 400 N to 800 N) in a linear fashion, however, the thrust force component is seen rather to fluctuate around the mean force of 600 N and thus remaining stable for all depths of cut irrespective of the rake angle of the cutting tool.

Observations:

- a. At 0.5mm depth of cut, it can be observed that the rake angles have no significant influence; at these shallow depths of cut the cutting action is analogous to grinding or rubbing action. For all rake angles the cutting force was observed to be lower than the thrust force.
- b. As the depth of cut increases so does the cutting force. The thrust force stabilises as the depth of cut increases.
- c. Force trace analysis has shown the visible increase of the cutting force component between the initial and the final depth of cut. The initial and final thrust force components appear to overlap with one another indicative of the stabilization of the thrust force.
- d. From Figure 4.18 and 4.21 it can be observed that the cutting force and the thrust force components decrease with increase in rake angle. Figure 4.19 shows a linear increase in cutting force as the depth of cut increases but the thrust force only marginally increases as shown in Figure 4.22.

4.5.1.2. High strength sample

4.5.1.2.1 Cutting test using 0° rake angle cutting tool

Figure 4.23 shows the variation of the cutting and thrust force with respect to the depth of cut. At 0.5 mm depth of cut the cutting force is lower than the thrust force and with increasing depth of cut, the cutting force also increases. Figure 4.24 and 4.25 shows the variation of the cutting force and thrust force trace for the initial and final depths of cut. From Figure 4.24 it can be observed that the rise in the cutting force while from Figure 4.25 it was observed that the thrust force traces were overlapping. Figure 4.26 a and 4.26 b shows the characteristics of the chips obtained at 0.5 mm and 2.5 mm depth of cuts respectively; the chip size increases with increasing depth of cut.

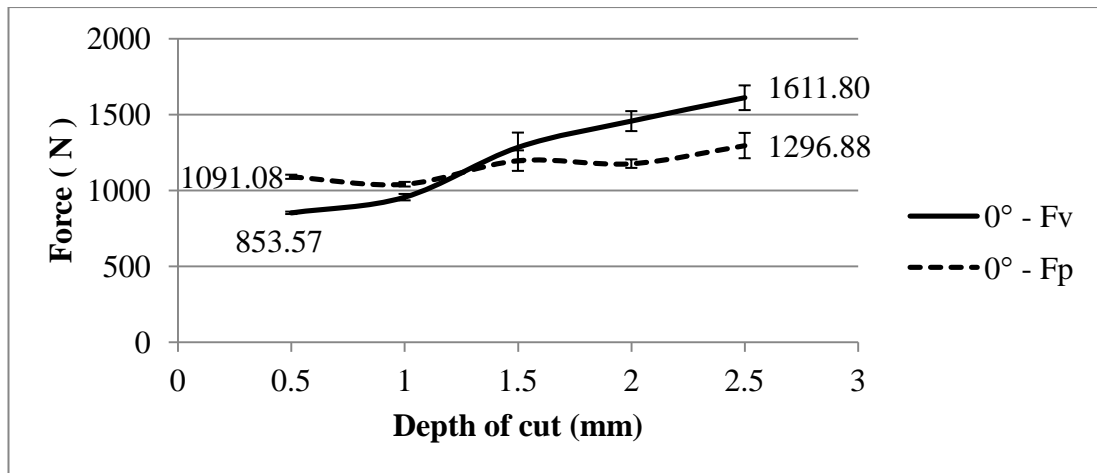


Figure 4.23 Variation of the cutting force (F_v) and thrust force (F_p) with respect to depth of cut using a 0° rake angle cutting tool

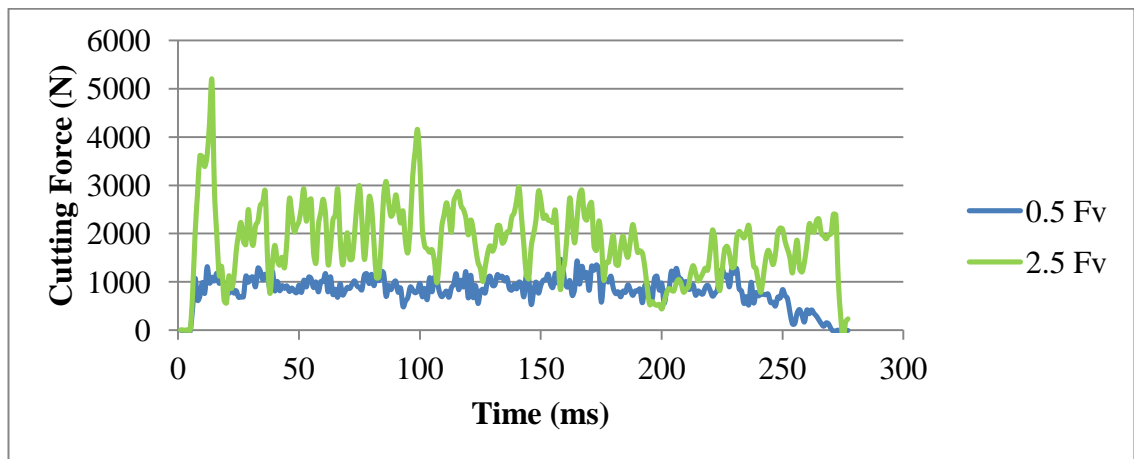


Figure 4.24 Comparison of typical cutting force trace at depth of cut 0.5 mm and 2.5 mm on a high strength sample using a 0° rake angle cutting tool

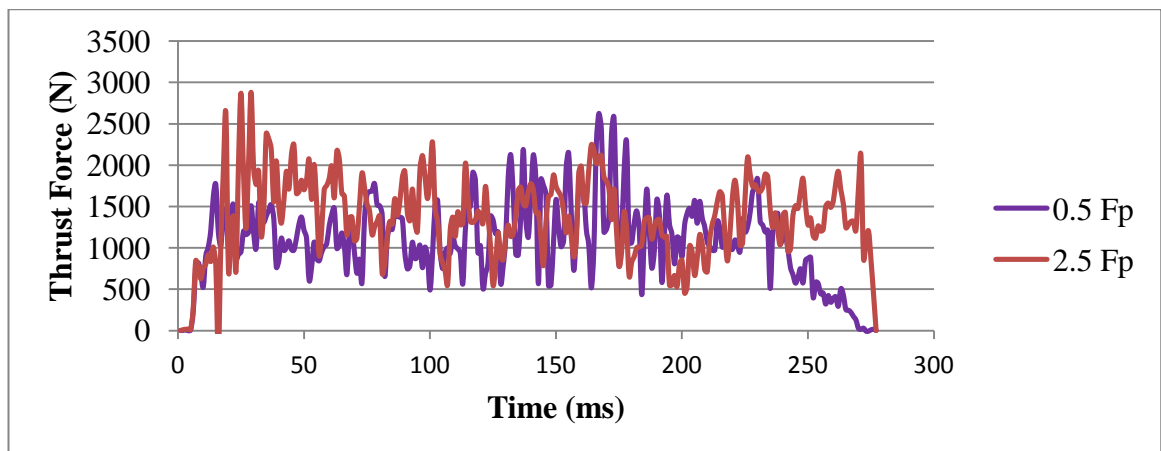
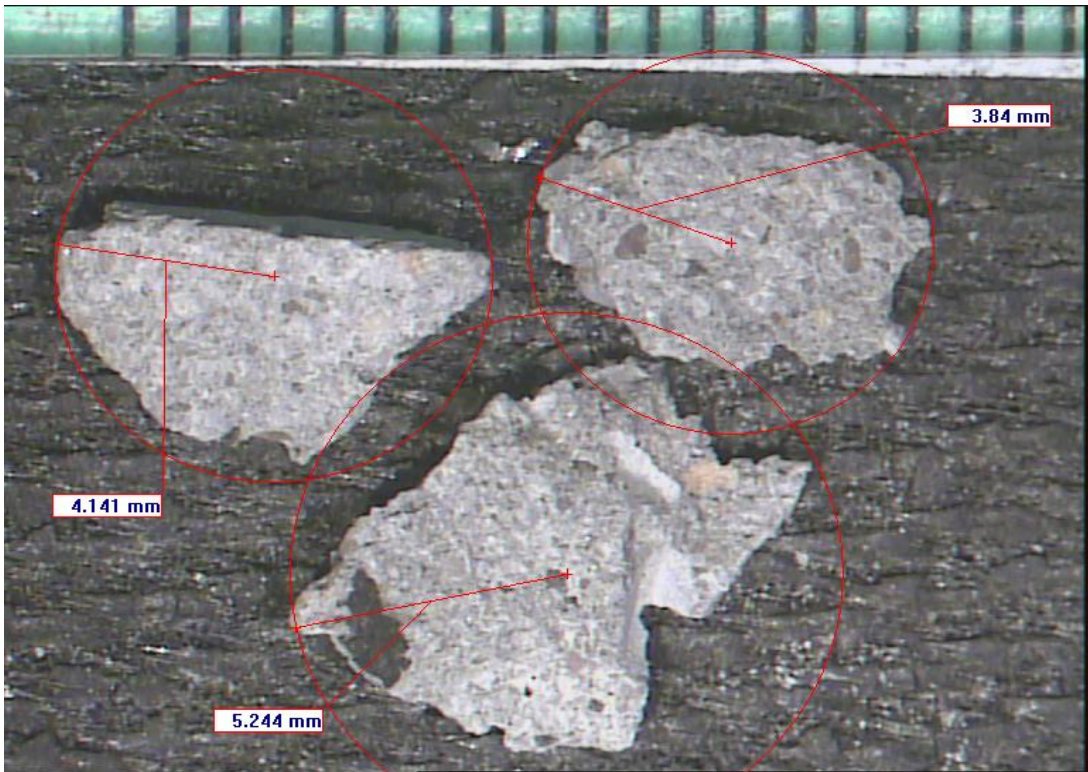


Figure 4.25 Comparison of typical thrust force trace depth of cut of 0.5mm and 2.5 mm on a high strength sample using a 0° rake angle cutting tool



(a)



(b)

Figure 4.26 Characteristics of chips obtained at (a) 0.5 mm and (b) 2.5 mm

4.5.1.2.2 Cutting test using 10° rake angle cutting tool

Figure 4.27 shows the variation of the cutting and thrust force with respect to the depth of cut.

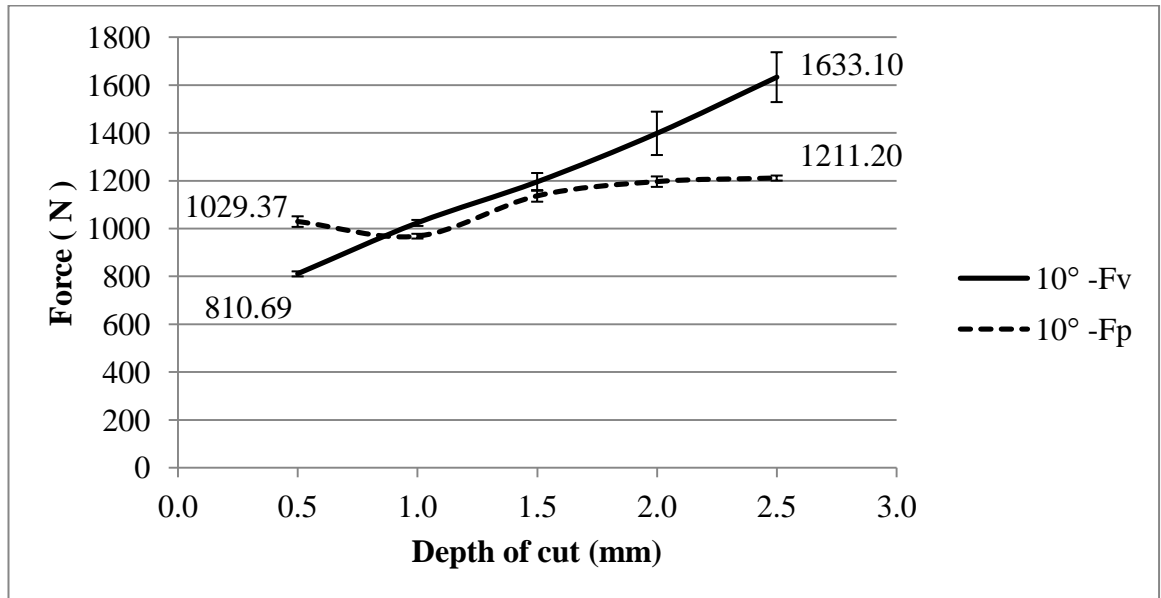


Figure 4.27 Variation of the cutting force (F_v) and thrust force (F_p) with respect to depth of cut using a 10° rake angle cutting tool

Figures 4.28 and 4.29 show the comparison of a typical cutting and thrust force trace obtained at depths of cut 0.5 and 2.5 mm respectively. Figure 4.30 shows the chips obtained at the initial and final depths of cut.

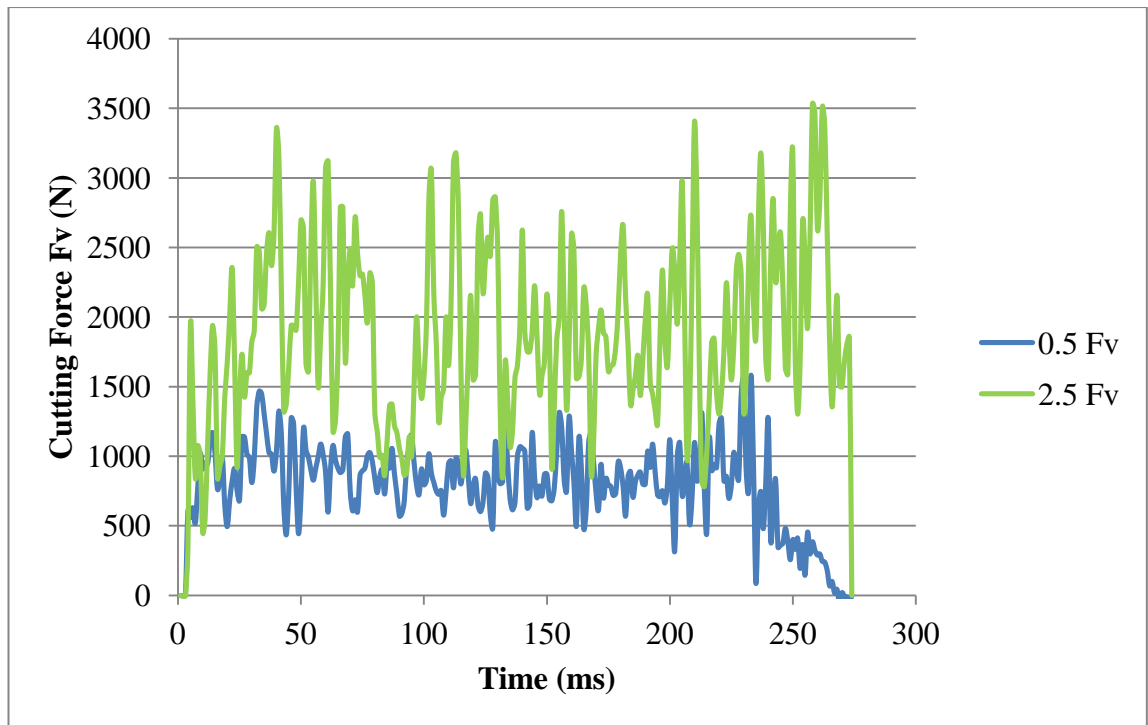


Figure 4.28 Comparison of typical cutting force trace at depth of cut 0.5 mm and 2.5 mm on a high strength sample using a 10° rake angle cutting tool

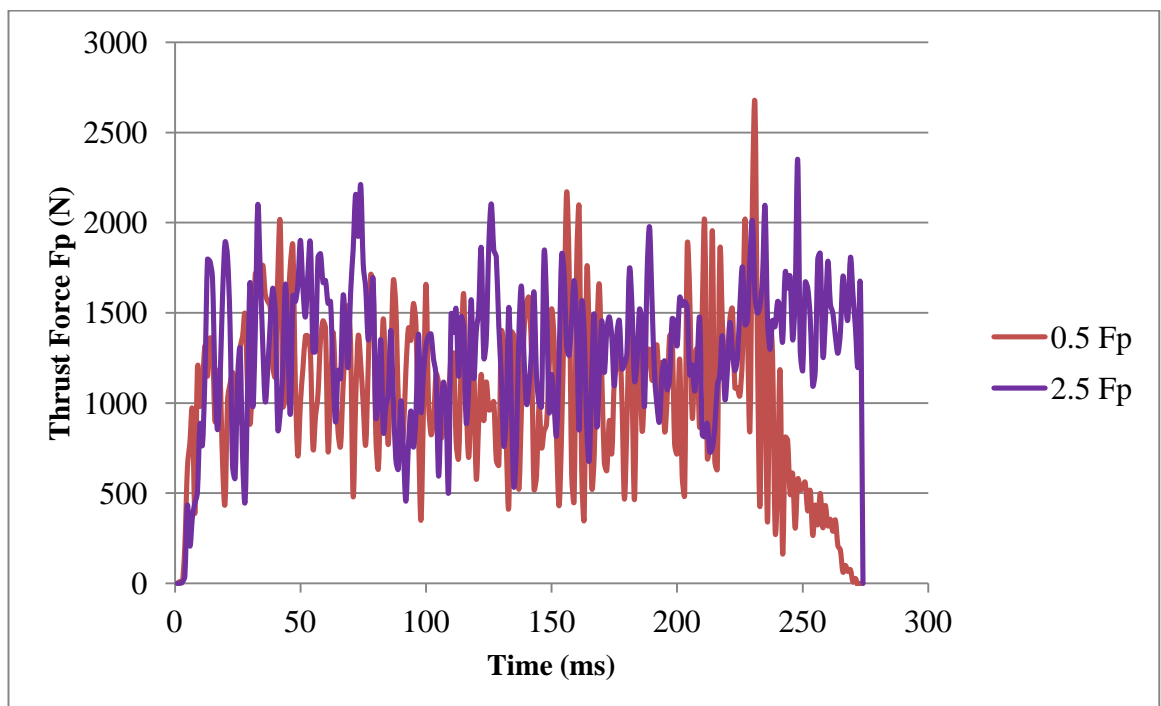
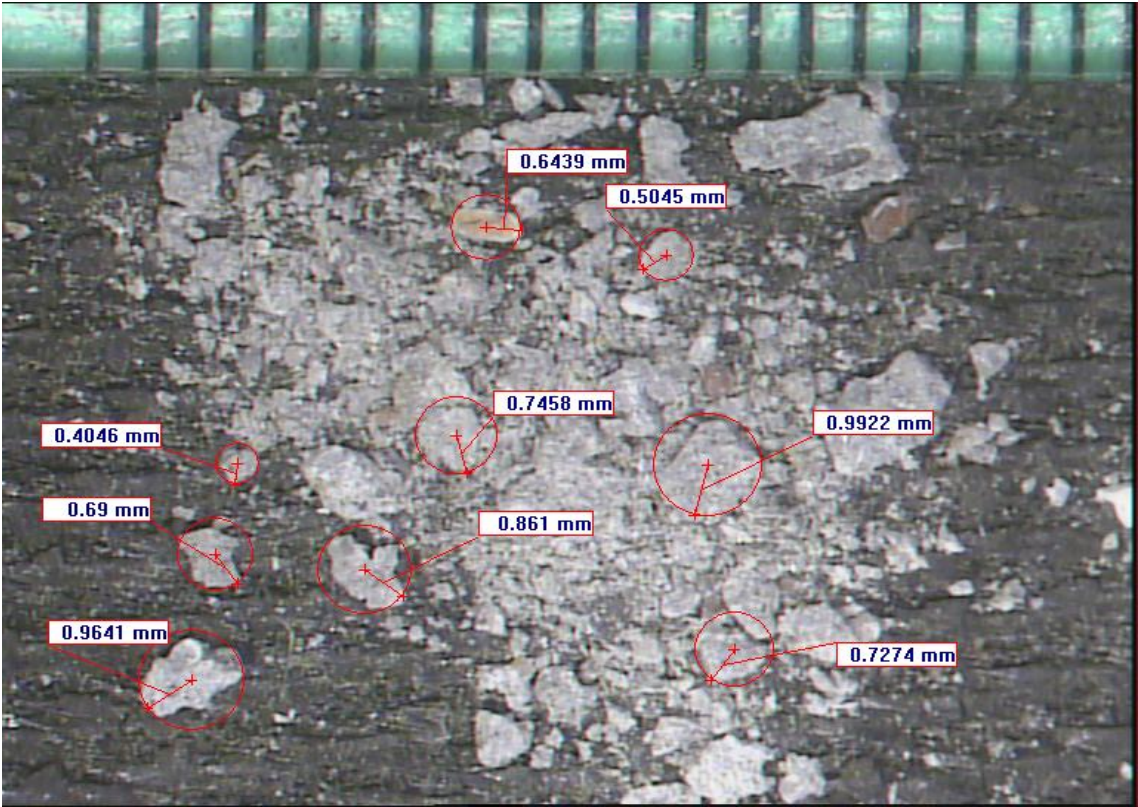
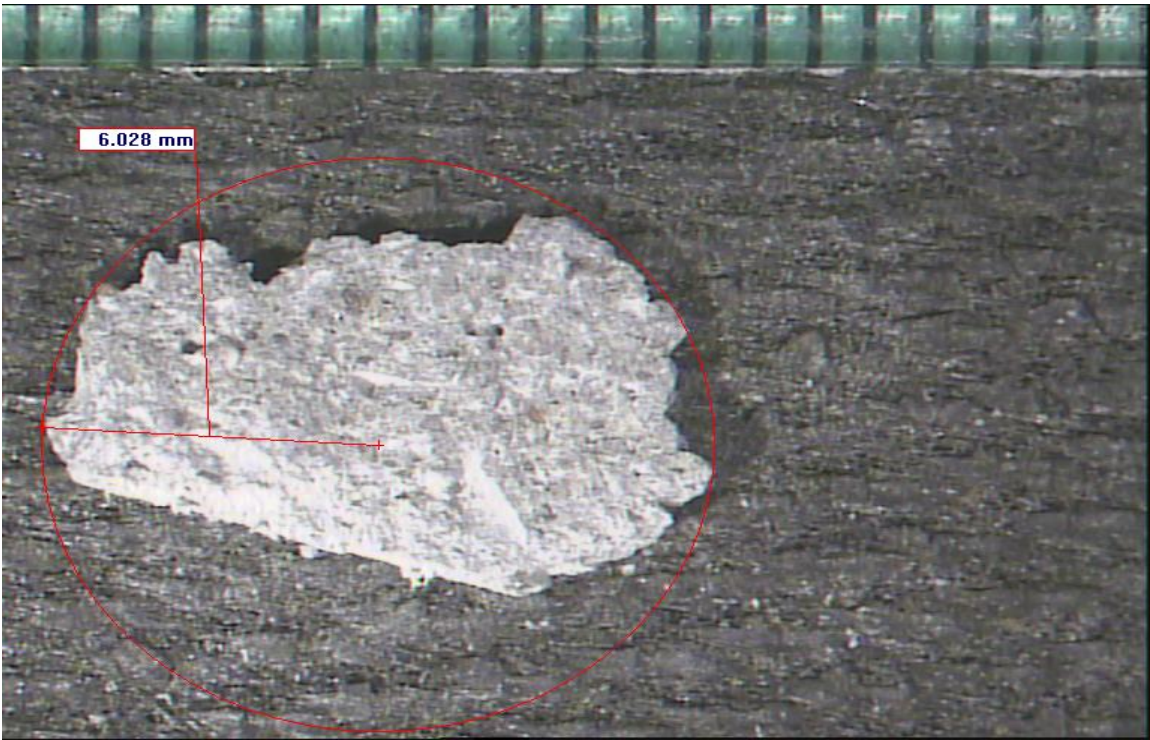


Figure 4.29 Comparison of typical thrust force trace at depth of cut 0.5 mm and 2.5 mm on a high strength sample using a 10° rake angle cutting tool



(a)



(b)

Figure 4.30 Characteristics of chips obtained at (a) 0.5 mm and (b) 2.5 mm

4.5.1.2.3. Cutting test using 20° rake angle cutting tool

Figure 4.31 shows the variation of the cutting and thrust force with respect to the depths of cut.

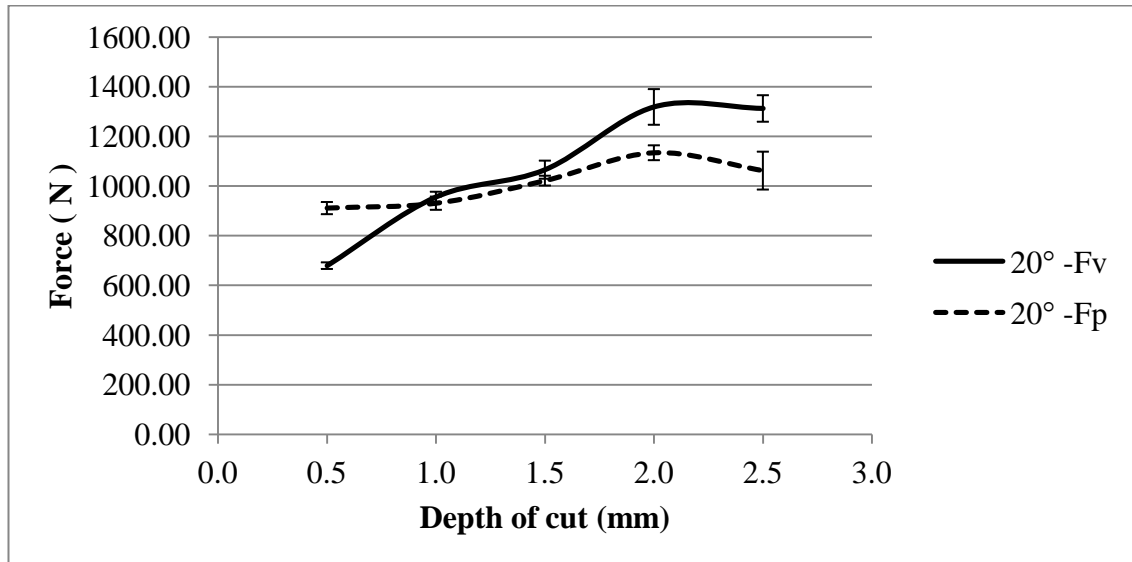


Figure 4.31 Variation of the cutting force (F_v) and thrust force (F_p) with respect to depth of cut using a 20° rake angle cutting tool

It is observed that the cutting force increases with depth of cut and usually it is lower than the thrust force at shallow depths of cut and becomes greater in magnitude as the depths of cut increases.

Figure 4.32 and 4.33 shows a comparison of force traces obtained while cutting at 0.5 mm and 2.5 mm depth of cut for cutting force and thrust force respectively. Figure 4.34 shows the characteristics of chips obtained at 0.5 and 2.5 mm depths of cut.

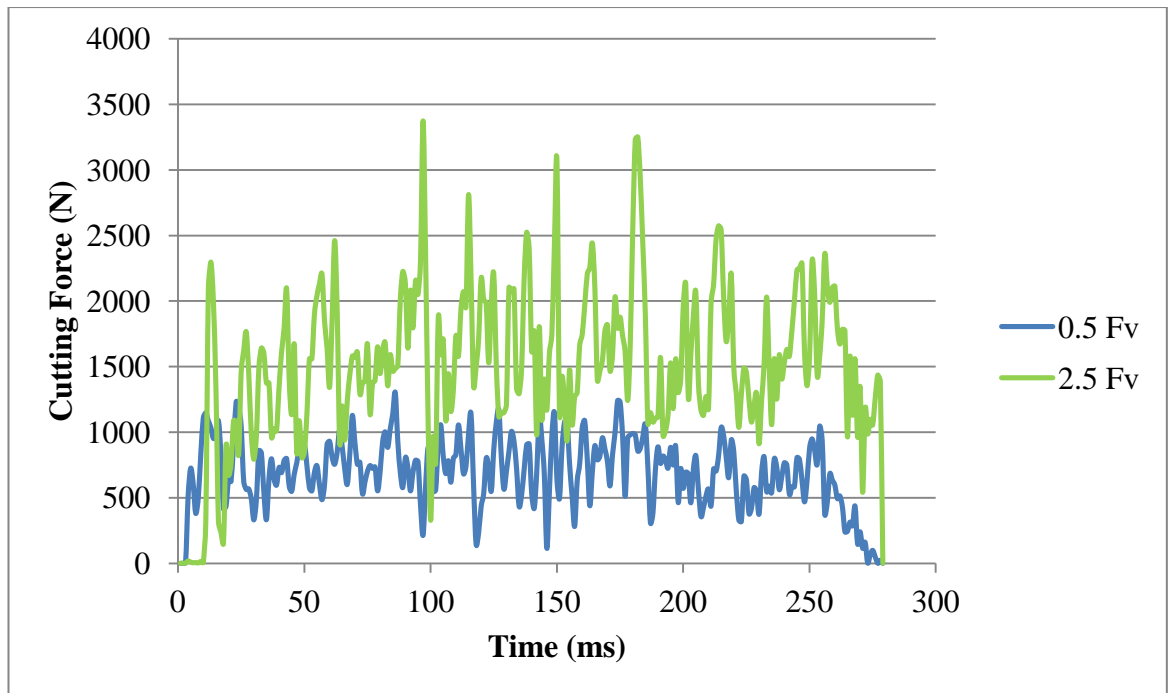


Figure 4.32 Comparison of typical cutting force trace at depth of cut 0.5 mm and 2.5 mm on a high strength sample using a 20° rake angle cutting tool

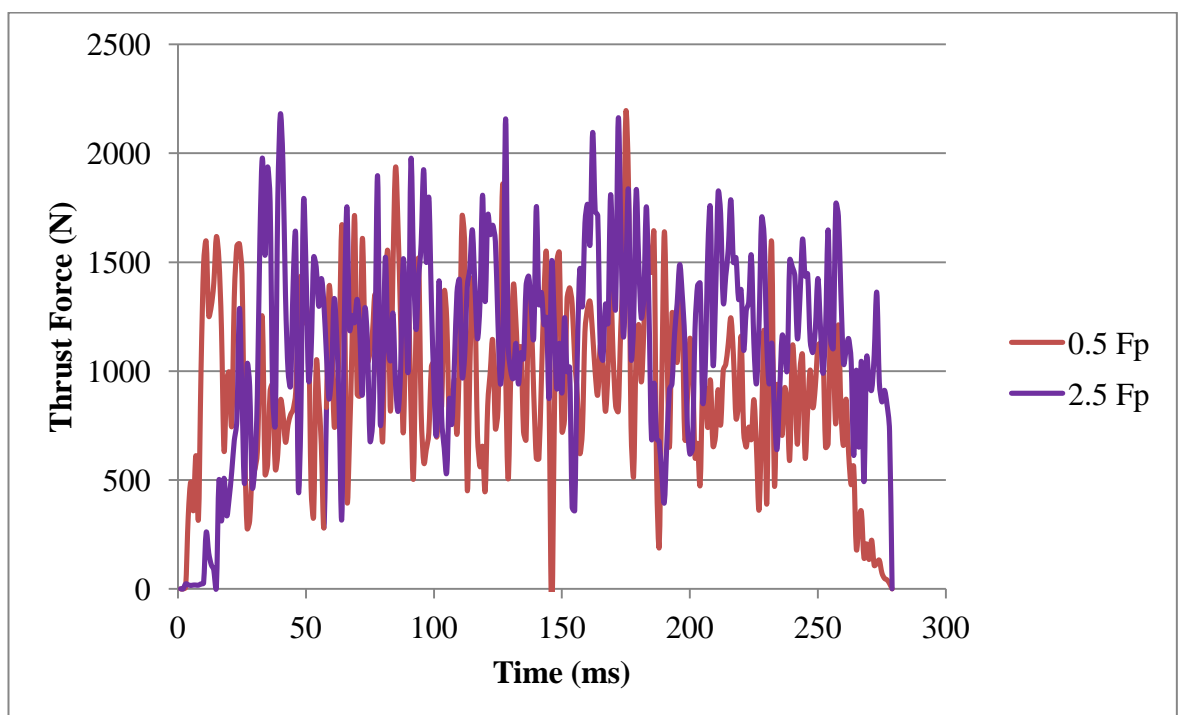
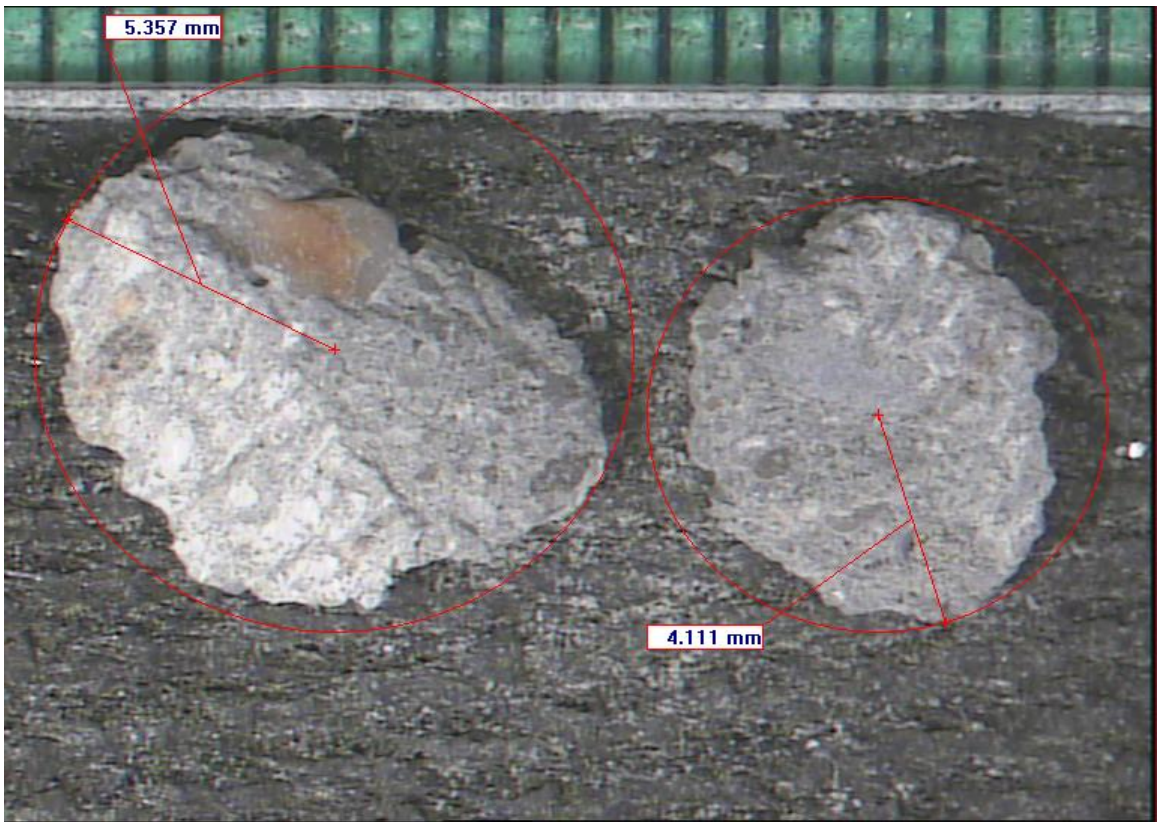


Figure 4.33 Comparison of typical thrust force trace at depth of cut 0.5mm and 2.5 mm on a high strength sample using a 20° rake angle cutting tool



(a)



(b)

Figure 4.34 Characteristics of chips obtained at (a) 0.5 mm and (b) 2.5 mm

4.5.1.2.4. Statistical analysis of cutting test on high strength sample

Statistical analysis to understand the influence of the rake angles on the cutting and thrust force for each depth of cut was carried out and the results are presented in Appendix D and E for cutting force and thrust force respectively.

Regression analysis was undertaken to find a predictive formula for cutting and thrust force due to the depth of cut and rake angle and are presented in this section.

Figure 4.35 shows the empirical relationship between cutting force and rake angle. A linear equation was obtained with an $R^2 = 0.05$, given as

$$F_v = -8.092 \times \text{Rake angle} + 1244.1 \quad (4.7)$$

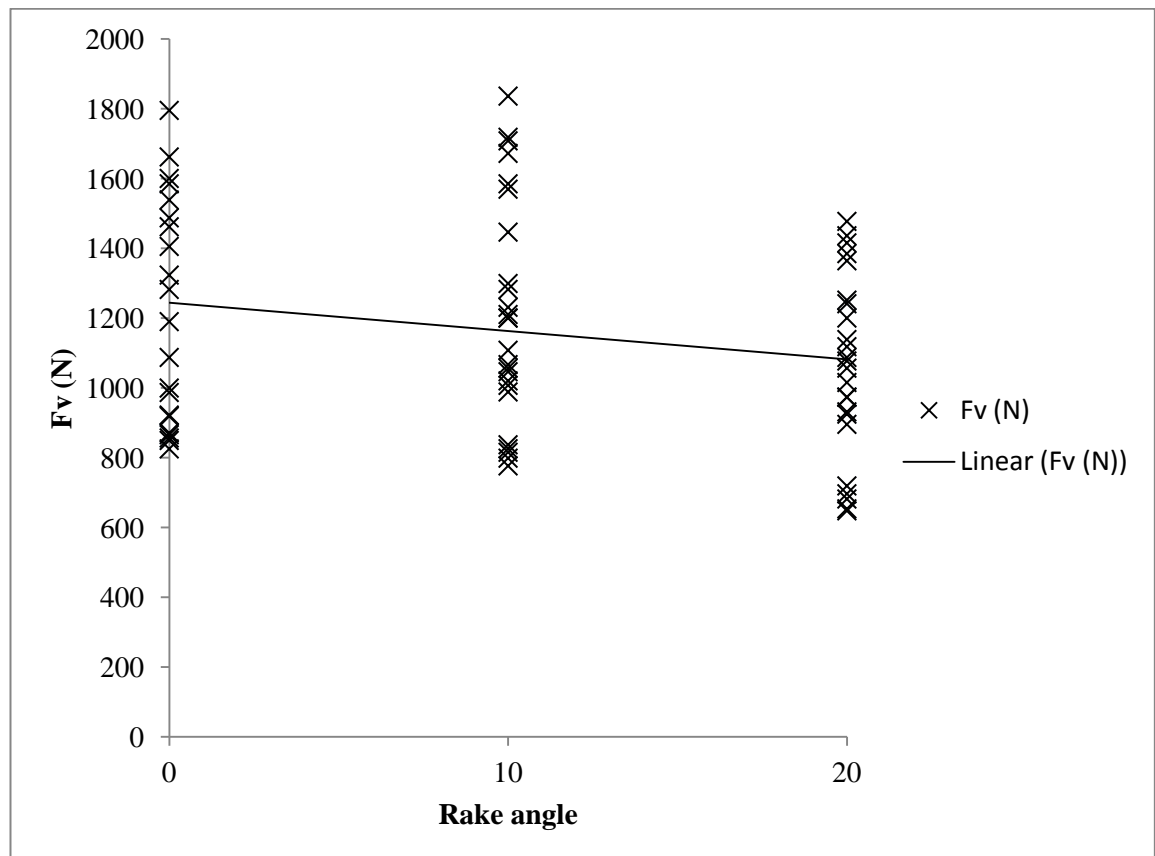


Figure 4.35 Empirical relation between cutting force and rake angle

Figure 4.36 shows the empirical relationship between cutting force and depth of cut. Linear equation was obtained at an R^2 value of 0.94.

$$F_v = 380.89 \times \text{Depth of cut} + 599.26 \quad (4.8)$$

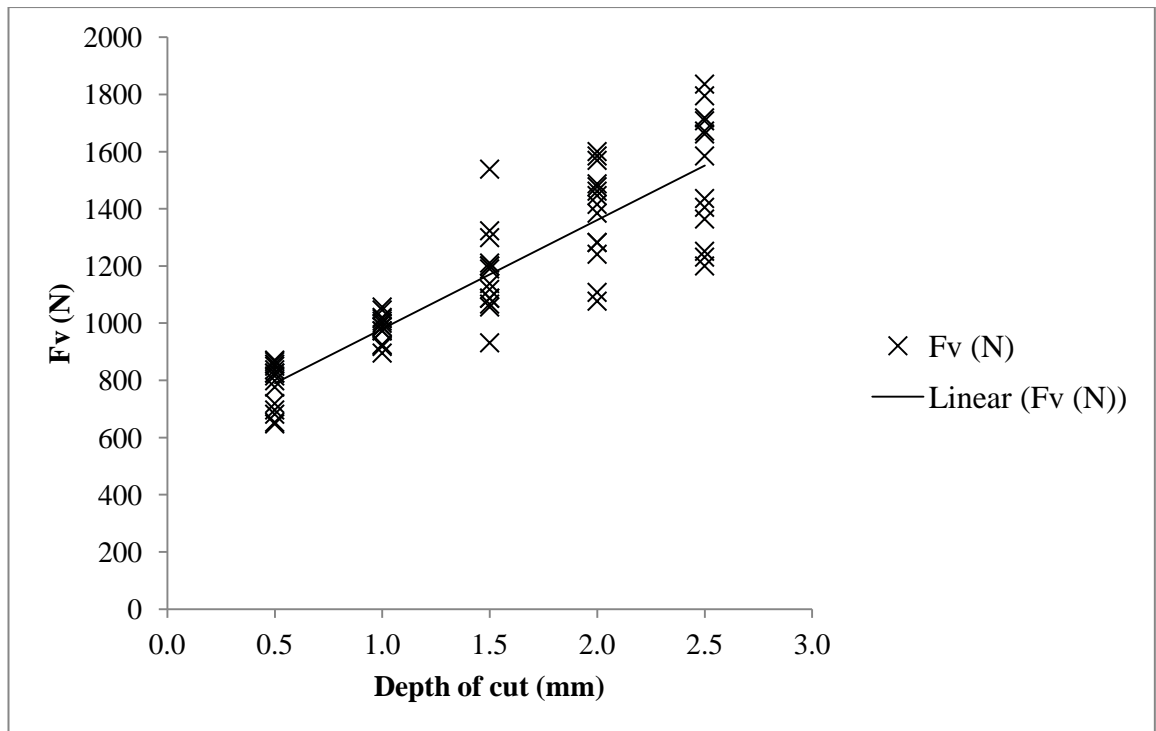


Figure 4.36 Empirical relation between cutting force and depth of cut

A regression analysis was conducted to find the relationship between the cutting force as the independent variable and the dependant variables being rake angle and depth of cut. At $R^2 = 0.83$, the linear predictor model obtained is given as:

$$F_v = 684.11 - 8.16 \text{ Rake angle} + 381.08 \text{ Depth of cut} \quad (4.9)$$

Residual plot for the above equation is shown in Figure 4.37; the random scatter supports the linear model.

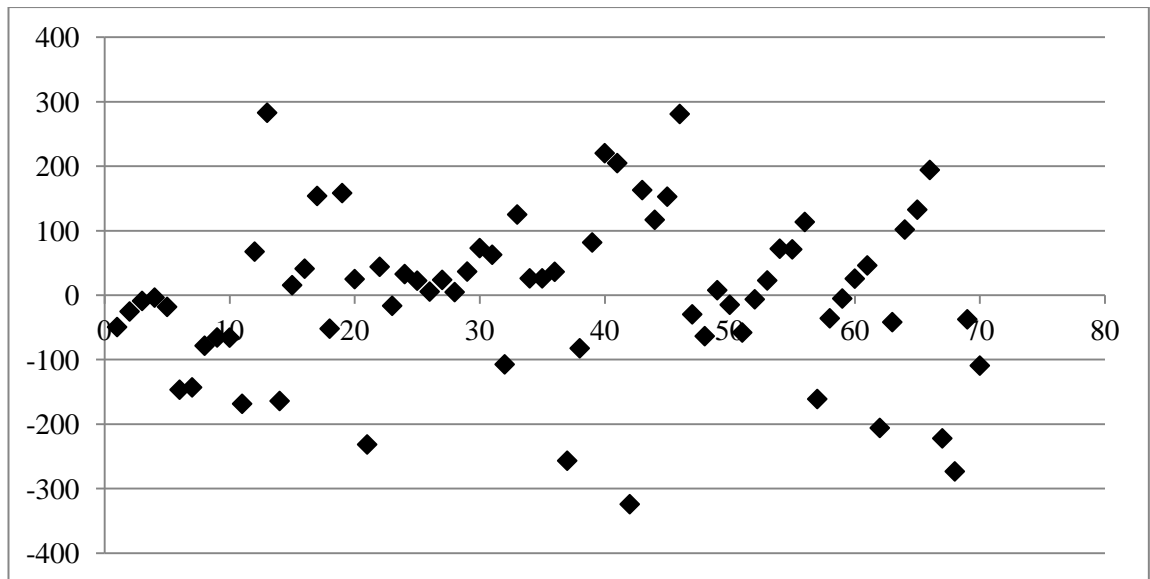


Figure 4.37 Residual plots obtained for cutting force via rake angle and depth of cut

Figures 4.38 and 4.39 shows the relationship between thrust force against the rake angle and depth of cut respectively.

From Figure 4.38 the empirical relationship is obtained at an $R^2=0.36$; the linear equation is given as:

$$F_p = -7.42 \times \text{Rake angle} + 1167 \quad (4.10)$$

The empirical relation between thrust force and depth of cut is observed from Figure 4.39; the linear equation is given as:

$$F_p = 110.52 \times \text{Depth of cut} + 927 \quad (4.11)$$

The R^2 value is given as 0.62.

A regression analysis of the independent variable, thrust force and the dependant variables, that is, rake angle and depth of cut was obtained at and R^2 value of 0.60. The linear predictor model is given as:

$$F_p = 1004.35 - 7.44 \times \text{Rake angle} + 110.70 \times \text{Depth of cut} \quad (4.12)$$

The predicted values of F_v and F_p are tabulated along with the experimentally derived values and shown in Table 4.6.

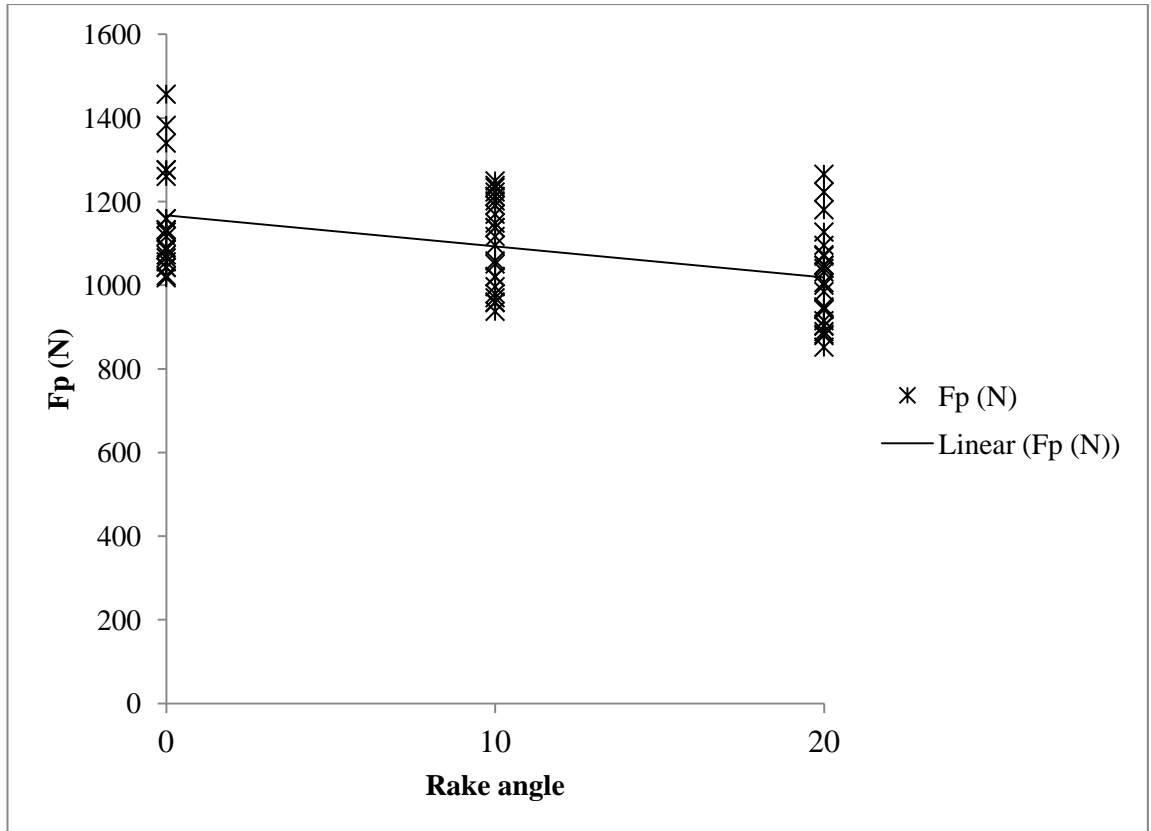


Figure 4.38 Empirical relation between thrust force and rake angle

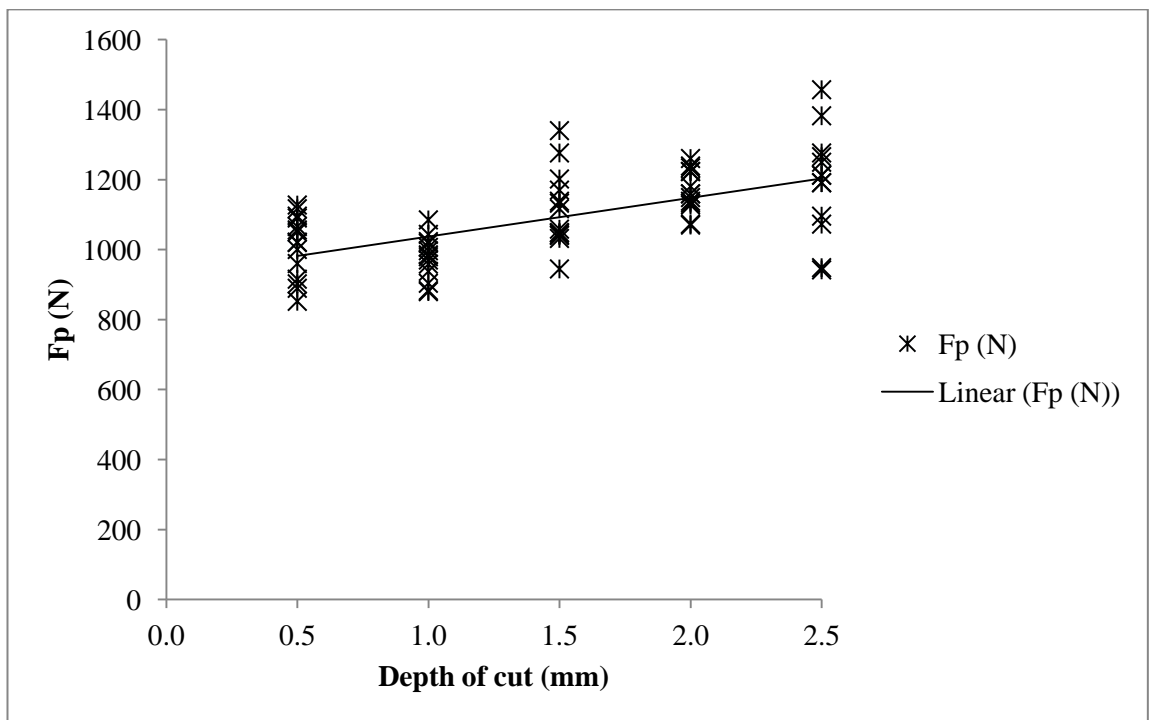


Figure 4.39 Empirical relation between thrust force and depth of cut

Table 4.6 Comparison of experimental and predicted forces for high strength sample

Rake angle	Depth of cut (mm)	Fv (N)	Predicted Fv (N)	Fp (N)	Predicted Fp (N)
0°	0.5	853.57	874.54	1091.08	1059.70
	1	956.81	1065.08	1042.10	1115.05
	1.5	1284.80	1255.62	1197.62	1170.40
	2	1457.90	1446.16	1177.70	1225.75
	2.5	1611.80	1636.70	1296.87	1281.10
10°	0.5	810.69	792.94	1029.37	985.30
	1.0	1023.75	983.48	968.36	1040.65
	1.5	1195.36	1174.02	1136.80	1096.00
	2.0	1398.20	1364.56	1196.32	1151.35
	2.5	1633.10	1555.1	1211.20	1206.7
20°	0.5	679.70	711.34	911.71	910.90
	1.0	956.55	901.88	931.38	966.25
	1.5	1066.41	1092.42	1022.35	1021.60
	2.0	1319.18	1282.96	1134.66	1076.95
	2.5	1313.03	1473.5	1062.69	1132.30

4.5.1.2.5. Summary of cutting test on high strength sample

The results from the test on high strength sample are similar in characteristics of cutting test on low strength sample. Some of the observations are described below:

- a. The cutting force is lower than the thrust force at initial depths of cut. As the depth of cut increased the cutting force also increased. Force trace of the cutting force and the thrust force show the change in magnitude of the recorded forces. Cutting force is seen to increase while the thrust force is stable around 1000 N.
- b. The size of the chip increases with increasing depth of cut.
- c. For high strength sample the cutting force and thrust force are greatly influenced by the depth of cut as evident from the regression analysis. But based on this research it can be concluded that cutting with a 20° rake angle produced lower magnitudes of Fv and Fp.

d. Based on the experimental data, a linear regression model was obtained to predict F_v and F_p . At R^2 value of 0.60 the predicted values were observed to be close to the experimentally obtained values.

4.5.2. Variation of specific energy

Specific energy (SE) is calculated as the energy expended in removing a given volume of rock. Figures 4.40 and 4.41 show the effect of depth of cut on the specific energy for different rake angles for low and high strength samples respectively.

General observations show that SE decreases with increasing depth of cut irrespective of rake angle of the cutting tool on both the samples, but the magnitude of the SE for high strength sample is at least twice that of low strength samples. Figure 4.42 provides a good comparative graph where it is observed that cutting a high strength sample required more energy than that required by the low strength sample; while SE for low strength sample at 0.5 mm depth of cut is approximately 53 MJ/m³ it is around 100 MJ/m³ for a high strength sample.

Cutting at a depth of 0.5 mm requires more energy as work is done to crush and break the sample into fine particles rather than well formed chips. Figure 4.43 shows the debris collected at various depths of cut using a 0° rake angle cutting tool on a high strength sample. At 0.5 mm depth of cut, the debris was made up of fine powder and irregular fragments with a maximum diametric size measuring approximately 5 mm. As the depth of cut increases, the fine powder was observed in all the cases but the fragment size increases, reaching nearly 14 mm in diameter at 2.5 mm depth of cut. Tables 4.7 and 4.8 presents the SE and average maximum size of the chips that were formed at various depth of cut and rake angles for low and high strength samples respectively. The SE was observed to decrease as the chip sizes increase, this has been observed in previous research by Friant [99]. It can be observed that the chip size produced from a high strength sample is slightly larger than those produced from a low strength sample for all depths of cut and rake angles. This is attributed to the sample strength as the low strength sample is easily crushed than the high strength sample despite both being brittle in nature. Characteristic chip images are provided in Appendix F which shows the variation in size for all depth of cut for both types of samples. It can be concluded that the specific energy is directly influenced by the depth of cut and sample strength.

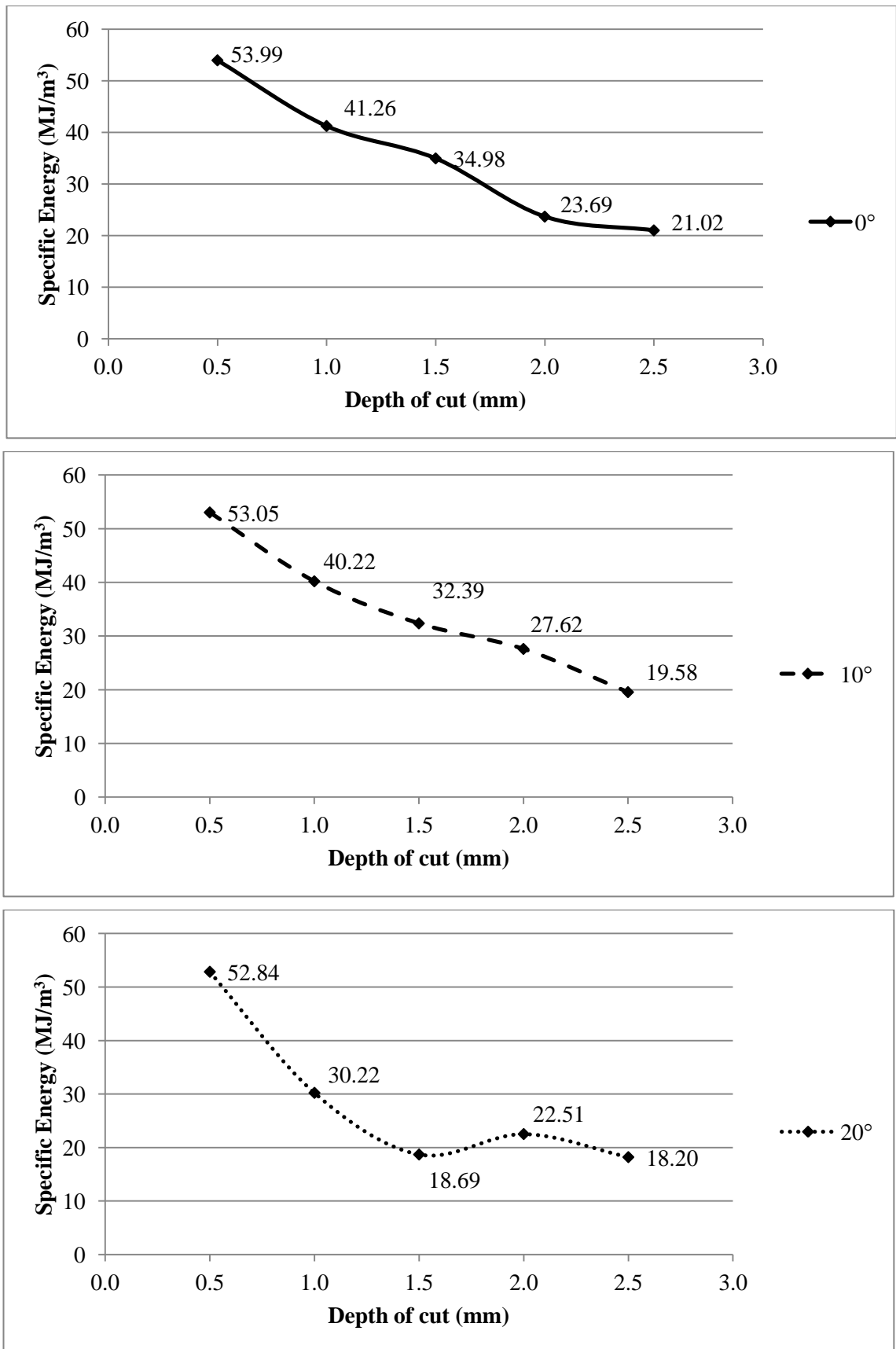


Figure 4.40 Variation of Specific Energies with depth of cut and rake angle for low strength sample

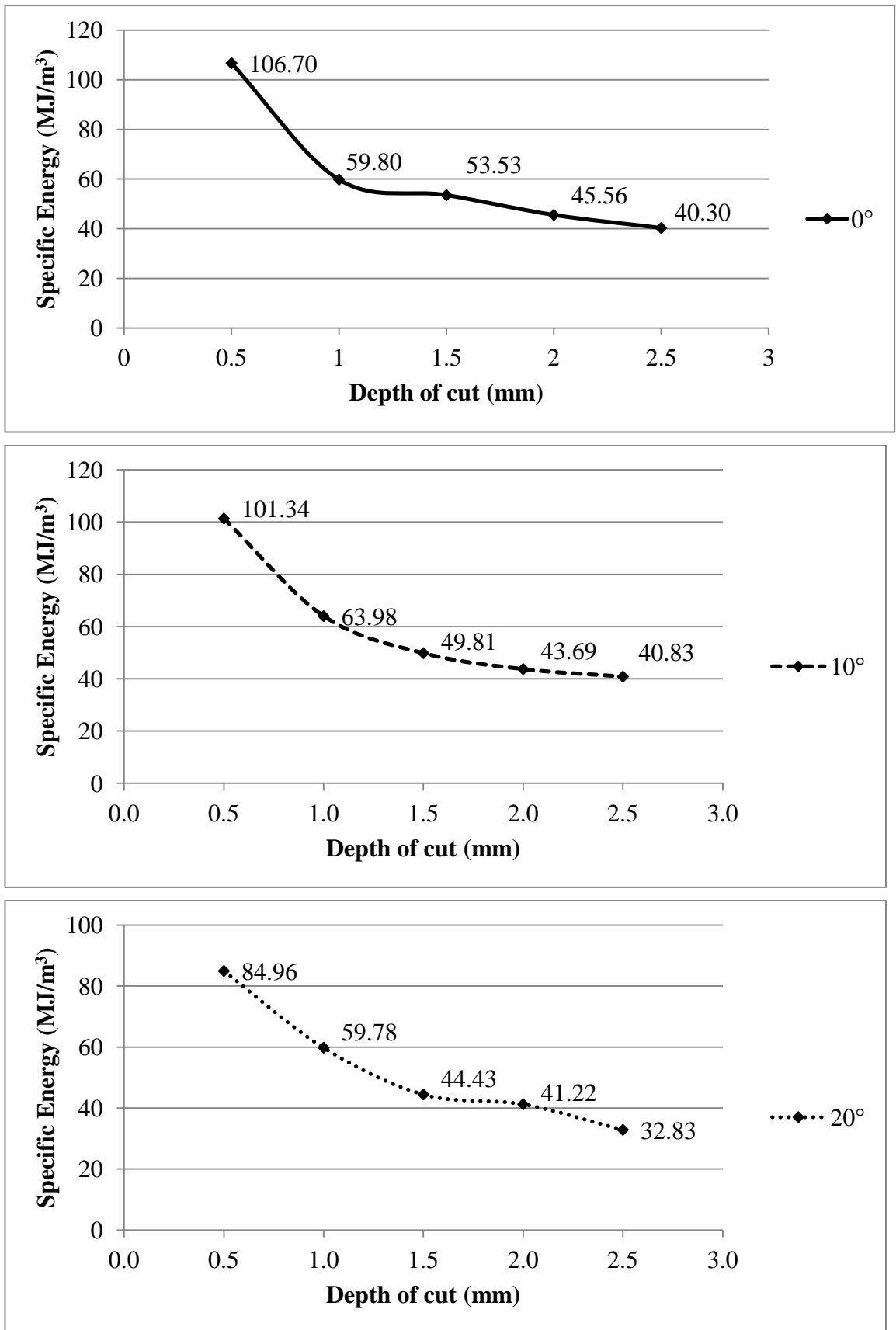


Figure 4.41 Variation of Specific Energies with depth of cut and rake angle for high strength sample

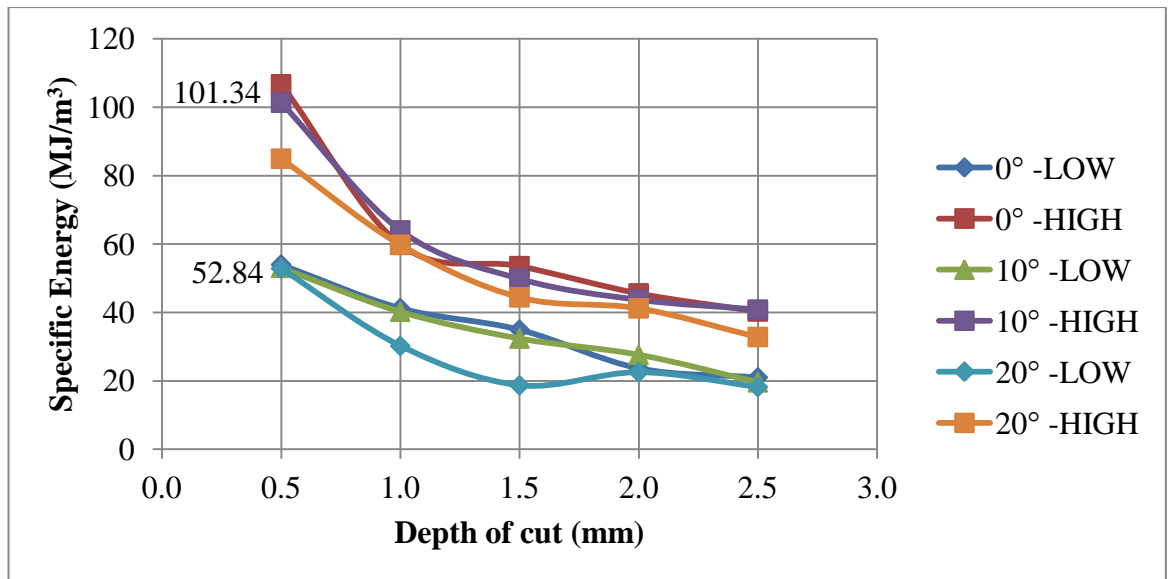


Figure 4.42 Comparison of specific energies

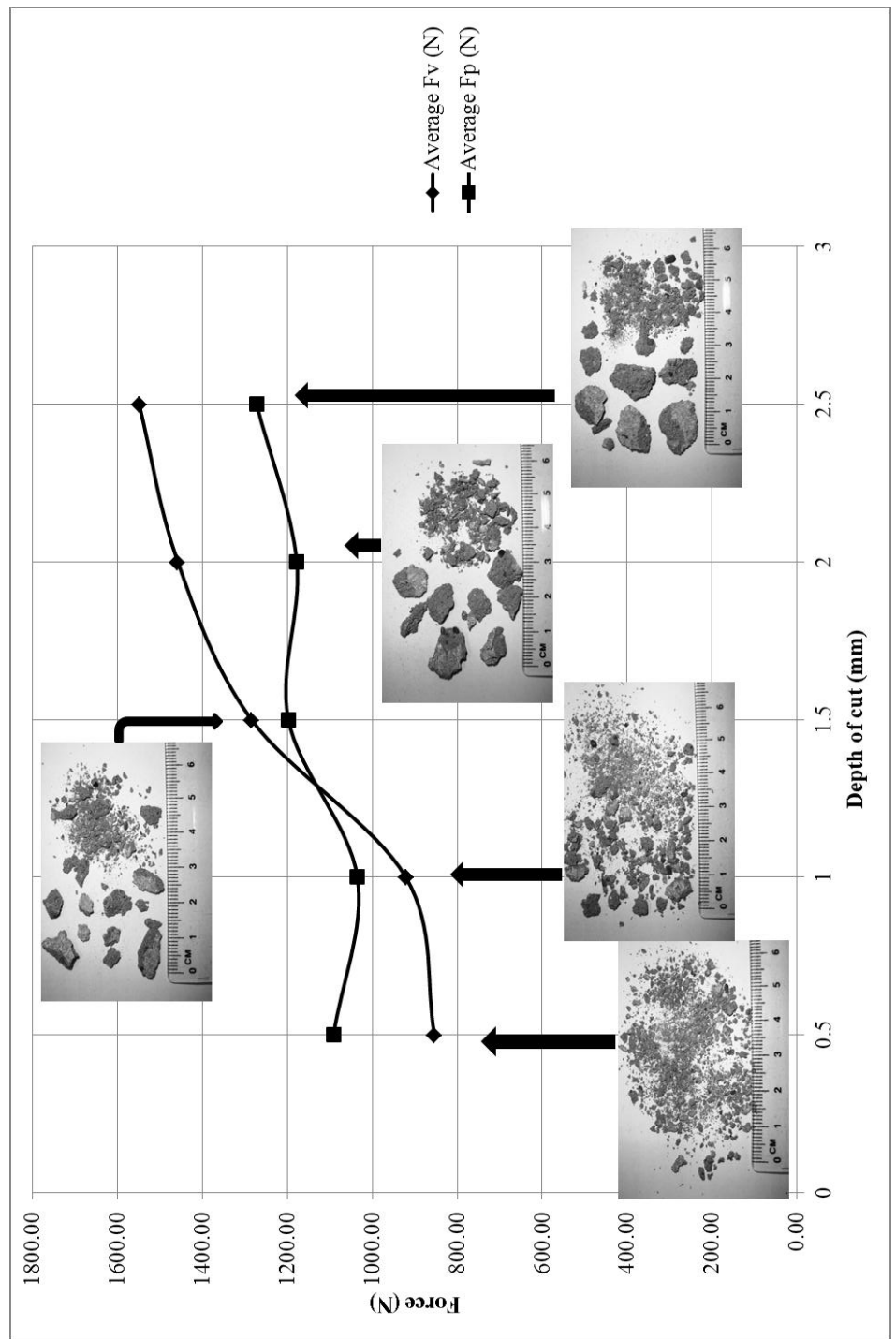


Figure 4.43 Variation of chip size with depth of cut while cutting with 0° rake angle tool for a high strength sample

Table 4.7 Average size of the chips for low strength material

Rake angle	Depth of cut (mm)	SE (MJ/m ³)	Average maximum size (mm)
0°	0.5	53.99	4
	1	41.26	6
	1.5	34.98	10
	2	23.69	12
	2.5	21.02	11
10°	0.5	53.05	6
	1	40.22	5
	1.5	32.39	11
	2	27.62	12
	2.5	19.58	10
20°	0.5	52.84	4
	1	30.22	6
	1.5	18.69	8
	2	22.51	8
	2.5	18.20	10

Table 4.8 Average size of the chips for high strength material

Rake angle	Depth of cut (mm)	SE (MJ/m ³)	Average maximum size (mm)
0°	0.5	106.7	5
	1	59.8	6
	1.5	53.53	10
	2	45.56	15
	2.5	40.3	14
10°	0.5	101.34	5
	1	63.98	8
	1.5	49.81	15
	2	43.69	16
	2.5	40.83	13
20°	0.5	84.96	5
	1	59.78	11
	1.5	44.43	13
	2	41.22	16
	2.5	32.83	15

4.6. Effect of the Crushed Zone on the Cutting Performance of the Tool

The crushed zone in rock cutting is analogous to the built-up edge in metal cutting, it is crucial to the force transmission from the tool to the rock by building up the stress ahead of the rock to a critical point whereby cracks initiate and propagate.

In this study, the use of force measurements, high speed videos and FEM/DEM modelling are used to provide models for the rock cutting mechanism and to explain the formation of the crushed zone and its influence in the chip formation process.

4.6.1. Characteristics of the crushed zone

High speed video recording of the cutting process was undertaken using a Phantom v7.3 camera produced by Vision Research. The videos were analysed using their proprietary software; features of the crushed zone were extracted and the chip removal process was carefully studied.

The shape of the crushed zone was observed to continuously evolve for the duration of a cut, that is, fine crushed material adhere to the tool tip and the deposit builds up until a crack forms and produces the chip, and when the chip is ejected from the surface then this crushed zone was also removed completely or partially. In order to study the geometric profile of this zone, the height and length of the crushed zone were measured at the instant of initiation of the chip forming crack. High speed videos were analysed frame-by-frame and visible major crack system which leads to chip formation was chosen; at the point where the crack just begins to form the dimensions of the crushed zone was obtained using the video analysis tool provided by Vision Research.

The Tables 4.9 and 4.10 shows the variation of the crushed zone at different depths of cut and rake angle for low strength and high strength sample respectively.

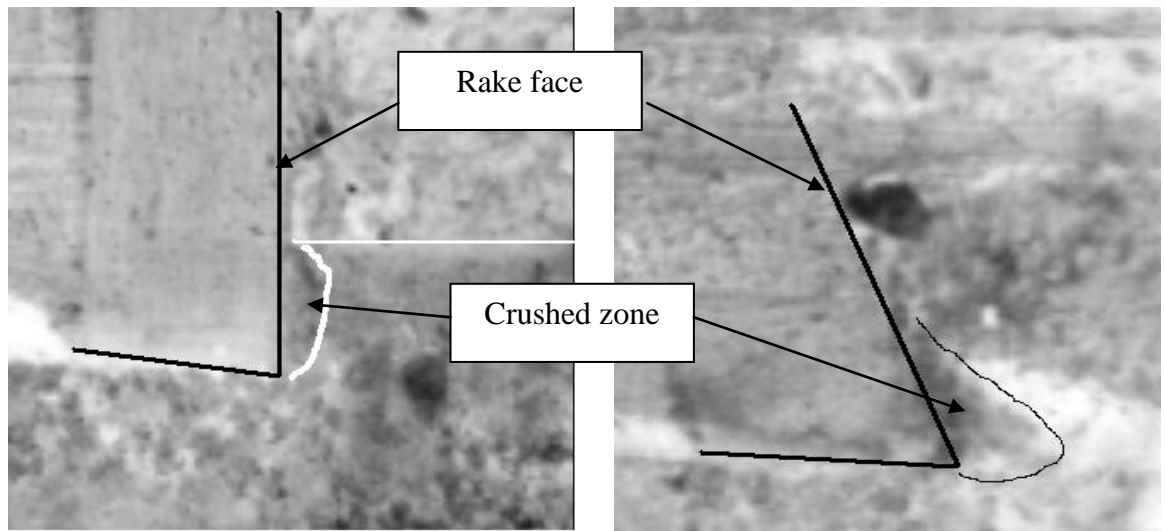
Table 4.9 Profile of crushed zone for low strength sample

Rake angle	Depth of cut (mm)	Height (mm)	Length (mm)
0°	0.5	0.6	0.41
	1.0	0.7	0.46
	1.5	0.68	0.4
	2.0	1.6	1.25
	2.5	2.3	1.9
10	0.5	0.4	0.27
	1.0	0.63	0.31
	1.5	0.69	0.38
	2.0	1.61	0.84
	2.5	1.8	1.3
20	0.5	0.3	0.16
	1.0	0.76	0.4
	1.5	0.67	0.38
	2.0	0.6	0.7
	2.5	1.3	0.5

Table 4.10 Profile of crushed zone for high strength sample

Rake angle	Depth of cut (mm)	Height (mm)	Length (mm)
0°	0.5	0.53	0.27
	1.0	0.7	0.23
	1.5	1.3	0.45
	2.0	1.37	0.37
	2.5	1.56	0.5
10	0.5	0.37	0.27
	1.0	0.5	0.3
	1.5	0.95	0.55
	2.0	1.1	1.3
	2.5	1	0.9
20	0.5	0.4	0.3
	1.0	0.4	0.5
	1.5	0.7	0.6
	2.0	0.7	0.45
	2.5	0.9	0.7

From Tables 4.9 and 4.10 it was found that as the depth of cut increases the length and width of the crushed zone also increases. The shape of the crushed zone differs based on the rake angle of the cutting tool; in this study it was observed that the 0° rake angle tool produced crushed zones in the shape of an hemisphere while the 10° and 20° produced wedge shaped crushed zones, these are shown in Figure 4.44.



a) A hemisphere shaped crushed zone b) A wedge shaped crushed zone highlighted in highlighted in white for a 0° rake angle cutting tool black for a 20° rake angle cutting tool

Figure 4.44 Profile of the crushed zone for different rake angles

Two kinds of chip formation process emerged from the high speed video analysis of the cutting process on both the samples and failure is always a combination of both:

Mode A: The chip is formed by shearing and this mode occurs in the absence of the crushed zone or when the crushed zone is just building up; and

Mode B: This mode of chip formation is characterised by fracture and is influenced heavily by the crushed zone.

Deliac and Fairhurst [100] in their rock cutting experiments involving a pick observed two basic modes of rock failure, one is through a combination of shear/compression fracture and the other is through fracture propagation.

4.6.1.1. Failure Mechanism in Mode A

In mode A failure mechanism, the chip formation is accomplished by shear fracture. Figure 4.45 shows the schematic diagram of Mode A failure for all rake angles; it can be seen that the failure occurs along a shear plane.

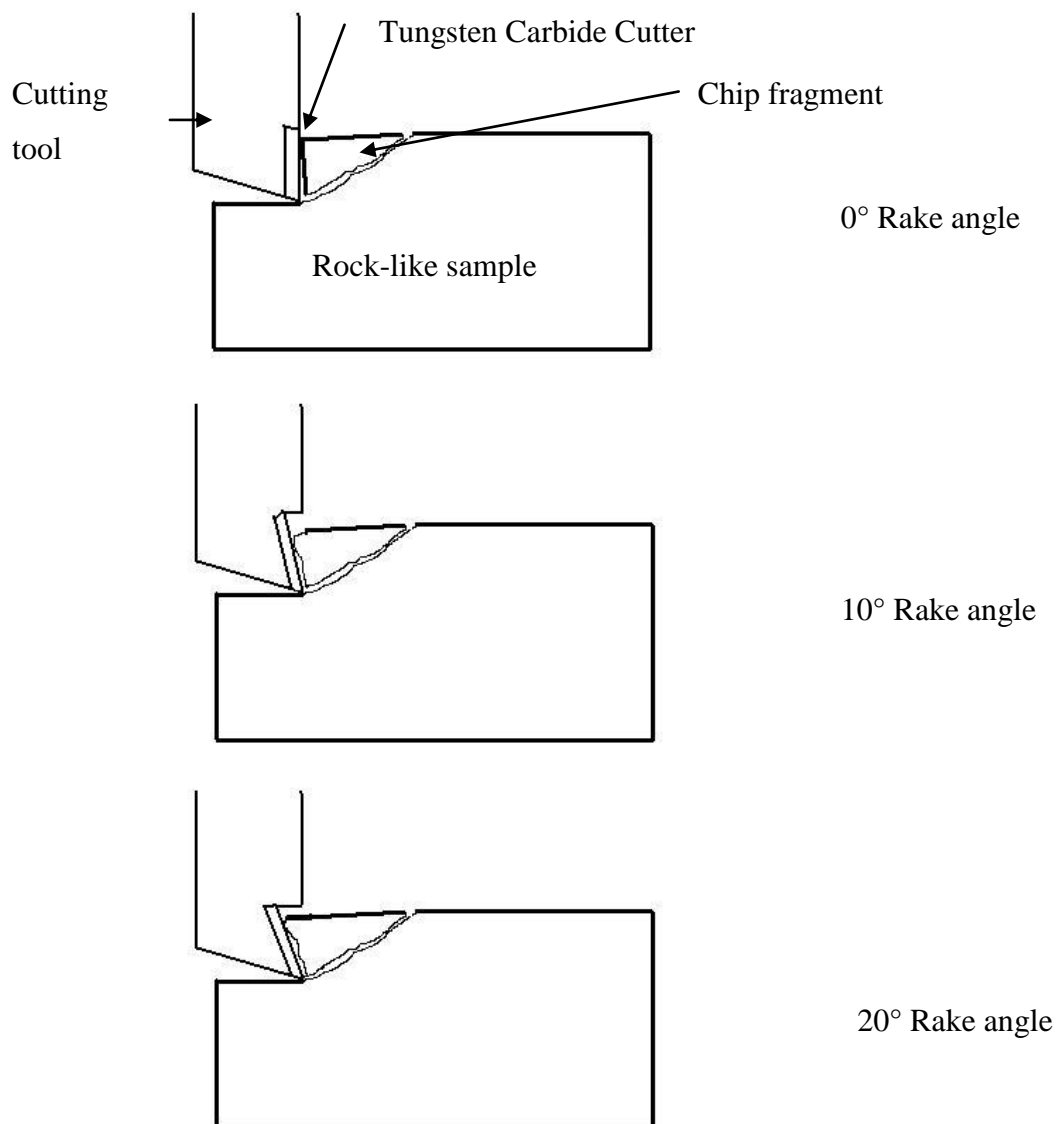


Figure 4.45 Mode A failure mechanisms

In this study, the direction of cut in Mode A failure were observed to range between 0° - 45° , and are not influenced by the rake angle of the tool. When the tool makes contact with the sample, a crack initiates immediately ahead of the tool tip and propagates to the free surface to produce a chip. Figure 4.46 shows a sequence of images which shows the Mode A failure in a high strength sample being cut with a 10° rake angle cutting tool at 2 mm depth of cut. At 0 second the tool impacts the sample, at 0.0014 s, cracks are found to have propagated into the sample in a direction parallel to the cut (approximate crack length= 9 mm), highlighted as white lines ahead of the tool tip. At 0.0019s the separation has taken place and a chip is about to be formed, at 0.0022s the cracks have reached the free surface and the chip is ejected from the specimen surface. It is observed here that the chip has already broken into two fragments before ejection. This type of fragmentation of the chip is observed when direction of the crack is at 0° . Figure 4.47 shows the types of chip profile observed in this study when Mode A failure occurs; Figure 4.47 (a) on top is the usually observed chip with the trailing edge thicker than the leading edge. Figure 4.47 (b) is representative of the type of chips formed when direction of the cracks is 0° . The chip behaves as a column and is found to buckle in the middle leading to splitting up of the original fragment into two. Figure 4.47 (c) shows layered fracture usually observed at depth of cut greater than 2 mm, usually a smaller chip layers off of the surface of the original fragment. The latter two occurrences can be explained by the influence of microcracks radiating away from the tool face; major cracks system coalesce with these microcracks forming the characteristic chip as observed.

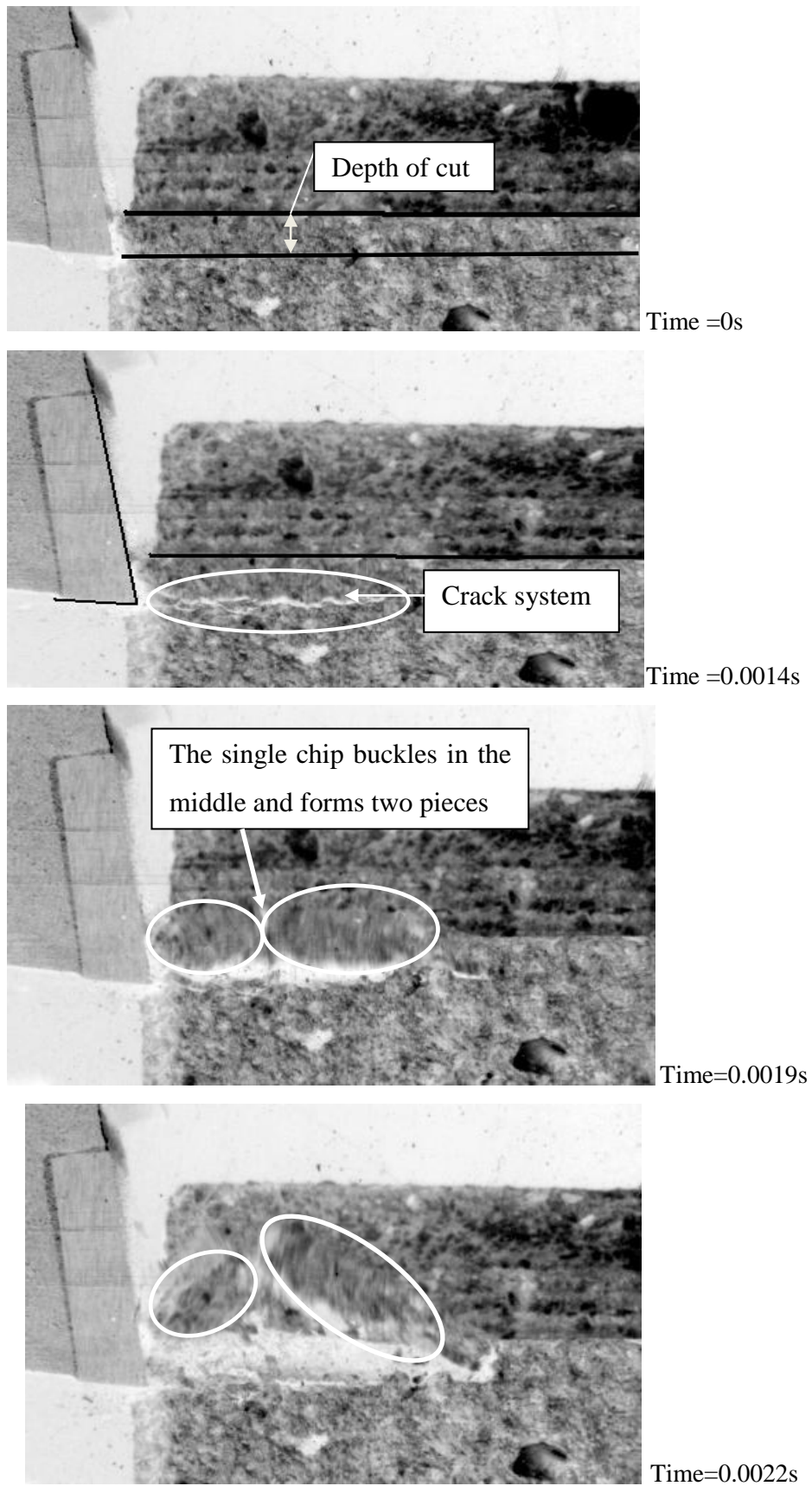


Figure 4.46 Sequence of images showing the shear failure of a high strength specimen cut with a 10° rake angle at 2 mm depth of cut

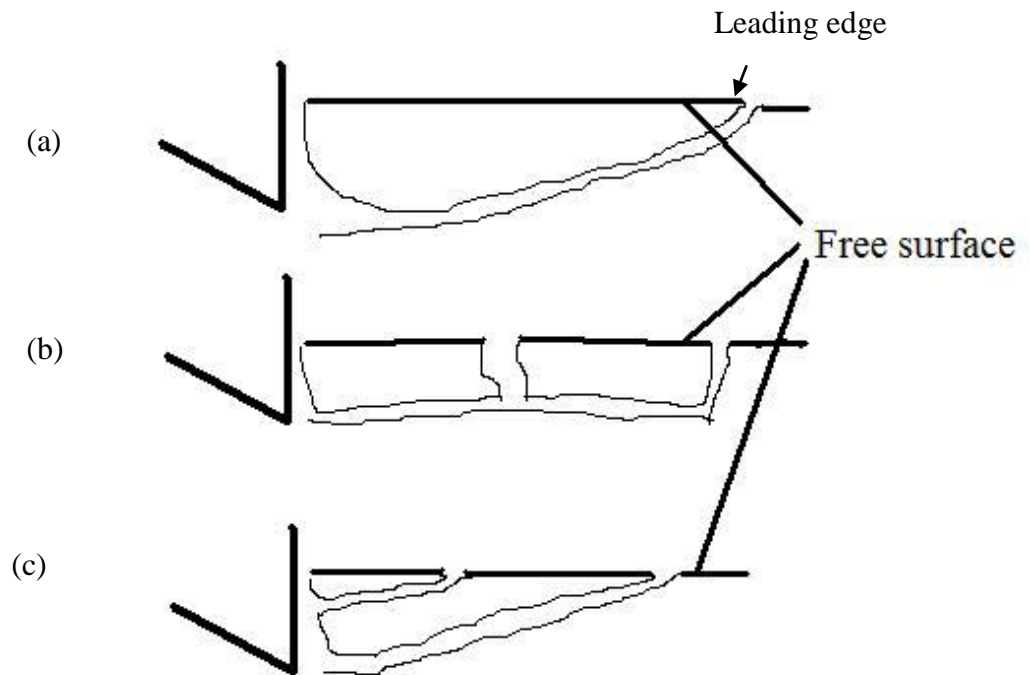


Figure 4.47 Types of Mode A chips

4.6.1.2. Fracture Mechanism in Mode B

In Mode B failure, the chip is formed under the influence of the crushed zone. The crushed zone changes the profile of the tip of cutting tool, thus the original rake angle and the sharp cutting edge is blunted by the crushed zone.

The crushed zone as discussed earlier was observed to take primarily two different shapes based on the cutting tool: a hemispherical shape when cutting with a rake angle of 0° and a wedge shape when rake angle is greater than 0° . The shape and thickness is critical to the transmission of the force from the tool to the specimen.

Figure 4.48 shows the schematic of a fracture failure for the three different rake angles and the characteristic shape of the crushed zone. The crushed zone is formed when fine powdered samples are compacted together to form a dense clump in the core, fine particles flow above or below this dense region and slowly begin to adhere to it thus increasing the size of the crushed zone. This crushed material creates a region of intense stress and when this reaches a critical limit then a crack forms on the upper level of this crushed zone and

quickly propagates down into the specimen and around the crushed zone; it usually propagates below the depth of cut leading to overcut and then propagates to the free surface and results in the formation of the chip.

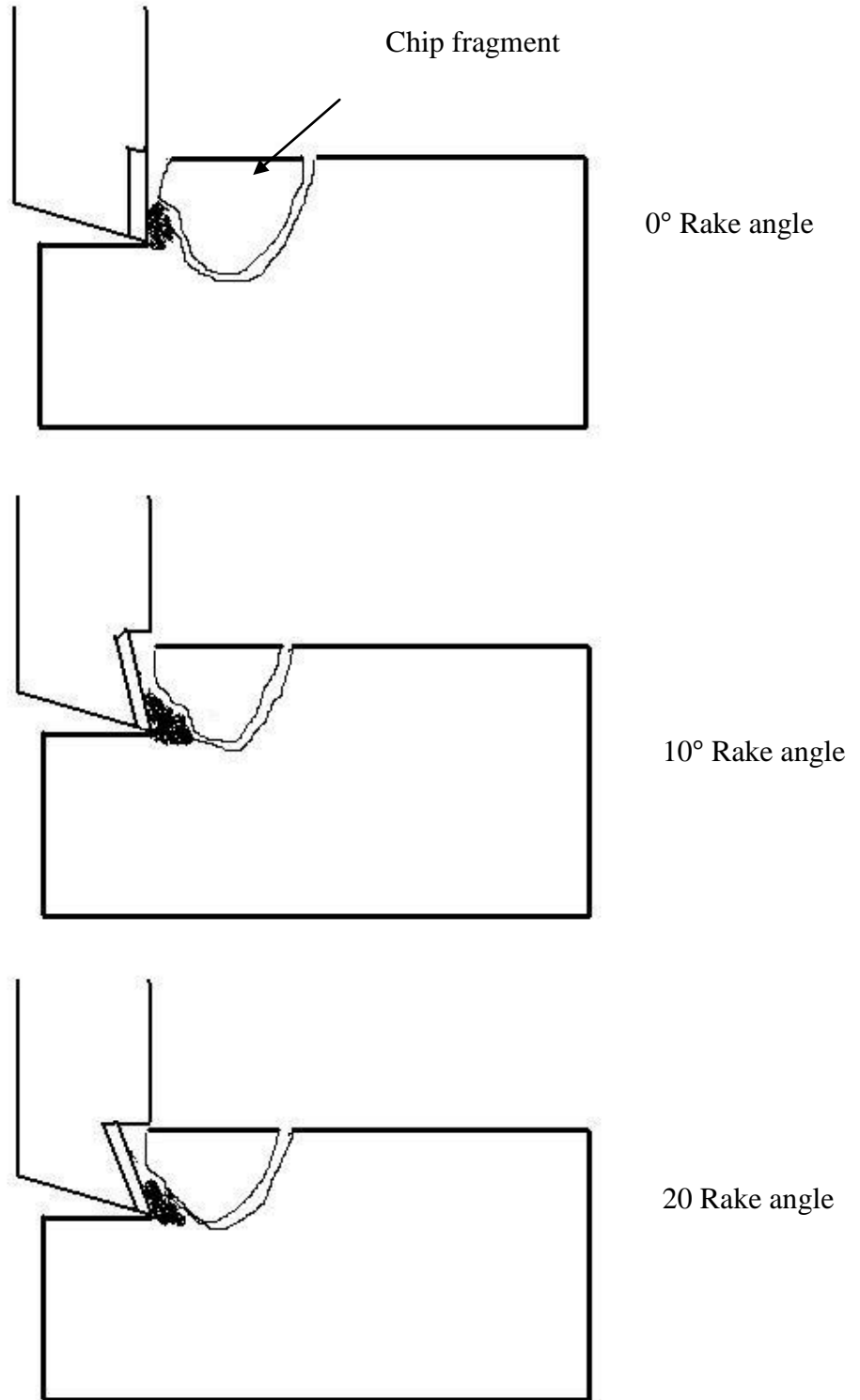


Figure 4.48 Mode B failure mechanisms

Figure 4.49 shows a sequence of photographs which show the formation of the crushed zone for rake angle 0° in a high strength sample having a depth of cut of 2 mm.

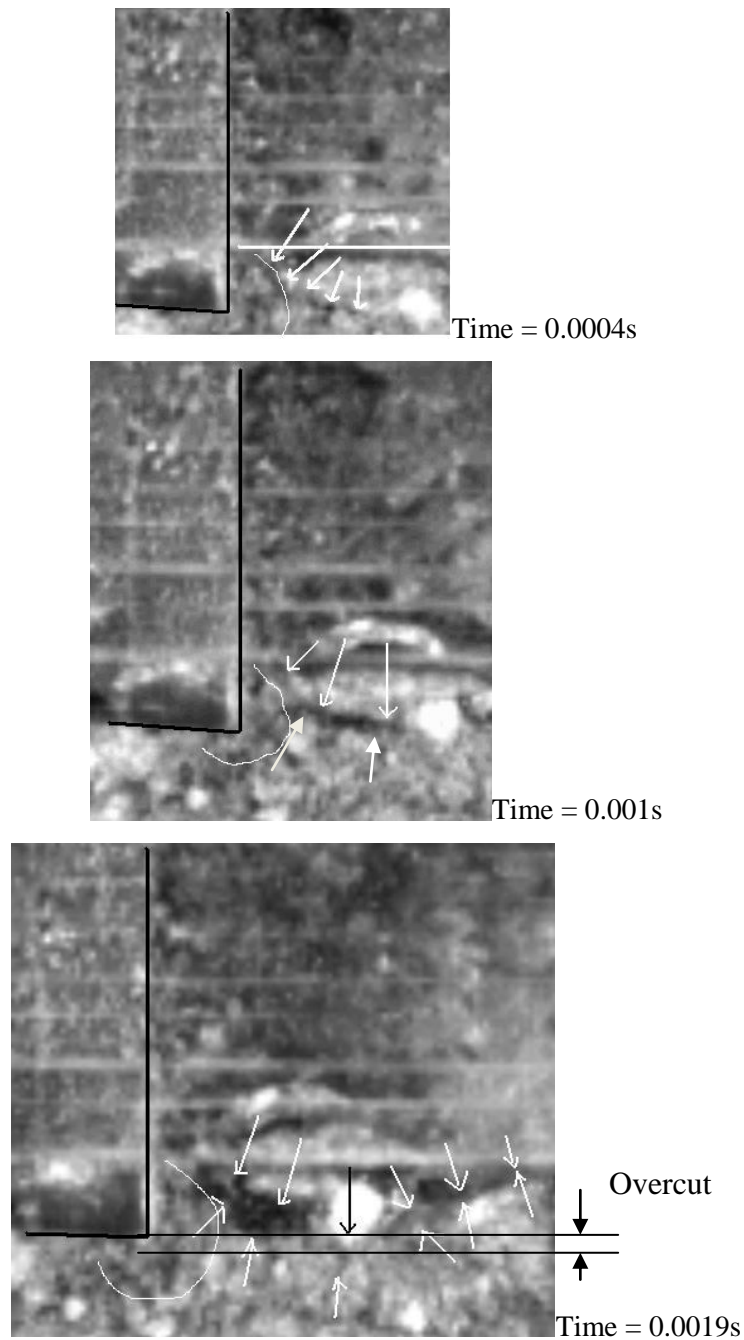


Figure 4.49 Sequence of images showing crushed zone influenced fracture

Figure 4.49 shows the formation of a crushed zone; at 0.0004s a crack appears above the crushed zone indicated by the first white arrow on the left, the other arrows mark the extension of the crack. As the tool moves forward, around 0.001s a darkened area (marked by arrows) is observed, this is the separation at the trailing edge of the chip while the

cracks are propagating forward and below into the sample. In the final image at time 0.0019s the chip being ejected can be seen. The arrows mark the sample and the chip edge and it also shows the overcut observed during this cut.

4.6.1.3. Force analysis

The crushed zone transmits the cutting force from the tool to the rock; to analyse this event, force trace signals were corroborated with the high speed video images.

Figure 4.50 (a) shows the cutting and thrust force trace of a high strength sample being cut with a 0° rake angle tool at 2.5 mm depth of cut. One group of force trace is isolated and shown in Figure 4.50 (b) and the sequence of the cutting process at regular time intervals captured by the high speed video is shown in Figure 4.50 (c). The force trace duration of interest is between 0.1s and 0.13s; from Figure 4.50 (b) it can be seen that the cutting force gradually increases from 500 N to 2000 N and so does the thrust force. The signals are interspersed by local maxima and minima peaks during this duration, this is due to microcracks opening up but not leading to chip formation. This build up of the cutting force and the thrust force coincides with the change in size of the crushed zone as seen in Figure 4.50c; the zone is highlighted by a white curve which is seen to evolve in size until a critical point is reached which leads to a fracture shown in the third photograph in the sequence; observation from video show that the finely crushed powder ‘flow’ around the crushed zone all the while compacting it until a critical stress is reached which results in fracture propagation. Tables 4.9 and 4.10 in Section 4.6.1 show the dimensions of the crushed zone at the point of crack propagation, though as the depth of cut increases there is a change in the dimensions but not significant enough to justify a trend.

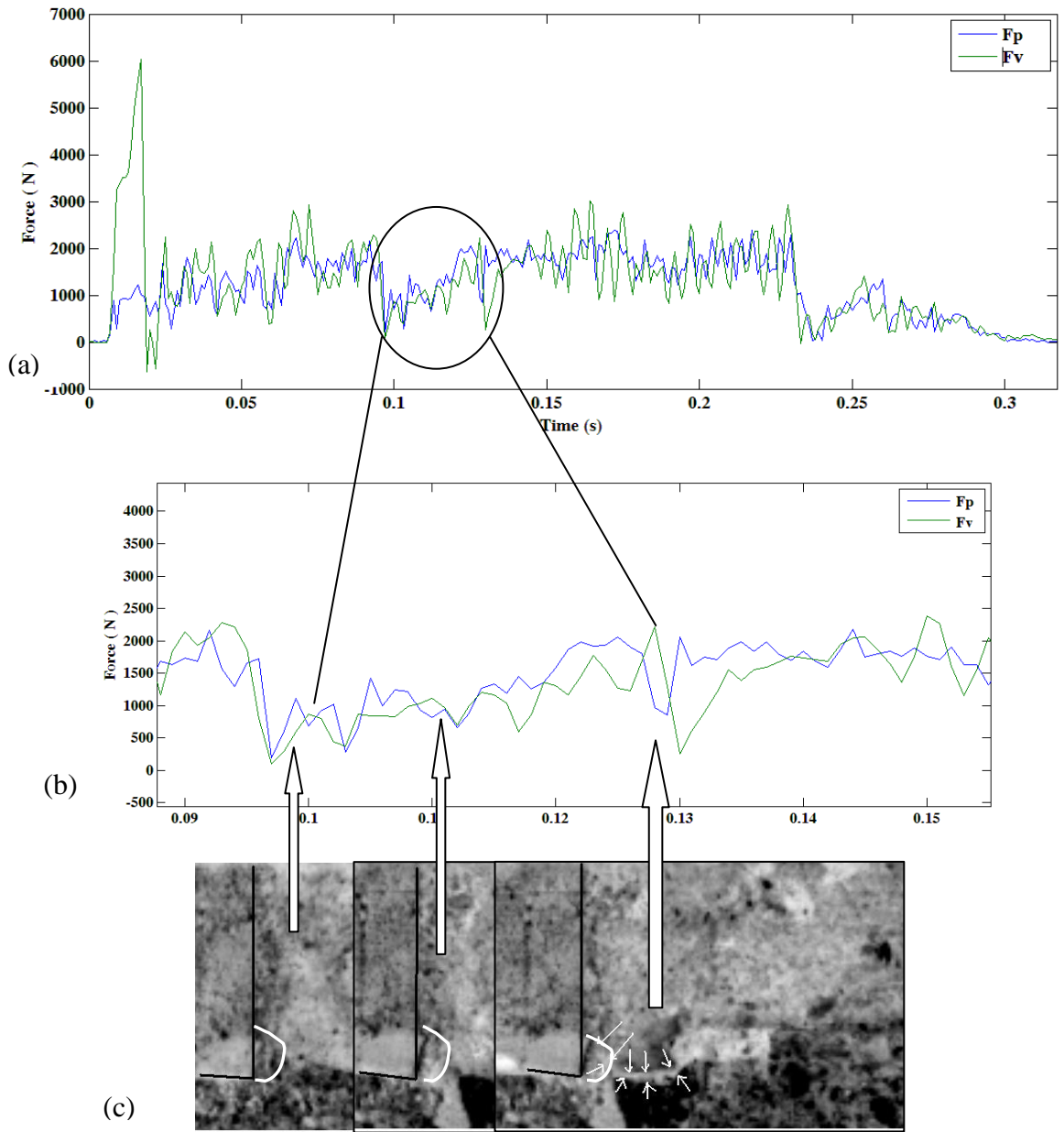


Figure 4.50 Influence of the crushed zone on the force signals

4.7. Numerical modelling of the cutting process

Finite element/Discrete element analysis was performed to understand the state of stress around the tool tip during cutting. A commercially available code called ELFEN (version 4.4.2) by Rockfield Software Ltd [18] was specially used for this analysis.

4.7.1 ELFEN

ELFEN employs a combination of finite and discrete element methods, and has both 2D and 3D capabilities. It seamlessly integrates the change from continuum to discontinuum state by adaptive remeshing.

Some of its important features include explicit and implicit solvers, adaptive remeshing, fracturing and fragmentation and constitutive material models such as the rotating crack and rankine model [18]. ELFEN has been applied in a wide variety of engineering problems but has found wider application in the following three areas:

- a. Geomechanics: ELFEN has advanced constitutive material models and discrete fracture modelling for use in stability analysis, mining and analysis of retaining walls. Analysis of wellbore design has been undertaken by the use of ELFEN to understand the wellbore stability. It has specialist suites such as ELFEN F_M which is a predictive tool to study the evolution of geological structures such as faults and folds, sedimentation and erosion process and tectonic erosion and compression. ELFEN R_G deals with reservoir Geomechanics and can be used to assess the state of stress, pore pressure and thermal distribution of a reservoir [101].
- b. Glass Modelling: ELFEN G_D is a software designed for glass modelling and some of its key features are – easy interface with CAD software to allow transfer of tool or glass container geometry, simulation of the forming process, stress analysis and failure prediction. ELFEN G_D has three modules: G_D FORMING to analyse the forming process and can be used to predict glass thickness and study the effect of cooling to name just a few. G_D DESIGN (static) can be used to study stress distribution and finally G_D DESIGN (dynamic) to study impact loading on glass containers [102].
- c. Advanced Finite element/Discrete element: Some of ELFENs' key features include contact procedures to represent impact and sliding between bodies, thermo-mechanical and thermo-mechanical-seepage coupling, discrete multi-body contact applications, adaptive

remeshing and frictional contact. The implicit and explicit analysis features of ELFEN host a variety of elements, material models, contact and loading conditions.

The mechanical implicit analysis module contains the following element topology – 2D/3D linear and quadratic isoparametric solid elements, shell elements, beam elements, structural and thermal contact elements, to name a few. Material models include the Von Mises and Tresca yield, Mohr-Coulomb, Drucker-Prager, Cam Clay and crushable foam model. For models which involve contact with either deformable or rigid surfaces, algorithms are available which take into account contact with or without friction, sliding contact and sticking contact.

The mechanical explicit analysis module is used in this research; some of the key features are the ability to manipulate elements, loads and contact boundaries during simulation; this is particularly useful for simulating fractures in intact specimen. Failure is initiated by some of the in-built constitutive material models such as Rotating crack and Rankine model, Soft Rock model, Mohr-Coulomb model, Drucker-Prager model, Orthotropic Cam Clay model and Johnson-Holmquist model, to name a few. Cracks are created when the tensile strength is overcome and the fracture propagates either within an element or between elements in the continuum state mesh, at which point the mesh is updated and discrete elements are formed. The elastic modulus is degraded in the direction of propagation of crack thus leading to crack growth. The element family in ELFEN - Explicit [103] are listed below :

1. 3D Continuums – 4 noded tetrahedral, 8 noded hexahedral
2. 2D Continuums – 3 noded plane stress/strain triangle, 4 noded plane stress/strain quadrilateral, 3 noded axisymmetric triangle and 4 noded axisymmetric quadrilateral.
3. 3D Shells – 3 noded thin and 4 noded thick shell
4. 3D Membranes – 3 noded 3 dimensional membranes, and
5. 2D and 3D bars – 2D/3D 2 noded pin jointed bar

ELFEN also hosts in-built material databases with specific application to geomechanical simulations and it also allows the users to create their own material database.

ELFEN has two types of mesh generation techniques: unstructured mesh generation by using advancing front or Delaunay algorithms and the structured mesh. Unstructured mesh uses triangular and quadrilateral elements in 2D and tetrahedral elements in 3D which are bounded by many sided surface or four sided curved surface; while the structured mesh uses 2D quadrilateral and 3D hexahedral elements bounded by four sided 2D or shell elements or six sided 3D volume entity.

ELFEN has a rich graphical user interface for its pre/post processor functions. The pre-processor allows the user to create the geometry, apply loading and boundary conditions, assigning materials and generating the mesh. It allows the user to also import CAD data to create the geometry. Geometry is created by the use of points, lines, surfaces, volumes, groups of lower order geometric entities, particle geometries (round and elliptical grains) and pre-existing fractures. Loads, constraints and boundary conditions can be applied to points, lines, surfaces, volumes, geometric groups and grains. Loading can be achieved by mechanical loads (point loading, face loading, applied acceleration and velocities, gravity, body force, etc.), thermal loads (internal generation, radiation, convection, etc.), fluid loads (velocity, pressure, flux and traction) and seepage loads (pore pressure, liquid saturation, gravity). The post-processor window has the capability to plot original and deformed mesh through contour or vector plots, graph plotting, selection of specific parts for analysis and display of modal shapes.

4.7.2 Modelling

The model was created using material properties found experimentally in this study; material input parameters were poisson's ratio, elastic modulus and density. Table 4.11 lists the material properties for the two types of samples and the cutting tool. It can be observed that the material property for the cutting tool is chosen so as to make it very stiff and thus reduce interaction with the sample.

Table 4.11 Material properties used in numerical simulation

Property	Value		
	Cutting tool	Low strength sample	High strength sample
Young's Modulus (N/mm ²)	211000	19400	34300
Poisson's Ratio	0.286	0.27	0.27
Density (Ns ² /mm ⁴)	7.838E-09	0.217E-09	0.219E-09

ELFEN explicit solver was used in this research as it is best suited to simulate non-linear fracturing simulations. The 2D geometric model in ELFEN 4.4.2 was created by defining points by inputting co-ordinates in the XY plane and then connecting the points by lines. The workpiece dimensions are similar to the experimental specimen dimension of 100 x 100 mm; Four points describe the input coordinates: (0,0) (100,0) (100,100) and (0,100). The points are joined together with lines and within these lines the workpiece surface is created, indicated by green lines in the Figure 4.51. The cutting tool is defined in a similar manner with four points, lines and a surface. The cutting tool dimensions were changed according to the rake angle used. Figure 4.51 shows the geometric model of the workpiece and the cutting tool.

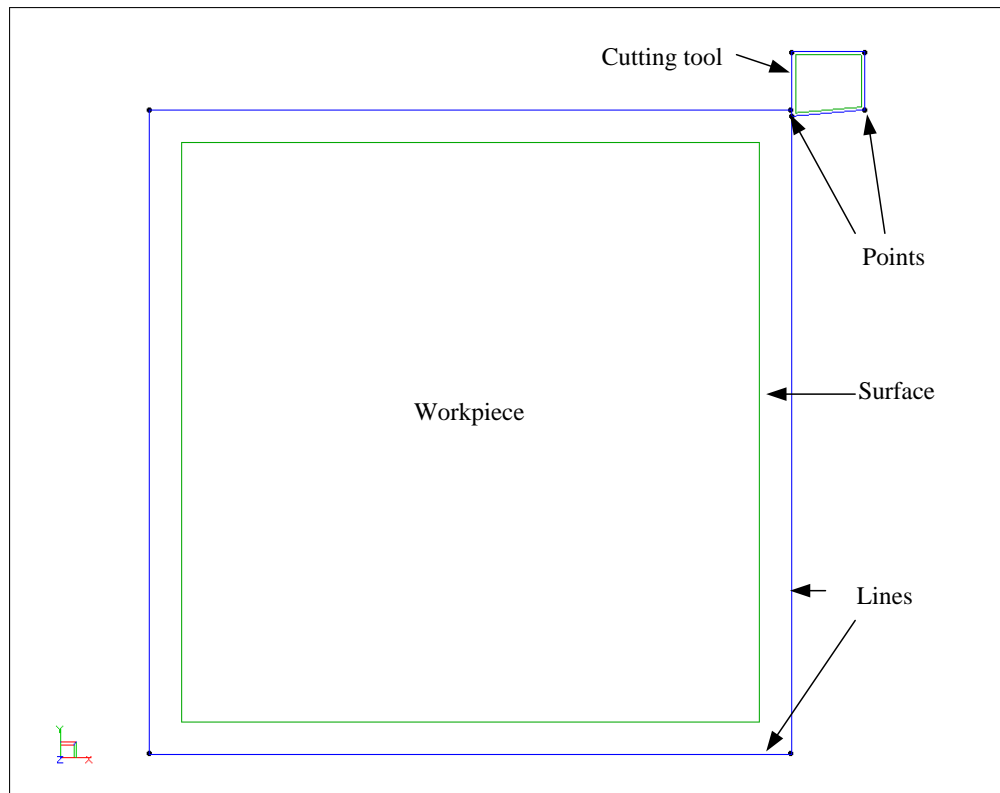


Fig 4.51 Geometric model of the workpiece and the cutting tool

A mechanical load was applied on the workpiece by use of a velocity load assigned to the cutting tool; this velocity load is equal to the cutting speed of the tool, that is, 333 mm/s in a direction moving from right to left, as show in Figure 4.52.

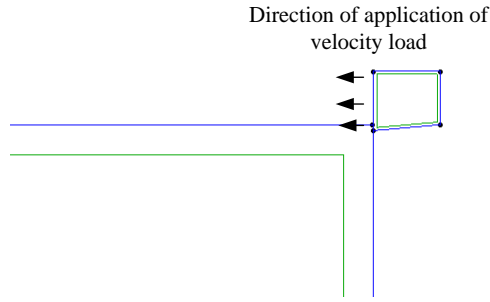


Figure 4.52 Direction of application of velocity load on the cutting tool

Boundary conditions were applied to the cutting tool and the workpiece; the workpiece had structural fixities applied to the lines on the left and the bottom, and the cutting tool had constraints applied to prevent it from moving in either direction along the y-axis and from rotating about the z-axis. Figure 4.53 shows the constraints applied to the geometry. The boundary conditions were based on the way the workpiece was secured and the tool held in the tool holder in the experimental test rig.

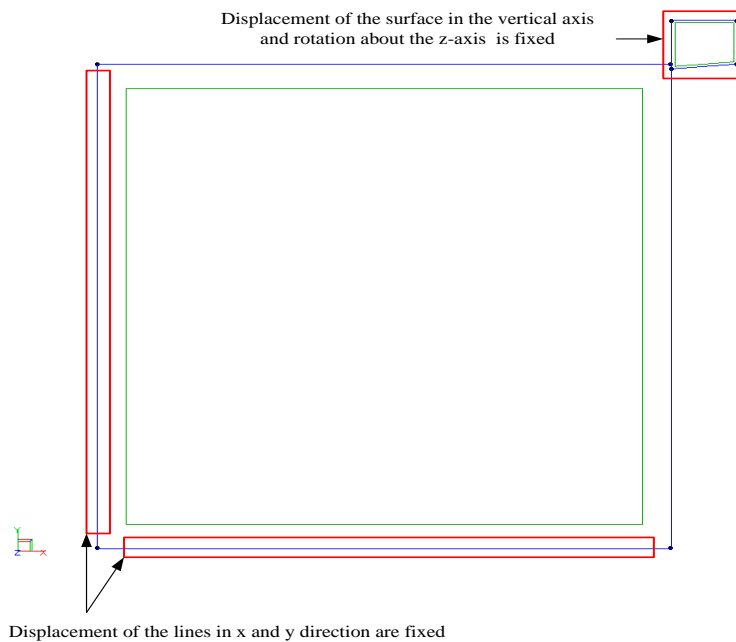


Figure 4.53 Boundary conditions applied to the model

Discrete element contact data was prescribed to the workpiece and the cutting tool which defines the way in which elements should behave when one or more nodes penetrate through an element. The data includes Young's modulus, coefficient of friction and length

of the side of the smallest element. The smallest element side length was assigned 0.5 mm to simulate the size of the debris observed during experiments as this will be the smallest size of the element that will be created during fracturing simulations. Material properties were assigned to the workpiece as listed in Table 4.11 and the tool was rendered very rigid with a Young's modulus of 211GPa so as not to distort by the load acting upon it during the cut. ELFEN-Explicit offers 13 types of elements covering both 2D and 3D options [103], in this study a 2D linear triangular element made up of 3 nodes was used. Each node has 2 degrees of freedom; U and V in the global coordinate system. An unstructured mesh was generated using linear triangular elements with a side length of the element of 5 mm for both the workpiece and the tool, but a finer mesh with side length of 1 mm was generated in the region where the tool interacts with the rock, as observed in Figure 4.54, this was done to produce realistic fracture patterns since the fracture depends on mesh size and density [20]. The mesh density was increased by assigning an element length of 1 mm on the line defining the top layer of specimen. Mesh generation methods used in this simulation was the Delaunay algorithm; this methods works by inserting nodal points and fitting triangular elements to these points and finally smoothing the final mesh. It can be observed from Figure 4.54 that the mesh extends away from the region of finer mesh size and gradually increases in element size until the an element mesh size of 5 mm is reached in the rest of the domain. The cutting tool does not require a fine mesh at the contact regions and hence only a few elements with side length of 5 mm were used in mesh generation.

The material constitutive model used in this simulation is a combination of the SR3 model which incorporates material hardening and softening properties and the Rotating Crack model with material properties such as tensile strength and fracture energy, these model produce rock failure by crack initiation, crack growth and coalescence, thus a fracture can be observed when the tensile strength of the material is exceeded. In the rotating crack model the cracks are initiated in a direction normal to the principal stress and a plane of failure remains normal to the major principal stress. Cracks are initiated when the limiting tensile strength is reached and then the material undergoes softening/hardening response governed by the fracture energy release rate [86]. The young's modulus is gradually degraded in the direction of failure leading to crack growth and coalescence.

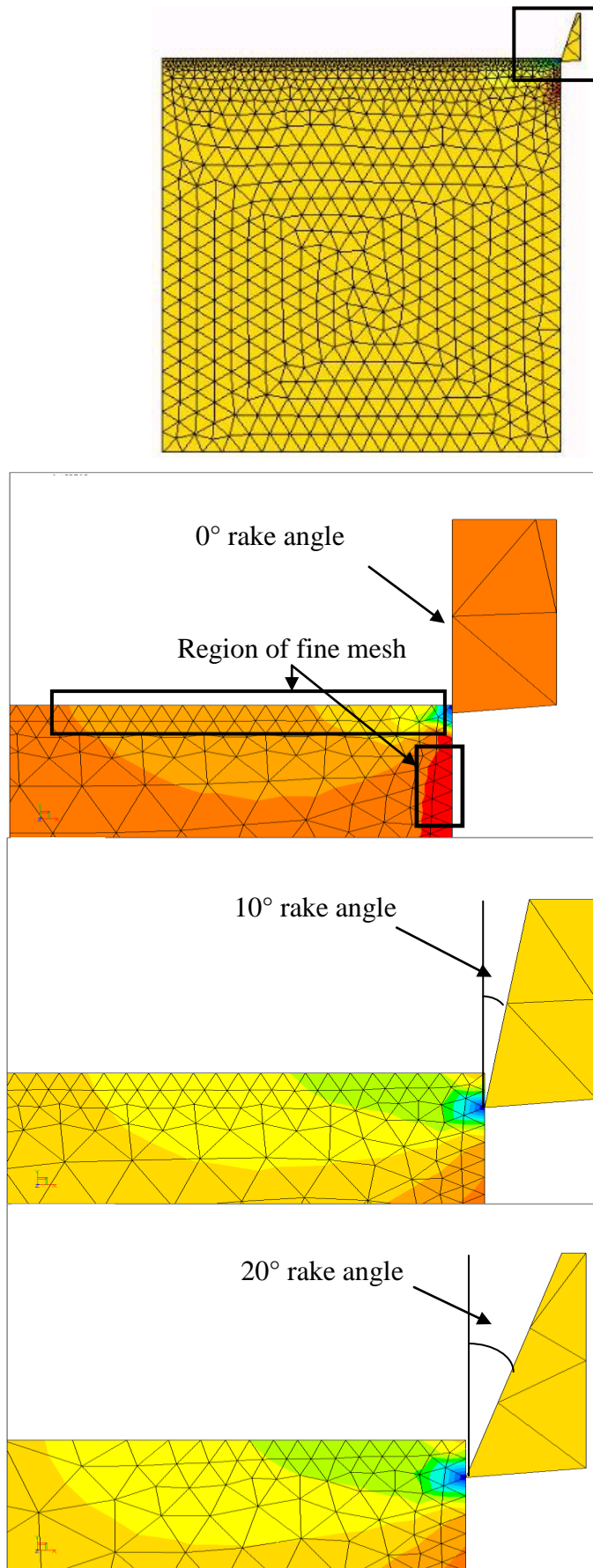


Figure 4.54 Numerical model of the sample and cutting tool

4.7.3. Numerical analysis of cutting process on low strength sample

Numerical analysis was performed to simulate the cutting process using three rake angles used in this study to understand the state of stress while cutting. Cutting simulations at 2 mm depth of cut are described in this section.

Figure 4.55 shows the cutting action for a 0° rake angle.

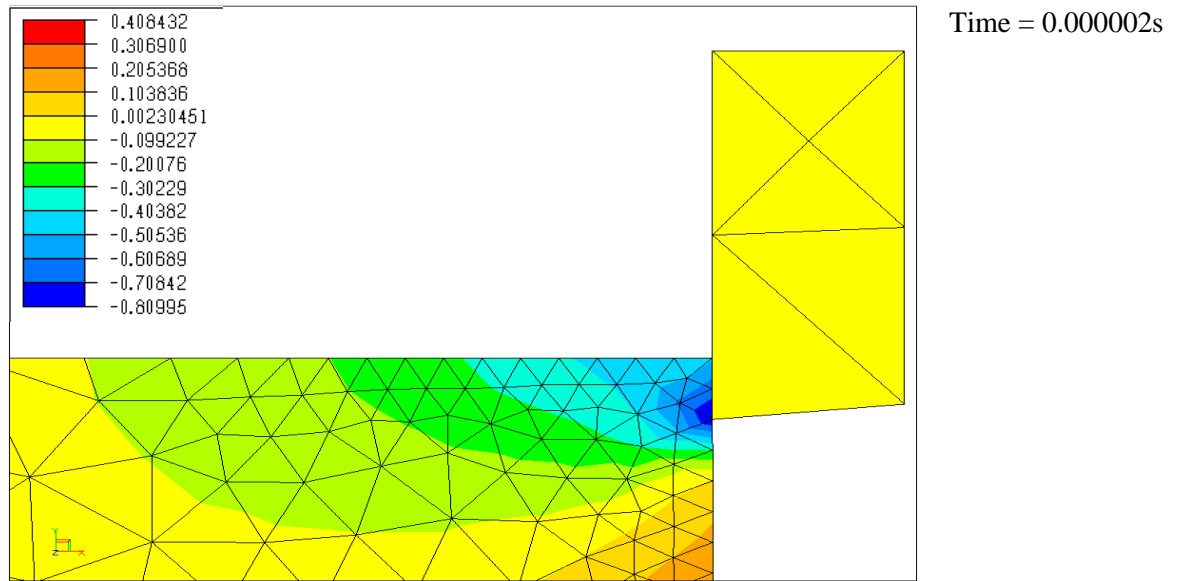


Figure 4.55 (a)

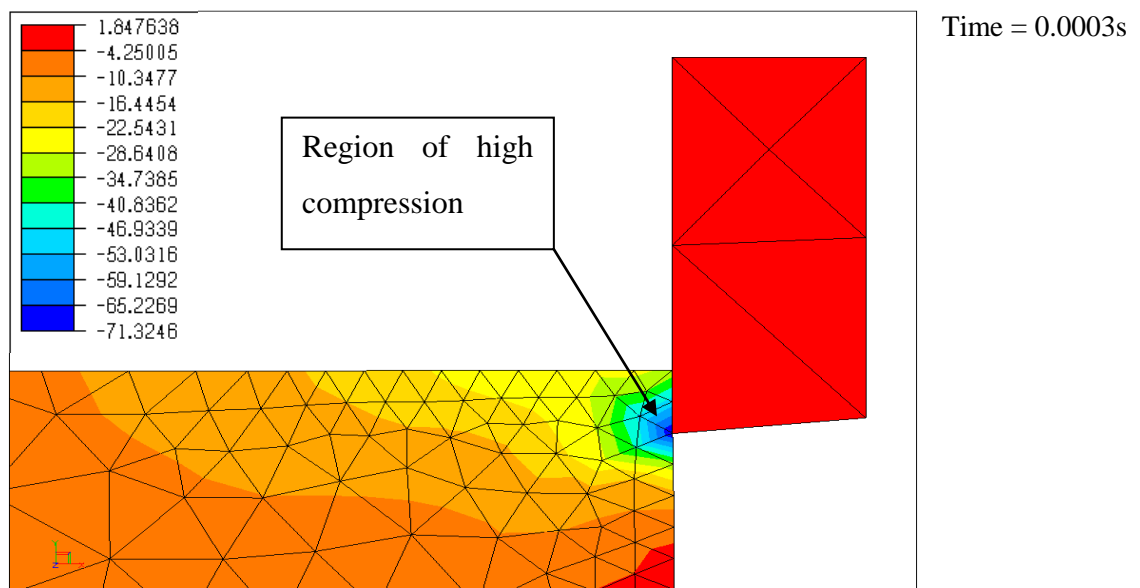


Figure 4.55 (b)

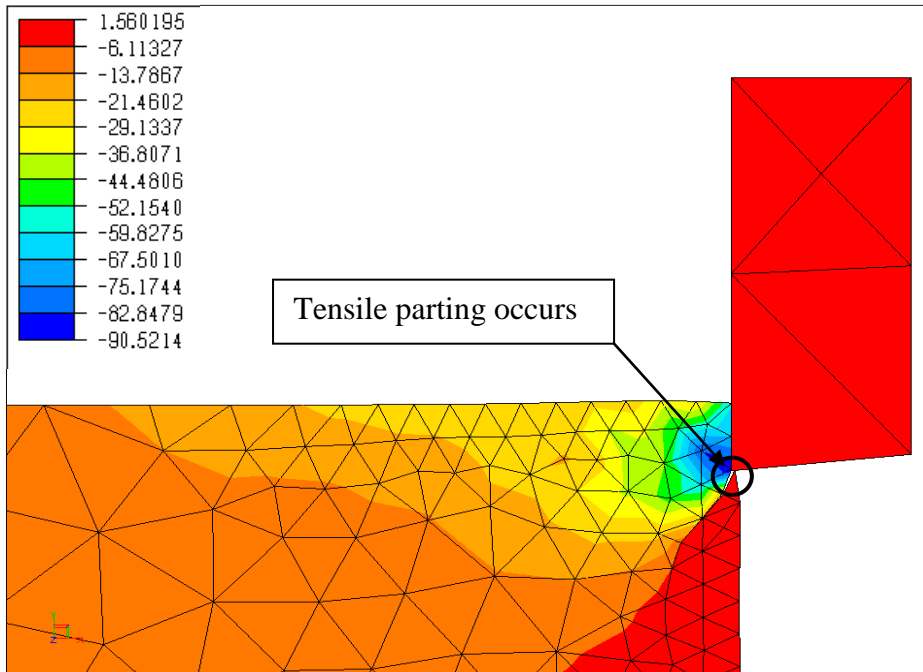


Figure 4.55 (c)

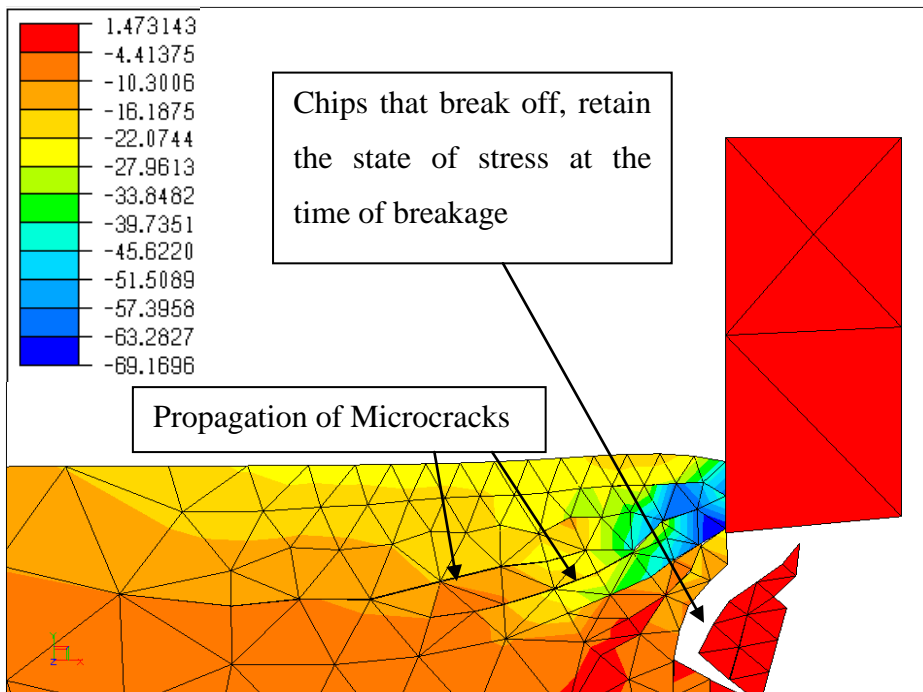


Figure 4.55 (d)

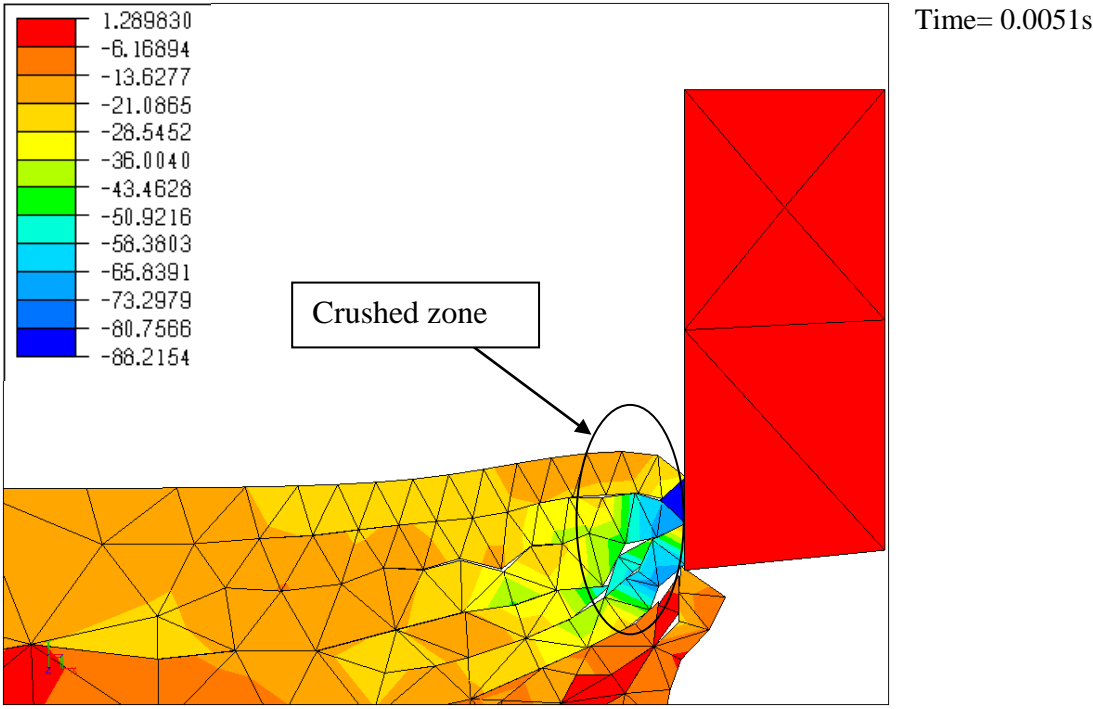


Figure 4.55 (e)

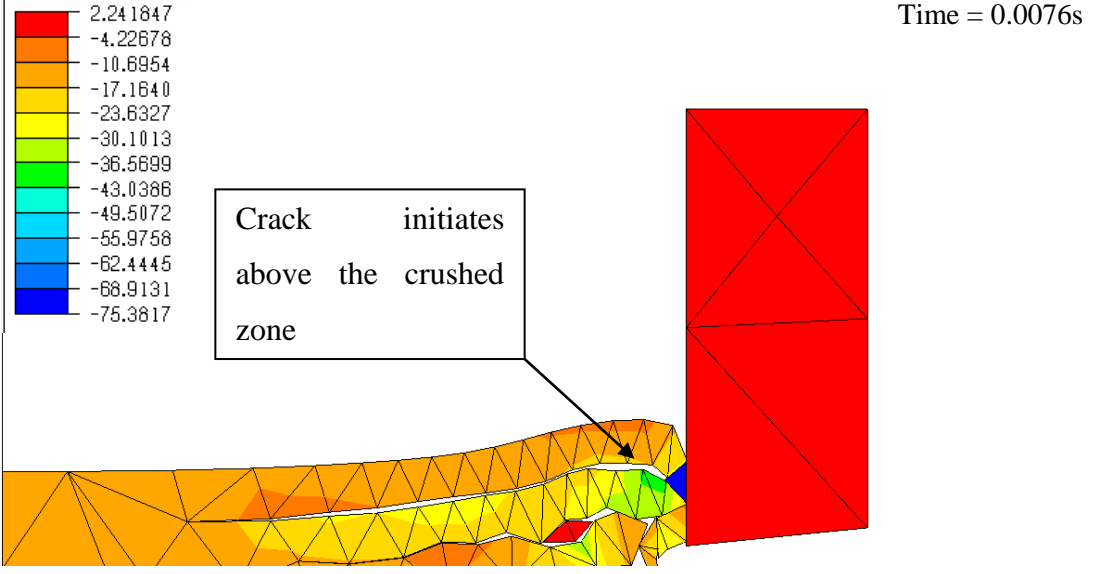


Figure 4.55 (f)

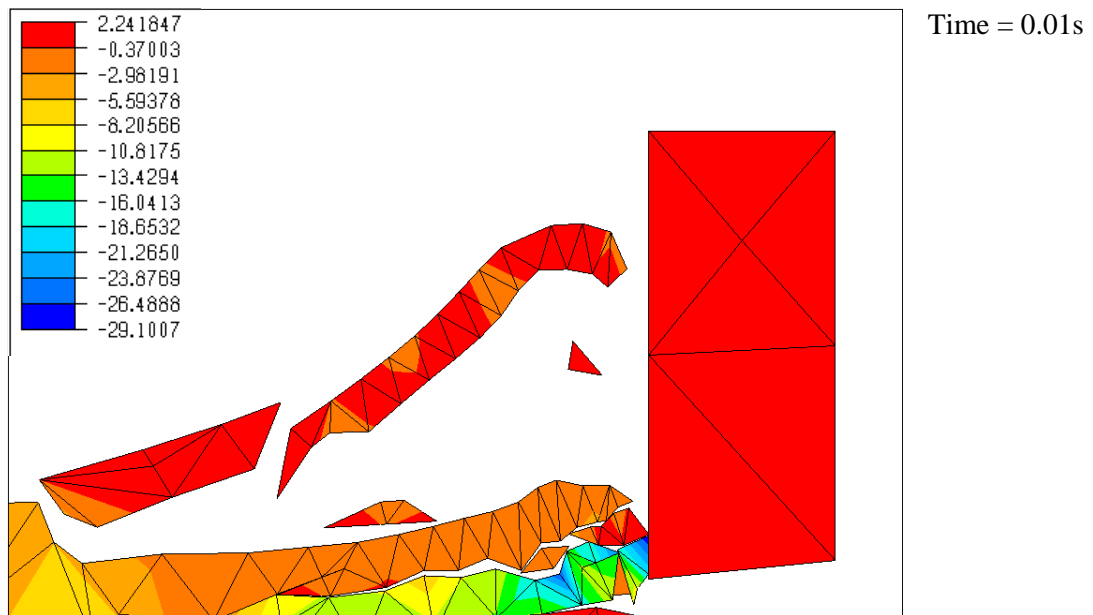
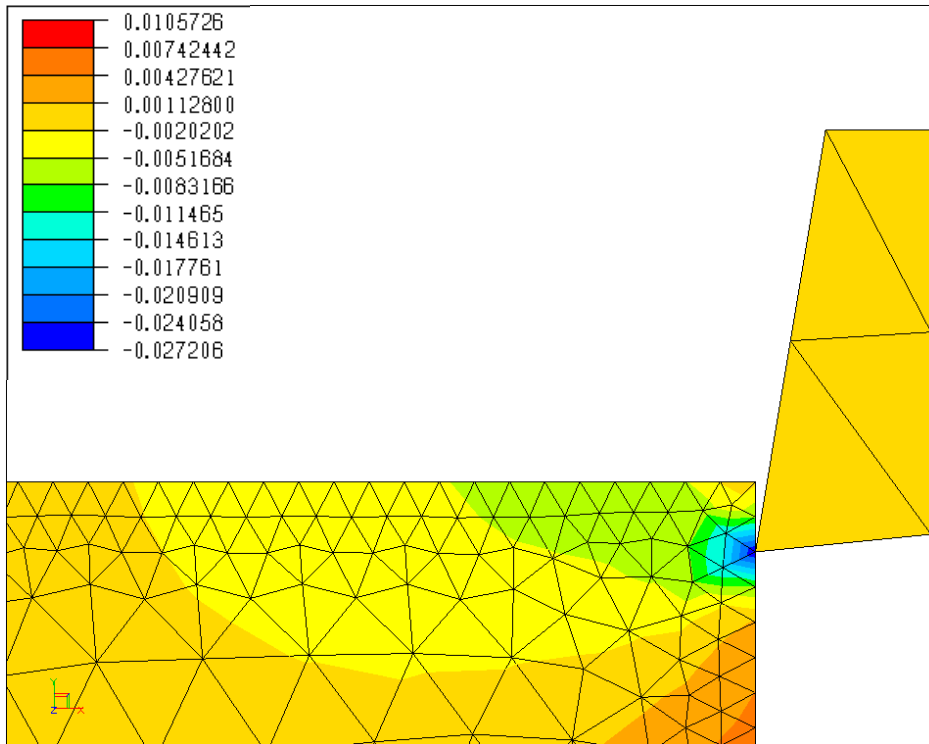


Figure 4.55 (g)

Figure 4.55 Sequence of images showing the numerical simulation of cutting a low strength sample at 2 mm depth of cut using a 0° rake angle cutting tool

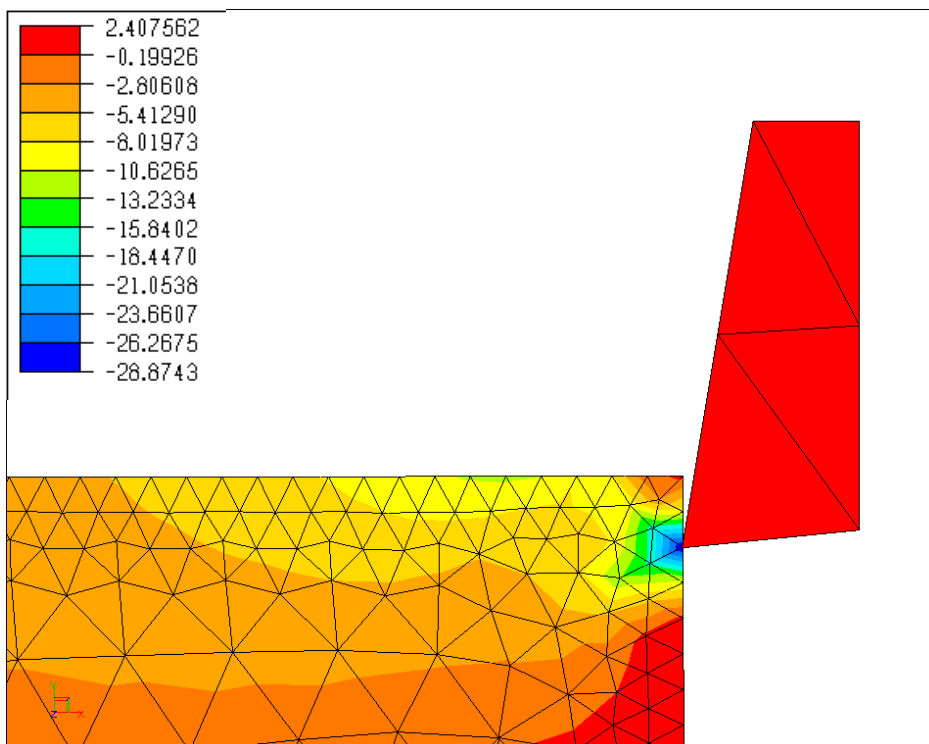
Figure 4.55 presents a sequence of the simulation while cutting at 2 mm depth of cut; at 0.000002s (Figure 4.55a) the tool is seen to contact the sample resulting in a region of compressive stress at points where the tool face is in contact with the sample, this region further shrinks and concentrates itself to the tool tip as seen at 0.0003 s. At 0.001s this region of compressive stress (indicated in blue) is seen to point towards the free surface while immediately below the tool tip a region of tensile stress is observed indicated in red. At 0.002s tensile parting has occurred and microcracks form and are observed to propagate down into the sample. The formation of the crushed zone is observed at 0.0051s which leads to major crack initiation and is observed at 0.0076s. At 0.01s the crack has reached the free surface and forms a chip which is ejected; the crushed zone of rock is still seen adhering to the tool tip.

Figure 4.56 presents a series of images for cutting with a 10° rake angle cutting tool; this simulation represents the shear failure usually observed in these rake angles.



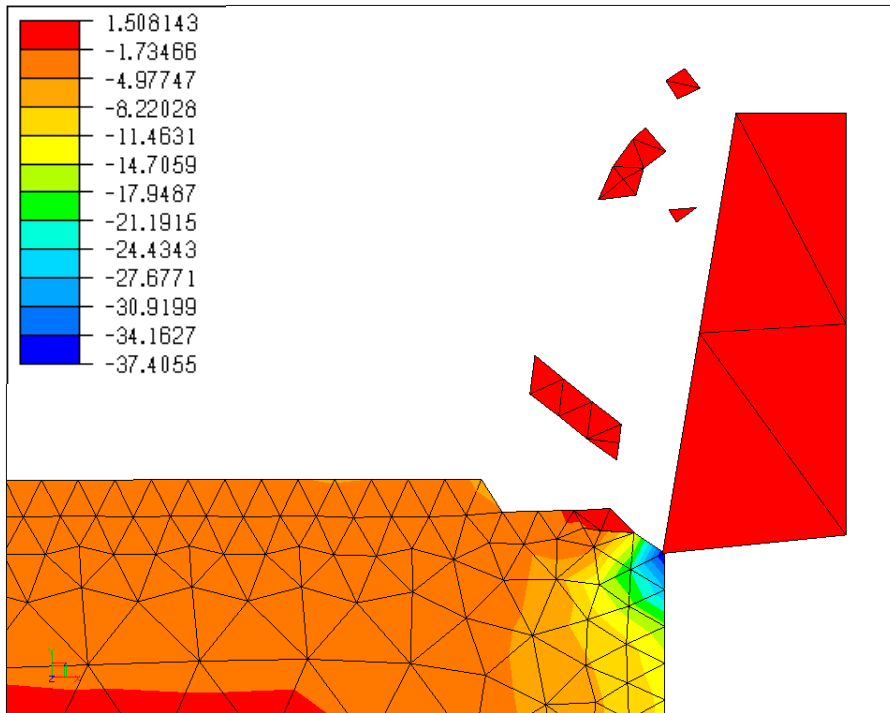
Time=0.0001s

Figure 4.56 (a)



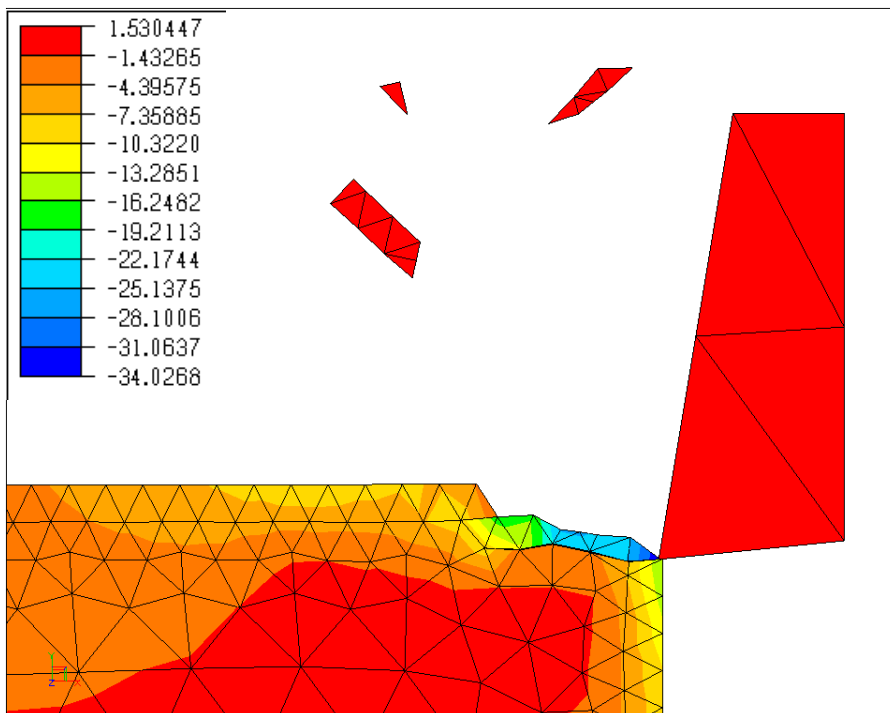
Time=0.00022s

Figure 4.56 (b)



Time=0.0003s

Figure 4.56 (c)



Time=0.0004s

Figure 4.56 (d)

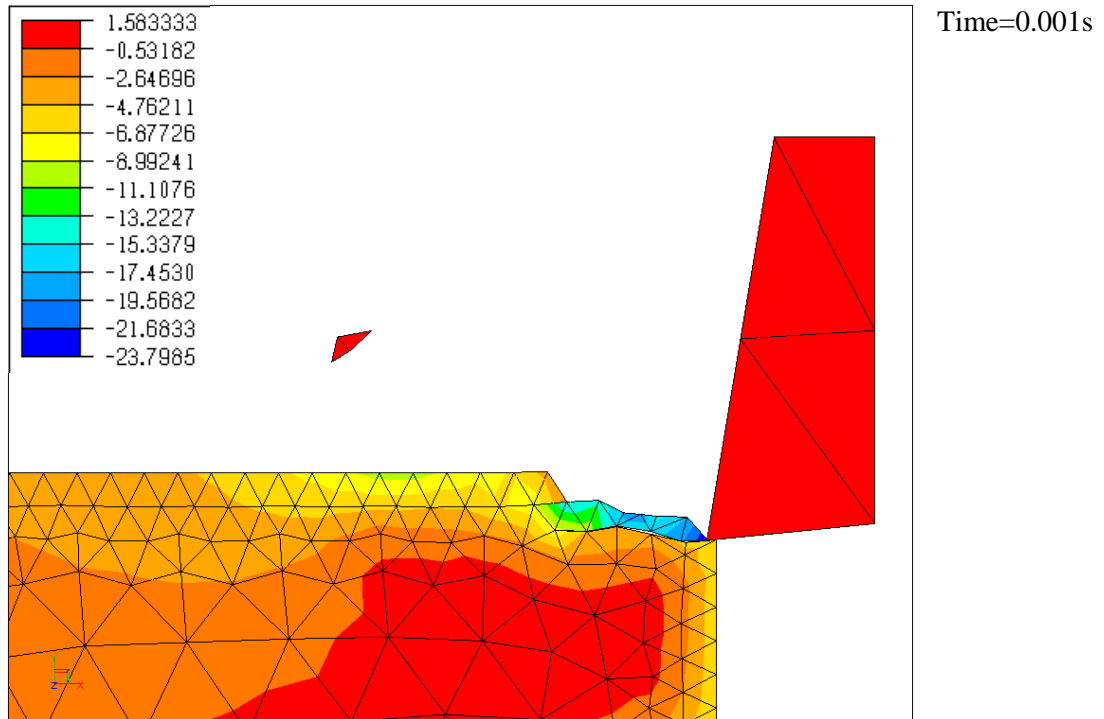


Figure 4.56 (e)

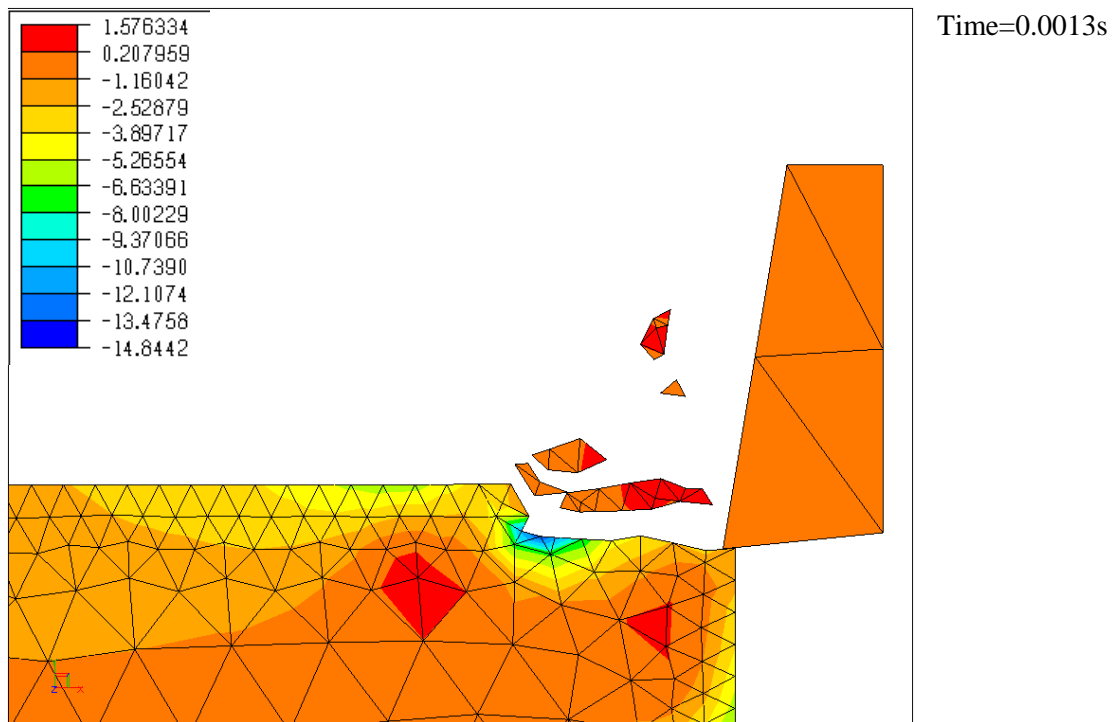


Figure 4.56 (f)

Figure 4.56 Sequence of images showing the numerical simulation of cutting a low strength sample at 2 mm depth of cut using a 10° rake angle cutting tool

Figure 4.56 presents a series of images for cutting with a 10° rake angle cutting tool at 2mm depth of cut on a low strength sample; at 0.0003s chips has been ejected from the surface by an action similar to the shear plane fracture. As the tool pushes in further, another chip is formed and ejected in a similar manner, this represents the layered chip formation whereby the top layer is ejected first followed by the one beneath it.

Simulation of the cutting process using a 20° rake angle follows a similar pattern as a 10° rake angle tool and is presented in Appendix G.

4.7.4. Numerical analysis of cutting process on high strength sample

Numerical analysis of the cutting process on high strength samples are presented in this section. The homogeneous rock material was modelled using the following experimentally obtained material properties- compressive strength of 53.5 MPa, tensile strength of 5.7 MPa, elastic modulus of 34.3 MPa.

Figure 4.57 shows cracks propagating from below the tool tip resulting in an over-cut, as seen at time sequence 0.003s; at 0.0061s a major crack has initiated from above the crushed zone and propagates into the sample. At 0.0017s the cracks have reached the free surface resulting in chip formation. The crushed zone is seen intact.

Appendix H presents the simulation while using a 20° rake angle cutting tool.

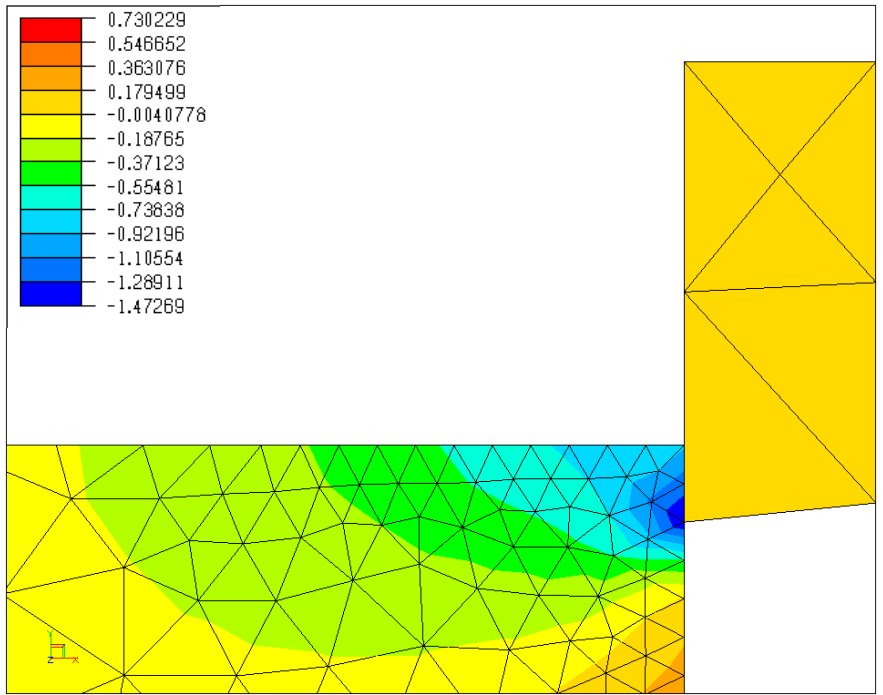


Figure 4.57 (a)

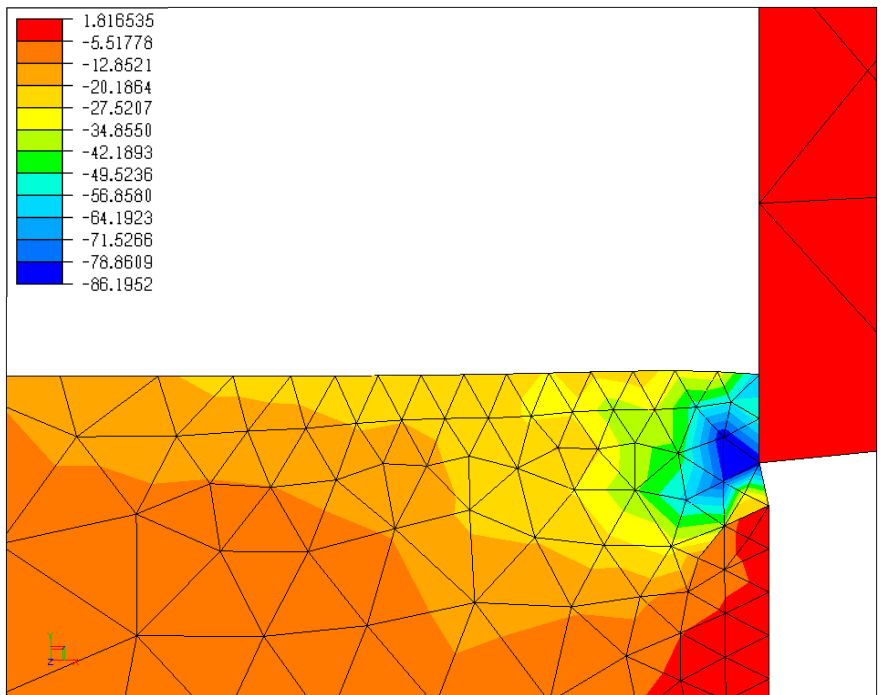
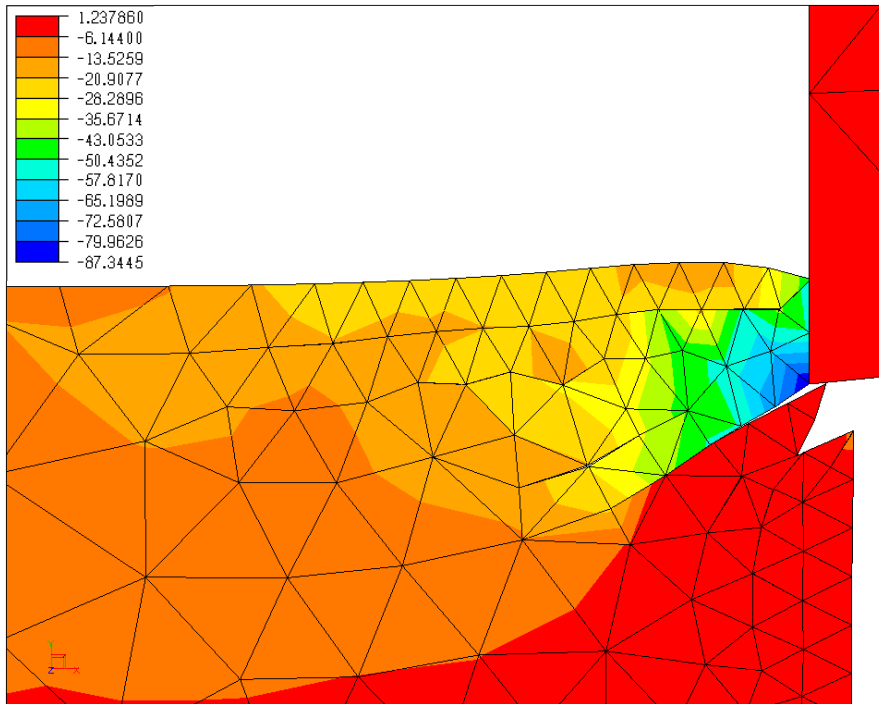
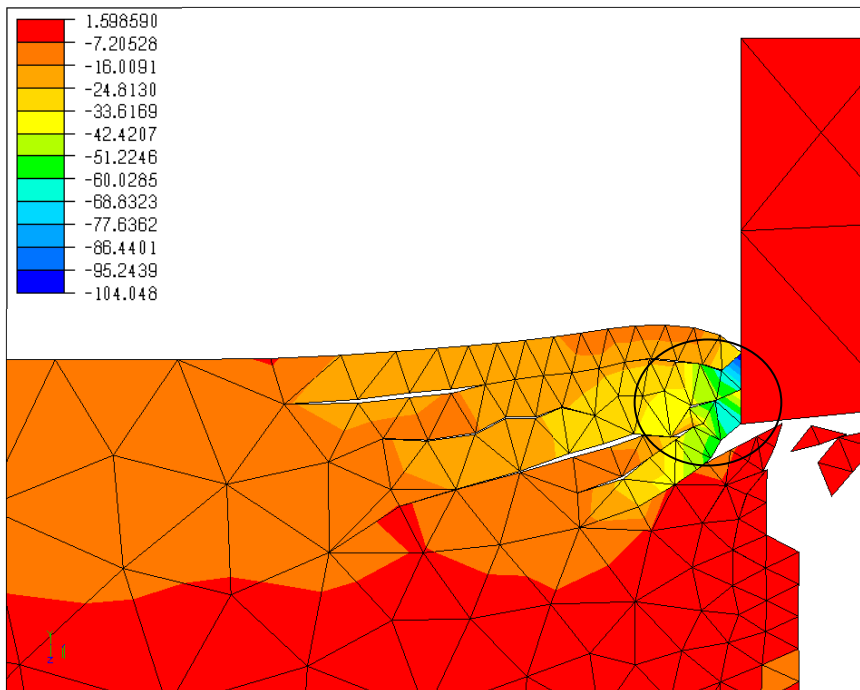


Figure 4.57 (b)



Time=0.003s
Cracks extend below
the tool tip

Figure 4.57 (c)



Time=0.0061s
Crushed zone is
formed.

Figure 4.57 (d)

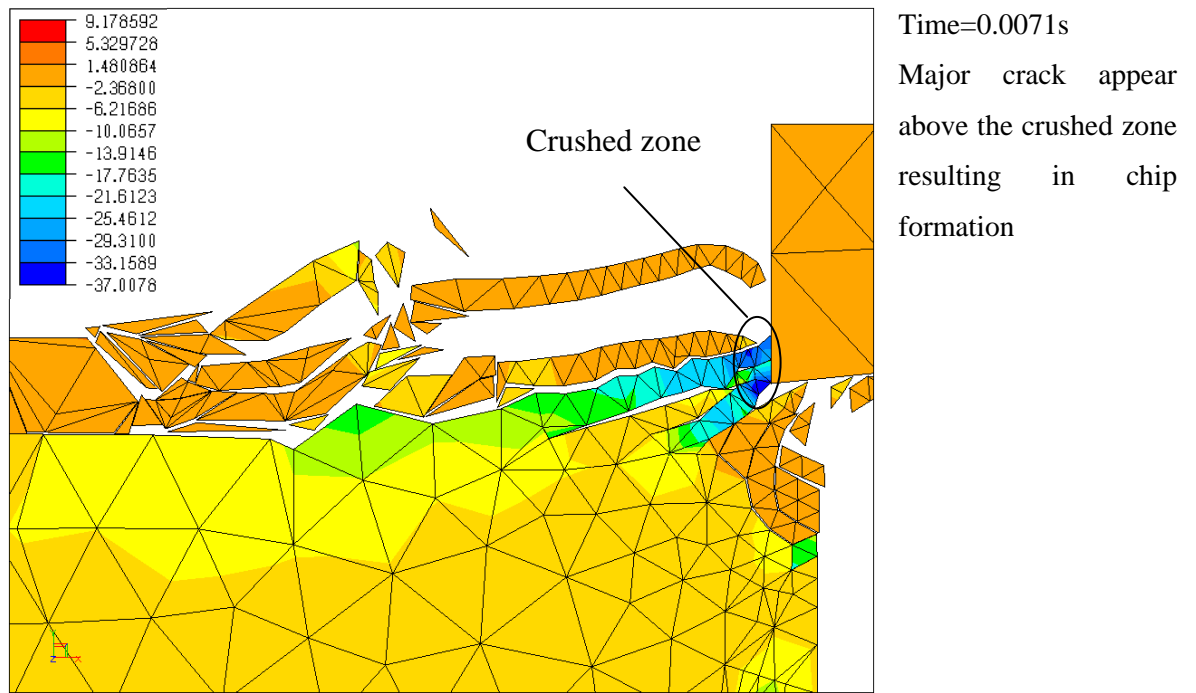


Figure 4.57 (e)

Figure 4.57 Sequence of images showing the numerical simulation of cutting a high strength sample at 2 mm depth of cut using a 0° rake angle cutting tool

4.7.5. Summary

The simulations showed the stress contours for a low and high strength homogeneous rock being cut using different rake angles. It was found that tensile parting of the material leading to crack opening formed the major fracture mechanism. This is attributed to the tensile strength of rock being lower than the compressive strength. It is also interesting to note the formation of the crushed zone and its influence over microcrack initiation, propagation and crack coalescence. A zone of highly pressurised rock at the tool tip is observed for all cuts just as the tool begins to cut into the rock, immediately followed by subsurface cracks initiating above and below this zone. The crack at the top propagates quicker than the one at the bottom, reaching the free surface resulting in the formation of the chip. The experimental and numerical simulation were found to be similar to previous work by Zeuch and Finger [104] who performed cutting test using PDC cutters on three different types of rocks and came to the conclusion that the chip formation process is similar in all rock types and that fractures are nucleated at the cutter tip. They also observed increase and drop in the cutting force over the duration of the cut and attributed it to the formation of the crushed zone. Wei *et al* [94] performed cutting tests on Diabase and Granite and concluded that the crushed zone and the chip formation process is formed under the action of tensile stress, which was found to be common observation in all the cuts leading to the build-up of the crushed zone before the crack initiates.

CHAPTER 5: CONCLUSIONS AND FUTURE WORK

5.1. Conclusions

The following conclusions were drawn from the experimental and numerical work

i) Influence of the cutting parameters

- The specific energy required for cutting decreases as the depth of cut increases in both samples and the magnitude of specific energy is higher in high strength sample than compared with low strength sample. Depth of cut and the sample strength are major factors which influence the specific energy.
- The mean cutting force in low strength sample is considerably less, by approximately 50% than those measured in high strength sample for all rake angles. The mean thrust force is always greater than the mean cutting force at shallow depths of cut but as depth of cut increases the cutting force becomes larger than the thrust force. Cutting at shallow depths of cut is similar to a grinding or rubbing process.
- For both samples, it was observed that the 20° rake angle cutting tool only reduced the cutting force and thrust force needed to make a cut.

ii) Mechanics of cutting

- Chip formation is characterised by brittle failure by a combination of shearing (Mode A) and fracturing (Mode B); as the cutting tool ploughs through the sample, the cutting force increases indicating the build up of critical stress and once this is breached, cracks initiate and follow unstable propagation through the specimen leading to the formation of a chip, as the chip breaks off, the cutting force abruptly falls. This results in local maxima and minima of the measured cutting and thrust

force. It is observed that volatile ejection of a chip is indicative of a higher thrust force.

- Force signal analysis of the cutting and thrust force indicate the influence of the crushed zone. As the crushed zone builds-up in size the cutting force increases.
- Crushed zone geometry is influenced by the tool rake angle; for a 0° rake angle a hemisphere shaped crushed zone is observed while a wedge shaped crushed zone is observed for 10° and 20° rake angle.
- The built-up edge of a fine layer of crushed material changes the profile of the cutting edge of the tool and is observed to continually change the profile during the cutting process as material are either deposited on or detached from the rake face. This changes the real rake angle to an apparent rake angle.
- Numerical simulation has provided an important tool in analysing the stress states ahead of the tool. The state of stress in the immediate vicinity of the tool tip is critical for the formation of the crushed zone and the crack initiation. Tensile parting of the material leading to the formation of cracks and chips has been found as the main mechanism in the simulations. High states of stress are observed during the formation of the crushed zone and microcracks are found to radiate away from this crushed zone. Crack coalescence was clearly observed in all simulations which lead to chip formation.

5.2. Critical Appraisal

In this work the material removal mechanism in rock cutting was investigated which helped establish a relationship between the formation of the crushed zone at the tool-rock interface and the cutting force. This layer of crushed rock transmits the force from the cutting tool to the rock and hence it is energy intensive process. This study provided a relationship between Specific energies and the cutting force, rake angles, depths of cut and material properties.

A critical review is presented here of this work which evaluates the methods used, data analysis, limitations and achievements:

- Force traces of the cutting force are interspersed with local maxima and minima, this has been attributed in previous literature to the brittle nature of the rocks and the chip formation process; this study while corroborating previous studies also shows the development of these peaks and troughs through the formation of the crushed zone.
- The crushed zone of rocks ahead of the tool tip has been established in this study to change shape according to the rake angle of the cutting tool. The rake angle also influences the cutting force; though in this study, cutting among the same samples the rake angles do not affect a significant change. This study was limited to zero and positive rake angles.
- Rock-like samples used as a model material was based on previous literature; this method reduced the time and effort needed towards procuring, machining and testing of different types of rocks. Since there is no standardised method or guidance in the preparation of such samples, the repetition of this process may vary sample characteristics due to different parameters such as substituting the materials mentioned in Table 3.1 with different grades of materials, change in water type or operator knowledge.
- High speed video recording of the cutting process has been a noteworthy feature of this research. It has provided a dynamic insight into the material removal process not previously used in such a manner but the analyses of such videos are time consuming.
- The predictive equations of the cutting and thrust force based on the rake angle and depths of cut are based on linear relationships. Linear relationships have been established in previous literatures and hence it has been made use of in this study. But it has been observed that there is a large scatter of data points (due to the sample materials and discontinuities inadvertently being introduced during preparation) and since they provide a useful tool in forming simple empirical equations the use of other curve fitting lines cannot be overlooked.
- A coupled finite-discrete element code was used to investigate the crack initiation and propagation. The study was limited to 2D and homogenous material and the results closely matched with that of experimentally observed failure mechanism.

5.3. Future Work

This work has highlighted important features of the fracture mechanics of rocks and it will be interesting to carry out further research into this field in few of the areas described below:

A full scale laboratory rig in the context of a drilling rig could be setup with similar instrumentation to observe the formation of the chip. All the experiments in this study were carried out under normal atmospheric temperature and pressure in dry cutting conditions. The full scale rig can be used to simulate similar conditions and furthermore special rigs can be designed to study the influence of pressure found in well bores, in the presence of a circulating fluid, on the fracture mechanism in greater detail.

A variety of actual rock samples with varying mechanical property are to be used for the cutting test along using cutting tools of various geometry having both positive and negative rake angles with the possible inclusion of side rake angles.

In-depth analysis of the cutting tool such as wear and dimensions of the edge radius were beyond the scope of this study hence any future research should try to incorporate these.

References

- [1]. **A. Ersoy and M. D. Waller.** Wear characteristics of PDC pin and hybrid core bits in rock drilling. *Wear*, 1995, **188**, pp. 150-165.
- [2]. **K. Thuro.** Drillability prediction: geological influences in hard rock drill and blast tunnelling. *International Journal of Earth Sciences*, 1997, **86**, pp. 426-438.
- [3]. **E. M. Trent and P. K. Wright.** Metal Cutting, in *The Essential Features of Metal Cutting*, 4th ed. Woburn, Butterworth-Heinemann, 2000, pp. 21-55.
- [4]. **Y. Nishimatsu.** The mechanics of rock cutting. *International Journal of Rock Mechanics and Mining Sciences & Geomechanics Abstracts*, 1972, **9**, pp. 261-270.
- [5]. **O. Alimov and L. Dvornikov.** The mechanism of rock fracture in rotary drilling by a hard-alloy bit. *Journal of Mining Science*, 1972, **8**, pp. 677-682.
- [6]. **N. G. W. Cook, M. Hood and F. Tsai.** Observations of crack growth in hard rock loaded by an indenter. *International Journal of Rock Mechanics and Mining Sciences & Geomechanics Abstracts*, 1984, **21**, pp. 97-107.
- [7]. **A. W. Momber.** Deformation and fracture of rocks loaded with spherical indenters. *International Journal of Fracture*, 2004, **125**, pp. 263-279.
- [8]. **C. Dong.** An investigation into the optimisation of the use of diamond abrasive tools for hard rock cutting, Ph.D. dissertation, Univ. of London, 1993.
- [9]. **S. Suwannapiniij.** The mechanical and cutting properties of rocks related to the application of tunnel boring machines, Ph.D. dissertation, Univ. Newcastle Upon Tyne, 1975.
- [10]. **P. A. Lindqvist and L. Hai-Hui.** Behaviour of the Crushed Zone in Rock Indentation. *Rock Mechanics and Rock Engineering*, 1983, **16**, pp. 199-207.
- [11]. **J. Rojek.** Discrete element modelling of rock cutting. *Computer Methods in Materials Science*, 2007, **7**, pp. 224-230.

- [12]. **L. Jing.** A Review of Techniques, Advances and Outstanding Issues in Numerical Modelling for Rock Mechanics and Rock Engineering. *International Journal of Rock Mechanics and Mining Sciences*, 2003, **40**, pp. 283-353.
- [13]. **L. Jing and J. A. Hudson.** Numerical methods in rock mechanics. *International Journal of Rock Mechanics and Mining Sciences*, 2002, **39**, pp. 409-427.
- [14]. **H. Y. Liu, S. Q. Kou, P. A. Lindqvist and C. A. Tang.** Numerical Modelling of the Heterogeneous Rock Fracture Process Using Various Test Techniques. *Rock Mechanics and Rock Engineering*, 2007, **40**, pp. 107-144.
- [15]. **H. Y. Liu, S. Q. Kou and P. A. Lindqvist.** Numerical simulation of the fracture process in cutting heterogeneous brittle material. *International Journal for Numerical and Analytical Methods in Geomechanics*, 2002, **26**, pp. 1253-1278.
- [16]. **H. Y. Liu, S. Q. Kou, P. A. Lindqvist and C. A. Tang.** Numerical simulation of the rock fragmentation process induced by indenters. *International Journal of Rock Mechanics and Mining Sciences*, 2002, **39**, pp. 491-505.
- [17]. **A. Carpinteri, B. Chiaia and S. Invernizzi.** Numerical analysis of indentation fracture in quasi-brittle materials. *Engineering Fracture Mechanics*, 2004, **71**, pp. 567-577.
- [18]. **Rockfield Software Ltd.** Overview to ELFEN. Internet: <http://www.rockfield.co.uk/elfen.htm> [October 23,2009],
- [19]. **M. Cai.** Influence of intermediate principal stress on rock fracturing and strength near excavation boundaries-Insight from numerical modeling. *International Journal of Rock Mechanics and Mining Sciences*, 2008, **45**, pp. 763-772.
- [20]. **M. Cai and P. K. Kaiser.** Numerical Simulation Of The Brazilian Test And The Tensile Strength Of Anisotropic Rocks And Rocks With Pre-Existing Cracks. *International Journal of Rock Mechanics and Mining Sciences*, 2004, **41**, pp. 478-483.
- [21]. **P. L. Rose and S. Drake.** The Pseudo-Aristotelian Questions of Mechanics in Renaissance Culture. *Studies in the Renaissance*, 1971, **18**, pp. 65-104.

- [22]. **J. R. Lund and J. P. Byrne.** Leonardo da Vinci's Tensile Strength Tests: Implications for the Discovery of Engineering Mechanics. *Civil Engineering and Environmental Systems*, 2001, **18**, pp. 243-250.
- [23]. **G. Galilei.** (1638) Dialogues Concerning Two New Sciences.[On-line]. Available: <http://ebooks.adelaide.edu.au/g/galileo/dialogues/index.html>, [January 20, 2013]
- [24]. **E. E. Gdoutos.** Introduction, in *Fracture Mechanics: An Introduction*, 2nd ed. Dordrecht, Netherlands, Springer,2005, pp. 5-7.
- [25]. **W. F. Hosford.** Mechanical Behavior of Materials, ed.: Cambridge University Press, 2005.
- [26]. **J. P. Harrison and J. A. Hudson.** Engineering Rock Mechanics - An Introduction to the Principles, 1st ed ed.: Elsevier Science, 2000.
- [27]. **J. W. Obreimoff.** The Splitting Strength of Mica. *Proceedings of the Royal Society of London. Series A*, 1930, **127**, pp. 290-297.
- [28]. **D. Gross and T. Seelig.** Fracture Mechanics: With an Introduction to Micromechanics, 2nd ed. ed.: Springer, 2011.
- [29]. **Z. T. Bieniawski.** Fracture Dynamics of Rock. *The International Journal of Fracture Mechanics*, 1968, **4**, pp. 415-430.
- [30]. **M. Ignjatovic, P. Chalkley and C. Wang.** The Yield Behaviour of a Structural Adhesive under Complex Loading, *Aeronautical and Maritime Research Laboratory*, Melbourne, Rep. DSTO-TR-0728, 1998.
- [31]. **K. Mogi.** Effect of the triaxial stress system on the failure of dolomite and limestone. *Tectonophysics*, 1971, **11**, pp. 111-127.
- [32]. **E. Hoek and E. T. Brown.** Empirical Strength Criterion for Rock Masses. *American Society of Civil Engineers*, 1980, **106**, pp. 1013-1035.
- [33]. **P. J. Sabatini, R. C. Bachus, P. W. Mayne, J. A. Schneider and T. E. Zettler.** Geotechnical Engineering Circular No. 5 Evaluation of Soil and Rock Properties, *U.S. Department of Transportation*, Washington, Rep. FHWA-IF-02-034, 2002.

- [34]. **E. Hoek and E. T. Brown.** Practical estimates of rock mass strength. *International Journal of Rock Mechanics & Mining Sciences & Geomechanics Abstracts*, 1997, **34**, pp. 1165-1186.
- [35]. **G. E. Andreev.** Brittle Failure of Rock Materials: Test Results and Constitutive Models, ed.: A.A. Balkema, 1995.
- [36]. **D. C. Drucker and W. Prager.** Soil mechanics and plastic analysis or limit design. *Quarterly of Applied Mathematics*, 1952, **10**, pp. 157-175.
- [37]. **T. Atkins.** The Science and Engineering of Cutting: The Mechanics and Processes of Separating and Puncturing Biomaterials, Metals and Non-metals, ed.: Elsevier Science, 2009.
- [38]. **I. Evans.** The force required to cut coal with blunt wedges. *International Journal of Rock Mechanics and Mining Sciences & Geomechanics Abstracts*, 1965, **2**, pp. 1-12.
- [39]. **H. R. Phillips.** Rock cutting mechanics related to the design of primary excavation systems, Ph.D. dissertation, Mining Eng., Univ. Newcastle Upon Tyne, 1975.
- [40]. **U. Beste.** On the nature of Cemented Carbide Wear in Rock Drilling, Ph.D. dissertation, Uppsala Univ., 2004.
- [41]. **U. Atici and A. Ersoy.** Correlation of specific energy of cutting saws and drilling bits with rock brittleness and destruction energy. *Journal of Materials Processing Technology*, 2009, **209**, pp. 2602-2612.
- [42]. **L. L. Kan, B. K. Gao, X. F. Wang and H. W. Liang.** Development of a high precision MWD system, in *8th IEEE Int. Conf. on Electronic Measurement and Instruments*, 2007, pp. 951–954.
- [43]. **K. P. Malloy.** A Probabilistic Approach to Risk Assessment of Managed Pressure Drilling in Offshore Applications, in, ed, 2008, pp.
- [44]. **R. Sweatman.** Deepwater: Drilling Trouble Zones and Well Integrity, in, ed, 2006, pp.

- [45]. **L. Tze-Pin, M. Hood, G. A. Cooper and L. Xiaohong.** Wear and failure mechanisms of polycrystalline diamond compact bits. *Wear*, 1992, **156**, pp. 133-150.
- [46]. **X. Tian and S. Tian.** The wear mechanisms of impregnated diamond bits. *Wear*, 1994, **177**, pp. 81-91.
- [47]. **A. W. Batchelor and G. W. Stachowiak.** Tribology in materials processing. *Journal of Materials Processing Technology*, 1995, **48**, pp. 503-515.
- [48]. **U. Beste, S. Jacobson and S. Hogmark.** Rock penetration into cemented carbide drill buttons during rock drilling. *Wear*, 2008, **264**, pp. 1142-1151.
- [49]. **Z. Q. Yue, C. F. Lee, K. T. Law and L. G. Tham.** Automatic monitoring of rotary-percussive drilling for ground characterization--illustrated by a case example in Hong Kong. *International Journal of Rock Mechanics and Mining Sciences*, 2004, **41**, pp. 573-612.
- [50]. **S. Kahraman, N. Bilgin and C. Feridunoglu.** Dominant rock properties affecting the penetration rate of percussive drills. *International Journal of Rock Mechanics and Mining Sciences*, 2003, **40**, pp. 711-723.
- [51]. **C. L. Jimeno, E. L. Jimeno, F. J. A. Carcedo and Y. V. D. Ramiro.** Drilling and blasting of rocks, revised, illustrated ed. ed.: Taylor & Francis, 1995.
- [52]. **E. Kuru and A. K. Wojtanowicz.** An experimental study of sliding friction between PDC drill cutters and rocks. *International Journal of Rock Mechanics and Mining Science & Geomechanics Abstracts*, 1995, **32**, pp. 277-283.
- [53]. **P. Kaitkay and S. Lei.** Experimental study of rock cutting under external hydrostatic pressure. *Journal of Materials Processing Technology*, 2005, **159**, pp. 206-213.
- [54]. **M. R. Thakare, J. A. Wharton, R. J. K. Wood and C. Menger.** Exposure effects of alkaline drilling fluid on the microscale abrasion-corrosion of WC-based hardmetals. *Wear*, 2007, **263**, pp. 125-136.

- [55]. **The Robbins Company.** Tunnel Boring Machine. Internet: <http://www.therobbinscompany.com/our-products/tunnel-boring-machines/single-shield/>, [April. 16, 2012]
- [56]. **Ellton Longwall Private Limited.** EBZ200 Roadheader. Internet: <http://www.elltonlongwall.com.au/index.php/EBZ200-Roadheader.html>, [April. 16, 2012]
- [57]. **M. Sarwar, M. Persson, H. Hellbergh and J. Haider.** Measurement of specific cutting energy for evaluating the efficiency of bandsawing different workpiece materials. *International Journal of Machine Tools and Manufacture*, 2009, **49**, pp. 958-965.
- [58]. **M. Sarwar, M. Perrson and H. Hellbergh.** Wear of the cutting edge in the bandsawing operation when cutting austenitic 17-7 stainless steel. *Wear*, 2007, **263**, pp. 1438-1441.
- [59]. **M. Sarwar.** Application of advanced surface engineering treatments to multi-point cutting edges. *Surface and Coatings Technology*, 1998, **108-109** pp. 612-619.
- [60]. **N. Bilgin, M. A. Demircin, H. Copur, C. Balci, H. Tuncdemir and N. Akcin.** Dominant rock properties affecting the performance of conical picks and the comparison of some experimental and theoretical results. *International Journal of Rock Mechanics and Mining Sciences*, 2006, **43**, pp. 139-156.
- [61]. **S.-H. Chang, S.-W. Choi, G.-J. Bae and S. Jeon.** Performance prediction of TBM disc cutting on granitic rock by the linear cutting test. *Tunnelling and Underground Space Technology*, 2006, **21**, pp. 271-271.
- [62]. **V. F. Vazhov, M. Y. Zhurkov, V. V. Lopatin and V. M. Muratov.** Electric-discharge cutting of rocks. *Journal of Mining Science*, 2008, **44**, pp. 176-182.
- [63]. **H. P. Rossmannith, A. Daehnke, R. E. Knasmillner, N. Kouzniak, M. Ohtsu and K. Uenishi.** Fracture mechanics applications to drilling and blasting. *Fatigue and Fracture of Engineering Materials and Structures*, 1997, **20**, pp. 1617-1636.
- [64]. **S. L. Huang and Z. W. Wang.** The mechanics of diamond core drilling of rocks. *International Journal of Rock Mechanics and Mining Sciences*, 1997, **34**, pp. 134.e1-134.e14.

- [65]. **H. Copur.** Linear stone cutting tests with chisel tools for identification of cutting principles and predicting performance of chain saw machines. *International Journal of Rock Mechanics and Mining Sciences*, **In Press, Corrected Proof**, pp.
- [66]. **O. Acaroglu, L. Ozdemir and B. Asbury.** A fuzzy logic model to predict specific energy requirement for TBM performance prediction. *Tunnelling and Underground Space Technology*, 2008, **23**, pp. 600-608.
- [67]. **J.-W. Cho, S. Jeon, S.-H. Yu and S.-H. Chang.** Optimum spacing of TBM disc cutters: A numerical simulation using the three-dimensional dynamic fracturing method. *Tunnelling and Underground Space Technology*, **25**, pp. 230-244.
- [68]. **H. Basarir, C. Karpuz and L. Tutluoglu.** Specific energy based rippability classification system for coal measure rock. *Journal of Terramechanics*, 2008, **45**, pp. 51-62.
- [69]. **F. F. Roxborough.** The Role of Some Basic Rock Properties in Assessing Cuttability, in *Seminar on Tunnels, Wholly Engineered Structures*, I.E. Aust./AFCC, Sydney, 1987, pp.
- [70]. **H. Tuncdemir, N. Bilgin, H. Copur and C. Balci.** Control of rock cutting efficiency by muck size. *International Journal of Rock Mechanics and Mining Sciences*, 2008, **45**, pp. 278-288.
- [71]. **N. Sengun and R. Altindag.** Prediction of specific energy of carbonate rock in industrial stones cutting process. *Arabian Journal of Geosciences*, pp. 1-8.
- [72]. **B. Tiryaki and A. C. Dikmen.** Effects of Rock Properties on Specific Cutting Energy in Linear Cutting of Sandstones by Picks. *Rock Mechanics and Rock Engineering*, 2006, **39**, pp. 89-120.
- [73]. **B. Stimpson.** Modelling materials for engineering rock mechanics. *International Journal of Rock Mechanics and Mining Sciences & Geomechanics Abstracts*, 1970, **7**, pp. 77-121.

- [74]. **Y. M. Tien, M. C. Kuo and C. H. Juang.** An experimental investigation of the failure mechanism of simulated transversely isotropic rocks. *International Journal of Rock Mechanics and Mining Sciences*, 2006, **43**, pp. 1163-1181.
- [75]. **M. U. Ozbay, T. Dede and J. A. L. Napier.** Physical and numerical modelling of rock fracture. *The Journal of the South African Institute of Mining Metallurgy*, 1996, pp. 317-323.
- [76]. **N. Cho, C. D. Martin and D. C. Sego.** Development of a shear zone in brittle rock subjected to direct shear. *International Journal of Rock Mechanics and Mining Sciences*, 2008, **45**, pp. 1335-1346.
- [77]. **R. H. C. Wong and K. T. Chau.** Crack coalescence in a rock-like material containing two cracks. *International Journal of Rock Mechanics and Mining Sciences*, 1998, **35**, pp. 147-164.
- [78]. **H. Y. Liu, S. Q. Kou, P. A. P. A. Lindqvist and C. A. Tang.** Numerical simulation of shear fracture (mode II) in heterogeneous brittle rock. *International Journal of Rock Mechanics and Mining Sciences*, 2004, **41**, pp. 14-19.
- [79]. **J. Gajewski, J. Podgórski, J. Jonak and Z. Szkuclarek.** Numerical simulation of brittle rock loosening during mining process. *Computational Materials Science*, 2008, **43**, pp. 115-118.
- [80]. **G. N. Pande, G. Beer and J. R. Williams.** Numerical methods in rock mechanics, ed.: John Wiley & Sons Inc, 1990.
- [81]. **J. Rojek, E. Onate, C. Labra and H. Kargl.** Discrete element simulation of rock cutting. *International Journal of Rock Mechanics and Mining Sciences*, 2011, **48**, pp. 996-1010.
- [82]. **M. P. J. Schöpfer, S. Abe, C. Childs and J. J. Walsh.** The impact of porosity and crack density on the elasticity, strength and friction of cohesive granular materials: Insights from DEM modelling. *International Journal of Rock Mechanics and Mining Sciences*, 2009, **46**, pp. 250-261.

- [83]. **A. Nardin and B. Schrefler.** Numerical simulation of rock behaviour through a discrete model. *International Journal of Solids and Structures*, 2004, **41**, pp. 5945-5965.
- [84]. **X. D. Pan and M. B. Reed.** A coupled distinct element-finite element for large deformation analysis of rock masses. *International Journal of Rock Mechanics & Mining Sciences & Geomechanics Abstracts*, 1991, **28**, pp. 93-99.
- [85]. **E. Oñate and J. Rojek.** Combination of discrete element and finite element methods for dynamic analysis of geomechanics problems. *Computer Methods in Applied Mechanics and Engineering*, 2004, **193**, pp. 3087-3128.
- [86]. **A. Vyazmensky, D. Elmo, D. Stead and J. R. Rance.** Combined finite-discrete element modelling of surface subsidence associated with block caving mining, in *1st Canada-U.S. Rock Mechanics Symposium*, Vancouver, Canada, 2007, pp. 467-475.
- [87]. **A. Vyazmensky, D. Stead, D. Elmo and A. Moss.** Numerical Analysis of Block Caving-Induced Instability in Large Open Pit Slopes: A Finite/Discrete Element Approach. *Rock Mechanics and Rock Engineering*, 2010, **43**, pp. 21-39.
- [88]. **T. D. Styles, J. S. Coggan and R. J. Pine.** Back analysis of the Joss Bay Chalk Cliff Failure using numerical modelling. *Engineering Geology*, 2011, **120**, pp. 81-90.
- [89]. **R. J. Pine, J. S. Coggan, Z. N. Flynn and D. Elmo.** The Development of a new Numerical Modelling Approach for Naturally Fractured Rock Masses. *Rock Mechanics and Rock Engineering*, 2006, **39**, pp. 395-419.
- [90]. **British Standards Institution.** Testing hardened concrete, Part 3: Compressive strength of test specimens, BS EN 12390-3:2009, 2009.
- [91]. **British Standards Institution.** Testing hardened concrete, Part 5: Flexural strength of test specimens, BS EN 12390-5:2009, 2009.
- [92]. **J. Jonak and J. Gajewski.** Identification of ripping tool types with the use of characteristic statistical parameters of time graphs. *Tunnelling and Underground Space Technology*, 2008, **23**, pp. 18-24.

- [93]. **H. J. R. Deketh, M. A. Grima, I. M. Hergarden, M. Giezen and P. N. W. Verhoef.** Towards the prediction of rock excavation machine performance. *Bulletin of Engineering Geology and the Environment*, 1998, **57**, pp.
- [94]. **X. Wei, C. Y. Wang, H. Yuan and Z. H. Xie.** Study on Fracture Mechanism of Rock Cutting. *Key Engineering Materials*, 2003, **250**, pp. 200-208.
- [95]. **S. Ranganath, A. B. Campbell and D. W. Gorkiewicz.** A model to calibrate and predict forces in machining with honed cutting tools or inserts. *International Journal of Machine Tools and Manufacture*, 2007, **47**, pp. 820-840.
- [96]. **S. Yagiz.** Assessment of brittleness using rock strength and density with punch penetration test. *Tunnelling and Underground Space Technology*, 2009, **24**, pp. 66-74.
- [97]. **F. F. Roxborough, P. King and E. J. Pedroncelli.** Tests on the cutting performance of a continuous miner. *International Journal of Rock Mechanics and Mining Sciences & Geomechanics Abstracts*, 1981, **18**, pp. 9-25.
- [98]. **F. F. Roxborough and E. J. Pedroncelli.** Practical evaluation of some coal-cutting theories using a continuous miner. *International Journal of Rock Mechanics and Mining Sciences & Geomechanics Abstracts*, 1983, **20**, pp. 145-156.
- [99]. **J. E. Friant.** Disc cutter technology applied to drill bits. *Natural Gas Conference: Emerging Technologies for the Natural Gas Industry*, 1997, pp.
- [100]. **E. P. Deliac and C. E. Fairhurst.** Theoretical and practical investigations of improved hard rock cutting systems, in *The 29th U.S. Symposium on Rock Mechanics (USRMS)*, Rotterdam, 1988.
- [101]. **Rockfield Software Ltd.** Geomechanical Solutions for Industry. Internet: <http://www.rockfield.co.uk/geomechanical-solutions-for-industry>, [25 April 2013]
- [102]. **Rockfield Software Ltd.** Glass Modelling. Internet: <http://www.rockfield.co.uk/glass-modelling>, [25 April 2013]
- [103]. **Rockfield Software Limited.** ELFEN Explicit Manual, Chap.4 Element Library, Version 4.4, Swansea, UK, August 2009.

[104]. **D. H. Zeuch and J.T.Finger.** Rock Breakage Mechanisms With a PDC Cutter, in *60th Annual Technical Conference and Exhibition of the Society of Petroleum Engineers*, Las Vegas, Nevada, 1985.

APPENDIX A: CALIBRATION RESULTS OF THE TRI-AXIAL DYNAMOMETER

A.1 Application of load on the z-axis: Thrust force calibration (Fp)

Table A.1 Applied load Vs Measured load data when load is applied in the z-axis

Applied load (kN)	Measured load Fs (kN)	Measured load Fv (kN)	Measured load Fp (kN)
0	0.00000	0.00000	0
0.5	0.00075	0.01600	0.55
1	0.00140	0.02963	1.08
1.5	0.01029	0.03904	1.6
2	0.01048	0.05722	2.14
2.5	0.01126	0.06631	2.66
3	0.01256	0.07410	3.2
3.5	0.01340	0.10331	3.74
4	0.01048	0.10558	4.27
4.5	0.04424	0.13122	4.81

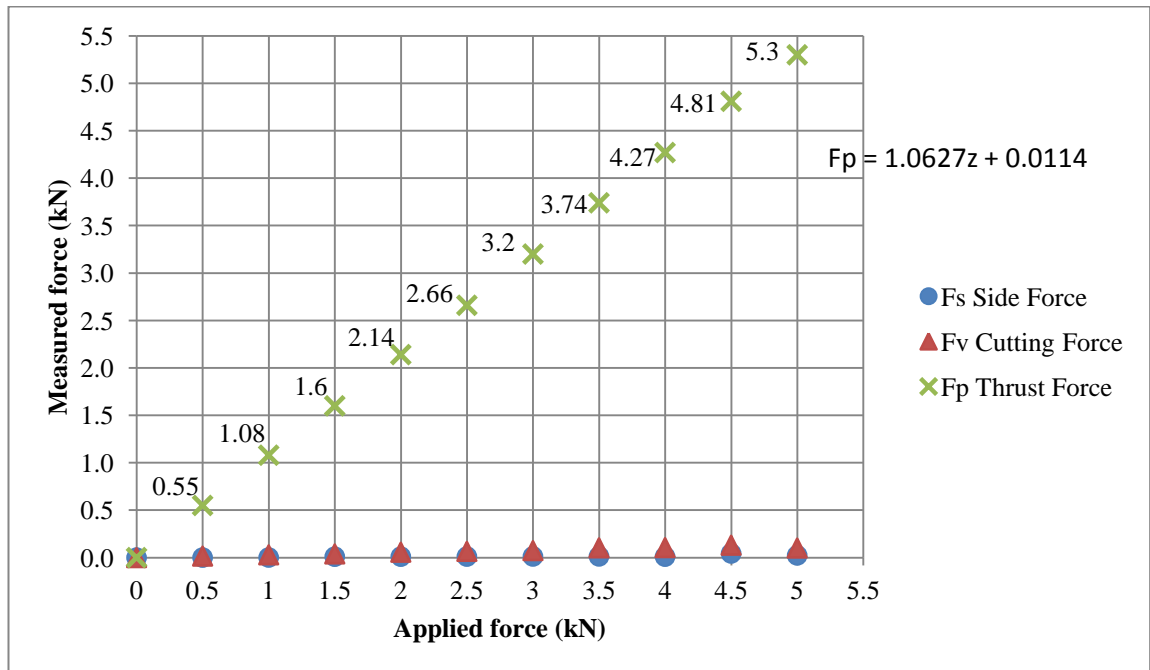


Figure A.1 Calibration curve for loads applied on the z-axis

Table A.1 shows the variation of the measured force along the z-axis; the results are plotted as a graph as shown in Figure A.1. A linear curve is fit to the thrust force component to obtain the equation of best fit. This equation is used to correct the subsequent measurements obtained during linear cutting tests. Similar results are plotted for the application of force on the y and x-axes.

A.2 Application of load on the y-axis: Cutting force calibration (Fv)

Table A.2 Applied load Vs Measured load data when load is applied in the y-axis

Applied load (kN)	Measured load Fs (kN)	Measured load Fv (kN)	Measured load Fp (kN)
0	0.0000	0.00	0.0000
0.5	0.0455	0.51	0.0351
1	0.1120	1.02	0.0705
1.5	0.1770	1.53	0.1160
2	0.2320	2.04	0.1720
2.5	0.2760	2.57	0.2250
3	0.2830	3.06	0.2480
3.5	0.2860	3.59	0.2940
4	0.2390	4.12	0.3530
4.5	0.2270	4.62	0.3840

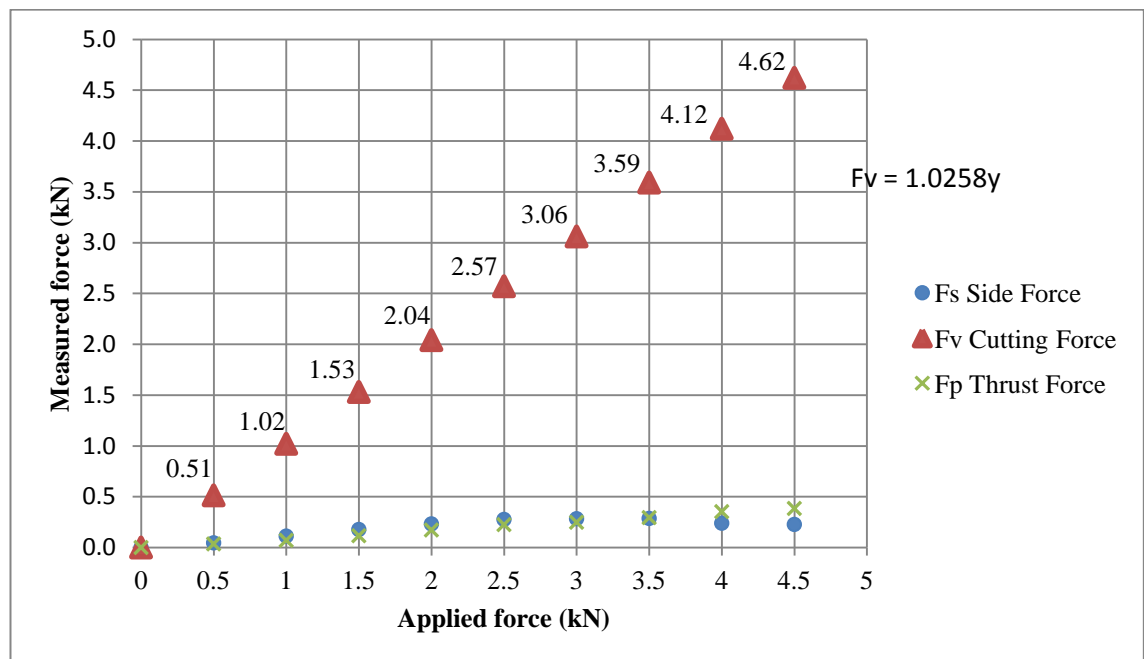


Figure A.2 Calibration curve for loads applied on the y-axis

A.3 Application of load on the x-axis: Side force calibration (Fs)

Table A.3 Applied load Vs Measured load data when load is applied in the x-axis

Applied load (kN)	Measured load Fs (kN)	Measured load Fv (kN)	Measured load Fp (kN)
0	0	0.0000	0.0000
0.5	0.508	0.0762	0.0251
1	1.03	0.1430	0.0952
1.5	1.54	0.2070	0.1330
2	2.06	0.2630	0.1650
2.5	2.59	0.3260	0.2220
3	3.1	0.3680	0.2810
3.5	3.61	0.4090	0.3370
4	4.14	0.4410	0.3670
4.5	4.65	0.4680	0.4230

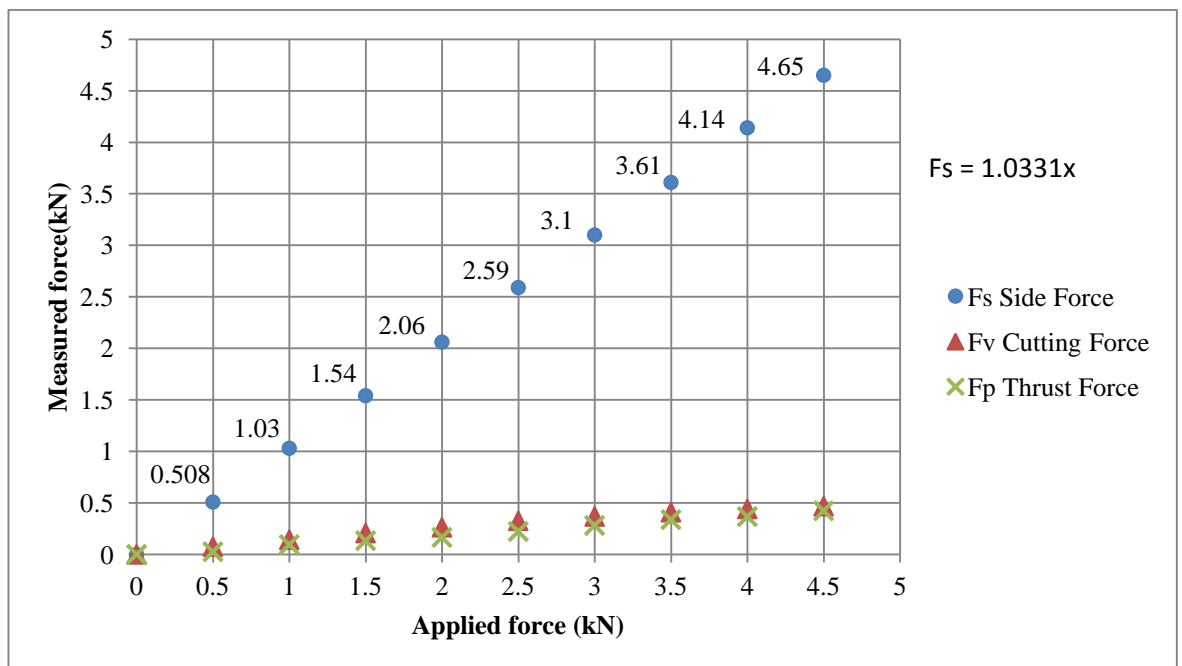
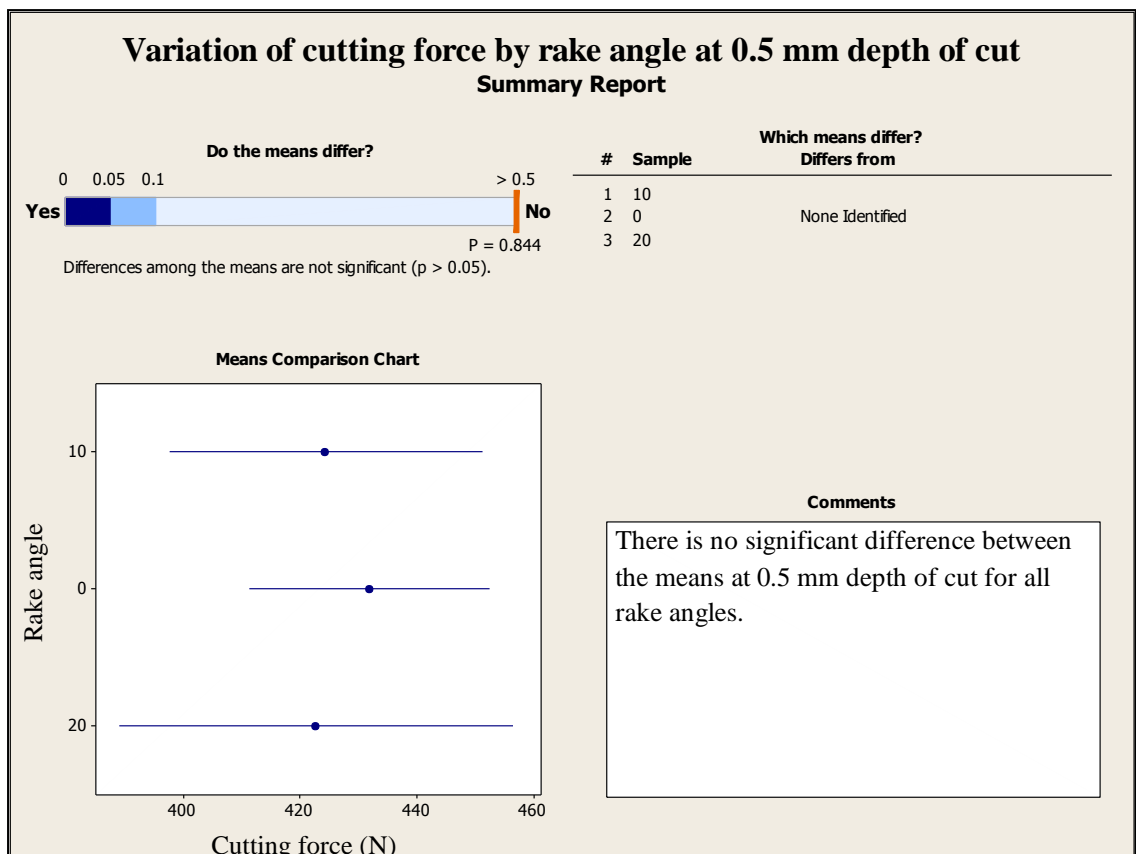


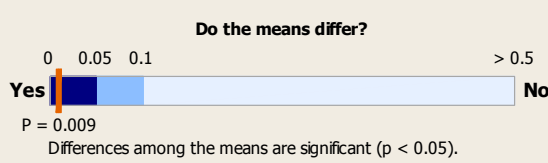
Figure A.3 Calibration curve for loads applied on the x-axis

APPENDIX B: STATISTICAL ANALYSIS OF THE INFLUENCE OF RAKE ANGLE ON THE CUTTING FORCE FOR LOW STRENGTH SAMPLE

Statistical analysis using MINITAB 16 was conducted to find the influence of rake angles on the cutting and thrust force. The means of the cutting force against rake angle is plotted for each depth of cut and a p-value for each show whether there is significant difference between the different means. Summary reports are generated and they contain the p-value, means comparison chart and a table to indicate which rake angle varied with respect to the other.

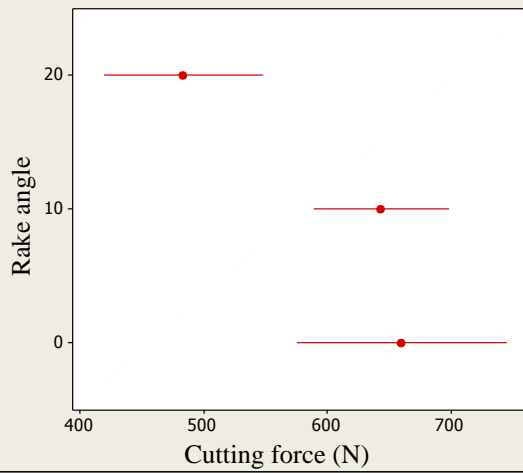


Variation of the cutting force by rake angle for 1.0 mm depth of cut Summary Report



#	Rake angle	Which means differ?	
		Differs from	
1	20	2	3
2	10	1	
3	0	1	

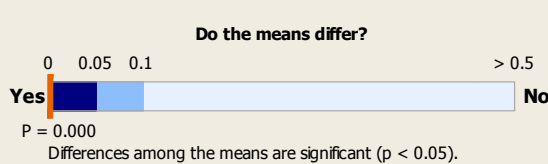
Means Comparison Chart
Red intervals that do not overlap differ.



Comments

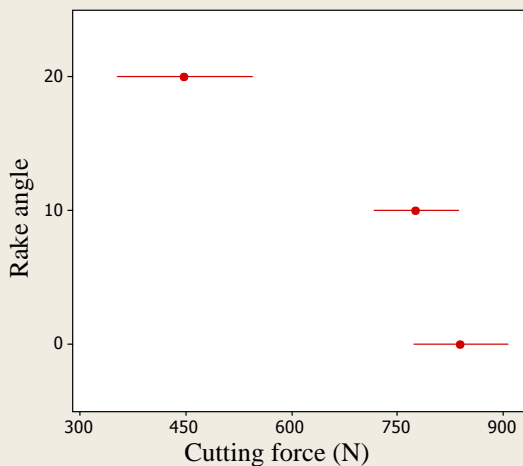
It can be concluded that there are differences among the means at the 0.05 level of significance. Cutting with a 20 rake angle cutting tool produces lower cutting forces than with 0 and 10 degree rake angle cutting tool

Variation of cutting force by rake angle for 1.5 mm depth of cut Summary Report



#	Rake angle	Which means differ?	
		Differs from	
1	20	2	3
2	10	1	
3	0	1	

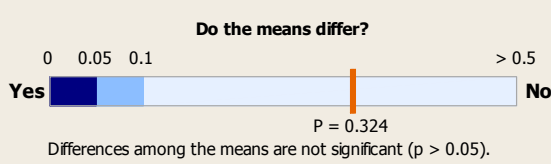
Means Comparison Chart
Red intervals that do not overlap differ.



Comments

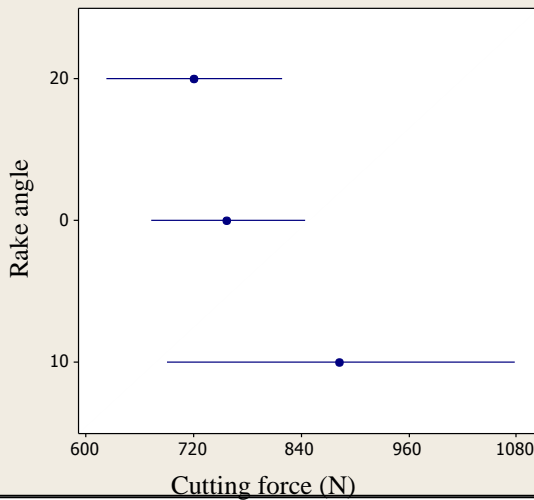
It can be concluded that there are differences among the means at the 0.05 level of significance. 20 rake angle produces lower readings of cutting force as compared to 0 and 10

Variation of cutting force by rake angle for 2 mm depth of cut Summary Report



#	Rake angle	Which means differ? Differs from
1	20	
2	0	None Identified
3	10	

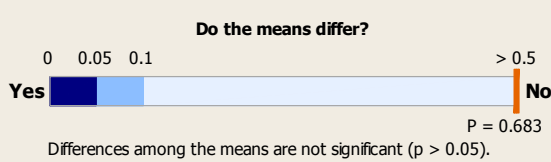
Means Comparison Chart



Comments

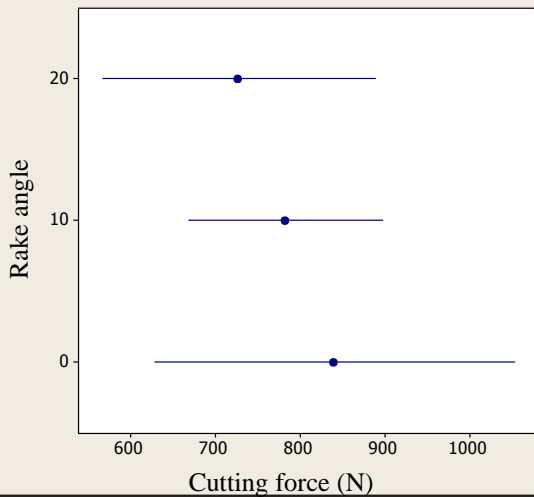
It cannot be concluded that there are differences among the means at the 0.05 level of significance.

Variation of cutting force by rake angle for 2.5 mm depth of cut Summary Report



#	Sample	Which means differ? Differs from
1	20	
2	10	None Identified
3	0	

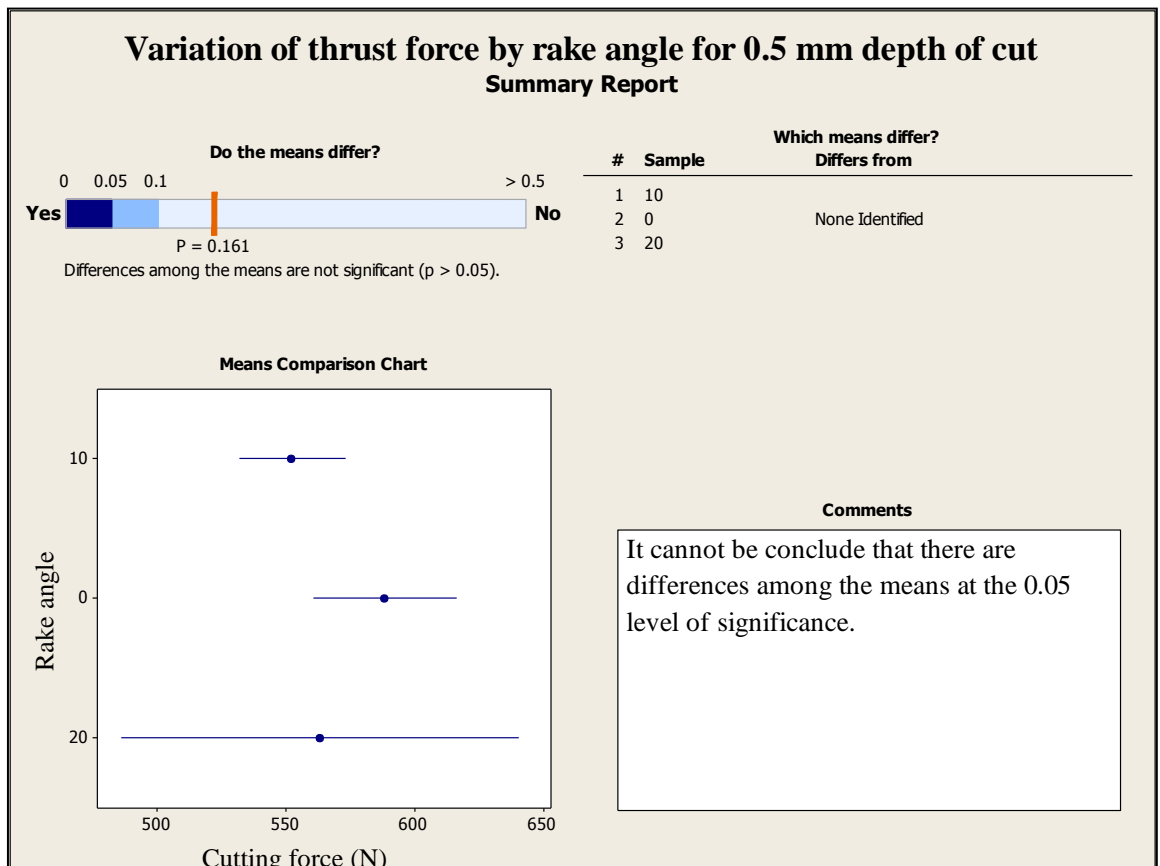
Means Comparison Chart



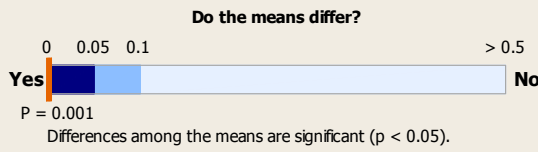
Comments

It cannot be concluded that there are differences among the means at the 0.05 level of significance.

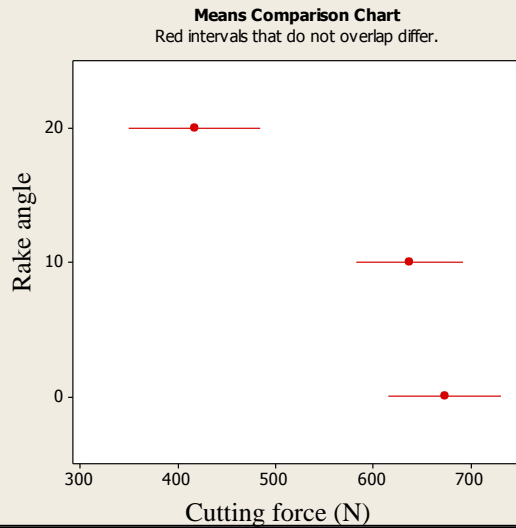
APPENDIX C: STATISTICAL ANALYSIS OF THE INFLUENCE OF RAKE ANGLE ON THE THRUST FORCE FOR LOW STRENGTH SAMPLE



Variation of thrust force by rake angle for 1 mm depth of cut Summary Report



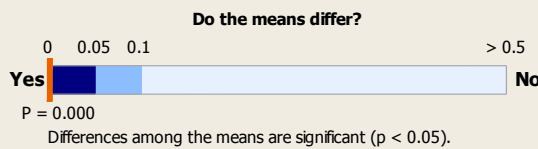
#	Sample	Which means differ? Differs from
1	20	2 3
2	10	1
3	0	1



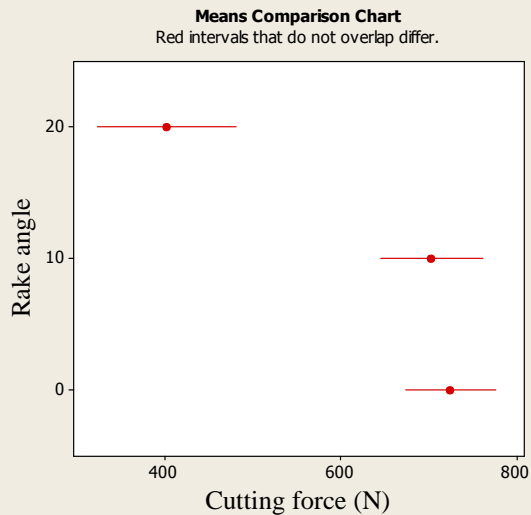
Comments

It can conclude that there are differences among the means at the 0.05 level of significance. Cutting with a 20 rake angle cutting tool produces lower thrust force value as compared to the other two rake angles.

Variation of thrust force by rake angle at 1.5 mm depth of cut Summary Report



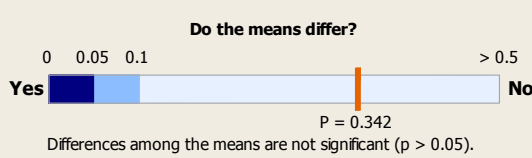
#	Sample	Which means differ? Differs from
1	20	2 3
2	10	1
3	0	1



Comments

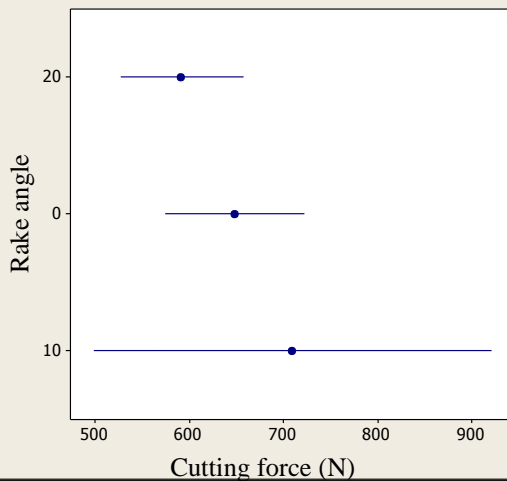
It can conclude that there are differences among the means at the 0.05 level of significance. Cutting with 20 rake angle cutting tool provides lower reading of thrust force

Variation of thrust force by rake angle for 2 mm depth of cut Summary Report



#	Sample	Which means differ? Differs from
1	20	None Identified
2	0	
3	10	

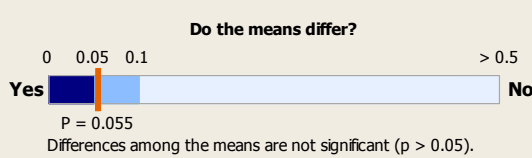
Means Comparison Chart



Comments

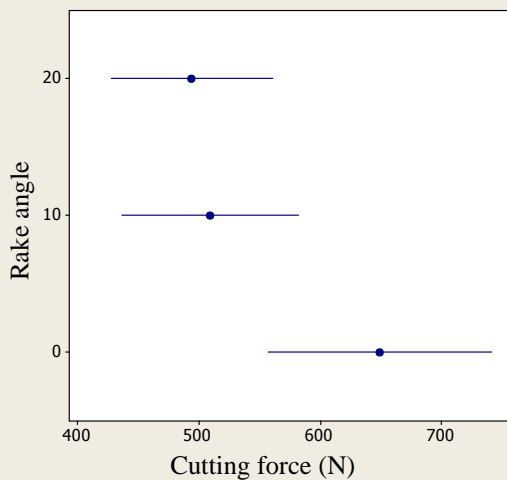
It cannot be concluded that there are differences among the means at the 0.05 level of significance.

Variation of thrust force by rake angle for 2.5 mm depth of cut Summary Report



#	Sample	Which means differ? Differs from
1	20	None Identified
2	10	
3	0	

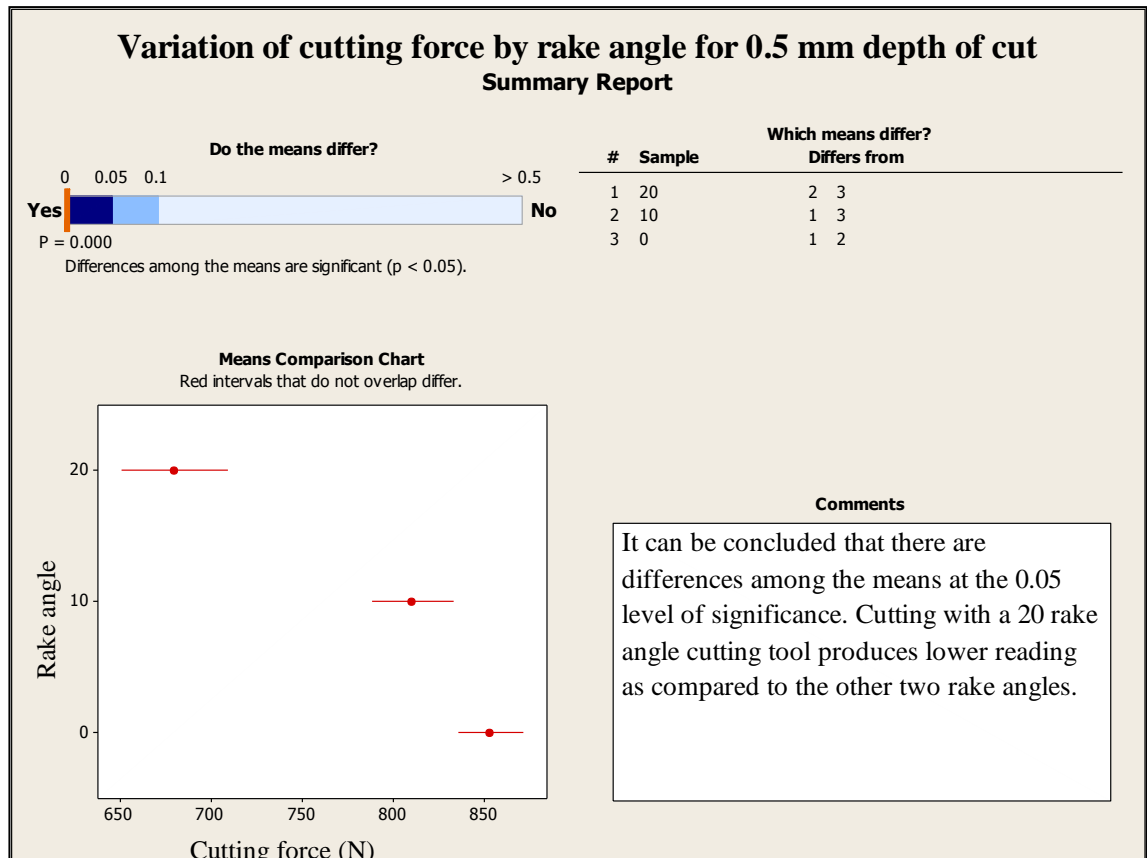
Means Comparison Chart



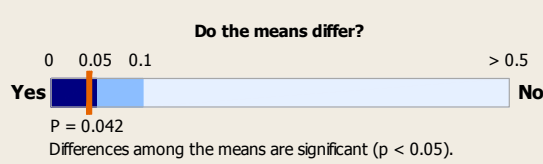
Comments

It cannot be concluded that there are differences among the means at the 0.05 level of significance.

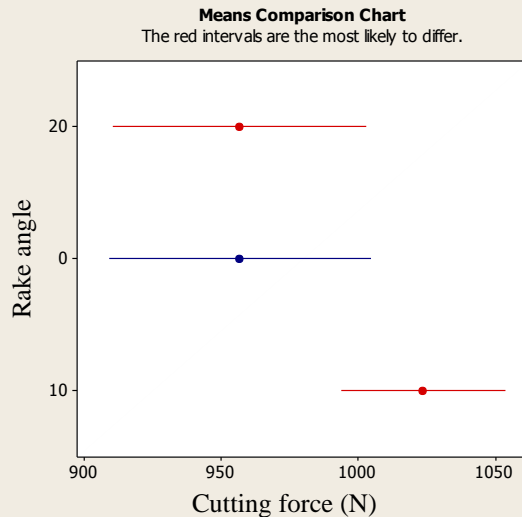
APPENDIX D: STATISTICAL ANALYSIS OF THE INFLUENCE OF RAKE ANGLE ON THE CUTTING FORCE FOR HIGH STRENGTH SAMPLE



Variation of cutting force by rake angle for 1 mm depth of cut Summary Report



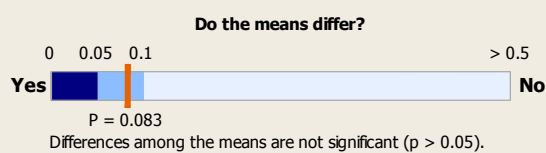
#	Sample	Which means differ? Differs from
1	20	3
2	0	
3	10	1



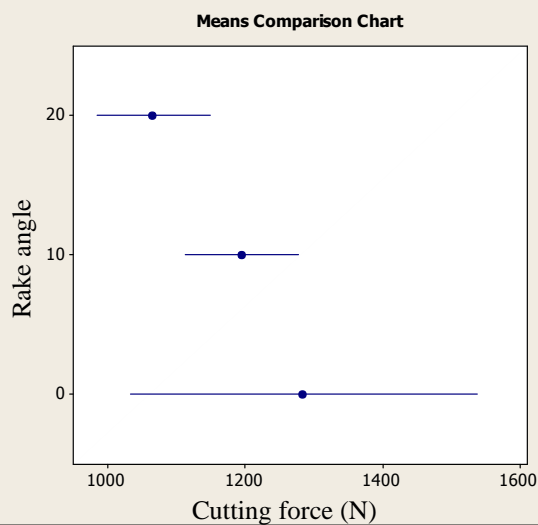
Comments

It can be concluded that there are differences among the means at the 0.05 level of significance. Cutting with 20 and 0 rake angle cutting tool provides lower reading of cutting force as compared with the 10 cutting tool

Variation of cutting force by rake angle for 1.5 mm depth of cut Summary Report



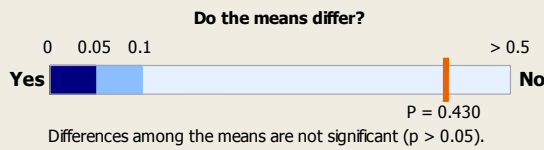
#	Sample	Which means differ? Differs from
1	20	
2	10	None Identified
3	0	



Comments

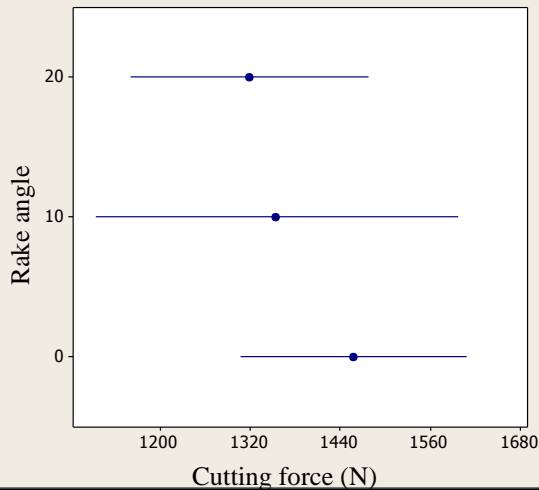
It cannot be concluded that there are differences among the means at the 0.05 level of significance.

Variation of cutting force by rake angle for 2 mm depth of cut Summary Report



#	Sample	Which means differ? Differs from
1	20	
2	10	None Identified
3	0	

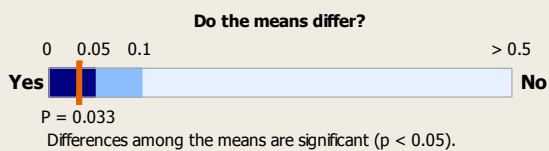
Means Comparison Chart



Comments

It cannot be concluded that there are differences among the means at the 0.05 level of significance.

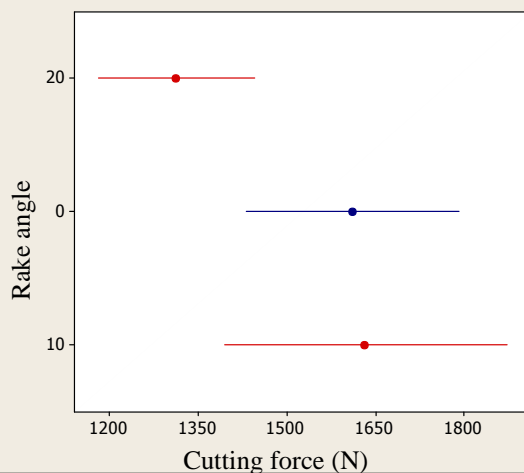
Variation of cutting force by rake angle for 2.5 mm depth of cut Summary Report



#	Sample	Which means differ? Differs from
1	20	3
2	0	
3	10	1

Means Comparison Chart

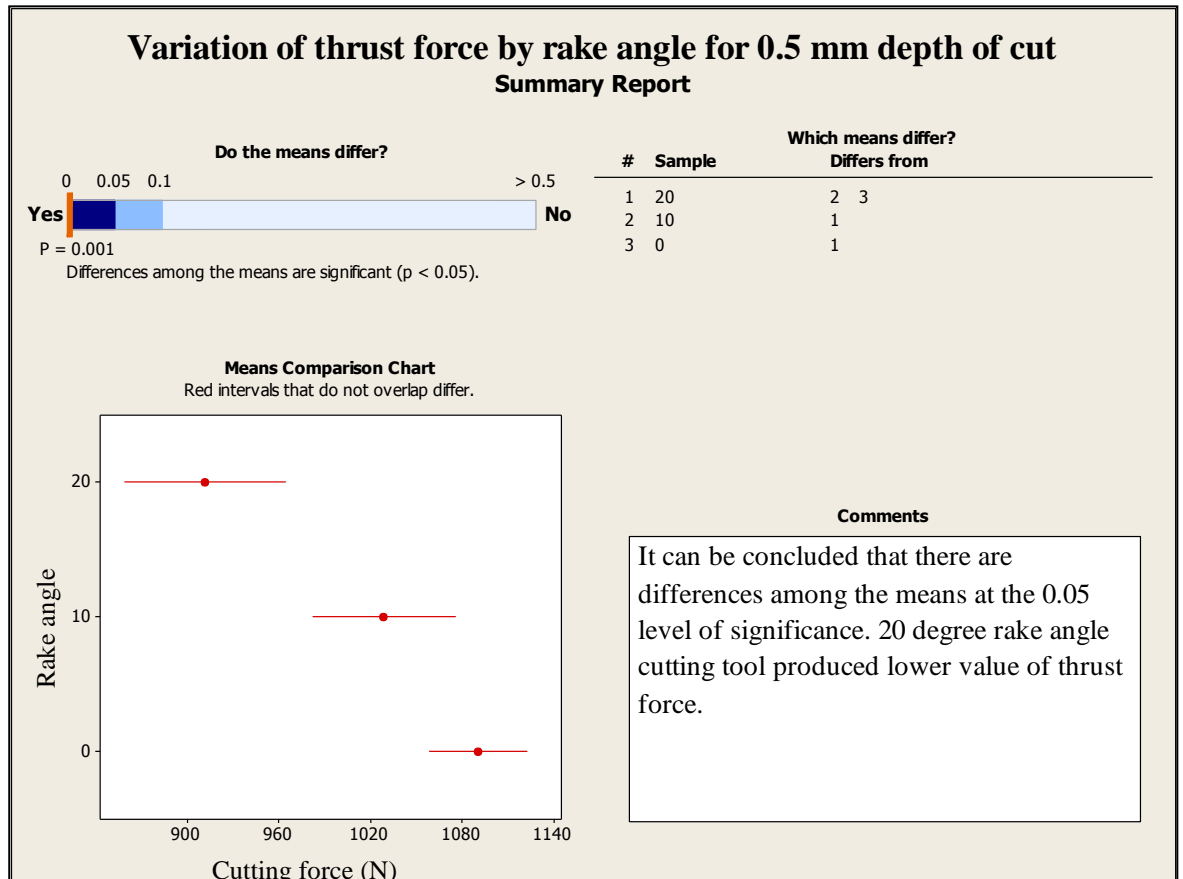
The red intervals are the most likely to differ.



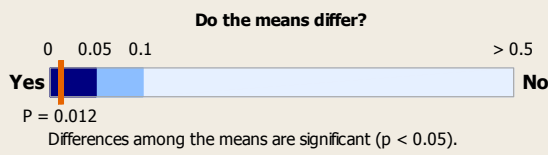
Comments

20 degree rake angle cutting tool produces lower reading of cutting force

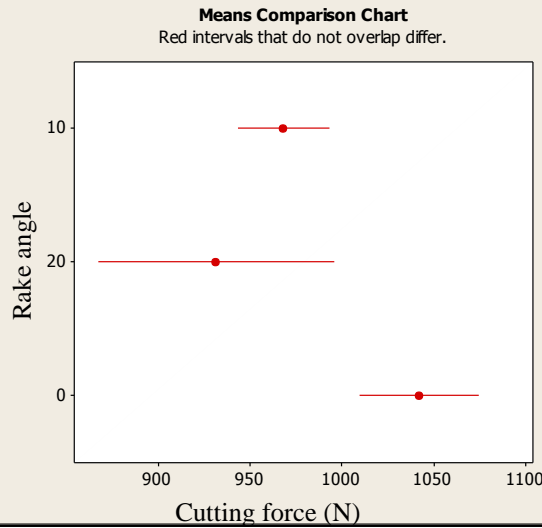
APPENDIX E: STATISTICAL ANALYSIS OF THE INFLUENCE OF RAKE ANGLE ON THE THRUST FORCE FOR HIGH STRENGTH SAMPLE



Variation of thrust force by rake angle for 1 mm depth of cut Summary Report



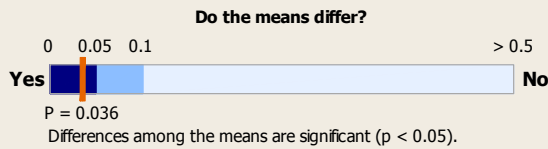
#	Sample	Which means differ?	
		Differs from	
1	10	3	
2	20	3	
3	0	1	2



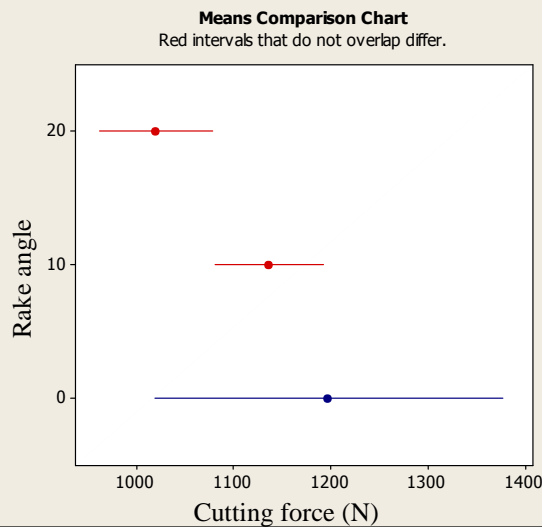
Comments

It can be concluded that there are differences among the means at the 0.05 level of significance. 20 rake angle produced lower values of thrust force

Variation of thrust force by rake angle for 1.5 mm depth of cut Summary Report



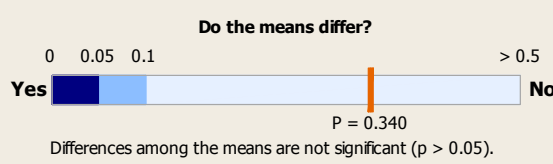
#	Sample	Which means differ?	
		Differs from	
1	20	2	
2	10	1	
3	0		



Comments

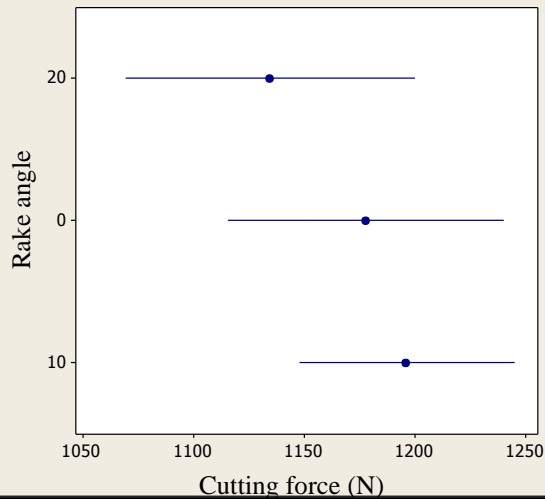
20 degree rake angle has comparatively lower reading of thrust force than that produced by 0 and 10 rake angle tools.

Variation of thrust force by rake angle for 2 mm depth of cut Summary Report



#	Sample	Which means differ? Differs from
1	20	
2	0	None Identified
3	10	

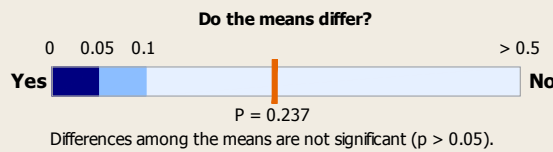
Means Comparison Chart



Comments

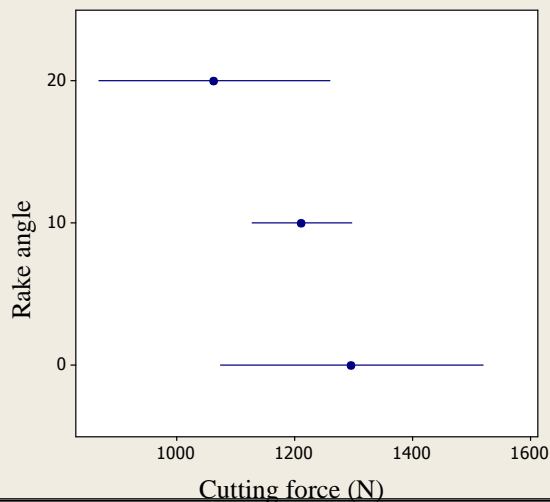
There are no significant differences in the means of the cutting forces.

Variation of thrust force by rake angle for 2.5 mm depth of cut Summary Report



#	Sample	Which means differ? Differs from
1	20	
2	10	None Identified
3	0	

Means Comparison Chart



Comments

No differences in means were found to be significant

APPENDIX F: CHARACTERISTICS OF CHIPS

A. CHARACTERISTICS OF CHIPS FORMED WHILE CUTTING A LOW STRENGTH SAMPLE WITH 0° RAKE ANGLE CUTTING TOOL



Figure F.1 DEPTH OF CUT: 0.5 mm

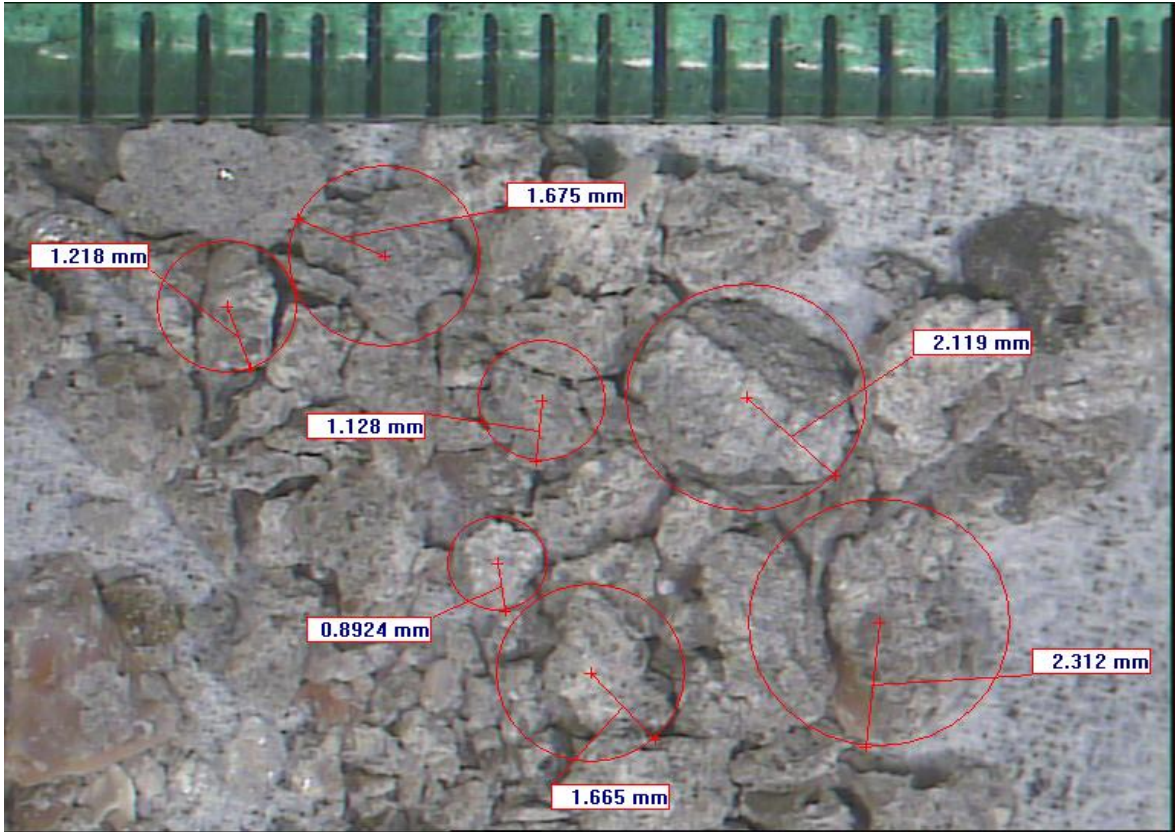


Figure F.2 DEPTH OF CUT: 1mm



Figure F.3 DEPTH OF CUT : 1.5 mm

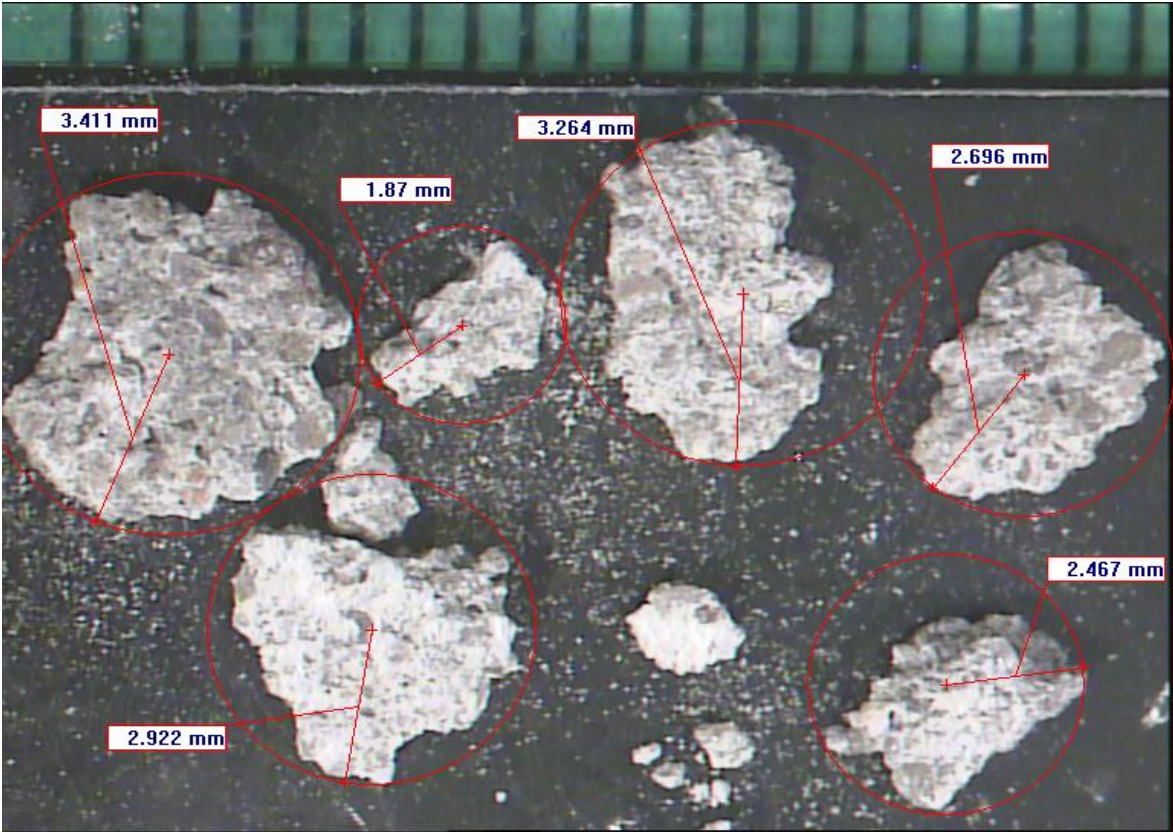


Figure F.4 DEPTH OF CUT: 2mm

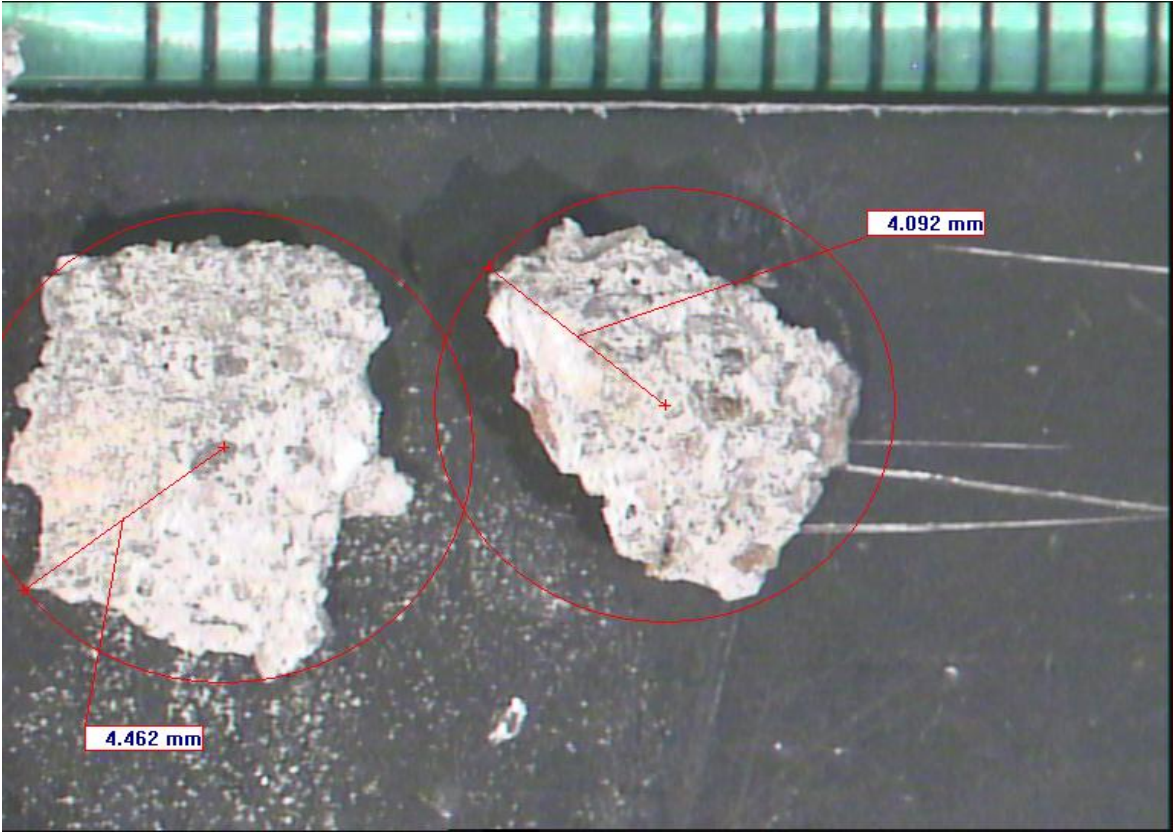


Figure F.5 DEPTH OF CUT : 2.5 mm

B. CHARACTERISTICS OF CHIPS FORMED WHILE CUTTING A LOW STRENGTH SAMPLE WITH 10° RAKE ANGLE CUTTING TOOL

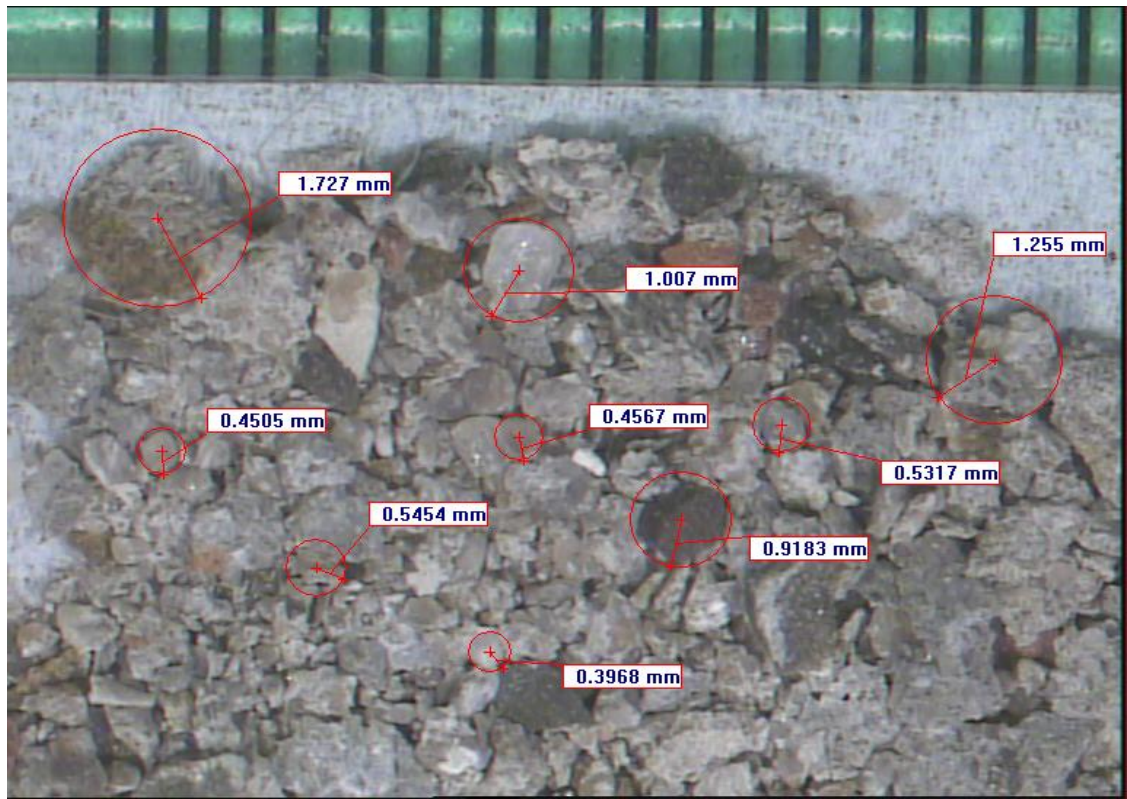


Figure F.6 DEPTH OF CUT : 0.5 mm



Figure F.7 DEPTH OF CUT : 1 mm

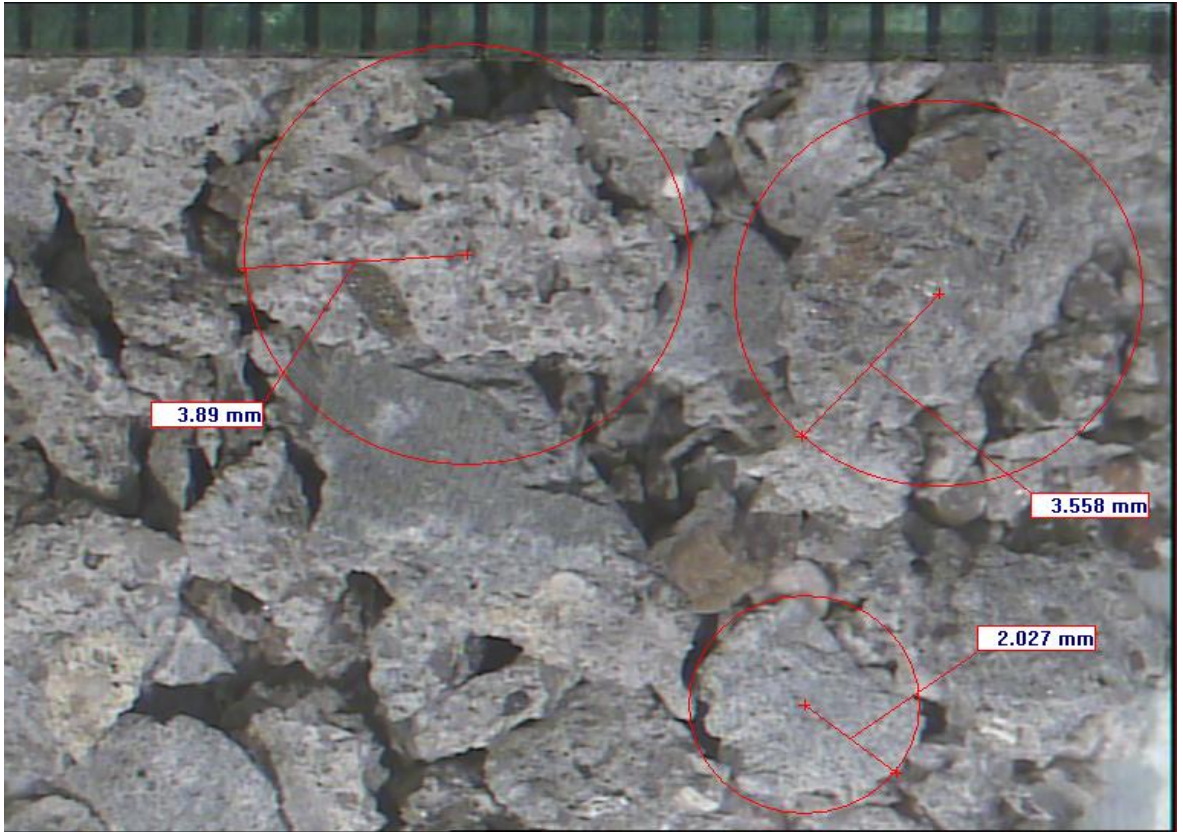


Figure F.8 DEPTH OF CUT : 1.5 mm

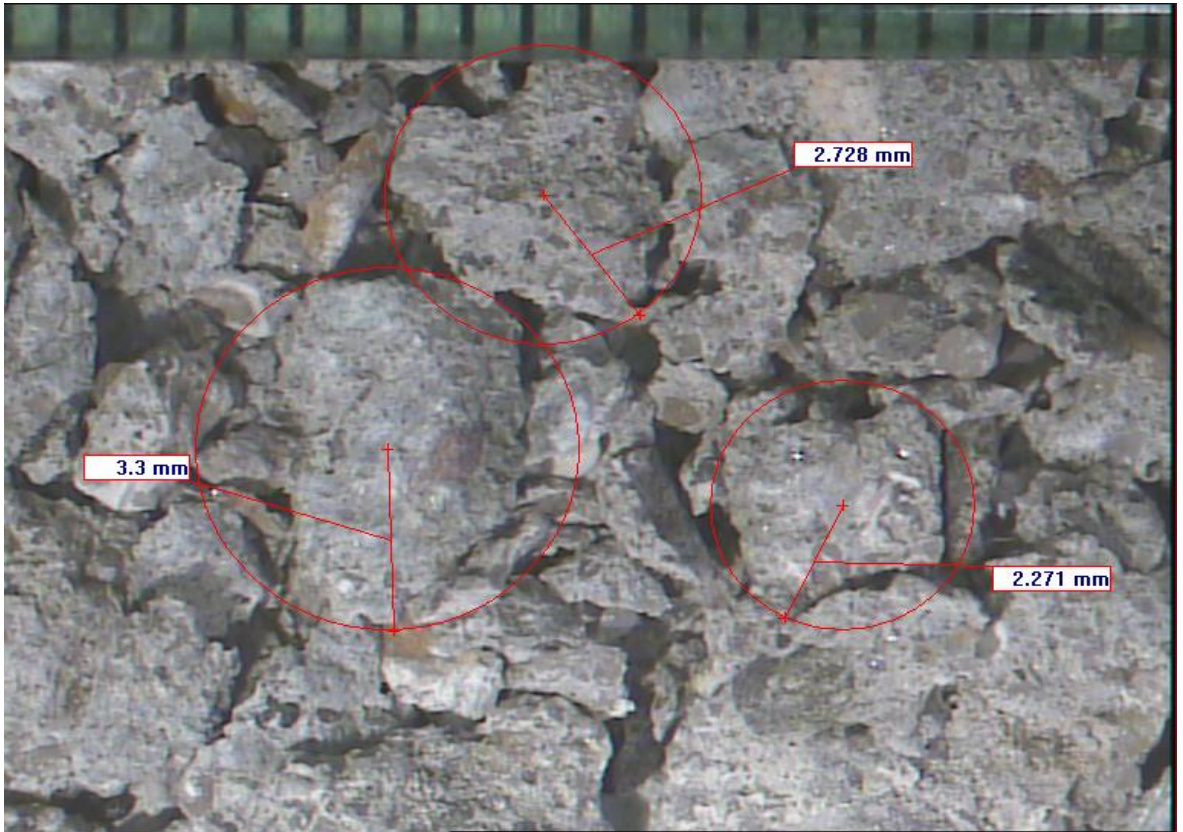


Figure F.9 DEPTH OF CUT: 2 mm



Figure F.10 DEPTH OF CUT: 2.5 mm

C. CHARACTERISTICS OF CHIPS FORMED WHILE CUTTING A LOW STRENGTH SAMPLE WITH 20° RAKE ANGLE CUTTING TOOL



Figure F.11 DEPTH OF CUT: 0.5 mm



Figure F.12 DEPTH OF CUT: 1 mm



Figure F.13 DEPTH OF CUT: 1.5 mm



Figure F.14 DEPTH OF CUT: 2 mm

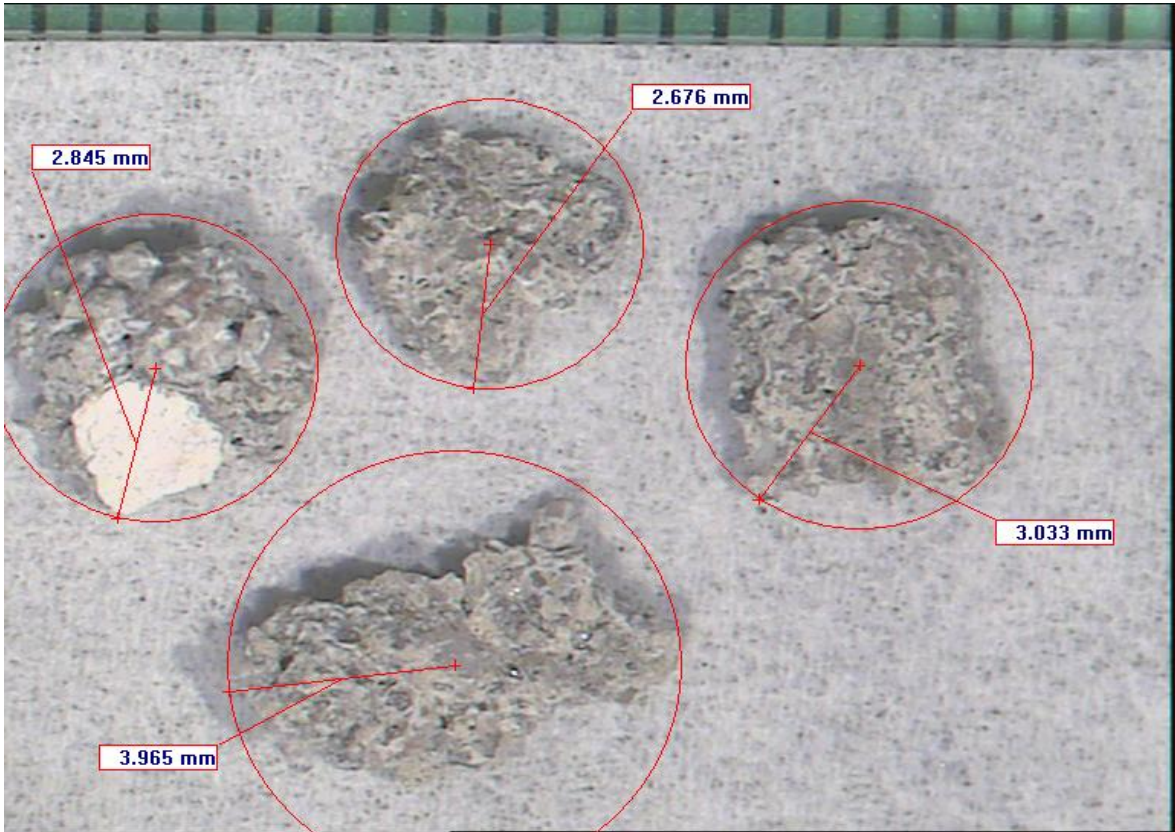


Figure F.15 DEPTH OF CUT : 2.5 mm

D. CHARACTERISTICS OF CHIPS FORMED WHILE CUTTING A HIGH STRENGTH SAMPLE WITH 0° RAKE ANGLE CUTTING TOOL

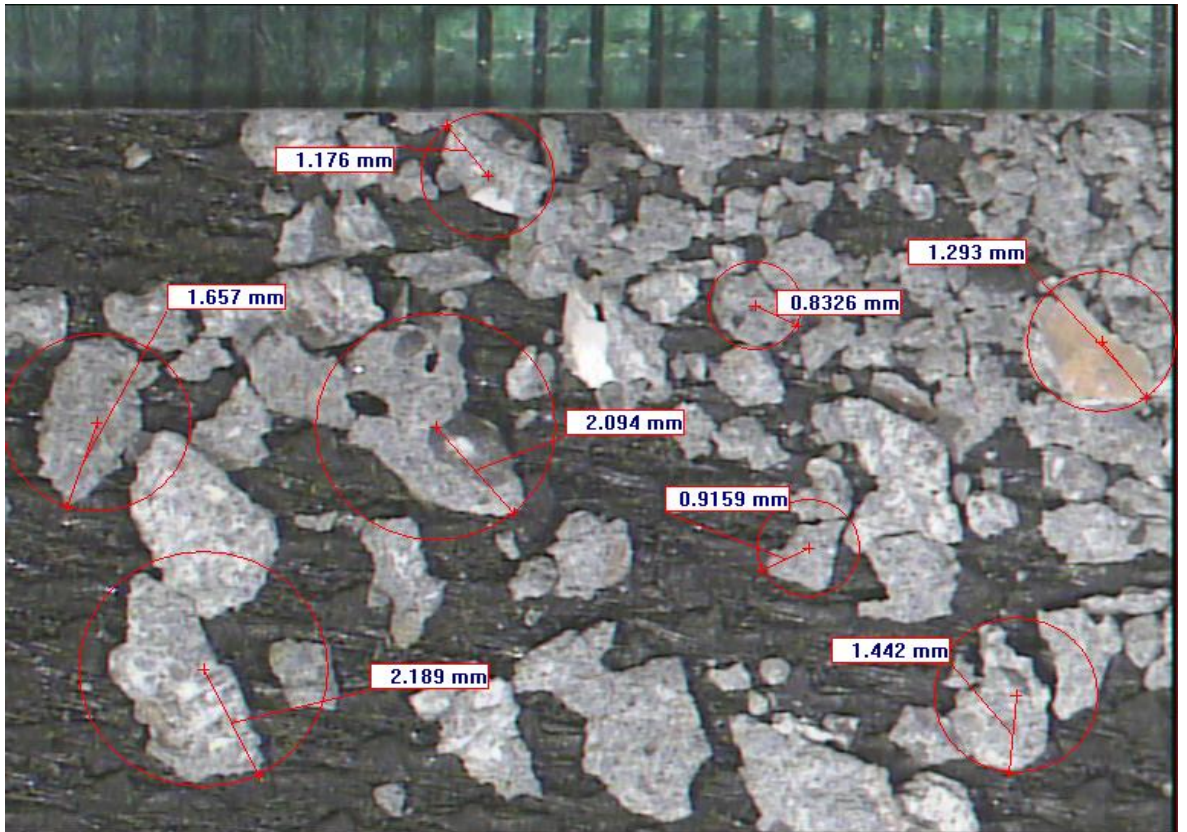


Figure F.16 DEPTH OF CUT: 0.5mm

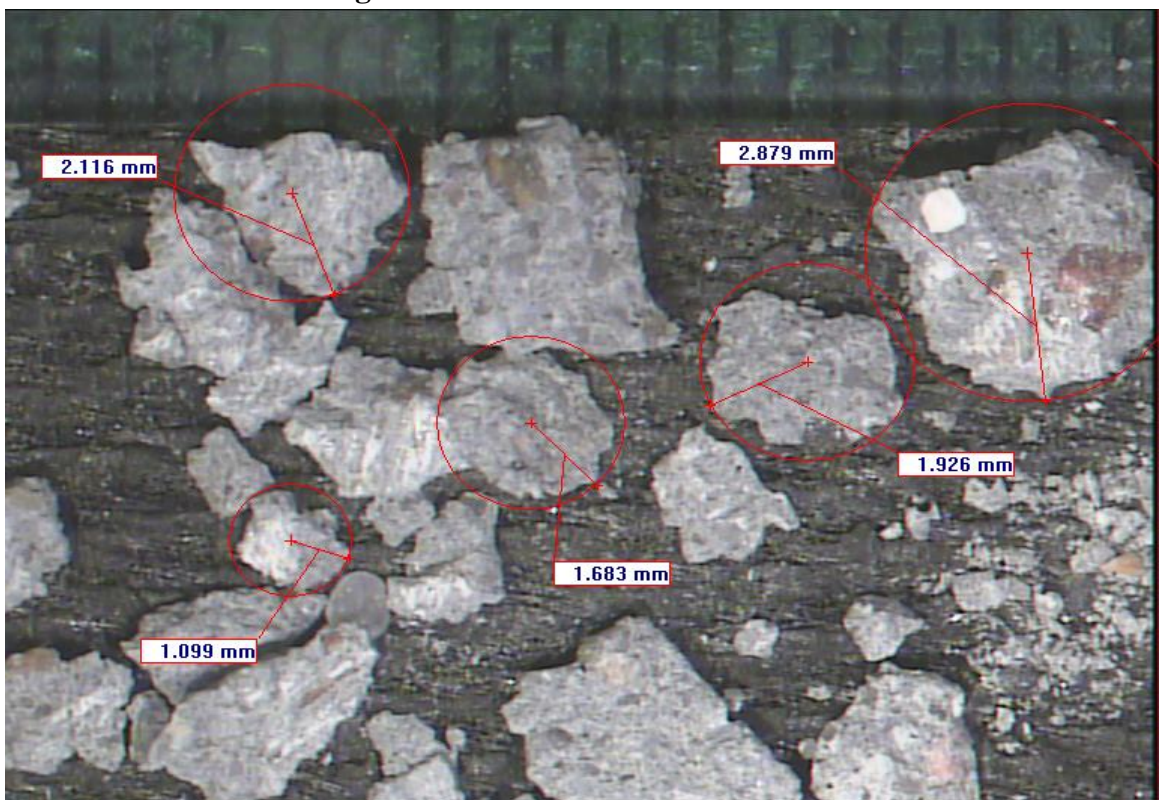


Figure F.17 DEPTH OF CUT : 1 mm

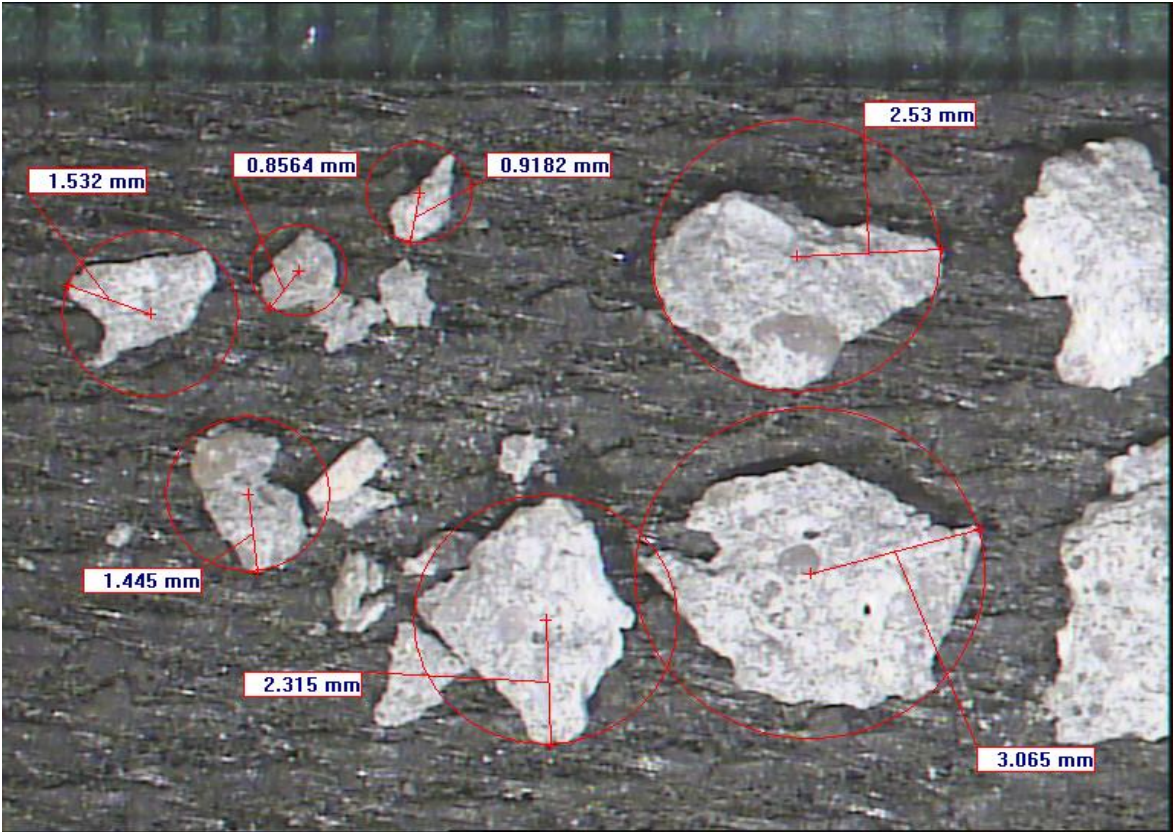


Figure F.18 DEPTH OF CUT: 1.5 mm

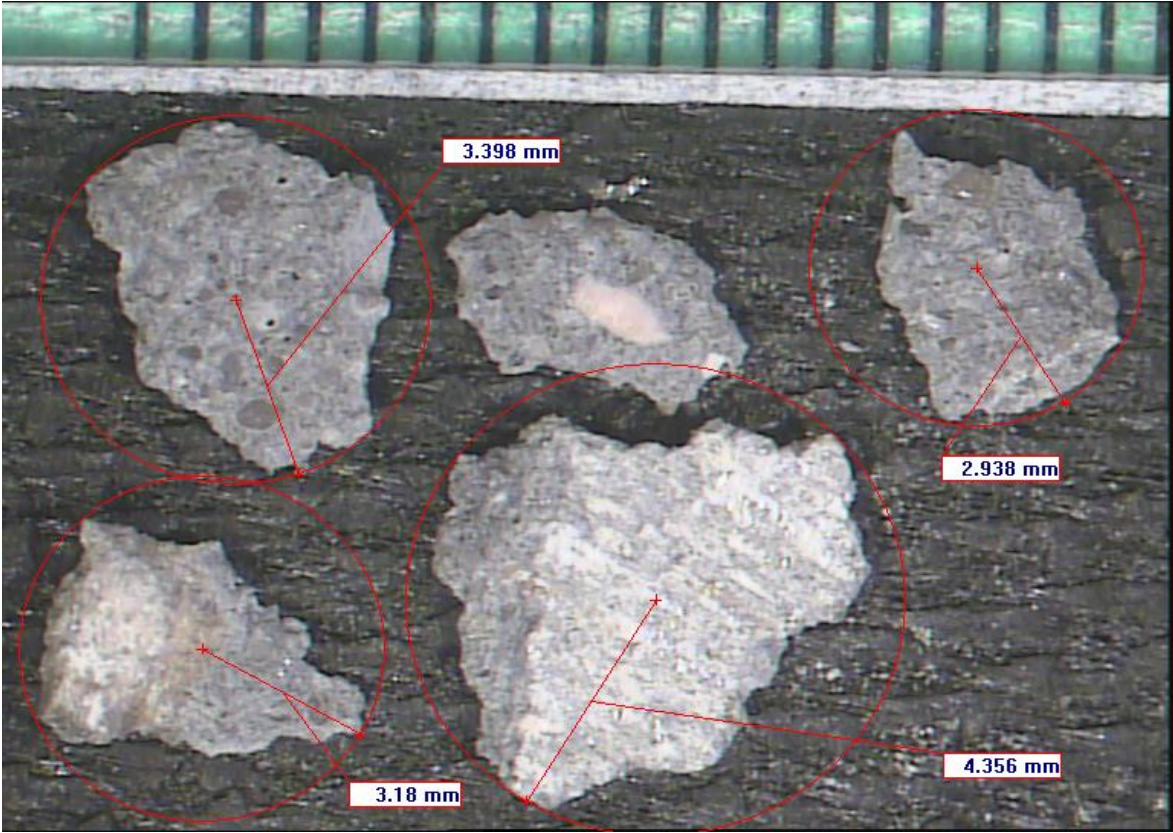


Figure F.19 DEPTH OF CUT : 2 mm

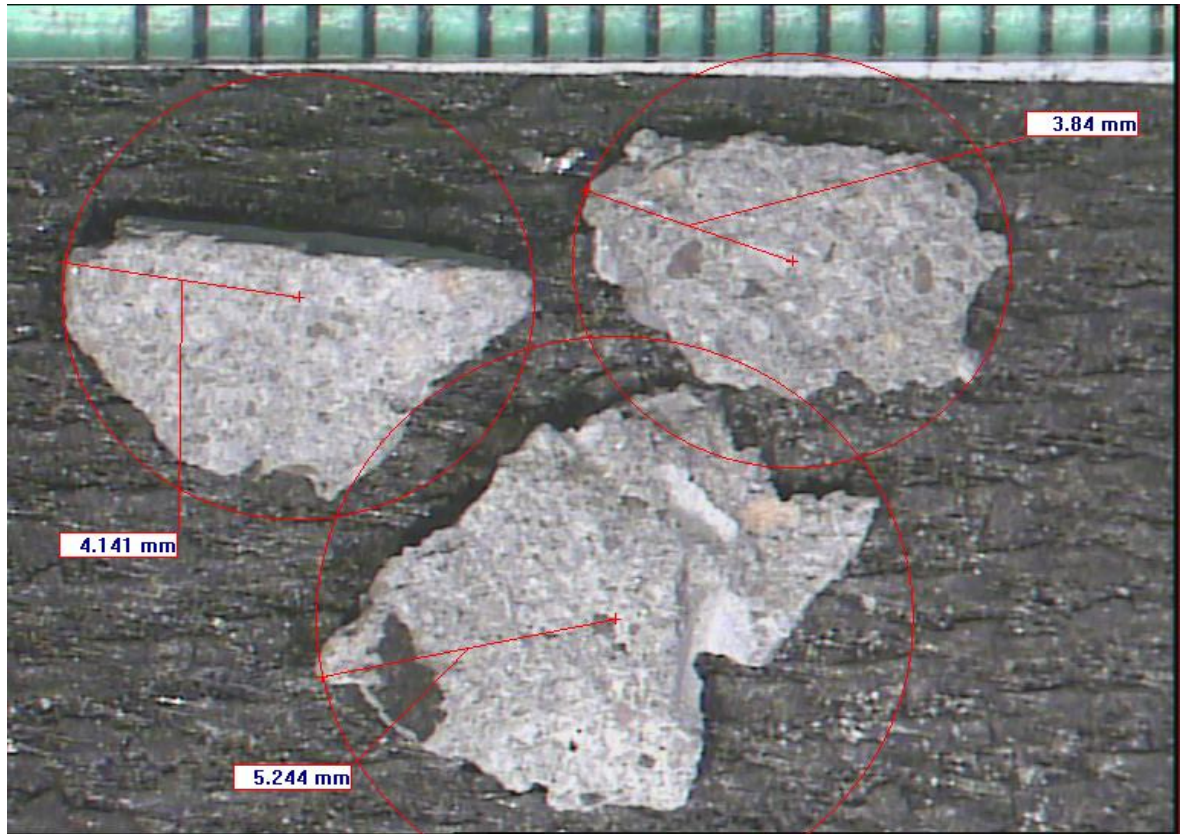


Figure F.20 DEPTH OF CUT: 2.5 mm

E. CHARACTERISTICS OF CHIPS FORMED WHILE CUTTING A HIGH STRENGTH SAMPLE WITH 10° RAKE ANGLE CUTTING TOOL

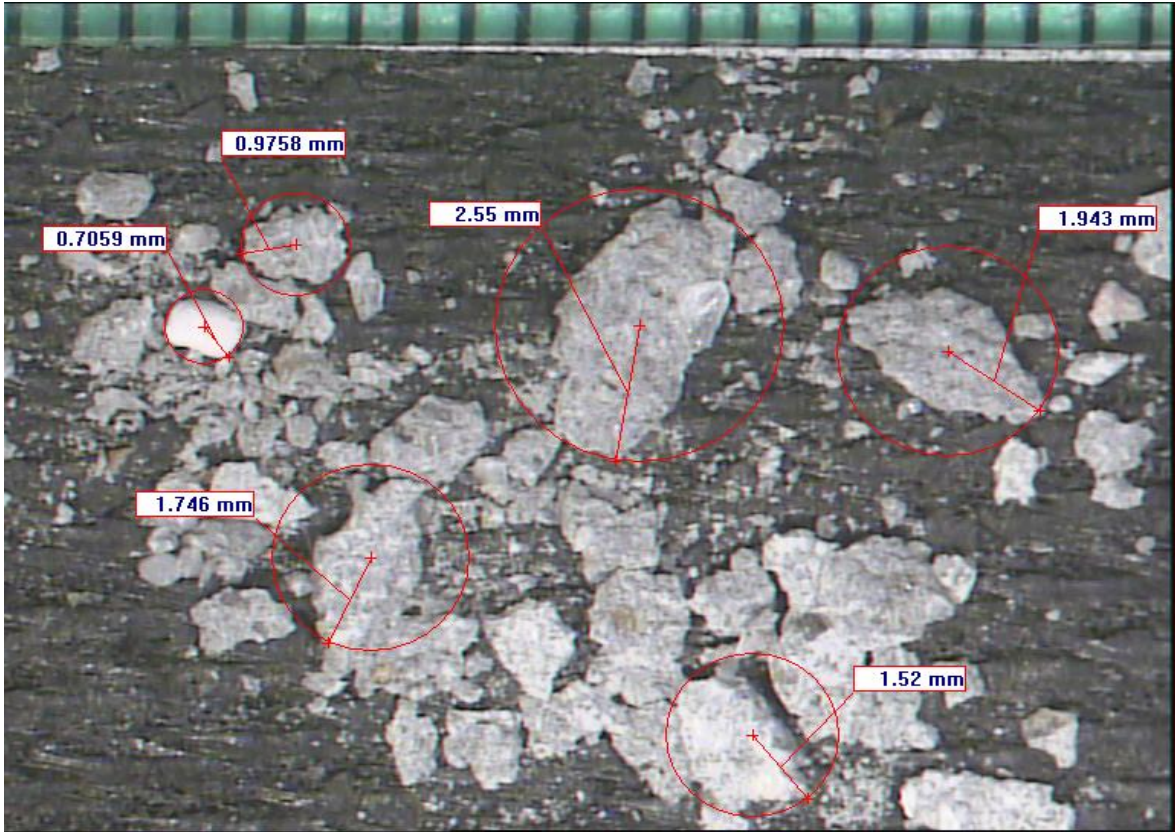


Figure F.21 DEPTH OF CUT: 0.5 mm

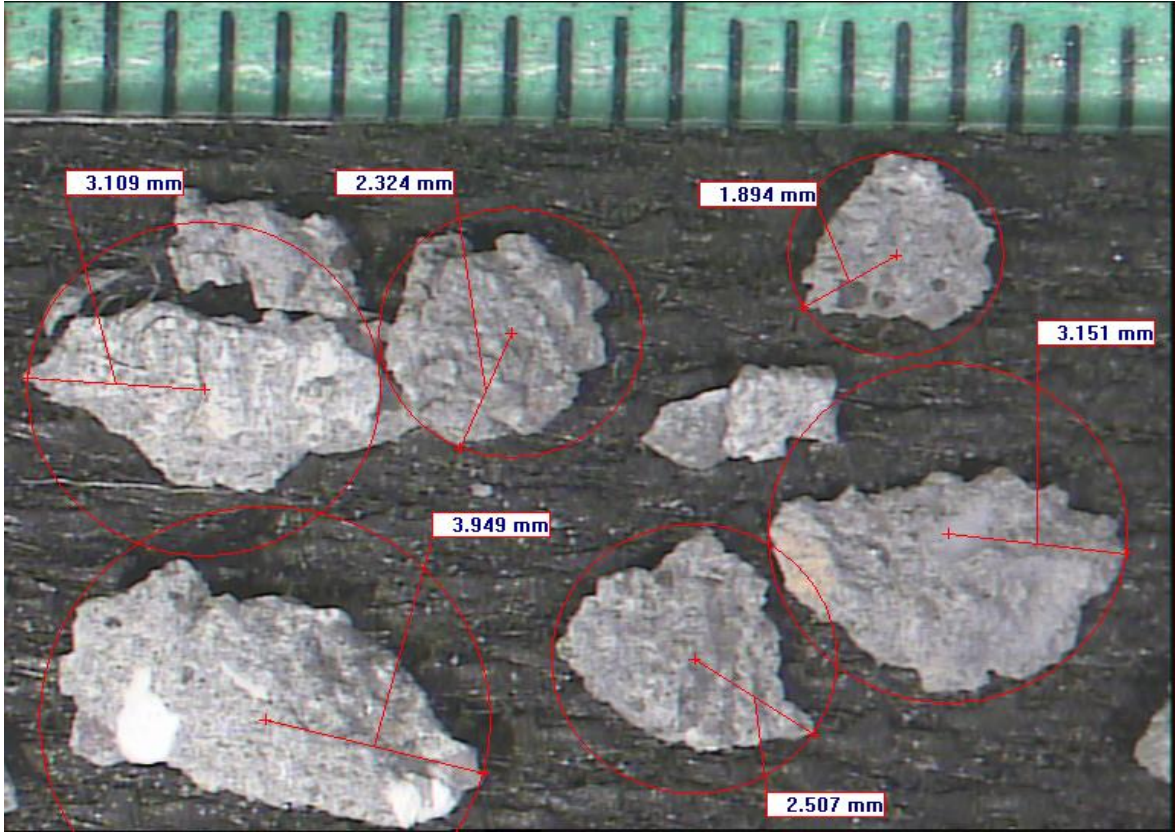


Figure F.22 DEPTH OF CUT: 1mm

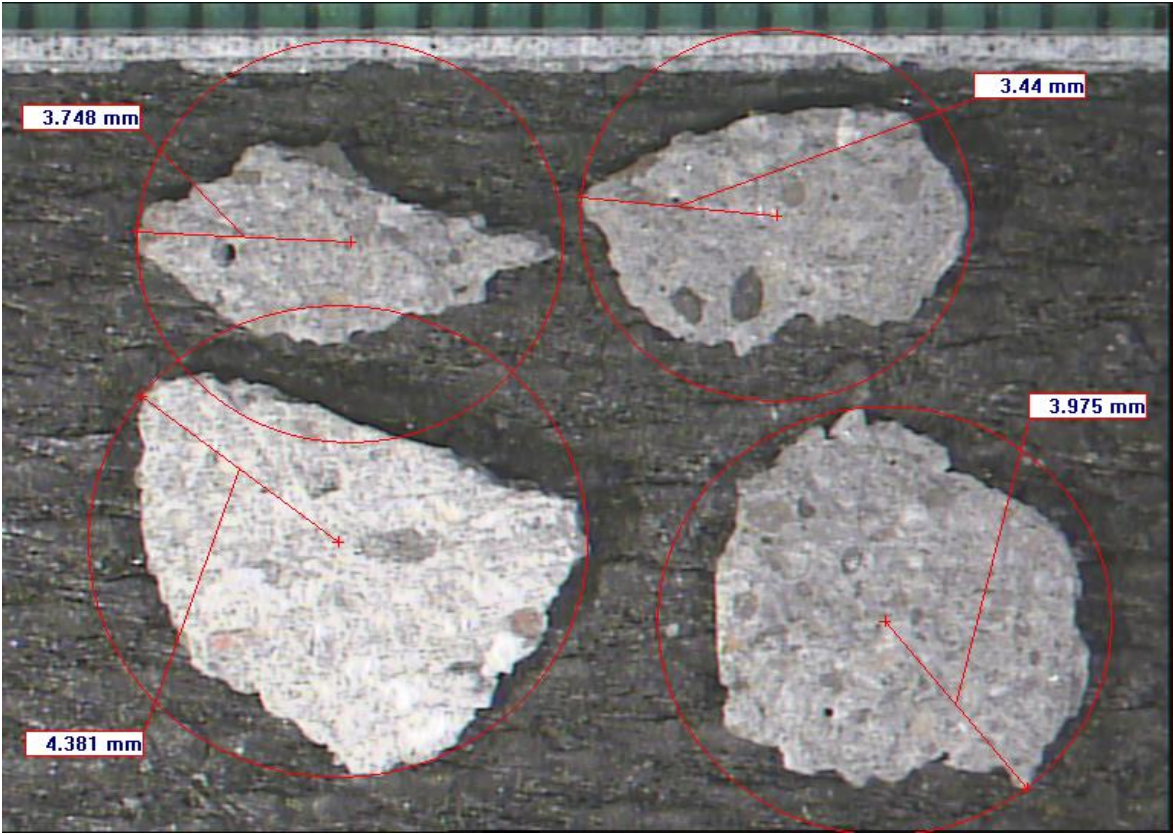


Figure F.23 DEPTH OF CUT: 1.5 mm

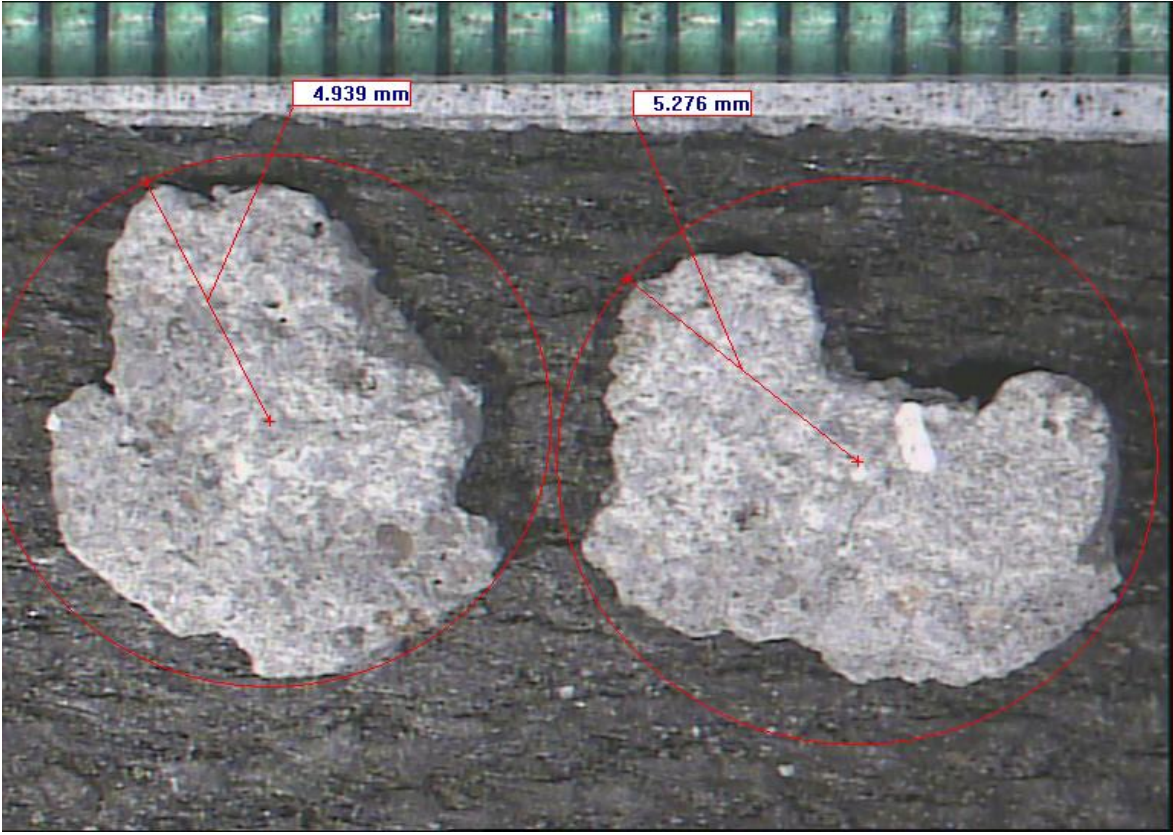


Figure F.24 DEPTH OF CUT: 2 mm

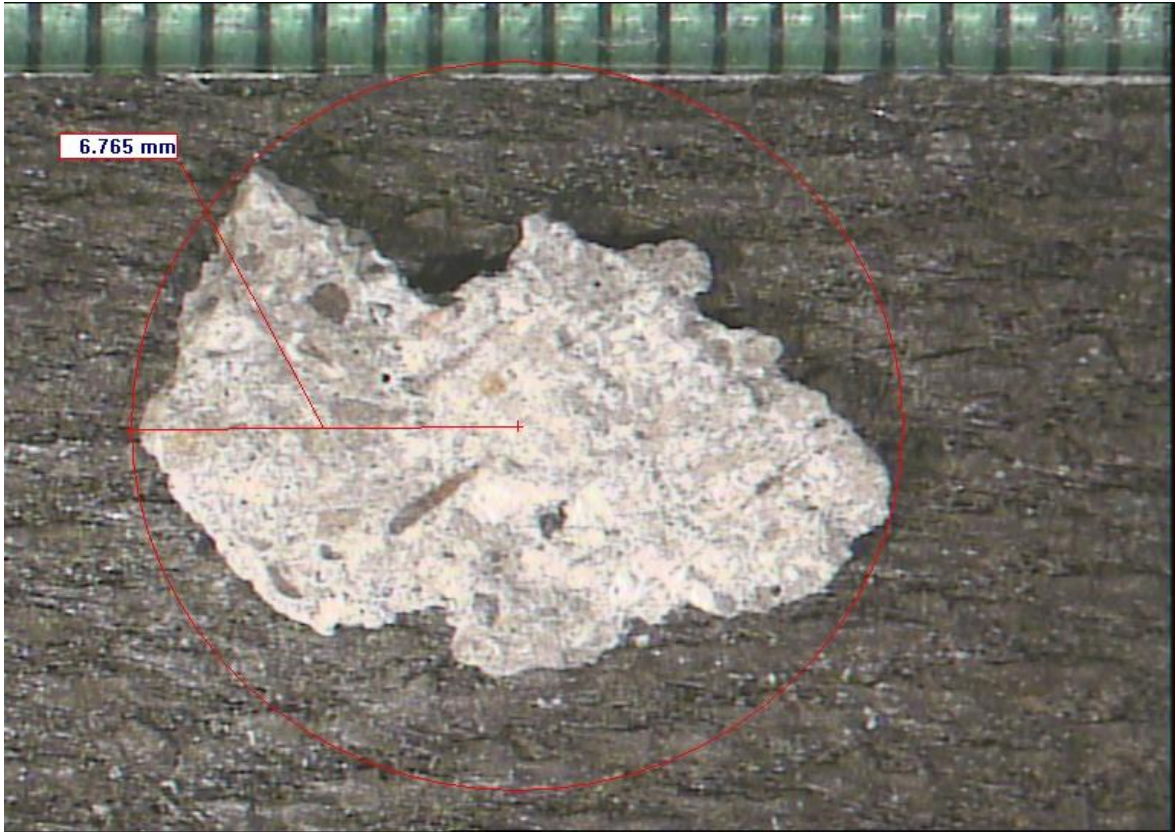


Figure F.25 DEPTH OF CUT: 2.5 mm

F. CHARACTERISTICS OF CHIPS FORMED WHILE CUTTING A HIGH STRENGTH SAMPLE WITH 20° RAKE ANGLE CUTTING TOOL

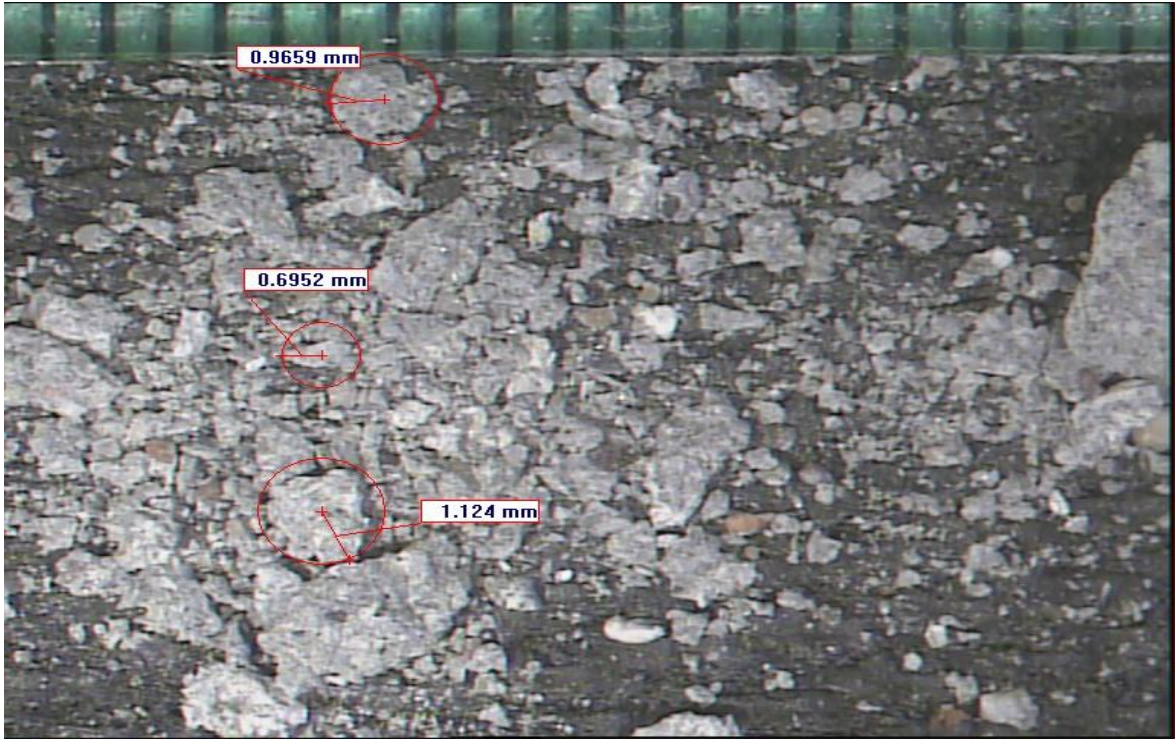


Figure F.26 DEPTH OF CUT: 0.5 mm

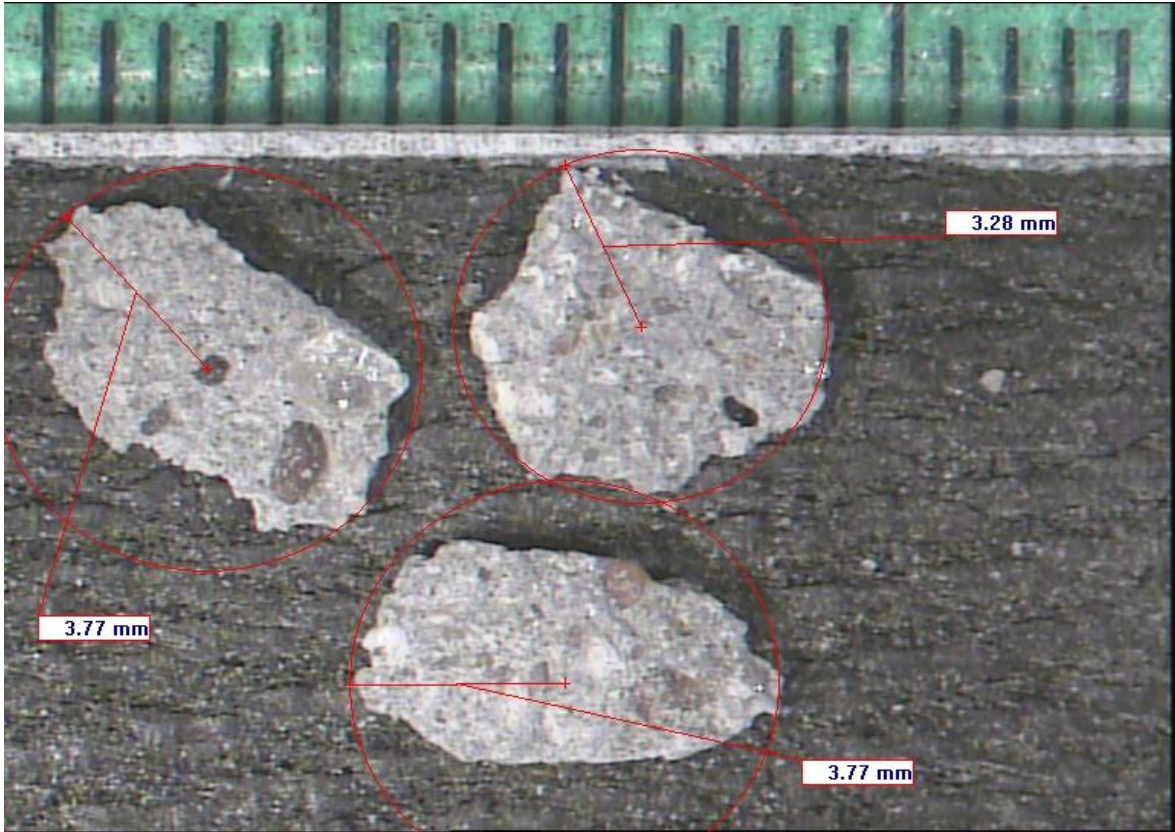


Figure F.27 DEPTH OF CUT: 1 mm

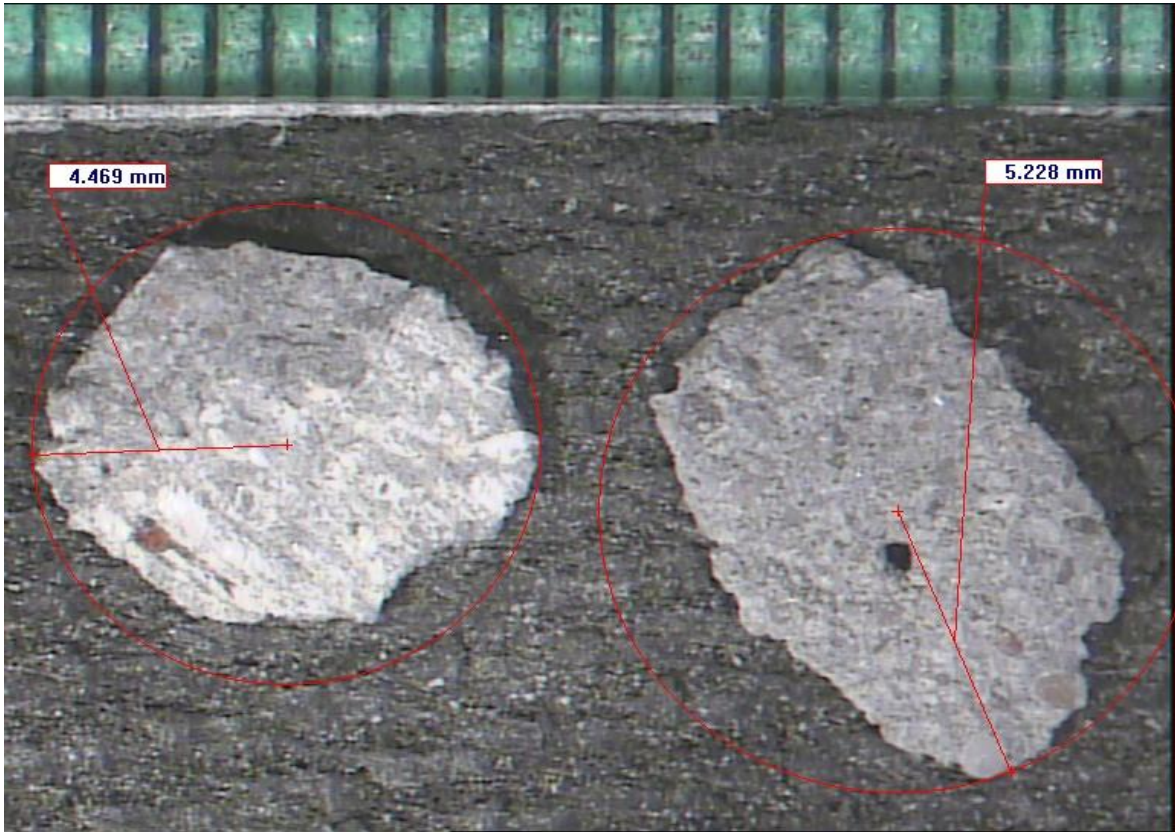


Figure F.28 DEPTH OF CUT: 1.5 mm



Figure F.29 DEPTH OF CUT: 2 mm

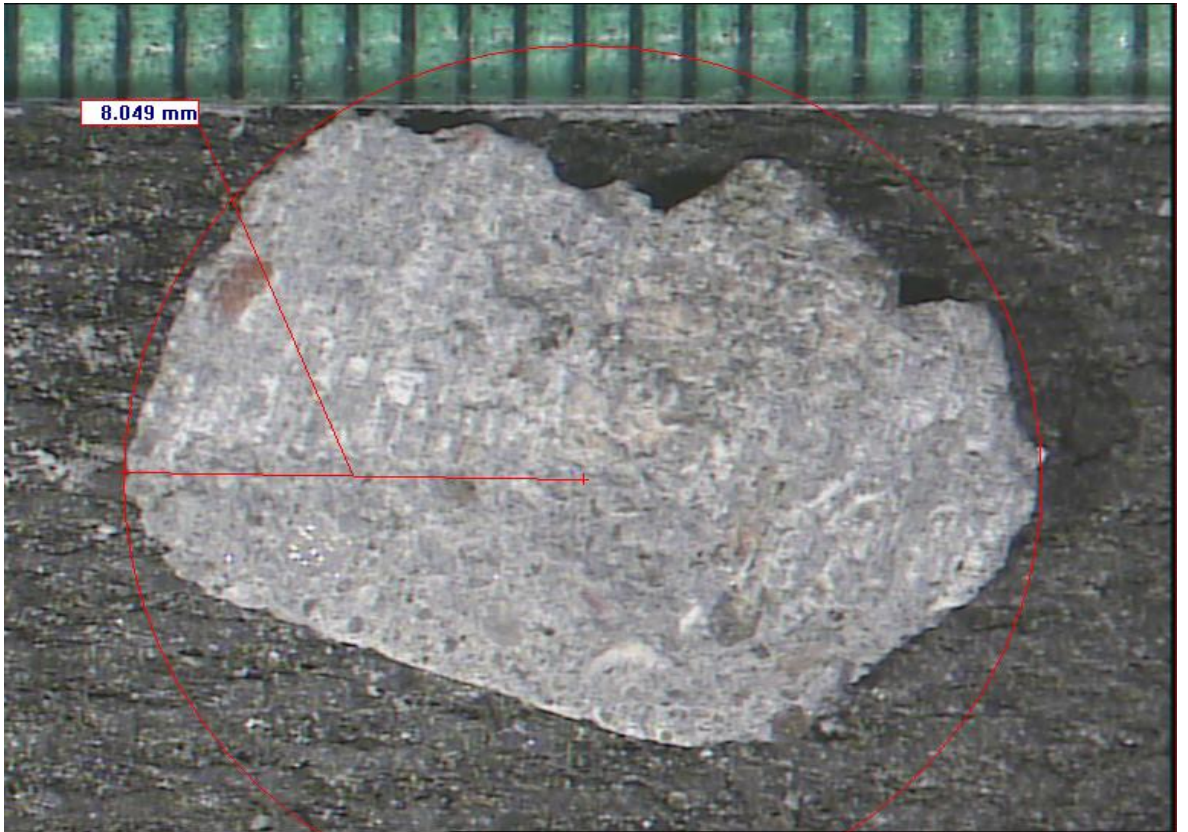
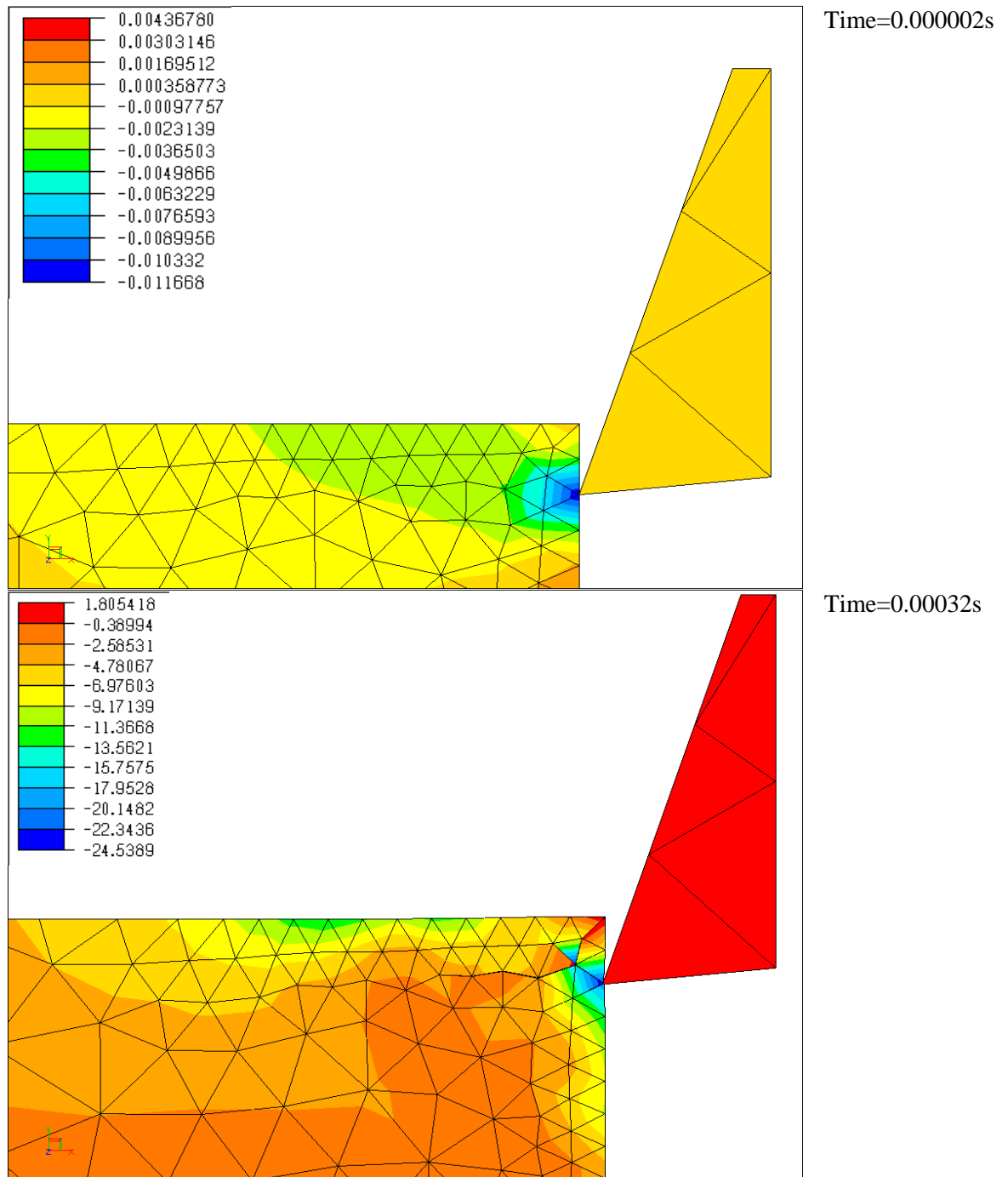
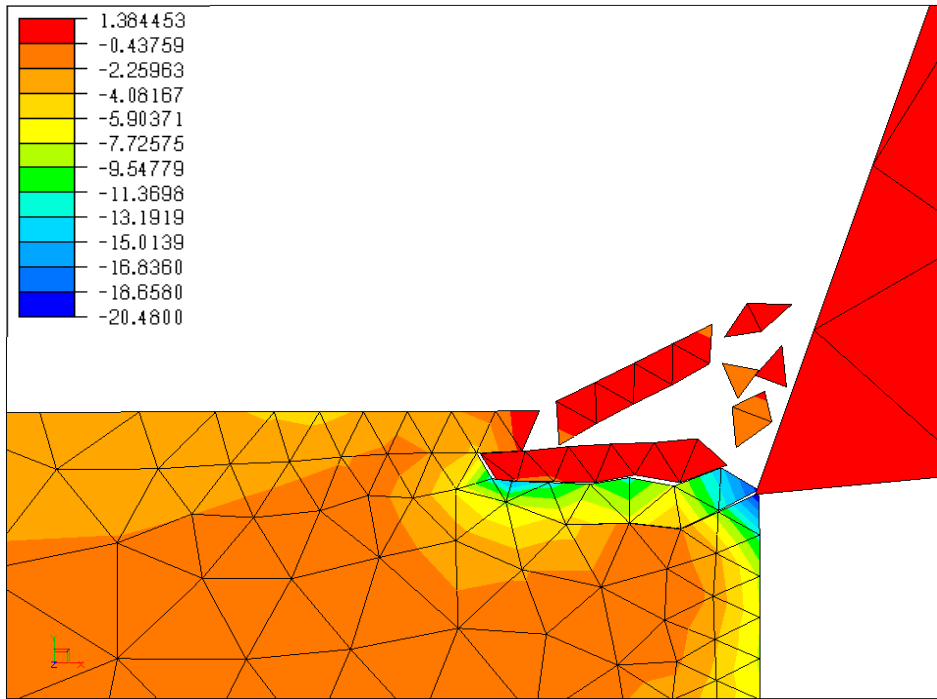


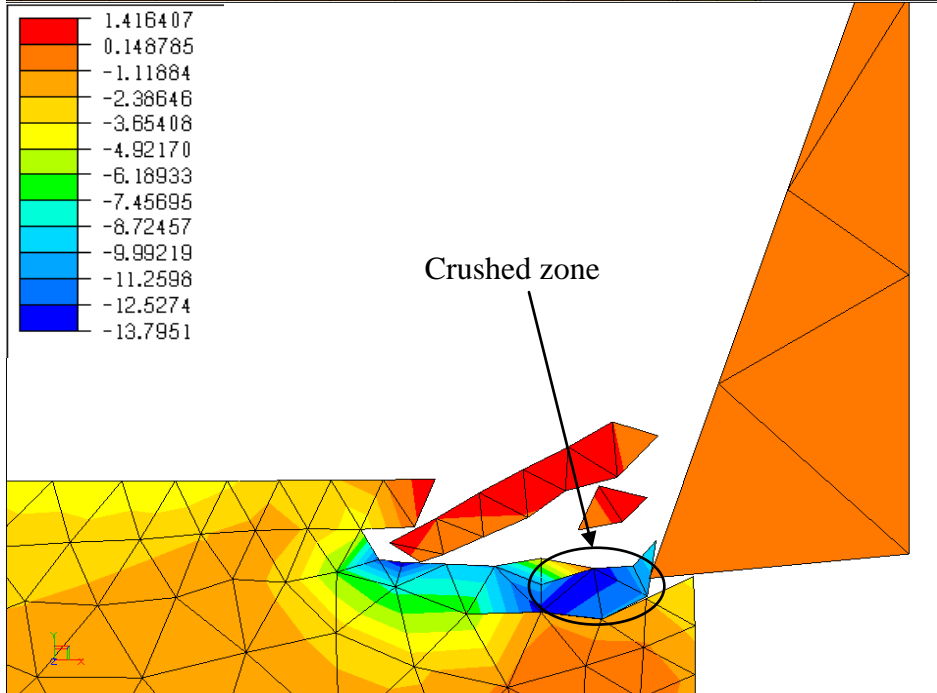
Figure F.30 DEPTH OF CUT: 2.5 mm

APPENDIX G: NUMERICAL SIMULATION OF CUTTING A LOW STRENGTH SAMPLE USING A 20° RAKE ANGLE CUTTING TOOL





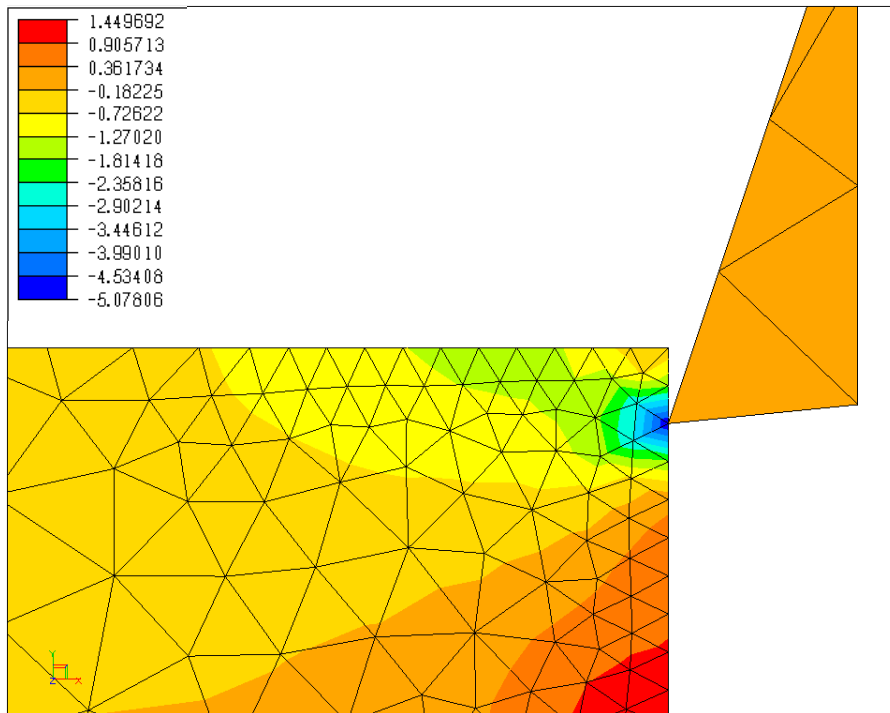
Time=0.0004s



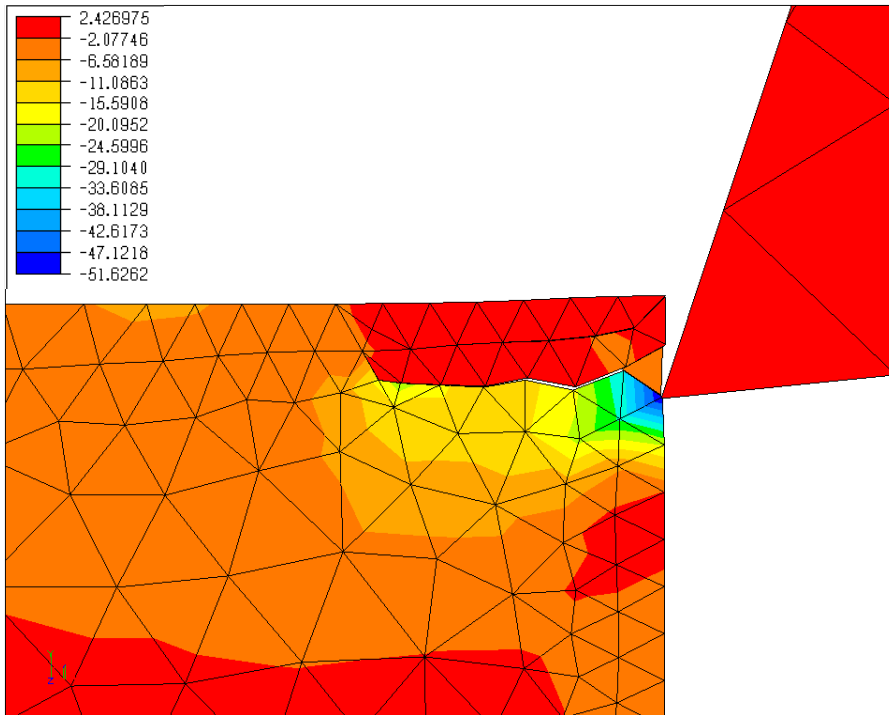
Time=0.003s

Formation of the crushed zone ahead of the tool tip is observed

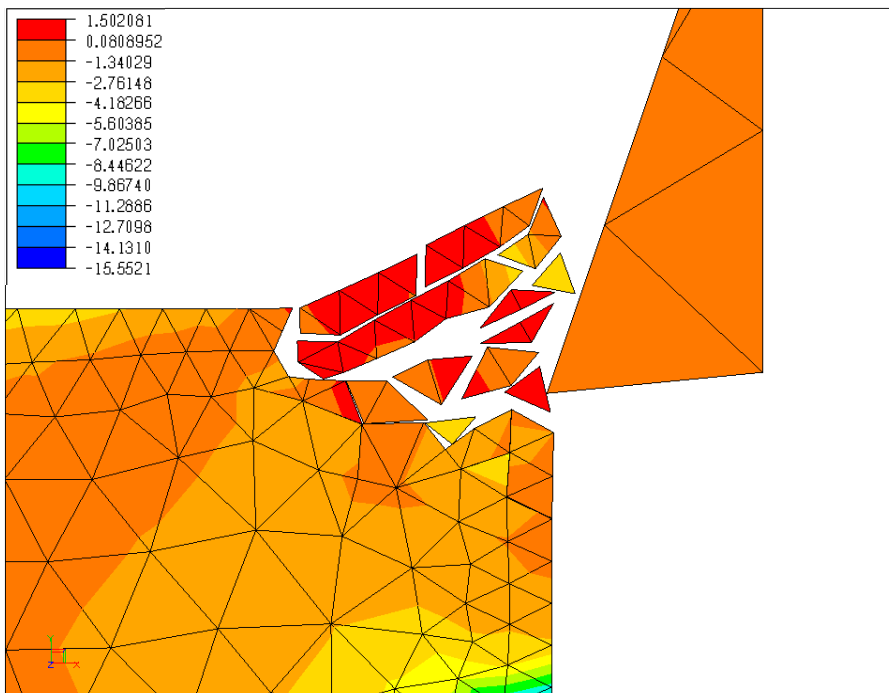
APPENDIX H: NUMERICAL SIMULATION OF CUTTING A HIGH STRENGTH SAMPLE USING A 20° RAKE ANGLE CUTTING TOOL



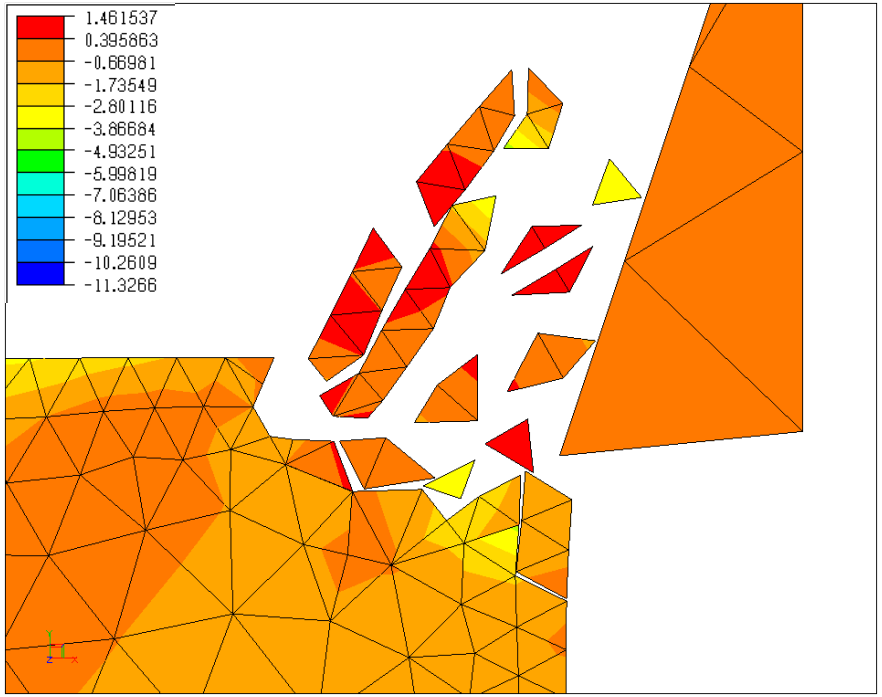
Time=0.0001s



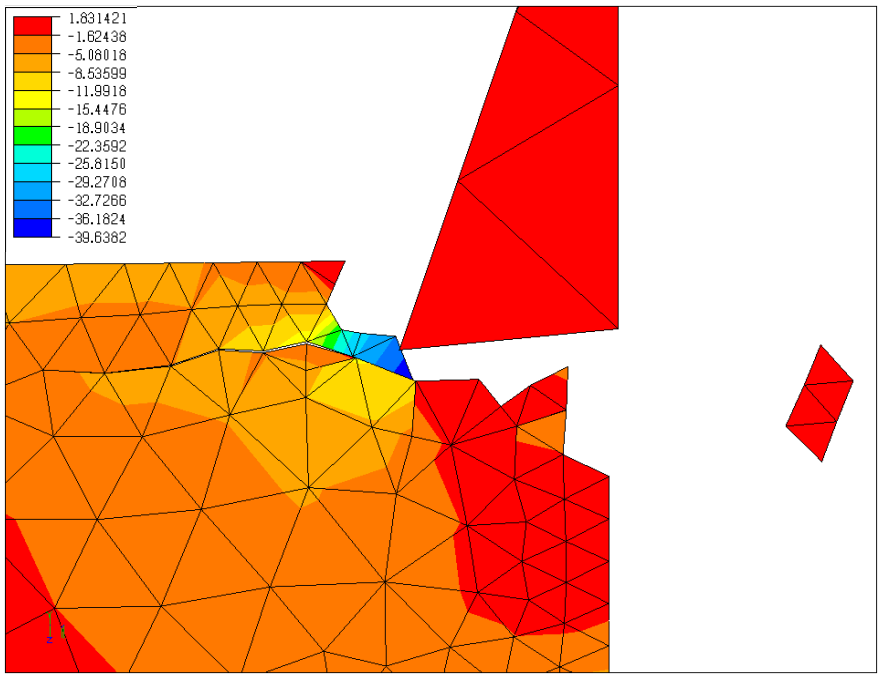
Time=0.0003s



Time=0.0004s



Time=0.0005s



Time=0.016s

